



**HAL**  
open science

# Fabrication, structural and spectroscopic studies of wide bandgap semiconducting nanoparticles of ZnO for application as white light emitting diodes

Yu Zhang

► **To cite this version:**

Yu Zhang. Fabrication, structural and spectroscopic studies of wide bandgap semiconducting nanoparticles of ZnO for application as white light emitting diodes. Material chemistry. Université de Lyon, 2020. English. NNT: . tel-03209228v1

**HAL Id: tel-03209228**

**<https://hal.science/tel-03209228v1>**

Submitted on 27 Apr 2021 (v1), last revised 21 Jun 2022 (v2)

**HAL** is a multi-disciplinary open access archive for the deposit and dissemination of scientific research documents, whether they are published or not. The documents may come from teaching and research institutions in France or abroad, or from public or private research centers.

L'archive ouverte pluridisciplinaire **HAL**, est destinée au dépôt et à la diffusion de documents scientifiques de niveau recherche, publiés ou non, émanant des établissements d'enseignement et de recherche français ou étrangers, des laboratoires publics ou privés.



# INSA

N°d'ordre NNT : 2020LYSEI046

**THESE de DOCTORAT DE L'UNIVERSITE DE LYON**  
opérée au sein de  
**l'INSA de Lyon**

**Ecole Doctorale N° 34**  
**MATÉRIAUX DE LYON**

**Spécialité/ discipline de doctorat :**

Matériaux

Soutenue publiquement le 30/06/2020, par :  
**Yu Zhang**

---

**Fabrication, structural and spectroscopic studies  
of wide bandgap semiconducting nanoparticles of  
ZnO for application as white light emitting diodes**

---

Devant le jury composé de :

Nom, prénom grade/qualité établissement/entreprise **Président.e (à préciser après la soutenance)**

|                      |   |                                  |
|----------------------|---|----------------------------------|
| Chadeyron, Geneviève | Professeure ICCF- Sigma Clermont          | <b>Rapporteuse</b>               |
| Charra, Fabrice      | Directeur de Recherche IRAMIS-CEA         | <b>Rapporteur</b>                |
| Andraud, Chantal     | Directrice de Recherche CNRS, LC-ENS Lyon | <b>Examinatrice , Présidente</b> |
| Rinnert, Hervé       | Professeur IJL-Univ. Lorraine             | <b>Examineur</b>                 |
| Masenelli, Bruno     | Professeur, INL-INSA Lyon                 | Directeur de thèse               |
| Apostoluk, Alexandra | Maitresse de conférence, INL-INSA Lyon    | <b>Co-directrice de thèse</b>    |
| Danièle, Stéphane    | Professeur, C2P2-UCBL1                    | <b>Invité</b>                    |



**Département FEDORA – INSA Lyon - Ecoles Doctorales – Quinquennal 2016-2020**

| <b>SIGLE</b>     | <b>ECOLE DOCTORALE</b>  | <b>NOM ET COORDONNEES DU RESPONSABLE</b>   |
|------------------|---|--|
| <b>CHIMIE</b>    | <b><u>CHIMIE DE LYON</u></b><br><a href="http://www.edchimie-lyon.fr">http://www.edchimie-lyon.fr</a><br>Sec. : Renée EL MELHEM<br>Bât. Blaise PASCAL, 3e étage<br><a href="mailto:secretariat@edchimie-lyon.fr">secretariat@edchimie-lyon.fr</a><br>INSA : R. GOURDON  | <b>M. Stéphane DANIELE</b><br>Institut de recherches sur la catalyse et l'environnement de Lyon<br>IRCELYON-UMR 5256<br>Équipe CDFA<br>2 Avenue Albert EINSTEIN<br>69 626 Villeurbanne CEDEX<br><a href="mailto:directeur@edchimie-lyon.fr">directeur@edchimie-lyon.fr</a>   |
| <b>E.E.A.</b>    | <b><u>ÉLECTRONIQUE,</u></b><br><b><u>ÉLECTROTECHNIQUE,</u></b><br><b><u>AUTOMATIQUE</u></b><br><a href="http://edeea.ec-lyon.fr">http://edeea.ec-lyon.fr</a><br>Sec. : M.C. HAVGOUDOUKIAN <a href="mailto:ecole-doctorale.eea@ec-lyon.fr">ecole-doctorale.eea@ec-lyon.fr</a>  | <b>M. Gérard SCORLETTI</b><br>École Centrale de Lyon<br>36 Avenue Guy DE COLLONGUE<br>69 134 Écully<br>Tél : 04.72.18.60.97 Fax 04.78.43.37.17 <a href="mailto:gerard.scorletti@ec-lyon.fr">gerard.scorletti@ec-lyon.fr</a>  |
| <b>E2M2</b>      | <b><u>ÉVOLUTION, ÉCOSYSTÈME,</u></b><br><b><u>MICROBIOLOGIE, MODÉLISATION</u></b><br><a href="http://e2m2.universite-lyon.fr">http://e2m2.universite-lyon.fr</a><br>Sec. : Sylvie ROBERJOT<br>Bât. Atrium, UCB Lyon 1<br>Tél : 04.72.44.83.62 INSA : H. CHARLES<br><a href="mailto:secretariat.e2m2@univ-lyon1.fr">secretariat.e2m2@univ-lyon1.fr</a> | <b>M. Philippe NORMAND</b><br>UMR 5557 Lab. d'Ecologie Microbienne<br>Université Claude Bernard Lyon 1<br>Bâtiment Mendel<br>43, boulevard du 11 Novembre 1918 69<br>622 Villeurbanne CEDEX<br><a href="mailto:philippe.normand@univ-lyon1.fr">philippe.normand@univ-lyon1.fr</a>  |
| <b>EDISS</b>     | <b><u>INTERDISCIPLINAIRE</u></b><br><b><u>SCIENCES-SANTÉ</u></b><br><a href="http://www.ediss-lyon.fr">http://www.ediss-lyon.fr</a><br>Sec. : Sylvie ROBERJOT<br>Bât. Atrium, UCB Lyon 1<br>Tél : 04.72.44.83.62<br>INSA : M. LAGARDE<br><a href="mailto:secretariat.ediss@univ-lyon1.fr">secretariat.ediss@univ-lyon1.fr</a>                         | <b>Mme Sylvie RICARD-BLUM</b><br>Institut de Chimie et Biochimie Moléculaires et Supramoléculaires<br>(ICBMS) - UMR 5246 CNRS - Université Lyon 1<br>Bâtiment Curien - 3ème étage Nord<br>43 Boulevard du 11 novembre 1918<br>69622 Villeurbanne Cedex Tel :<br>+33(0)4 72 44 82 32 <a href="mailto:sylvie.ricard-blum@univ-lyon1.fr">sylvie.ricard-blum@univ-lyon1.fr</a> |
| <b>INFOMATHS</b> | <b><u>INFORMATIQUE ET</u></b><br><b><u>MATHÉMATIQUES</u></b><br><a href="http://edinfomaths.universite-lyon.fr">http://edinfomaths.universite-lyon.fr</a><br>Sec. : Renée EL MELHEM<br>Bât. Blaise PASCAL, 3e étage<br>Tél : 04.72.43.80.46 <a href="mailto:infomaths@univ-lyon1.fr">infomaths@univ-lyon1.fr</a>                                      | <b>M. Hamamache KHEDDOUCI</b><br>Bât. Nautibus<br>43, Boulevard du 11 novembre 1918<br>69 622 Villeurbanne Cedex France<br>Tel : 04.72.44.83.69<br><a href="mailto:hamamache.kheddouci@univ-lyon1.fr">hamamache.kheddouci@univ-lyon1.fr</a>  |
| <b>Matériaux</b> | <b><u>MATÉRIAUX DE LYON</u></b><br><a href="http://ed34.universite-lyon.fr">http://ed34.universite-lyon.fr</a><br>Sec. : Stéphanie CAUVIN<br>Tél : 04.72.43.71.70<br>Bât. Direction<br><a href="mailto:ed.materiaux@insa-lyon.fr">ed.materiaux@insa-lyon.fr</a>   | <b>M. Jean-Yves BUFFIÈRE</b><br>INSA de Lyon<br>MATEIS - Bât. Saint-Exupéry<br>7 Avenue Jean CAPELLE<br>69 621 Villeurbanne CEDEX<br>Tél : 04.72.43.71.70 Fax : 04.72.43.85.28 <a href="mailto:jean-yves.buffiere@insa-lyon.fr">jean-yves.buffiere@insa-lyon.fr</a>  |
| <b>MEGA</b>      | <b><u>MÉCANIQUE, ÉNERGÉTIQUE,</u></b><br><b><u>GÉNIE CIVIL, ACOUSTIQUE</u></b><br><a href="http://edmega.universite-lyon.fr">http://edmega.universite-lyon.fr</a><br>Sec. : Stéphanie CAUVIN<br>Tél : 04.72.43.71.70<br>Bât. Direction<br><a href="mailto:mega@insa-lyon.fr">mega@insa-lyon.fr</a>  | <b>M. Jocelyn BONJOUR</b> INSA<br>de Lyon<br>Laboratoire CETHIL<br>Bâtiment Sadi-Carnot<br>9, rue de la Physique<br>69 621 Villeurbanne CEDEX <a href="mailto:jocelyn.bonjour@insa-lyon.fr">jocelyn.bonjour@insa-lyon.fr</a>   |
| <b>ScSo</b>      | <b><u>ScSo*</u></b><br><a href="http://ed483.univ-lyon2.fr">http://ed483.univ-lyon2.fr</a><br>Sec. : Véronique GUICHARD<br>INSA : J.Y. TOUSSAINT<br>Tél : 04.78.69.72.76<br><a href="mailto:veronique.cervantes@univ-lyon2.fr">veronique.cervantes@univ-lyon2.fr</a>  | <b>M. Christian MONTES</b><br>Université Lyon 2<br>86 Rue Pasteur<br>69 365 Lyon CEDEX 07 <a href="mailto:christian.montes@univ-lyon2.fr">christian.montes@univ-lyon2.fr</a>   |

\*ScSo : Histoire, Géographie, Aménagement, Urbanisme, Archéologie, Science politique, Sociologie, Anthropologie



## Acknowledgement

This thesis was accomplished under the direction of my two supervisors, Bruno Masenelli and Aleksandra Apostoluk, who helped me in so many ways throughout the PhD years, from resolving scientific issues, to planning personal career, and to adapting to local environment. It was reassuring to have two mentors to whom I could always turn for help when needed. They always encouraged me to become an independent researcher and gave me invaluable advice without reservation on how to achieve it. The lessons I learnt from them not only assisted me in conquering the biggest challenge in my life, but will also benefit me in the long term, both professionally and personally. I am forever grateful for their guidance.

The projects in the thesis would not have been possible without our collaborators, the team of Stéphane Daniele from C2P2, IRCELYON, and Lotus Synthesis SAS. The preparation of the materials is attributed to Nicolas Le Bail, Thibaut Cornier, Christophe Theron, and Timoté Gard. The expertise of the team in the chemical processes is valuable and their cooperation in the design of the materials is highly appreciated.

My heartfelt appreciation also goes to those who provided their assistance in certain characterizations and analyses. I would like to thank Karine Masenelli-Varlot for her expertise in TEM and Bruno Canut for his expertise in RBS. Jean-Marie Bluet helped me with several characterizations, including FTIR and PLE measurements. Fabien Mandorlo shared his knowledge in CIE color space and calculated the positions of the spectra of our samples in UCS diagrams. Sandrine Cardinal provided technical and scientific assistance in the acquisition of XRD spectra. I learnt a great deal from each of them and I am grateful for their kind help and shared knowledge.

We are indebted to the team of Christophe Dujardin from iLM for their contribution in the characterization of thermal stability. In particular, I wish to thank Gilles Ledoux for his thorough guidance in the experiments.

The thesis program was supported by the cooperation between INSA Lyon and China Scholarship Council. My sincerest gratitude is obliged to both establishments, for providing me with the opportunity to join the excellent team at Institute of Nanotechnology of Lyon (INL). The scientific platform provided by INL is deeply appreciated and I am grateful for the administration team and the technical staff as they made my time at the laboratory easy and enjoyable.

I would like to express my thanks to the colleagues at INL whom I have the honor to call my friends, Ali Jaffal, Nicolas Gaignebet, Florian Berry, Benoit Guillo-Lohan, Nelly Moulin, Xiao Li, Benjamin Fornacciari, Solène Brottet, Alexander Singaevsky, and Sofia Rodichkina, for sharing some of the most memorable moments in my PhD years. It has been a great pleasure to work and discuss with them. I

would also like to acknowledge many other friends, for their support and encouragement, especially the PhD holders, for sharing their personal experience and wisdom.

Finally, I cannot thank enough my family and Tazman Davies for their full support throughout the PhD.

# **Fabrication, études structurales et spectroscopiques de nanoparticules semi-conductrices à large bande interdite de ZnO pour application en diodes électroluminescentes blanches**

## **Résumé**

L'industrie de l'éclairage est actuellement dominée par les luminophores à base de terres rares. Une utilisation à si grande échelle d'éléments de terres rares est à l'origine de problèmes environnementaux et contribue au changement climatique. Grâce à ses défauts intrinsèques, ZnO a été considéré comme un luminophore potentiellement exempt de terres rares pour les diodes électroluminescentes blanches (WLEDs). L'objectif de cette thèse est de développer un matériau électroluminescent blanc efficace et stable à base de nanoparticules de ZnO. Un système nanohybride de nanoparticules de ZnO incorporées dans des mésosphères d'acide polyacrylique (PAA) a été développé par voie d'hydrolyse. Trois défis doivent être relevés pour que le système nanohybride ZnO / PAA soit applicable aux WLEDs. La première consiste à régler la couleur, ou la chaleur, d'émission du système, pour répondre aux exigences spécifiques des WLEDs; la deuxième est d'améliorer le rendement quantique de photoluminescence (PL QY); la dernière consiste à améliorer la stabilité thermique du système, car les WLEDs fonctionnent généralement au-dessus de la température ambiante. Deux études sont menées pour aborder ces questions.

Dans la première étude, le dopage par des éléments autres que des terres non rares est employé pour régler la couleur d'émission de ZnO. L'objectif est d'acquérir une compréhension générale de l'effet du dopage sur les propriétés structurales et optiques du nanohybride ZnO / PAA. Une série de dopants métalliques de nature, taille, valence et concentration différentes sont introduits indépendamment dans le système nanohybride au cours du processus d'hydrolyse. On constate que la présence de dopant a un impact sur la structure mésosphérique. Des concentrations de dopage élevées peuvent rendre les mésosphères plus grosses et les gros ions peuvent même inhiber la formation des mésosphères. La taille des cristaux de ZnO est également affectée par le dopage. Les nanohybrides dopés présentent une large émission visible, avec un décalage vers le rouge du pic d'émission de 2,47 eV de ZnO non dopé jusqu'à 2,08 eV. Le décalage dépend de la nature, de la valence et de la concentration du dopant. Le PL QY est généralement réduit par le dopage, quel que soit le dopant. Cependant, il peut être maintenu ou même amélioré en dopant avec de petits ions à une faible concentration de dopage (0,1 at%). La couleur d'émission du ZnO dopé peut être réglée entre 2,47 eV et 2,17 eV sans dégrader PL QY.

Dans la deuxième étude, un revêtement de silice est adopté pour améliorer le PL QY et la stabilité thermique du nanohybride ZnO / PAA. Différents précurseurs de ZnO / PAA sont enrobés de silice par l'hydrolyse d'orthosilicate de tétraéthyle (TEOS) en présence d'ammoniac ( $\text{NH}_4\text{OH}$ ). Les quantités de TEOS et de  $\text{NH}_4\text{OH}$  sont deux facteurs corrélés qui déterminent l'intégrité des mésosphères de PAA et

l'épaisseur du revêtement de silice. Les effets de la dose de TEOS et de la concentration d'ammoniac sont étudiés indépendamment. La structure cristallographique des nanocristaux de ZnO n'est pas modifiée par le revêtement de silice, qui est incorporé sous forme de phase amorphe. Le PL QY est aisément amélioré par un revêtement de silice dans la plupart des cas, avec une amélioration optimale du PL QY de 619 % par rapport à celle du précurseur ZnO / PAA. Un modèle de structure est établi pour expliquer l'évolution des mésosphères au cours du processus de revêtement. Le cœur du modèle est l'amination des groupes COOH dans les chaînes de PAA, qui dégrade les mésosphères. L'amélioration optimale de PL QY est obtenue lorsque les mésosphères sont conservées par une quantité appropriée d'ammoniac et sont renforcées par un revêtement de silice d'une épaisseur appropriée.

Enfin, la stabilité thermique du ZnO / PAA dopé au métal ou revêtu de silice est examinée de la température ambiante à 100 ° C. Pour les deux matériaux, l'intensité de l'émission visible diminue à mesure que la température augmente. Le revêtement de silice réduit l'impact de la chaleur sur le matériau en améliorant considérablement le PL QY. Le problème est atténué dans une certaine mesure mais pas complètement éliminé.

## Abstract

The lighting industry is currently dominated by rare-earth-based phosphors. Such large-scale use of rare-earth elements is causing environmental issues and contributing to the climate change. Owing to its intrinsic defects, ZnO has been considered a potential rare-earth-free phosphor for white light-emitting diodes (WLEDs). The objective of the thesis is to develop an efficient and stable white light-emitting material based on ZnO nanoparticles. A nanohybrid system comprising mainly ZnO nanocrystals embedded in polyacrylic acid (PAA) mesospheres has been developed via hydrolysis route. Three challenges are to be met for the ZnO/PAA nanohybrid system to be applicable in WLEDs. The first is to tune the emission color, or warmth, of the system, to meet specific requirements of WLEDs; the second is to improve the photoluminescence quantum yield (PL QY); the last is to enhance the thermal stability of the system, for WLEDs usually operate above room temperature. Two studies are carried out to undertake the above issues.

In the first study, doping of non-rare-earth elements is employed to tune the emission color of ZnO. The aim is to gain a general understanding of the effect of doping on the structural and optical properties of the ZnO/PAA nanohybrid. A series of metal dopants of different nature, size, valence, and concentration are independently introduced into the nanohybrid system during the hydrolysis process. It is found that the presence of dopant has an impact on the mesospheric structure. High doping concentrations may render bigger mesospheres and large ions can even inhibit the formation of the mesospheres. The crystal size of ZnO is also affected by doping. The doped nanohybrids exhibit a broad visible emission, with a redshift of emission peak from 2.47 eV of undoped ZnO to as far as 2.08 eV. The redshift is dependent on the nature, valence, and concentration of the dopant. The PL QY is generally reduced by doping, regardless of the dopant. However, it can be maintained or even improved by doping small ions at a low doping concentration (0.1 at%). The emission color of doped ZnO can be tuned between 2.47 eV and 2.17 eV without degrading PL QY.

In the second study, silica coating is adopted to improve the PL QY and the thermal stability of ZnO/PAA nanohybrid. Different ZnO/PAA precursors are coated by silica via hydrolysis of tetraethyl orthosilicate (TEOS) under the presence of ammonia ( $\text{NH}_4\text{OH}$ ). The amounts of TEOS and  $\text{NH}_4\text{OH}$  are two correlated factors that determine the integrity of the PAA mesospheres and the thickness of silica coating. The effects of TEOS loading and ammonia concentration are investigated independently. The crystallographic structure of ZnO nanocrystals is not modified by silica coating, which is incorporated as an amorphous phase. The PL QY is readily improved by silica coating in most cases, with an optimal PL QY improvement by 619 % from that of ZnO/PAA precursor. A structure model is established to explain the evolution of mesospheres during the coating process. The core of the model is the amination of COOH groups in PAA chains, which degrades the mesospheres. The optimal PL QY improvement is

achieved when the mesospheres are preserved under an appropriate amount of ammonia and are strengthened by silica coating with an appropriate thickness.

Finally, the thermal stability of both metal-doped and silica-coated ZnO/PAA is examined from room temperature to 100 °C. For both materials, the intensity of the visible emission decreases as the temperature increases. Silica coating reduces the impact of heat on the material by drastically improving the PL QY. The issue is alleviated to some extent but not completely eliminated.

# Contents

|  |     |
|--|-----|
| <b>Résumé</b> .....                                    | I   |
| <b>Abstract</b> .....                                  | III |
| <b>List of Acronyms and Abbreviations</b> .....        | v   |
| <b>List of Figures</b> .....                           | vii |
| <b>Chapter 1 State-of-the-Art</b> .....                | 1   |
| Context .....  | 1   |
| 1.1 White light-emitting diodes (WLEDs) .....          | 1   |
| 1.1.1 WLEDs criteria.....                              | 2   |
| 1.1.1.1 Quantum efficiency .....                       | 2   |
| 1.1.1.2 Correlated color temperature .....             | 3   |
| 1.1.1.3 Color rendering index.....                     | 3   |
| 1.1.1.4 Other criteria.....                            | 5   |
| 1.1.2 UV-excited phosphors .....                       | 5   |
| 1.1.3 Blue-excited phosphors .....                     | 6   |
| 1.1.4 ZnO as RE-free phosphor .....                    | 8   |
| 1.2 Undoped ZnO .....                                  | 9   |
| 1.2.1 Photoluminescence of undoped ZnO.....            | 9   |
| 1.2.2 UV emission .....                                | 11  |
| 1.2.3 Visible emission .....                           | 14  |
| 1.3 Doping of ZnO .....                                | 17  |
| 1.3.1 Rare-earth doping .....                          | 17  |
| 1.3.2 Non-rare-earth doping .....                      | 21  |
| 1.3.3 Summary on doping .....                          | 25  |
| 1.4 ZnO nanostructures .....                           | 26  |
| <b>Chapter 2 Materials and Characterizations</b> ..... | 29  |
| 2.1 Syntheses of ZnO-based nanomaterials.....          | 29  |

|   |  |           |
|---|--|-----------|
| 2.1.1   | Hydrolysis of ZnEt <sub>2</sub> .....                                | 29        |
| 2.1.2   | Metal-doped ZnO nanohybrids.....                                     | 30        |
| 2.1.3   | Silica-coated ZnO nanohybrids .....                                  | 32        |
| 2.2   | Structural characterizations .....                                   | 33        |
| 2.2.1   | X-Ray Diffraction.....   | 34        |
| 2.2.2   | Transmission Electron Microscopy .....                               | 36        |
| 2.2.3   | Rutherford Backscattering Spectrometry .....                         | 38        |
| 2.2.4   | Fourier Transform Infrared spectroscopy.....                         | 39        |
| 2.3   | Optical characterizations .....                                      | 41        |
| 2.3.1   | Photoluminescence spectroscopy .....                                 | 41        |
| 2.3.2   | Photoluminescence Excitation spectroscopy.....                       | 42        |
| 2.3.3   | Measurement and calculation of photoluminescence quantum yield ..... | 43        |
| 2.3.4   | Photoluminescence at high temperature .....                          | 47        |
| <b>Chapter 3 Metal-Doped ZnO Nanohybrids.....</b> |  | <b>49</b> |
| 3.1   | Microstructure of metal-doped ZnO nanohybrids.....                   | 49        |
| 3.1.1   | Morphology .....   | 49        |
| 3.1.2   | Crystal structure indexing.....                                      | 52        |
| 3.1.3   | Presence of PAA.....   | 54        |
| 3.1.4   | Presence of dopants .....  | 55        |
| 3.1.5   | Effect of dopant on the microstructure .....                         | 57        |
| 3.1.5.1   | Mesosphere structure.....  | 57        |
| 3.1.5.2   | Crystal structure.....   | 58        |
| 3.1.5.3   | Crystal size .....   | 61        |
| 3.1.5.4   | Summary .....  | 62        |
| 3.2   | Optical properties of metal-doped ZnO nanohybrids.....               | 62        |
| 3.2.1   | Photoluminescence .....  | 62        |
| 3.2.1.1   | Effect of dopant type .....  | 63        |
| 3.2.1.2   | Effect of doping concentration .....                                 | 64        |

|  |   |           |
|--|---|-----------|
| 3.2.1.3  | Effect of valence.....                        | 64        |
| 3.2.1.4  | Summary .....                                 | 67        |
| 3.2.2  | Photoluminescence quantum yield .....         | 68        |
| 3.2.3  | Photoluminescence excitation .....            | 69        |
| 3.2.4  | Role of dopant .....                          | 70        |
| 3.2.4.1  | Dopants during hydrolysis synthesis .....     | 70        |
| 3.2.4.2  | Dopants in the nanohybrid.....                | 72        |
| 3.2.5  | Photoluminescence at high temperature .....   | 74        |
| 3.3  | Conclusion.....                               | 75        |
| <b>Chapter 4 Silica-Coated ZnO Nanohybrids .....</b> |   | <b>77</b> |
| 4.1  | Instability of ZnO/PAA precursors .....       | 77        |
| 4.2  | Effect of TEOS ratio.....                     | 81        |
| 4.2.1  | Microstructure .....                          | 81        |
| 4.2.1.1  | X-ray diffraction.....                        | 81        |
| 4.2.1.2  | Transmission electron microscopy .....        | 83        |
| 4.2.1.3  | Fourier transform infrared spectroscopy ..... | 84        |
| 4.2.1.4  | Summary .....                                 | 85        |
| 4.2.2  | Optical properties .....                      | 86        |
| 4.2.2.1  | Photoluminescence .....                       | 86        |
| 4.2.2.2  | Photoluminescence quantum yield .....         | 86        |
| 4.3  | Effect of ammonia content .....               | 87        |
| 4.3.1  | Microstructure .....                          | 88        |
| 4.3.1.1  | X-ray diffraction.....                        | 88        |
| 4.3.1.2  | Transmission electron microscopy .....        | 89        |
| 4.3.1.3  | Rutherford backscattering spectrometry.....   | 92        |
| 4.3.1.4  | Structure model .....                         | 93        |
| 4.3.2  | Optical properties .....                      | 94        |
| 4.3.2.1  | Photoluminescence .....                       | 94        |

|   |                                       |     |
|---|---------------------------------------|-----|
| 4.3.2.2   | Photoluminescence quantum yield ..... | 96  |
| 4.3.2.3   | Photoluminescence excitation .....    | 97  |
| 4.3.3   | Thermal stability.....                | 98  |
| 4.4   | Role of silica coating.....           | 101 |
| 4.5   | Conclusion.....                       | 102 |
| <b>General Conclusions</b> .....  |                                       | 105 |
| <b>References</b> .....   |                                       | 107 |
| <b>Appendix I</b> XRD spectra of metal-doped ZnO nanohybrids .....                  |                                       | 121 |
| <b>Appendix II</b> HRTEM images of metal-doped ZnO nanohybrids .....                |                                       | 124 |
| <b>Appendix III</b> FTIR spectra of metal-doped ZnO nanohybrids.....                |                                       | 126 |
| <b>Appendix IV</b> RBS spectra of metal-doped ZnO nanohybrids.....                  |                                       | 131 |
| <b>Appendix V</b> PL spectra of metal-doped ZnO nanohybrids.....                    |                                       | 133 |
| <b>Appendix VI</b> EDX spectrum of silica-coated ZnO/PAA nanohybrid (3.8Si-1A)..... |                                       | 138 |
| <b>Appendix VII</b> PL spectra of silica-coated ZnO/PAA nanohybrids .....           |                                       | 139 |

## List of Acronyms and Abbreviations

|          |  |
|----------|--|
| BBE      | Band to Band Emission                            |
| CB       | Conduction Band                                  |
| CCD      | Charge-Coupled Device                            |
| CCT      | Correlated Color Temperature                     |
| CIE      | Commission Internationale de l'Éclairage         |
| CRI      | Color Rendering Index                            |
| DAP      | Donor-Acceptor Pairs                             |
| DLE      | Deep Level Emission                              |
| EDS, EDX | Energy Dispersive X-Ray Spectroscopy             |
| EQE      | External Quantum Efficiency                      |
| FFT      | Fast Fourier Transform                           |
| FTIR     | Fourier Transform Infrared Spectroscopy          |
| HAADF    | High Angle Annular Dark-Field                    |
| HRTEM    | High-Resolution Transmission Electron Microscopy |
| IQE      | Internal Quantum Efficiency                      |
| IR       | Infrared   |
| LED      | Light-Emitting Diode                             |
| MBE      | Molecular Beam Epitaxy                           |
| NBE      | Near Band Edge Emission                          |
| $O_i$    | Oxygen Interstitial                              |
| $O_{Zn}$ | Oxygen Anti-Site                                 |
| PAA      | Polyacrylic Acid                                 |
| PAAH     | Protonated Polyacrylic Acid                      |
| PL       | Photoluminescence                                |

|                           |  |
|---------------------------|--|
| PLE                       | Photoluminescence Excitation                                       |
| QE                        | Quantum Efficiency   |
| RBS                       | Rutherford Backscattering Spectrometry                             |
| RE                        | Rare Earth   |
| REE                       | Rare Earth Elements  |
| RGB                       | Red, Green and Blue  |
| RT                        | Room Temperature   |
| STEM                      | Scanning Transmission Electron Microscopy                          |
| TEM                       | Transmission Electron Microscopy, Transmission Electron Microscope |
| TEOS                      | Tetraethyl Orthosilicate   |
| TM                        | Transition Metal   |
| UV                        | Ultraviolet  |
| VB                        | Valence Band   |
| $V_{\text{O}}$            | Oxygen Vacancy   |
| $V_{\text{O}}\text{Zn}_i$ | Oxygen Vacancy Zinc Interstitial Defect Complex                    |
| $V_{\text{Zn}}$           | Zinc Vacancy   |
| WLED                      | White Light-Emitting Diode   |
| XPS                       | X-ray Photoelectron Spectroscopy                                   |
| XRD                       | X-Ray Diffraction  |
| YAG:Ce                    | Cerium-doped Yttrium Aluminum Garnet                               |
| PL                        | Photoluminescence  |
| PL QY                     | Photoluminescence Quantum Yield                                    |
| $\text{ZnEt}_2$           | Diethyl Zinc   |
| $\text{Zn}_{\text{O}}$    | Zinc Anti-Site   |
| $\text{Zn}_i$             | Zinc Interstitial  |

## List of Figures

|   |    |
|---|----|
| <b>Figure 1.1</b> Three approaches to generate white light with LEDs: (a) with single RGB LEDs, (b) with full conversion of UV LED, and (c) with partial conversion of blue LED. [7].....   | 2  |
| <b>Figure 1.2</b> (a) Commission Internationale de l'Éclairage (CIE, 1931) diagram with a black-body radiation curve (black solid line) and CCT values. (b) Luminescence spectrum of YAG:Ce and human eye sensitivity curve in grey-shaded spectrum. [7].....                                     | 4  |
| <b>Figure 1.3</b> PL spectra of $\text{Ba}_2\text{Ca}(\text{B}_3\text{O}_6)_2:0.04\text{Eu}^{2+}, y\text{Mn}^{2+}$ phosphors ( $\lambda_{\text{ex}} = 330 \text{ nm}$ ). Inset shows the dependence of the energy transfer efficiency $\eta_T$ on the $\text{Mn}^{2+}$ content ( $y$ ). [18]..... | 6  |
| <b>Figure 1.4</b> PL excitation and PL emission spectra of 2 mol% Ce-doped YAG ( $\lambda_{\text{em}} = 532 \text{ nm}$ , $\lambda_{\text{ex}} = 470 \text{ nm}$ ). [29].....   | 7  |
| <b>Figure 1.5</b> (a) Wurtzite crystal structure of ZnO with indicated lattice parameters $a$ and $c$ . (b) Calculated band structure of ZnO. The energy of the valence band maximum was set to zero. [55] .....  | 9  |
| <b>Figure 1.6</b> Photoluminescent processes in ZnO. ....   | 10 |
| <b>Figure 1.7</b> PL spectra from ZnO epilayer obtained at (a) low temperature and (b) room temperature. The inset in (a) displays the details of the PL spectrum at near band edge (NBE) region. [65] .....  | 12 |
| <b>Figure 1.8</b> Normalized PL spectra of ZnO thin films for various excitation intensities at (a) room temperature and at (b) 550 K. [60] .....   | 13 |
| <b>Figure 1.9</b> Thermodynamic transition levels for defects in ZnO. [78].....   | 14 |
| <b>Figure 1.10</b> Transition levels (measured with respect to the edge of the conduction band) of defects in ZnO reported in literature by different groups. (a) Ref [83]. (b) Ref [84]. (c) Ref [85]. (d) Ref [86]. (e) Ref [87]. (f) Ref [78]. (g) Ref [88], [89].....                         | 15 |
| <b>Figure 1.11</b> Schematic diagram for the mechanism of visible emission from Ce-doped ZnO. [105]..   | 18 |
| <b>Figure 1.12</b> XRD patterns of Ce-doped ZnO nanoparticles. [110].....   | 19 |
| <b>Figure 1.13</b> (a) PL spectra of undoped ZnO and Ce-doped ZnO. The inset shows a schematic diagram of $\text{Ce}^{3+}$ electronic levels in ZnO bandgap. (b) Normalized PL spectra in the visible range of undoped and Ce-doped ZnO.....  | 20 |
| <b>Figure 1.14</b> Schematic of the energy level diagram of Cu-doped ZnO system. [131] .....  | 22 |

|   |    |
|---|----|
| <b>Figure 1.15</b> Various morphologies of ZnO nanostructures: (a) and (b) tetrapod structures; (c) variable diameter structures; (d) nanosheets; (e) nanoshells; (f) multipods; (g), (h), and (i) nanorods. [120] .....  | 26 |
| <b>Figure 1.16</b> Illustration of the mechanism on the origin of the visible emission in ZnO nanocrystal..   | 27 |
| <b>Figure 2.1</b> Mesospheres of ZnO nanocrystals embedded in PAA matrix. The inset permits to notice small nanocrystals of ZnO, smaller than 10 nm. [187].....   | 29 |
| <b>Figure 2.2</b> PL spectrum of ZnO nanohybrid obtained in previous study. [187].....  | 30 |
| <b>Figure 2.3</b> XRD setup for the study of polycrystalline materials. ....  | 34 |
| <b>Figure 2.4</b> X-ray scattering from crystalline planes. ....  | 35 |
| <b>Figure 2.5</b> Theoretical diffraction lines of polycrystalline wurtzite ZnO.....  | 35 |
| <b>Figure 2.6</b> Schemes of imaging mode (left) and diffraction mode (right) of TEM.....   | 37 |
| <b>Figure 2.7</b> Structure indexing via fast Fourier transform (FFT) in HRTEM image. ....  | 37 |
| <b>Figure 2.8</b> Schematic of a Michelson interferometer. ....   | 40 |
| <b>Figure 2.9</b> Exemplary IR spectrum of bulk ZnO. The transmittance is normalized between 0 and 1. [193] .....   | 40 |
| <b>Figure 2.10</b> PL spectroscopy experimental setup.....  | 42 |
| <b>Figure 2.11</b> Typical PLE spectrum (in blue) of ZnO along with its PL spectrum (in green). $\lambda_{em} = 577$ nm, $\lambda_{ex} = 266$ nm. [195].....  | 43 |
| <b>Figure 2.12</b> Illustration of three configurations with an integrating sphere for PL QY measurement. (a) The sample is not present in the sphere. (b) The sample is present but the laser is not directed onto the sample. (c) The sample is present and the laser is directed onto the sample. .... | 44 |
| <b>Figure 2.13</b> Schematic of the setup for PL QY measurements.....   | 45 |
| <b>Figure 2.14</b> Reflectance spectrum of Spectralon coating material of the integrating sphere. ....  | 45 |
| <b>Figure 2.15</b> Typical laser profile and emission profile from measurement (c) for ZnO nanohybrids. The emission profile is enlarged 30 times. ....   | 46 |
| <b>Figure 3.1</b> Morphologies of (a) 0.1 % Mn-doped ZnO nanohybrid and (b) 5 % Mn-doped ZnO nanohybrid.....  | 50 |
| <b>Figure 3.2</b> Morphologies of ZnO nanohybrids doped with different elements at 0.1 %. (a) Cu(II) doping. (b) Bi doping.....   | 51 |
| <b>Figure 3.3</b> XRD spectra of Co-doped ZnO nanohybrids at 0.1 %, 1 % and 5 % doping concentrations. ....   | 52 |

|   |    |
|---|----|
| <b>Figure 3.4</b> HRTEM images of (a) 0.1 % Mn, (b) 5 % Mn, (c) 0.1 % Cu(II) and (d) 0.1 % Bi doping, showing nanocrystals of ZnO. The insets are FFT images of each HRTEM image, indexed to wurtzite ZnO polycrystalline structure, respectively. More HRTEM images of these samples can be found in Appendix II. .... | 53 |
| <b>Figure 3.5</b> FTIR spectra of Co-doped ZnO nanohybrids at 0.1 %, 1 % and 5 % doping. ....   | 54 |
| <b>Figure 3.6</b> RBS spectrum of 5 % Mn-doped ZnO nanohybrid with simulated curve (red curve) and contribution of each element (other colored curves). The inset shows contribution from Mn in detail. ....  | 56 |
| <b>Figure 3.7</b> EDX spectrum of 5 % Mn-doped ZnO nanohybrid. ....   | 57 |
| <b>Figure 3.8</b> XRD spectra of Bi-doped ZnO nanohybrids. ....   | 59 |
| <b>Figure 3.9</b> XRD spectra of Ag-doped ZnO nanohybrids. ....   | 59 |
| <b>Figure 3.10</b> XRD spectra of Ag-doped ZnO nanohybrids after calcination at 400 °C for 4 hours. ....  | 60 |
| <b>Figure 3.11</b> Diffraction domain size of doped ZnO nanohybrids estimated by Scherrer equation in function of dopants and doping concentration. The dopants are arranged in the ascending order of the ionic radius. ....   | 61 |
| <b>Figure 3.12</b> Normalized PL spectra of Co-, Fe(III)-, Mn- and Cu(II)-doped ZnO nanohybrids at 0.1 % doping concentration in comparison with the PL spectrum of undoped ZnO nanohybrid. ....  | 63 |
| <b>Figure 3.13</b> PL spectra of undoped ZnO nanohybrid and Fe(II)-, Fe(III)-, Cu(I)-, and Mn-doped ZnO nanohybrids at (a) 0.1 %, (b) 1 %, and (c) 5 % doping concentrations. ....  | 65 |
| <b>Figure 3.14</b> PL spectra of Cu-doped ZnO nanohybrids with two different Cu valences (+1 and +2) at (a) 0.1 %, (b) 1 %, and (c) 5 % doping concentrations. ....   | 66 |
| <b>Figure 3.15</b> PL spectra peak position of the doped-ZnO nanohybrids in energy (eV) and wavelength (nm). The horizontal dashed line indicates the peak position of undoped ZnO nanohybrid. ...  | 67 |
| <b>Figure 3.16</b> PL QY of doped ZnO nanohybrids normalized to the PL QY of undoped ZnO nanohybrid. ....   | 68 |
| <b>Figure 3.17</b> PLE spectra of Cu(II)-doped ZnO nanohybrids at three doping concentrations. ....   | 70 |
| <b>Figure 3.18</b> Role of dopant during hydrolysis synthesis and in the nanohybrid composite ....  | 71 |
| <b>Figure 3.19</b> Position of the spectra of selected doped samples in the gamut chart in Judd's UCS diagram (figure produced by Fabien Mandorlo). ....  | 73 |
| <b>Figure 3.20</b> PL spectra of 0.1 % Fe(III) doped ZnO nanohybrid obtained at various temperatures from room temperature (RT) to 100 °C. ....   | 74 |

|  |    |
|--|----|
| <b>Figure 4.1</b> Normalized PL spectra of ZnO/PAA synthesized in two different batches.....   | 78 |
| <b>Figure 4.2</b> Absolute PL QY values of 14 samples of ZnO/PAA precursor. The 15 <sup>th</sup> uncoated sample was obtained in the same manner as the silica-coated samples but without any TEOS coating and is used as a reference. The red dashed lines indicate a PL QY window between 9 % and 19 %.....  | 79 |
| <b>Figure 4.3</b> Distribution of PL QY of 15 uncoated ZnO/PAA samples.....  | 79 |
| <b>Figure 4.4</b> XRD spectra of $x$ Si-1A ( $x = 2, 3$ and $10$ ) ZnO nanohybrids (a) before calcination and (b) after calcination at $400\text{ }^{\circ}\text{C}$ for $4\text{ h}$ .....  | 82 |
| <b>Figure 4.5</b> TEM images of $x$ Si-1A ZnO nanohybrids. (a) TEM and HAADF image (inset) of 3.8Si-1A. (b) HRTEM image of 3.8Si-1A with the inset showing fast Fourier transformed (FFT) image of the red square area. (c) HRTEM of 1.1Si-1A. (d) HRTEM of 10Si-1A. ....  | 83 |
| <b>Figure 4.6</b> FTIR spectra of ZnO/PAA and 3.8Si-1A nanohybrids. ....   | 85 |
| <b>Figure 4.7</b> Normalized PL spectra of silica-coated ZnO/PAA with different amount of TEOS loading. ....   | 86 |
| <b>Figure 4.8</b> PL QY improvement of $x$ Si-1A samples in function of TEOS:ZnO ratio. ....   | 87 |
| <b>Figure 4.9</b> XRD spectra of 3.8Si- $y$ A ( $y = 1, 2$ and $4$ ) ZnO/PAA nanohybrids.....  | 88 |
| <b>Figure 4.10</b> Diffraction domain size of ZnO (squares) and the unassigned phase (diamonds) of three silica-coated samples (3.8Si- $y$ A ( $y = 1, 2,$ and $4$ )) in function of the amount of $\text{NH}_4\text{OH}$ in solution A. The size of the unassigned phase is estimated by Scherrer equation from the peak at $2\theta = 33.4^{\circ}$ . .... | 89 |
| <b>Figure 4.11</b> TEM images of 3.8Si- $y$ A silica-coated ZnO nanohybrids. (a) and (b) 3.8Si-1A; (c) and (d) 3.8Si-2A; (e) and (f) 3.8Si-4A.....   | 91 |
| <b>Figure 4.12</b> RBS spectra of 3.8Si- $y$ A ( $y = 1, 2,$ and $4$ ) samples. ....   | 92 |
| <b>Figure 4.13</b> Atomic ratio of Si to Zn in 3.8Si- $y$ A samples calculated by RBS. ....  | 92 |
| <b>Figure 4.14</b> Structure model of silica-coated ZnO/PAA nanohybrids under different concentrations of $\text{NH}_4\text{OH}$ in solution A. ....   | 93 |
| <b>Figure 4.15</b> Normalized PL spectra of (a) 3.8Si-1A, (b) 3.8Si-2A, and (c) 3.8 Si-3A, with the spectrum of their respective uncoated ZnO/PAA precursor as the reference. ....   | 95 |
| <b>Figure 4.16</b> PL QY improvement of 3.8Si- $y$ A silica-coated ZnO nanohybrids compared to their respective uncoated ZnO/PAA precursor in function of the ratio of $\text{NH}_4\text{OH}$ $y$ in solution A..  | 96 |
| <b>Figure 4.17</b> PLE spectra at $\lambda_{\text{em}} = 550\text{ nm}$ of ZnO/PAA precursor and 3.8Si- $y$ A ( $y = 1$ and $2$ ) samples. The spectra are normalized to the intensity at $\lambda_{\text{ex}} = 266\text{ nm}$ .....  | 97 |

**Figure 4.18** PL spectra of (a) ZnO/PAA, (b) 3.8Si-1A and (c) 3.8Si-2A at different temperatures from 25 °C to 100 °C. .... 99

**Figure 4.19** Evolution of (a) maximum PL intensity and (b) retention of maximum PL intensity relative to the initial maximum at different temperatures up to 100 °C of uncoated ZnO/PAA, 3.8Si-1A, and 3.8Si-2A. The three points standing alone at 25 °C in (b) represent the retentions of maximum PL intensity after cooling down. .... 100



## Chapter 1 State-of-the-Art

### Context

The world today is faced with increasing severity of climate change and environmental issues related to energy supply crisis. While new sources of sustainable energy are being developed, global reduction in energy consumption comes to be of prime urgency. The production of artificial lighting accounts for approximately 6.5 % of the global consumption of primary energy and 16 % of the world's total generated electrical energy. [1] While white light is essential in modern life, conventional white light sources are gradually losing their ground due to relatively low luminous efficacy, low color rendering index (CRI) and short lifespan, compared to new generation of lighting – light emitting diodes (LEDs). Akasaki, Amano and Nakamura, laureates of the Nobel Prize in Physics in 2014, first demonstrated efficient blue GaN LEDs in 1990s, opening the era of bright and energy-saving white light sources. [2], [3] The use of current LED technology is estimated to decrease the world electricity consumption by 40 % (a reduction of annual costs of 130 billion euros), saving 670 million tons of CO<sub>2</sub> per year. [4] While the contribution of LED to the lighting industry is tremendous, the pursuit of better white lighting (high CRI, high brightness, low cost and long lifetime) did not cease there but continues up till today. Due to policies banishing obsolete halogen lamps and the decrease of LED manufacturing costs, a considerable amount of LED products will enter the lighting market to reduce energy consumption, resulting in potential crisis in rare-earth elements (REEs) supply, since the current LEDs heavily rely on REEs. Therefore, developing rare-earth-free LEDs is crucial for the upcoming transformation of lighting industry.

### 1.1 White light-emitting diodes (WLEDs)

An LED is a semiconducting, electrically powered device that emits light, the wavelength of which depends on the bandgap structure of the emitting material. Red and green LEDs based on GaAs and GaP were developed and commercialized long before blue GaN LED because high-quality crystalline GaN were difficult to grow. [5] White light generation relies on these LEDs, in particular blue to UV LEDs that can be utilized as excitation source in WLED devices. WLEDs include two main categories, inorganic and organic LEDs (OLEDs), the latter being more cost effective yet less attractive due to moisture sensitivity and ageing issues.

There are three approaches to generate white light with LEDs. The first approach involves three independent LED chips emitting primary colors – red, green and blue (RGB) – as demonstrated in

**Figure 1.1** (a). These chips are highly efficient InGaN single quantum wells (blue and green LEDs) or GaAlAs (red LED) with high power and high brightness. [6] Despite the high CRI, the complex structure and high fabrication cost of this polychromatic LED device make it impossible for industrialization on a large-scale so far. On the other hand, the second (**Figure 1.1** (b)) and third (**Figure 1.1** (c)) approaches utilize inorganic phosphors to convert high-energy excitation source into low-energy visible light to generate white light, a simple process also known as down-shifting. Thanks to the simplicity of down-shifting, the phosphor-converted WLEDs have been industrialized and remain the research cornerstone of lighting industry.

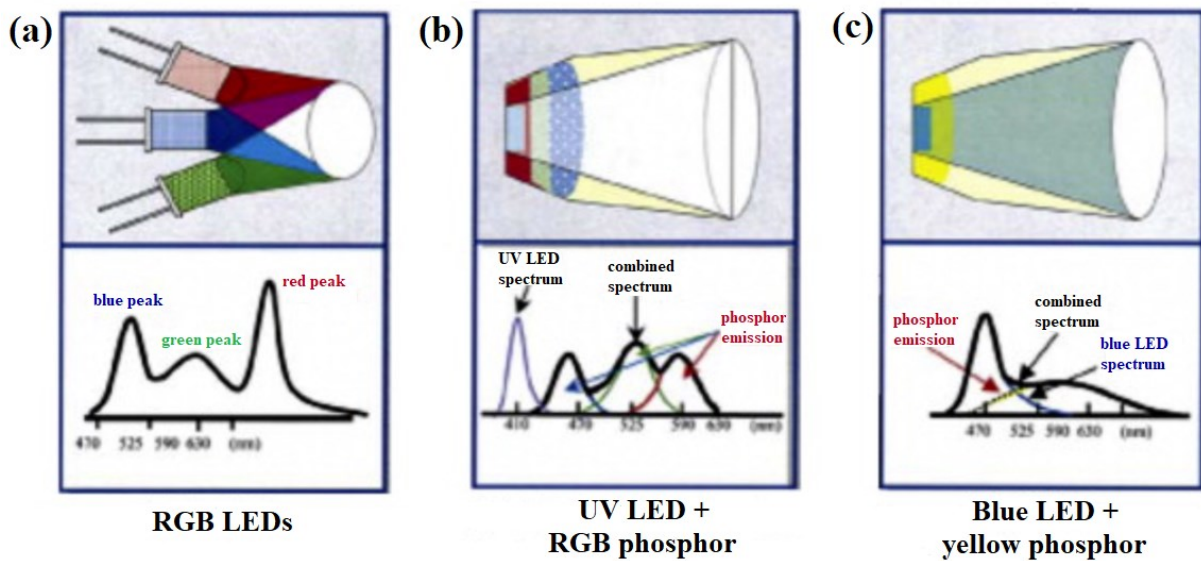


**Figure 1.1** Three approaches to generate white light with LEDs: (a) with single RGB LEDs, (b) with full conversion of UV LED, and (c) with partial conversion of blue LED. [7]

In this section, the selection criteria for WLED materials will be introduced first. Then, phosphor materials for down-shifting will be discussed in two parts, UV-excited phosphors (in full conversion as shown in **Figure 1.1** (b)) and blue-excited phosphors (in partial conversion as shown in **Figure 1.1** (c)) with a focus on YAG:Ce, the industrially used WLED material, the emission spectrum of which is shown in **Figure 1.2** (b). Finally, ZnO as a new down-shifting phosphor will be briefly introduced.

## 1.1.1 WLEDs criteria

### 1.1.1.1 Quantum efficiency

There are a couple of definitions of quantum efficiency (QE) for WLED devices. First, the internal quantum efficiency (IQE) is defined as the ratio of the number of photons emitted from electron-hole recombination to the total number of recombinations (radiative and non-radiative). To put it more

simply, IQE determines the efficiency of light generation of a material. Second, the external quantum efficiency (EQE) is the product of IQE and the extraction efficiency of the WLED device. EQE depends on both the inherent characteristics of the semiconducting material and the device architecture. While IQE describes the inherent characteristic of a material, EQE is usually adopted by the industry to describe the performance of a WLED device. In the present thesis, IQE will be our main concern, as this parameter is a determining factor for the EQE of the LED device. However, the total number of recombinations is rather difficult to determine. The term photoluminescence quantum yield (PL QY), defined as the ratio of the number of photons emitted to the number of photons absorbed, is therefore adopted to represent IQE in the present thesis. Note that PL QY is sometimes referred as EQE in the literature, in which case the device efficiency is beyond consideration. The details on how to calculate PL QY will be presented in Section 2.3.3. In order to obtain high PL QY, a strong absorption of the excitation source radiation by the luminescent material is essential.

#### 1.1.1.2 Correlated color temperature

Correlated color temperature (CCT) describes the warmth of the emitted white light. The performance of a WLED is compared with a reference source, usually a black-body radiator in thermal equilibrium. According to Planck's law of radiation in Equation (1.1):

$$B_{\lambda}(\lambda, T) = \frac{2hc^2}{\lambda^5} \frac{1}{e^{hc/(\lambda k_B T)} - 1}, \quad (1.1)$$

where  $B$  is the spectral radiance of a physical body,  $\lambda$  the wavelength,  $T$  the absolute temperature,  $h$  the Planck constant,  $c$  the speed of light in the medium, and  $k_B$  the Boltzmann constant, the emission spectrum of an incandescent black body depends on its temperature. The chromatic points corresponding to its radiation at different temperatures are represented in the CIE diagram as a black solid curve called Planckian locus, as illustrated in **Figure 1.2** (a). [7] The higher the CCT is, the colder human beings perceive the light. The dotted line represents all perceived colors that can be obtained from YAG:Ce by additive mixing. The luminescence spectrum of YAG:Ce is presented in **Figure 1.2** (b). The possibility to tune the CCT of a phosphor material is a prerequisite for specific applications based on the same material.

#### 1.1.1.3 Color rendering index

Color rendering index (CRI) defines the ability of a WLED to render the true colors of an object to human visual perception with respect to a reference light source (*e.g.*, natural daylight). CRI is rated on a scale from 0 to 100, with 100 meaning colors of the object illuminated by the WLED would appear

the same as those illuminated by the reference source. The industrialized YAG:Ce has a CRI lower than 75 due to low spectral power distribution situated in the red region. [8]

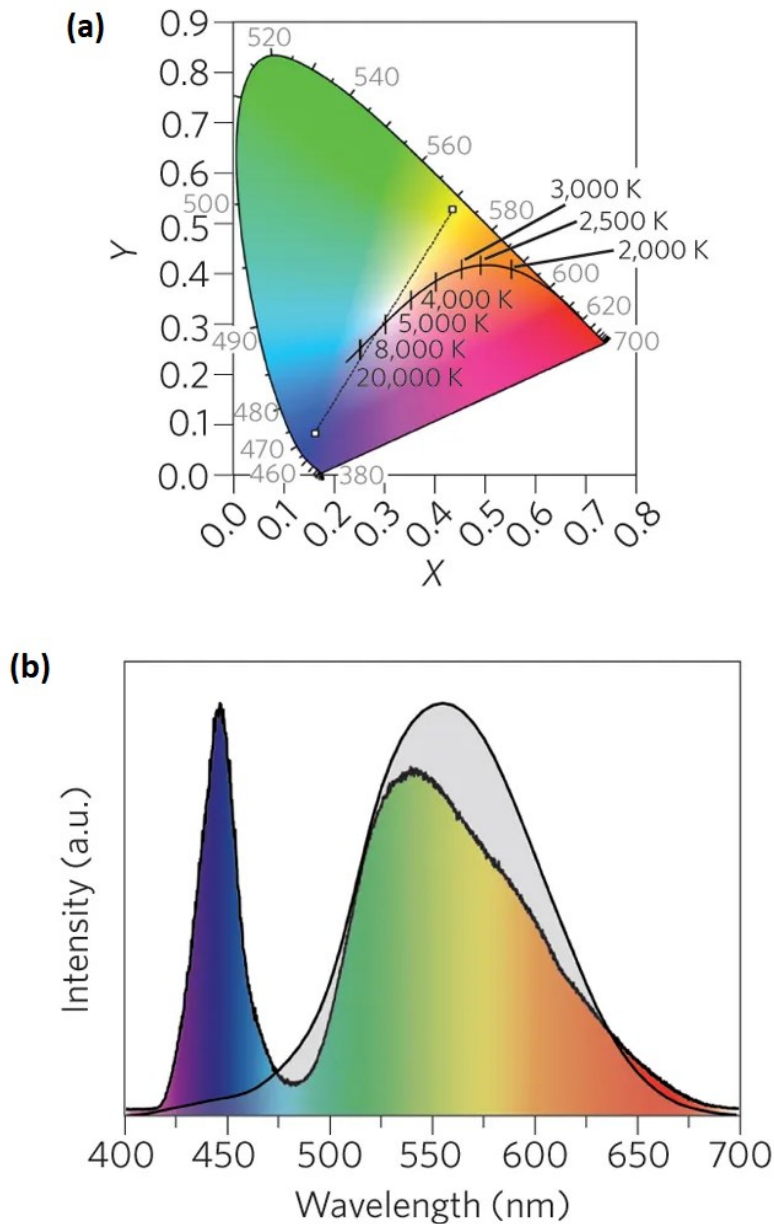


**Figure 1.2** (a) Commission Internationale de l'Éclairage (CIE, 1931) diagram with a black-body radiation curve (black solid line) and CCT values. (b) Luminescence spectrum of YAG:Ce and human eye sensitivity curve in grey-shaded spectrum. [7]

#### 1.1.1.4 Other criteria

For a longer lifetime of WLED devices, the phosphor material should meet some other criteria. Small thermal degradation is required to maintain the brightness and color coordinates of WLEDs over long period of time, since the luminescence process generates heat. Chemical stability is necessary for usage under ambient atmosphere. For high-power and high-brightness WLEDs, small luminance saturation is obligatory to retain luminance under high power or high flux density irradiations. [9]

### 1.1.2 UV-excited phosphors

As demonstrated in **Figure 1.1** (b), a UV-excited phosphor is incorporated in a full-conversion WLED device where a violet or ultra-violet (UV) excitation source is converted into red, green and blue light by the phosphor. Since a large Stokes shift (wavelength shift, or energy shift, between absorbed photon and emitted photon) is observed in full conversion, such WLED devices inherently suffer from low efficiency, which is the major drawback of full-conversion devices. On the bright side, the UV-excited phosphors have high CRI (up to 98), high luminous efficiency and stable color temperature, making them highly desirable for indoor lighting.

The majority of the UV-excited phosphors relies on  $\text{Eu}^{2+}$  or  $\text{Ce}^{3+}$  doping, because they can absorb UV light efficiently and emit blue or green light. Bright and persistent luminescence from  $\text{Eu}^{2+}$  doping was first reported by Matsuzawa *et al.* in  $\text{SrAl}_2\text{O}_4:\text{Eu}^{2+}$  co-doped with  $\text{Dy}^{3+}$  ions. [10] Ever since, numerous phosphors doped with  $\text{Eu}^{2+}$  have been developed in various luminescent compounds. [11]–[15]  $\text{Ce}^{3+}$  has long been utilized as an activator in phosphors, especially in blue-excited phosphors (to be discussed in Section 1.1.3). [16]  $\text{Eu}^{2+}$  and  $\text{Ce}^{3+}$  are excellent activators in luminescent materials thanks to the nature of their electron shell structure. Visible emission from these rare-earth (RE) ions generally originates from  $5d \leftrightarrow 4f$  transition. The emission peak positions can be easily tuned over a wide range, depending on the local coordination environment of the dopant ion in the crystal structure of the phosphor. [17] In order to obtain a broadband emission, it is often required to co-dope  $\text{Eu}^{2+}$  or  $\text{Ce}^{3+}$  with  $\text{Mn}^{2+}$ , since  $\text{Mn}^{2+}$  can be a good source of red emission. Co-doping makes it possible to generate white light with a single-phase phosphor, which has been the endeavor of many researchers. [18]–[21]

**Figure 1.3** gives typical emission spectra of single-phase phosphors co-doped with  $\text{Eu}^{2+}$  and  $\text{Mn}^{2+}$ . [18] The blue emission band (at around 459 nm) is ascribed to  $5d-4f$  transition of  $\text{Eu}^{2+}$  and the red band (608 nm) originates from  $\text{Mn}^{2+}$ . The quenching of blue emission and the increase of red emission intensity allow tuning of the emission from blue to white and then to red under UV excitation by adjusting the amount of  $\text{Mn}^{2+}$ , which closely correlates to the energy transfer efficiency  $\eta_T$  from  $\text{Eu}^{2+}$  to  $\text{Mn}^{2+}$ , as shown in the inset of **Figure 1.3**. Other examples of single-phase phosphors involve co-doping with

$\text{Ce}^{3+}\text{-Mn}^{2+}$ ,  $\text{Eu}^{2+}\text{-Ce}^{3+}$ ,  $\text{Bi}^{3+}\text{-Eu}^{2+}$ ,  $\text{Ce}^{3+}\text{-Tb}^{3+}$ , *etc.*, with white light emission consisting of two or three emission peaks from the blue band to the red band. [22]–[28]

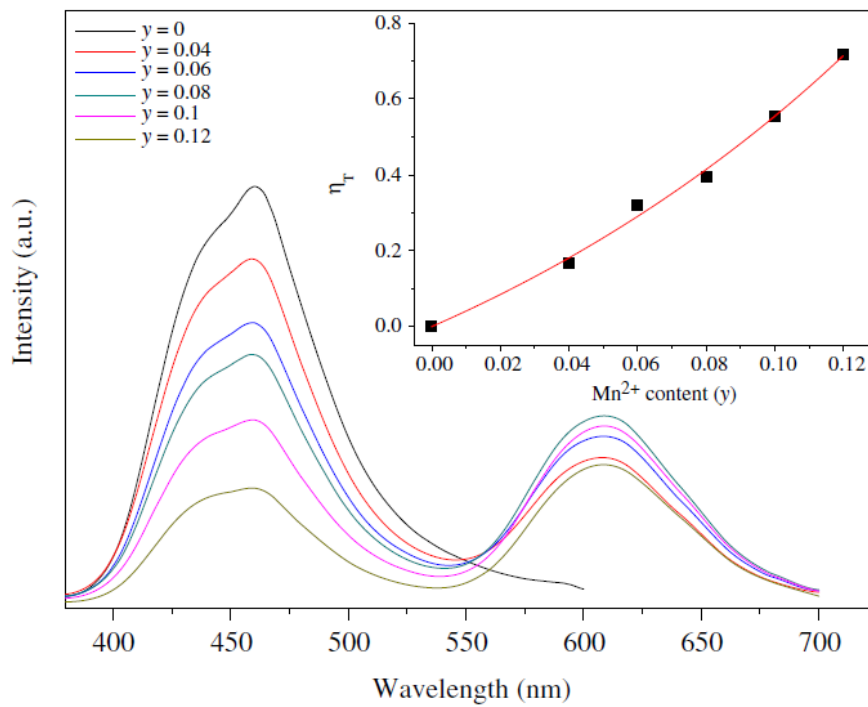


**Figure 1.3** PL spectra of  $\text{Ba}_2\text{Ca}(\text{B}_3\text{O}_6)_2:0.04\text{Eu}^{2+}, y\text{Mn}^{2+}$  phosphors ( $\lambda_{\text{ex}} = 330 \text{ nm}$ ). Inset shows the dependence of the energy transfer efficiency  $\eta_T$  on the  $\text{Mn}^{2+}$  content ( $y$ ). [18]

Besides single-phase phosphors, the excitation of a mixture of RGB phosphors by UV light is another approach to obtaining white light. These phosphors also rely on  $\text{Eu}^{2+}$  doping or  $\text{Ce}^{3+}$  doping, or even co-doping. The red component, however, is scarce, and requires careful design of the energy transfer between different luminescent centers (such as  $\text{Mn}^{2+}$ ,  $\text{Eu}^{3+}$ ), because the red phosphor can usually absorb not only UV light, but also visible light emitted from green and blue phosphors.

### 1.1.3 Blue-excited phosphors

As demonstrated in **Figure 1.1** (c), a blue-excited phosphor is incorporated in a partial-conversion WLED device, where a blue excitation source is partially converted into yellow light by the phosphor. The currently industrialized WLEDs is a partial-conversion device employing a blue GaN LED chip covered by Ce-doped yttrium aluminum garnet phosphor  $\text{Y}_3\text{Al}_5\text{O}_{12}:\text{Ce}^{3+}$  (YAG:Ce). Smaller Stokes shift in this design ensures higher efficiency compared to full-conversion WLEDs. Other merits of YAG:Ce are easy fabrication and low cost, which made its industrialization possible. What is unsatisfactory, though, is the low CRI (lower than 75) due to lack of red component in the emission of YAG:Ce phosphor. Therefore, much effort is still devoted to the improvement of CRI in YAG:Ce.

**Figure 1.4** demonstrates a typical excitation and emission spectra of YAG:Ce. [29] In this particular case, it is evident that white light can be generated by combining blue excitation at 470 nm and yellow emission peaking at 532 nm, unfortunately, with no red component in the final emitted spectrum. The photoluminescence of YAG:Ce was thoroughly studied and discussed in several articles. [16], [30]–[33] Strong crystal field splitting of  $5d$  energy level of  $Ce^{3+}$  in terms of its coordination environment allows not only such excitation and emission as shown in **Figure 1.4**, but also the tuning of the bands to fit specific requirements such as obtaining red emission. The most common method to add red component in YAG:Ce is, again, co-doping with other activators such as  $Cr^{3+}$ ,  $Pr^{3+}$ ,  $Tb^{3+}$  and  $Sm^{3+}$ . [34]–[39] These activators can introduce new luminescent centers or modify the crystal field splitting of  $Ce^{3+}$ , resulting in enhancement of red emission. [38] Nevertheless, while CRI is enhanced by co-doping other activators, the luminous efficiency tends to decrease. It is still a challenge to balance CRI and luminous efficiency of YAG:Ce.

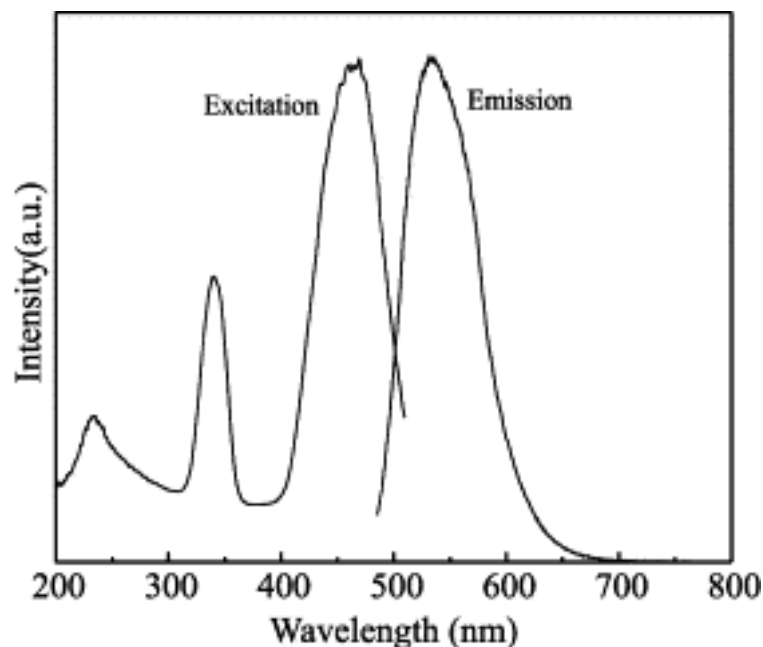


**Figure 1.4** PL excitation and PL emission spectra of 2 mol% Ce-doped YAG ( $\lambda_{em} = 532$  nm,  $\lambda_{ex} = 470$  nm). [29]

Another challenge with YAG:Ce is the thermal quenching, especially for applications in high-power WLEDs. The working temperature of YAG:Ce in commercially available LED products can reach well above 450 K mainly due to the heat generated from pn-junction. Decrease of the intensity of yellow emission was reported by many, but in fact, the intrinsic quenching temperature of YAG:Ce is well above 700 K. [33] Quenching at lower temperature is actually related to the concentration of  $Ce^{3+}$ . Therefore, low doping is preferred for high-power WLEDs in order to minimize the thermal quenching phenomenon.

Besides YAG:Ce, other garnet phosphors and non-garnet oxides, sulfides, nitrides and oxynitrides can also be excited by blue LED to generate white light. Numerous compounds are summarized in some review articles. [9], [11], [34], [40]–[44] The luminescence of these compounds, like UV-excited phosphors, relies on doping or co-doping with RE ions, principally  $\text{Ce}^{3+}$  and  $\text{Eu}^{2+}$ . Therefore, other materials without RE elements are attractive to replace YAG:Ce for their lower environmental impact.

#### 1.1.4 ZnO as RE-free phosphor

As mentioned above, either UV-excited or blue-excited, the most common luminescent phosphors all rely heavily on RE elements such as  $\text{Ce}^{3+}$  and  $\text{Eu}^{2+}$ . RE elements are expensive and the existing mining industry related to them has serious impacts on the environment concerning soil and water. Furthermore, they are essential for the development of innovative technologies in the information era. As the consumption of electricity in lighting increases, RE-free materials are more suitable for large-scale application in the lighting industry. Therefore, it is of great significance to develop RE-free materials to replace YAG:Ce as the new phosphor for WLEDs.

There are four main strategies to design RE-free phosphors: 1) using transition metals as luminescent centers, 2) creating defects, 3) using quantum dots, and 4) designing inorganic-organic hybrid phosphors. [45] Among these strategies, creating defects is particularly interesting and practical for metallic oxides such as zinc oxide (ZnO). ZnO possesses many intrinsic defects, making it an inherent phosphor of great potential for WLEDs.

ZnO has been considered as a complement or even an alternative for GaN for optoelectronic device applications because ZnO has a wide direct bandgap of  $\sim 3.3$  eV and a large exciton binding energy of 60 meV (much larger than 24 meV of GaN) at room temperature (RT). Thanks to its good optical properties, ZnO is widely applied in the field of UV photodetectors, solar cells, photodiodes, sensing, *etc.* [46]–[54] More interestingly, ZnO can be an excellent material for WLEDs due to broad absorption band in the UV range and broad emission band in the visible range, as well as strong bandgap emission (also in the UV). The visible emission originates from various native point defects such as oxygen interstitials ( $\text{O}_i$ ), oxygen vacancies ( $V_{\text{O}}$ ), oxygen anti-sites ( $\text{O}_{\text{Zn}}$ ), zinc interstitials ( $\text{Zn}_i$ ), zinc vacancies ( $V_{\text{Zn}}$ ), and zinc anti-sites ( $\text{Zn}_{\text{O}}$ ). These defects have a significant impact on the photoluminescence of ZnO. It is, therefore, imperative to understand and to be able to manipulate the defects for the development of specific devices.

## 1.2 Undoped ZnO

### 1.2.1 Photoluminescence of undoped ZnO

Photoluminescence (PL) is the process of light emission from a material under photoexcitation. An electron is excited by the absorbed photon to a higher energy state. After relaxation to the lowest available energy level of the energy band to which the electron was excited, the electron returns to the ground state and a lower-energy photon (as compared to the excitation photon) is released. Down-shifting is PL with a given Stokes shift. Visible PL from ZnO is usually accompanied by a large Stokes shift.

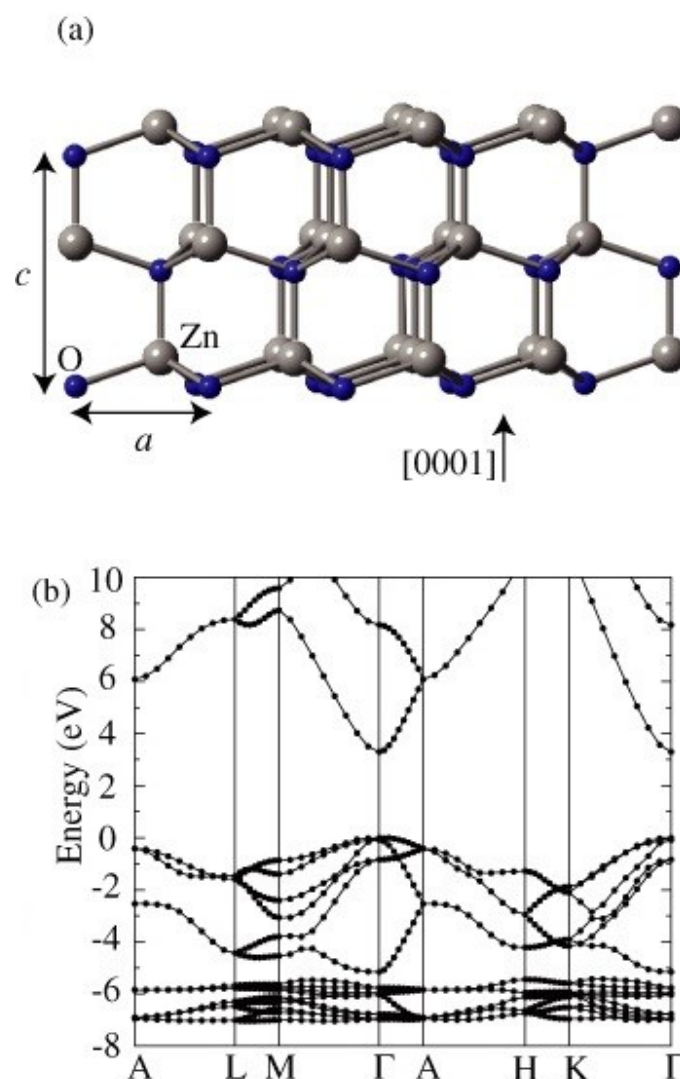


**Figure 1.5** (a) Wurtzite crystal structure of ZnO with indicated lattice parameters  $a$  and  $c$ . (b) Calculated band structure of ZnO. The energy of the valence band maximum was set to zero. [55]

ZnO is an important II-VI semiconductor with a wide direct bandgap that crystallizes in wurtzite structure under ambient conditions, where  $a = 3.25 \text{ \AA}$  and  $c = 5.20 \text{ \AA}$  (see **Figure 1.5**). It belongs to the space

group  $C_{6v}^4$ , or  $P6_3mc$ . Hexagonal close packed (*hcp*) sublattices of Zn and O interpenetrate each other along the  $c$  axis. Each Zn atom is surrounded by four O atoms at the corners of a tetrahedron, and vice versa. The direct bandgap of ZnO makes it easy for radiative recombinations to occur since no crystal momentum is required. The radiative recombination is the reason for PL. The large exciton binding energy indicates that efficient excitonic emission can persist at room temperature or higher.

PL from ZnO occurs in two manners, namely, band to band emission (BBE) and deep level emission (DLE), as demonstrated in **Figure 1.6**. When excited by UV light, an electron can absorb a UV photon and jump up to the conduction band (CB), leaving a hole in the valence band (VB). The resulting electron-hole pair ( $e^-h^+$ ) due to Coulomb interaction is called an exciton. For BBE (*i.e.*, excitonic emission), the electron and hole recombine after thermalization (*i.e.*, the non-radiative relaxation which takes a few picoseconds through interaction with phonons), emitting a photon with an energy equal to the bandgap minus the exciton binding energy. The decay time of BBE is on a timescale of  $\sim 1$  ns. For DLE, the electron or the hole can be trapped by deep-level defects. This trapping process takes about 1 ns. When the electron and hole recombine, a photon is emitted, its energy equal to the energy difference between the trap level and the top of VB or the bottom of CB. The decay time of DLE is much longer, ranging from several ns to hundreds of ns. The decay time of BBE is thus much shorter than that of DLE, meaning BBE is usually the dominant emission in ZnO. However, DLE can also dominate when the defect density increases. The two types of PL of ZnO can be applied in many fields, notably in laser diodes for BBE and LEDs for DLE.

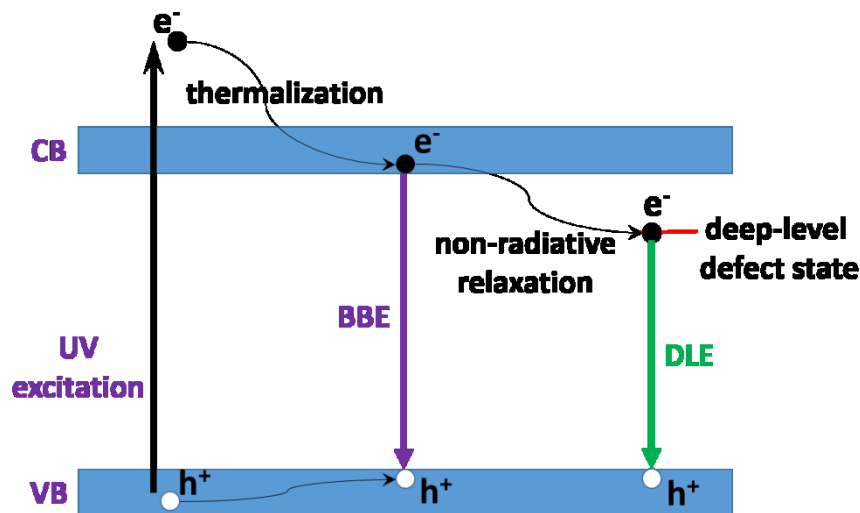


**Figure 1.6** Photoluminescent processes in ZnO.

## 1.2.2 UV emission

ZnO is a potential candidate for room temperature UV or violet laser diodes, owing to its large exciton binding energy (60 meV at RT), which allows efficient excitonic lasing mechanisms at room temperature, even under low excitation intensity. Stimulated UV emission and lasing were first observed at cryogenic temperature in the 60s and 70s. [56]–[59] The materials in question then were bulk ZnO of very high quality in platelet form, pumped by an electron beam. Since late 90s, many researchers have reported optically pumped lasing in ZnO. [60]–[65] Such lasing has been realized at RT and at low pump power thanks to the growth techniques such as laser-assisted molecular beam epitaxy (MBE), which produces ZnO micro- or nanostructures of even higher quality. Stimulated UV emission at RT can be attributed to the exciton-exciton collision, an important process for the realization of low-threshold lasing, in which one exciton is scattered into continuum state and the other recombines radiatively, generating one photon and an exciton scattered into  $n = 2$  state. [61]

Nevertheless, leaving lasing aside and focusing on PL, the UV emission spectrum can be rather complex. Numerous peaks and shoulders are strongly superimposed at low temperature so it requires various experimental techniques to fully explain the emission mechanisms. **Figure 1.7** (a) and **Figure 1.7** (b) give a typical example of PL spectra of ZnO at low temperature (10 K) and at RT, respectively. [65] The spectra are comprised of three emission regions: near band edge emission (NBE), low energy tail extending from NBE, and DLE. The first two regions are in the UV range, with  $I_9$  line at 3.347 eV being the dominant peak, which is assigned to the recombination of excitons bound to neutral donors or acceptors. Other peaks are associated with longitudinal optical phonon replicas. PL at room temperature shows a dominant emission from free exciton near 3.2 eV. **Table 1.1** tabulates some observed excitonic peak energies reported from high-quality ZnO single crystals by techniques such as reflectance, photoreflectance, absorption, and PL measurements. [66] Reference [66] describes in detail the free excitons as listed in

**Table 1.1**, as well as bound excitons, two-electron satellites, donor-acceptor pairs (DAP), and longitudinal optical phonon replicas, which are all characteristic of UV emission of ZnO. Controversy on the assignment of certain peaks due to the complexity of UV emission from ZnO stimulates continuous investigation by many researchers. At RT, the origin of the UV emission peak is believed to be a combination of multiple peaks from free excitons, phonon replica, *etc.*, whose positions are red-shifted from those at low temperature.

When the temperature increases up to room temperature, lasing of ZnO can persist under two conditions. One is good crystal quality with decreased number of impurities and defects (such as  $V_O$ ), the other is quantum confinement effect related to nanostructure of ZnO crystals. [65] Therefore, many ZnO nanostructures have been developed for blue-UV laser diodes. Bagnall *et al.* employed plasma-enhanced

MBE to grow ZnO thin films on *c*-plane sapphire, which exhibited UV lasing not only at room temperature but also at temperature as high as 550 K, as manifested by the EHP (electron-hole plasma) line in **Figure 1.8**. [60] In polycrystalline ZnO, where the particle size is less than its emission wavelength, random lasing can be observed due to strong optical scattering among self-formed cavities (similar to the so-called Anderson localization of electrons in disordered systems). [76] In quantum wells of ZnO-based alloys, stimulated emission is made possible by the enhancement of the binding energy. [77]

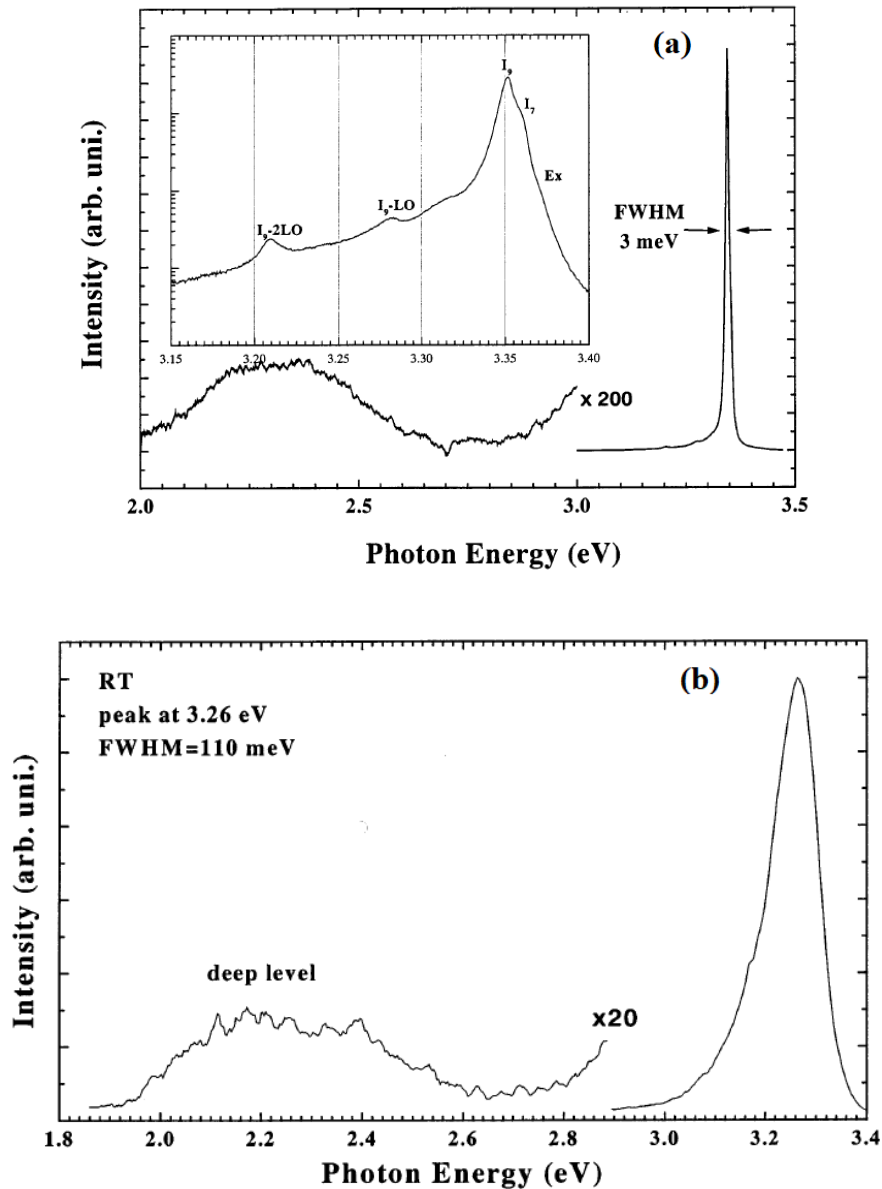


**Figure 1.7** PL spectra from ZnO epilayer obtained at (a) low temperature and (b) room temperature. The inset in (a) displays the details of the PL spectrum at near band edge (NBE) region. [65]

**Table 1.1** Excitonic peak energies (eV) in ZnO single crystals. *A*, *B*, and *C* refer to three excitons of distinct symmetry, *i.e.*, three transitions between the conduction band and three split valence bands, namely, heavy hole (*A*), light hole (*B*), and crystal-field split band (*C*). [66]

|          | $FX_A^{n=1}(\Gamma_5)$ | $FX_A^{n=1}(\Gamma_6)$ | $FX_A^{n=2}(\Gamma_5)$ | $FX_A^{n=2}(\Gamma_6)$ | LPB <sub>A</sub> | UPB <sub>A</sub> | $FX_B^{n=1}$ | $FX_B^{n=2}$ | $FX_C^{n=1}$ | $FX_C^{n=2}$ |
|----------|------------------------|------------------------|------------------------|------------------------|------------------|------------------|--------------|--------------|--------------|--------------|
| Ref [67] | 3.3771                 | 3.3757                 | 3.4220                 | 3.4206                 | 3.3740           | 3.3810           | 3.3898       |              |              |              |
| Ref [68] | 3.3773                 | 3.3756                 | 3.4221                 | 3.4209                 |                  |                  | 3.3895       |              |              |              |
| Ref [69] | 3.3793                 | 3.3775                 |                        |                        | 3.3743           | 3.3829           |              |              |              |              |
| Ref [70] | 3.378                  |                        |                        |                        | 3.374            |                  | 3.385        |              |              |              |
| Ref [71] | 3.40 (295 K)           |                        |                        |                        |                  |                  | 3.45 (295 K) |              | 3.55 (395 K) |              |
|          | 3.455 (77 K)           |                        |                        |                        |                  |                  | 3.516 (77 K) |              | 3.60 (77 K)  |              |
| Ref [72] |                        |                        | 3.4231                 |                        | 3.3768           | 3.3783           |              | 3.4290       |              | 3.4679       |
| Ref [73] | 3.3931                 |                        | 3.4243                 |                        |                  |                  | 3.4331       |              | 3.4696       |              |
| Ref [74] | 3.3768                 |                        |                        |                        |                  |                  | 3.3828       |              | 3.4208       |              |
| Ref [75] | 3.3781                 |                        | 3.4282                 |                        |                  |                  | 3.3856       | 3.4324       | 3.4264       | 3.4722       |

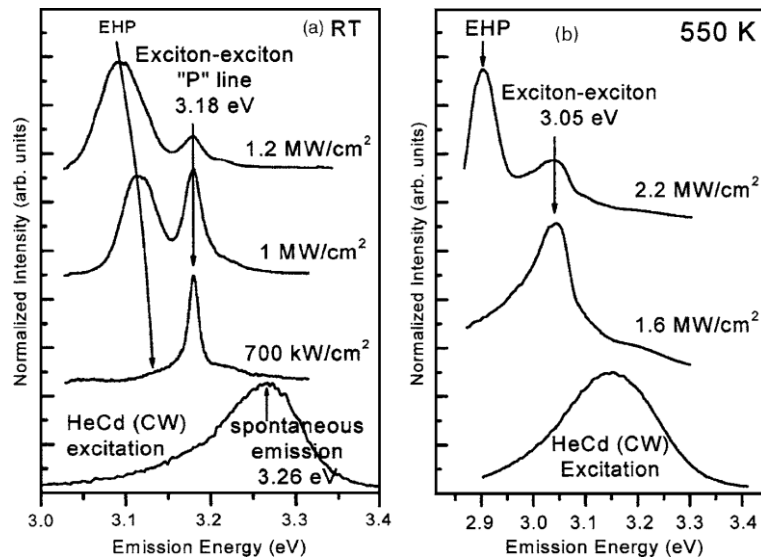


**Figure 1.8** Normalized PL spectra of ZnO thin films for various excitation intensities at (a) room temperature and at (b) 550 K. [60]

### 1.2.3 Visible emission

As indicated above, low density of defects are favored for UV applications; on the other hand, defects in ZnO can trap electrons or holes and induce visible emissions, which is a great example of turning a demerit into a merit. Despite the fact that most defects act as quenching centers inducing non-radiative recombination, the native defects, or intrinsic defects, play a significant role in rendering visible luminescence from ZnO. These defects strongly influence the minority carrier lifetime, luminescence efficiency and diffusion mechanisms related to the growth and degradation processes. Therefore, it is of tremendous importance to study the intrinsic defects in ZnO if visible LEDs based on ZnO are to be developed.

Janotti and Van de Walle performed a comprehensive first-principles investigation of all six native point defects in ZnO based on density functional theory. [78] Defects often introduce intermediate levels in the band gap of semiconductors and these levels involve transitions between different charge states of the same defect. **Figure 1.9** shows the position of the transition levels in the band gap for all the native point defects in ZnO. Their results provide theoretical indication that  $V_{Zn}$  is a deep acceptor that is a possible source of green luminescence in ZnO, and that  $V_O$  is a deep donor, which is a potential source of compensation in *p*-type ZnO.  $V_{Zn}$  is the dominant defect under O-rich conditions, while  $V_O$  is more abundant than  $Zn_i$  under Zn-rich conditions. Other defects have higher formation energies ( $Zn_i$ ,  $Zn_O$  of donor characteristic and  $O_i$ ,  $O_{Zn}$  of acceptor characteristic) and they are not likely to exist stably in significant concentrations.

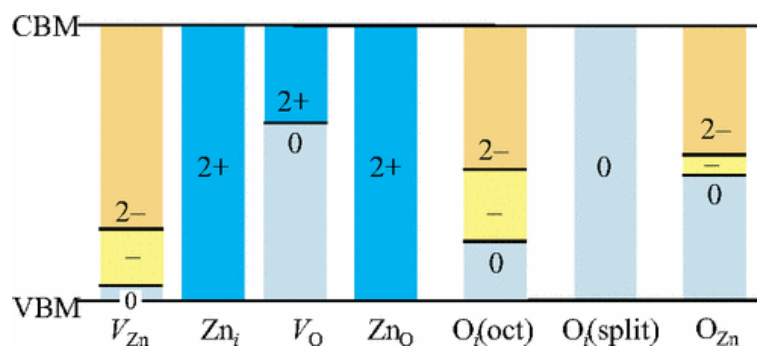


**Figure 1.9** Thermodynamic transition levels for defects in ZnO. [78]

In parallel, based on experimental results from different groups, **Figure 1.10** schemes the transition levels of the native defects in the band gap of ZnO. [79] The position of  $V_{Zn}$  is in good agreement with calculated results and among different reports; but for other defects, there is no consensus yet on their positions in the band gap. Another thing that is agreed in the literature is that these defects are the sources of visible emissions from ZnO. **Table 1.2** lists some emission colors and possible energy transitions related to defects proposed by different research groups. [79] Different colors over the entire visible range have been reported, but their origins are still controversial because of the complexity of native

defects in ZnO fabricated under different conditions. Many experimental attempts have been made to resolve the controversies and PL is one simple and universal technique for analyzing the components of the visible emission of ZnO. Via deconvolution of the broad spectrum, emissions of ZnO are generally discussed over three emission bands: blue (short wavelength), green (middle wavelength), and red (long wavelength).

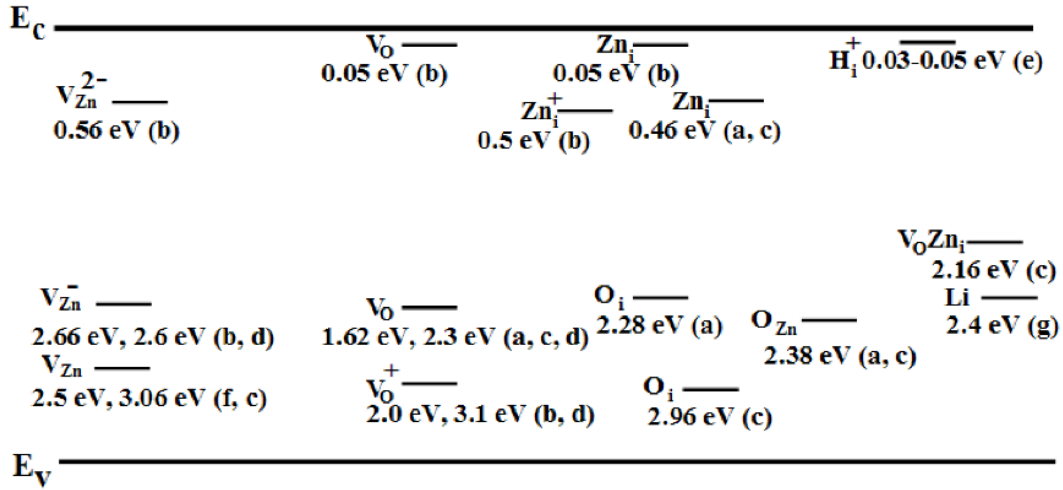


**Figure 1.10** Transition levels (measured with respect to the edge of the conduction band) of defects in ZnO reported in literature by different groups. (a) Ref [83]. (b) Ref [84]. (c) Ref [85]. (d) Ref [86]. (e) Ref [87]. (f) Ref [78]. (g) Ref [88], [89].

**Table 1.2** Some reported emission colors from ZnO and proposed energy transitions from point defects. (Adapted from Ref [79])

| Emission color (nm) | Proposed deep level transition   |
|---------------------|--|
| Violet              | $Zn_i$ to VB   |
| Blue                | $Zn_i$ to $V_{Zn}$ , CB to $V_{Zn}$ , $Zn_i$ to VB, CB to $O_i$  |
| Green               | CB to $V_O$ or $V_{Zn}$ , $V_O$ to $V_{Zn}$ , $Zn_i$ to $V_O$ , CB to $O_i$ , CB to $O_{Zn}$                           |
| Yellow              | CB to Li, CB to $O_i$ , surface OH groups  |
| Orange              | CB to $O_i$ , $Zn_i$ to $O_i$ , surface OH groups  |
| Red                 | Lattice disorder along the c-axis ( <i>i.e.</i> , due to $Zn_i$ ),<br>O-related defects ( $O_i$ , $V_O$ , $V_O Zn_i$ ) |

Blue emission is primarily associated with Zn defects. This remark is made on the basis of the calculated and measured energy levels of Zn defects, as demonstrated in **Figure 1.9** and **Figure 1.10**.  $Zn_i$  locates near the bottom of the CB (0.22 eV below CB, as reported in Ref [80]) and  $V_{Zn}$  can be found near the top of the VB (0.30 eV above VB, as reported in Ref [81] and Ref [82]). Three transitions related to Zn defects can possibly give rise to blue emission, *i.e.*,  $Zn_i$  to VB,  $Zn_i$  to  $V_{Zn}$ , CB to  $V_{Zn}$ . The exact position of  $Zn_i$  and  $V_{Zn}$  varies within a small range, depending on the annealing and other conditions, so the blue emission is also dispersed in a reasonable range. However, it is yet difficult to discriminate different transitions responsible for blue emission.

Green emission is the most reported emission that has been attributed to various defects including intrinsic defects and extrinsic defects, such as copper impurities. Extrinsic defects will be discussed in Section 1.3. As far as intrinsic defects are concerned,  $V_O$  is the primary origin of green emission. Calculations of  $V_O$  level suggested very different positions of  $V_O$  in the band gap, as shown in **Figure 1.10**. Unsurprisingly, different transitions are proposed, such as singly charged oxygen vacancy ( $V_O^+$ ) to VB,  $V_O$  or another donor level to  $V_{Zn}$ ,  $Zn_i$  to  $V_O$  and CB to  $V_O$ . Two other intrinsic defects were also proposed to induce green emission. One involves transition from CB to  $O_i$ , if we assume the  $O_i$  level to be at 1.09 eV above VB. [90], [91] The other concerns transition from CB to  $O_{Zn}$ , which is located at 2.38 eV below CB. [85] Without doubt, green emission band is often a superposition of luminescence from multiple transitions involving different intrinsic defects. More interestingly, defects residing in the bulk ZnO and on the surface or at grain boundary-induced depletion regions give rise to different green emissions. [92]–[94] Thus, the microstructure of the material plays an important role in the green luminescence. The overall green emission band depends on the contribution of emissions from the bulk and the surface.

Coming to the long wavelength emission, the lack of red component in WLED phosphors also applies to ZnO-based materials. Despite many reports on yellow-orange emission from ZnO, red emission is either difficult to obtain or too weak. The enhancement of red emission from ZnO is urgently needed to produce white light with higher CRI. The origin of red emission has long been associated with excess oxygen. Various annealing studies in oxygen and forming gas atmosphere suggested a greater density of surface oxygen could enhance the intensity of the red component. [95] No specific transitions were proposed for the red emission although oxygen-related defects, such as  $O_i$  and  $V_O$ , and defect complex, such as  $V_OZn_i$ , are believed to be responsible. [96], [97] As for the yellow-orange emission, possible sources are extrinsic Li impurities and transitions involving OH groups at the surface. [97]–[99]

Broad visible emission can be obtained from different undoped ZnO structures and by different synthesis methods, but the interpretation of the emission components is a persevering difficulty despite the efforts in both theoretical calculations and experimental investigations. From the perspective of practical

application in WLEDs, the priority here is to find the key to control the visible photoluminescence and enhance its intensity.

### 1.3 Doping of ZnO

Doping is the intentional introduction of impurities into a semiconductor to modulate its electrical, optical, magnetic and other properties. Doping of ZnO has been extensively studied, with a particular interest in achieving p-type doping for realizing high quality p-n homojunction for applications in optoelectronics. The difficulty to obtain p-type ZnO arises from the nature of native defects ( $V_O$  and  $Zn_i$ ) and unintentional doping of hydrogen, which are the sources of n-type conductivity. When it comes to photoluminescence of ZnO, the type of carriers is not the first concern for optical properties, but the defects introduced by unintentional doping and intentional doping are of critical significance for the production of visible emission. In this section, doping of ZnO will be introduced in two categories, namely, rare-earth doping and non-rare-earth doping. For both categories, the focus is placed on the influence of dopant on the optical properties of ZnO.

#### 1.3.1 Rare-earth doping

As discussed in Section 1.1, RE elements are widely used in phosphors as activators for visible luminescence. RE elements include Sc, Y and the lanthanide series. Lanthanides have a unique electron configuration where  $4f$  electron shell is incompletely filled. Sc and Y are classified as “rare earths”, albeit lacking  $4f$  electrons, because they have similar chemical properties as lanthanides and have the same separation difficulties in ore bodies. [17] There are two types of optical transitions of RE ions in crystals: intraconfigurational- $4f^n$  transitions and interconfigurational transitions. [100] The former usually yields narrow absorption and emission lines due to small crystal field splitting. The latter gives broadband emissions in two ways:  $4f^n - 4f^{n-1}5d$  transitions and charge-transfer transitions.  $4f^n - 4f^{n-1}5d$  transitions occur for RE ions that like to be oxidized, while charge-transfer transitions are found for the ions that like to be reduced. [101] More details on RE luminescence can be found in references [17], [100], [101]. The interest in doping ZnO with RE elements stems from their stable luminescence in ZnO crystals and high luminescence quantum yield. [102]–[104] Studies of ZnO (co-)doped with RE elements are numerous in the literature. Herein, only cerium will be discussed as a dopant in ZnO as the aim of the present thesis is to design RE-free phosphors.

*Ce doping.* Ce is one of the most studied RE dopants in ZnO for the modification of its optical properties. Trivalent cerium ions ( $Ce^{3+}$ ) have a single  $4f$  electron shielded by closed  $5s$  and  $5p$  shells. Spin-orbit coupling effect causes  $^2F_{5/2}$  and  $^2F_{7/2}$  levels of the ground states of  $Ce^{3+}$ , as illustrated in the energy level

diagram in **Figure 1.11**. [17], [105], [106] The  $4f$  electron can be excited to  $5d$  level, giving absorption in the UV range, which is in line with the absorption of ZnO. The return of the electron from the lowest  $5d$  level to the ground states yields two sharp emission bands. Despite the satisfactory electron energy levels of  $Ce^{3+}$  to generate visible emission, the intensity of the luminescence can be poor. One possible reason is that  $Ce^{3+}$  tends to be oxidized to non-luminescent tetravalent state  $Ce^{4+}$ ; the other is the aggregation of  $Ce^{3+}$  ions that leads to the so-called concentration quenching. [107] With regard to practical applications, Ce doping is generally beneficial for the enhancement of blue or green emission in ZnO, but it is not yet ideal for the generation of white light of high CRI.

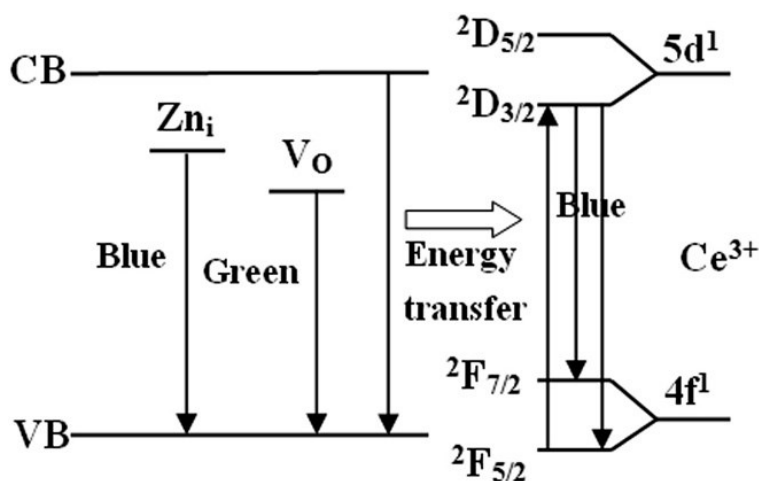


**Figure 1.11** Schematic diagram for the mechanism of visible emission from Ce-doped ZnO. [105]

$Ce^{3+}$  ions can easily incorporate into ZnO crystal lattice. They can substitute Zn ions or occupy interstitial sites. At low doping concentrations, incorporation at interstitial sites is favored; at higher doping concentrations, substitution and incorporation occur at comparable rates. [108] **Figure 1.12** shows typical XRD patterns of Ce-doped ZnO. Various X-ray diffraction (XRD) studies have shown that  $Ce^{3+}$  ions can be uniformly incorporated into ZnO without impurity phases even at high doping concentrations (up to 19 at%). [109], [110] Since the ionic radius of  $Ce^{3+}$  is bigger than that of  $Zn^{2+}$ , the diffraction peaks of wurtzite ZnO exhibit a shift towards lower angles with increasing doping concentration. Doping of  $Ce^{3+}$  also affects the morphology of ZnO. One prominent observation is that the crystallite size of ZnO reduces after doping. [106], [109], [111], [112] Such size reduction can be explained by the formation of complex of  $Ce^{3+}$  and surface oxygen that hinders the growth of ZnO crystallites. [113] It is also related to the degradation of ZnO crystalline quality arising from the formation of defects during the crystal growth. [114] On the other hand, some evidence also suggests that  $Ce^{3+}$  doping tends to increase the crystal size of ZnO. [115], [116] Either way, the interaction between  $Ce^{3+}$  and oxygen or ligand (if any exists in solution-based syntheses) plays an important role in determining ZnO crystal size and the morphology of the material. Understanding such interaction and

the trend of crystal size evolution will assist the precise control of the synthesized material morphology to meet specific requirements.

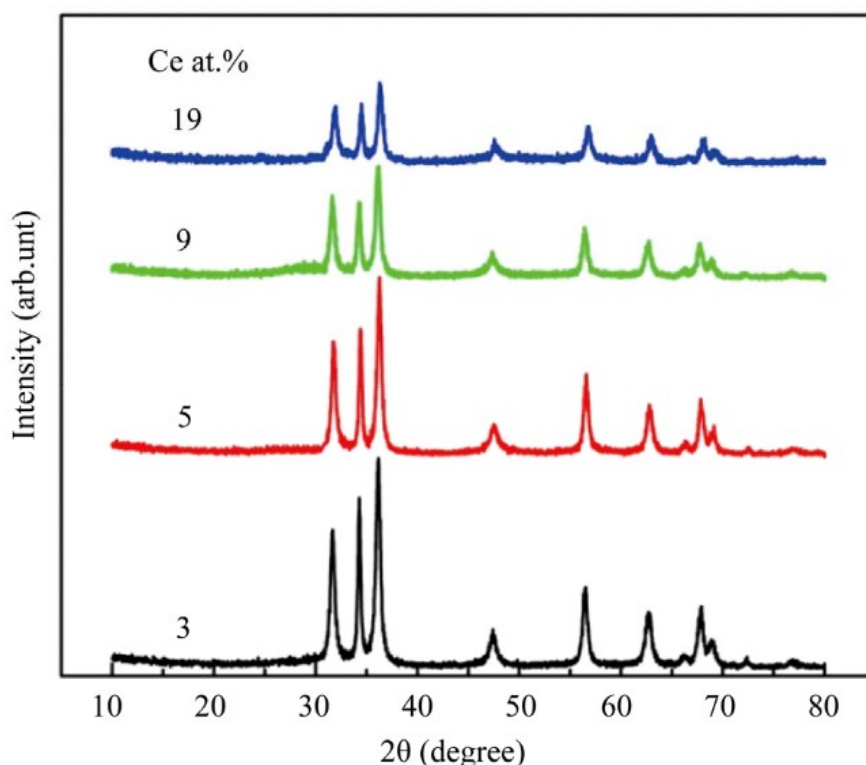


**Figure 1.12** XRD patterns of Ce-doped ZnO nanoparticles. [110]

It is well known that  $\text{Ce}^{4+}$  is more stable than  $\text{Ce}^{3+}$ . When  $\text{Ce}^{3+}$  is used as the source of Ce doping in ZnO, it is likely that both states are present in ZnO. The co-existence of  $\text{Ce}^{3+}$  and  $\text{Ce}^{4+}$  can be proved by X-ray Photoelectron Spectroscopy (XPS). [106], [109], [113], [117] Since  $\text{Ce}^{4+}$  is non-luminescent, the luminescence of Ce-doped ZnO is affected by the transition between the two valence states.

**Figure 1.13** shows an example of PL spectra of Ce-doped ZnO in comparison with that of undoped ZnO. The PL spectra are composed of a sharp UV emission at 384 nm and a broad visible emission between 500 nm and 700 nm. The UV emission ascribed to the excitonic emission is quenched by Ce doping because doping increases the density of non-radiative defects. [109] Possibly present  $\text{Ce}^{4+}$  ions may trap the excited electron and then reduce to  $\text{Ce}^{3+}$ , hence inhibiting excitonic recombination while giving rise to visible emissions. [112] The reduction of ZnO grain size can also result in such quenching effect. Besides the quenching effect of Ce doping, some studies also reported the shift of the UV emission. The red shift is attributed to shallow defects near the CB, or to the bandgap reduction, which is caused by localized Ce electron states (*i.e.*, impurity band) at the lower edge of the CB as the new lowest unoccupied molecular orbital. [115], [118] The blue shift is caused by extra electrons of  $\text{Ce}^{4+}$  donors that introduce radiative electron levels at the bottom of the CB. [111]

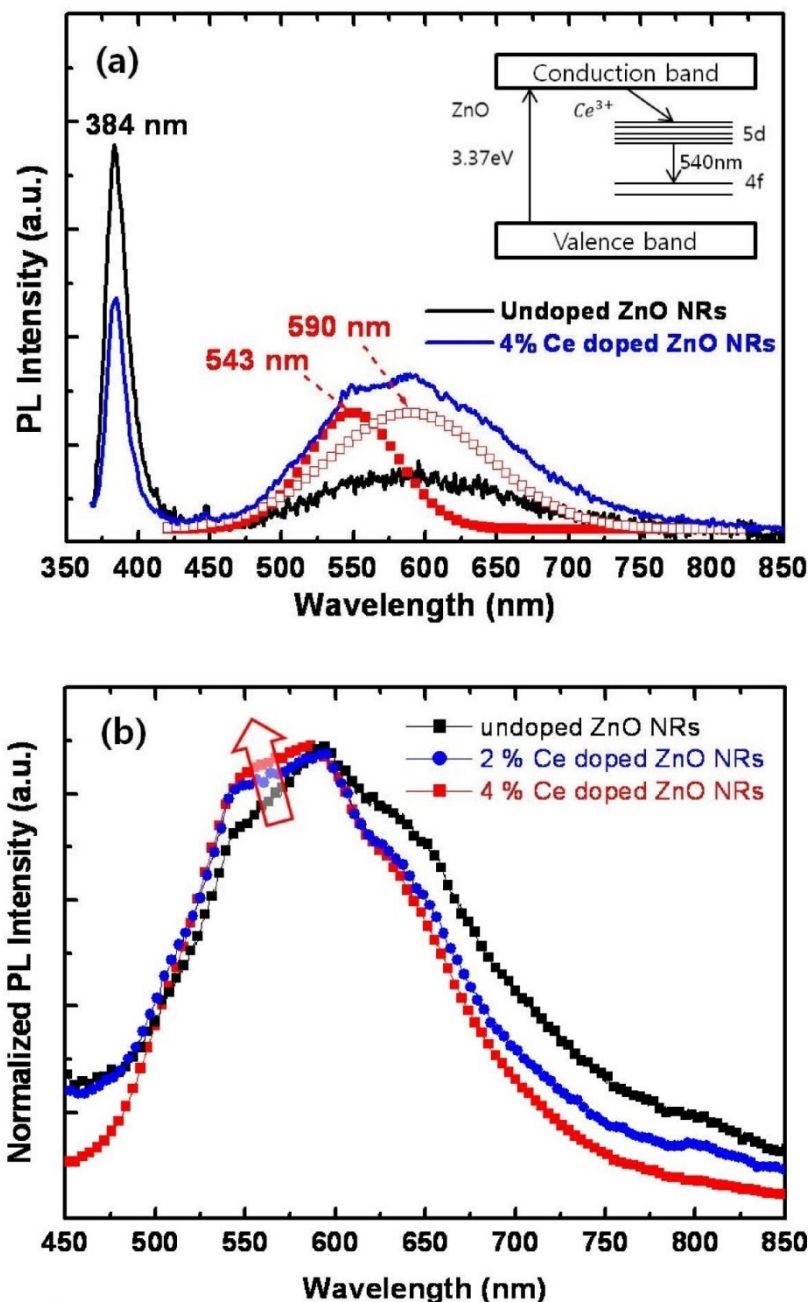


**Figure 1.13** (a) PL spectra of undoped ZnO and Ce-doped ZnO. The inset shows a schematic diagram of  $\text{Ce}^{3+}$  electronic levels in ZnO bandgap. (b) Normalized PL spectra in the visible range of undoped and Ce-doped ZnO.

In **Figure 1.13** (a), the enhancement of visible emission is evident with Ce doping. While undoped ZnO possesses intrinsic defects that bring about visible emissions, Ce acts as new luminescent centers thanks to the  $5d \rightarrow 4f$  transitions. The deconvoluted peaks are therefore attributed to both intrinsic defects (590 nm) and Ce impurity (543 nm). The peak at 543 nm actually consists of two peaks corresponding to transitions to the two ground states of  $\text{Ce}^{3+}$  in the crystal. In cases where  $\text{Ce}^{4+}$  is used as dopant source or where  $\text{Ce}^{4+}$  ions coexist with  $\text{Ce}^{3+}$  ions, the visible luminescence is also found to increase with the

doping, because part of the electrons in the CB can be utilized to convert  $Ce^{4+}$  ions into  $Ce^{3+}$  ions. [112] **Figure 1.13** (b) exemplifies that the relative intensity of green emissions from  $Ce^{3+}$  centers increases with increasing doping concentration from 0 at% up to 4 at%. However, the increase of the green emission can also result from the increase in  $V_O$  concentration after doping. [110] On the other hand, blue emission is more common in Ce-doped ZnO since the energy of  $5d \rightarrow 4f$  transitions is comparable to the energy of blue light, as demonstrated in **Figure 1.11**. The energy of the excited electrons in the CB can be transferred to  $Ce^{3+}$  ions, which in turn leads to  $5d \rightarrow 4f$  transitions. Another factor for blue emission enhancement is the increase of  $Zn_i$  concentration. [105] The maximal enhancement of the blue emission was found at 0.3 mol% doping concentration. At higher Ce concentration, the energy transfer is less effective and phase separation may occur, leading to strong carrier localization, which significantly affects the PL characteristics. [119] Finally, it is worth pointing out that Ce doping decreases the relative intensity of the red component of the PL spectra in **Figure 1.13** (b) because Ce doping does not introduce energy levels responsible for red emission, making it not suited for WLEDs applications.

### 1.3.2 Non-rare-earth doping

Non-RE doping in ZnO has been studied extensively not only for optoelectronics but for sensing, photocatalysis and other applications as well. [120]–[122] Non-RE dopant ions usually have smaller ionic size than lanthanides, so they have higher solubility in ZnO. Easier incorporation of these dopants makes it easier to modulate the properties of ZnO. Some of the most researched non-RE dopants belong to transition metals (TMs), some of which (*e.g.*, Co, Fe, Mn) are excellent candidates for introducing ferromagnetism into non-ferromagnetic ZnO. In the aspect of optical properties, copper and chromium are some of the most studied non-RE elements. Herein, a selection of dopants for ZnO will be discussed in detail, primarily on the doping effect on the optical properties of ZnO.

*H doping.* Hydrogen is the most common unintentional dopant because it is present in all growth methods for ZnO and large amounts of hydrogen can easily diffuse into ZnO crystals, owing to its good mobility. First-principles calculations suggested that hydrogen is positioned close to the bottom of the CB in the band gap in charged state  $H^+$ , as demonstrated in **Figure 1.10**. The exciton can be bound to  $H^+$  at low temperature and the recombination of such hydrogen-donor-bound exciton leads to near-band-edge emission (NBE). Intentional hydrogen doping was performed to study the effects of hydrogen impurity on the PL of ZnO. [123], [124] A trade-off relation was established between the enhancement of NBE and the reduction of deep-level emission. NBE can be enhanced by hydrogenation while the deep level-related visible emission is quenched, as the deep donor and acceptor states are passivated by electron transfer from hydrogen to the defects. [125] Therefore, the extent of enhancement of NBE also depends on the defect type and concentration in the initial ZnO.

Besides existing as an interstitial, which is the aforementioned shallow donor  $H^+$ , hydrogen can also substitute oxygen vacancy to form  $H_O$ , also a donor but more stable. [126], [127] Under oxygen-poor ambient, hydrogen can be trapped at  $V_O$ , hence increasing NBE and reducing emission from transitions related to  $V_O$ . [128] With subsequent annealing of hydrogenated ZnO in the air, it is found that hydrogen interstitials diffuse out at about 150 °C while  $H_O$  can be completely annealed out at 700 °C. The understanding of hydrogen in ZnO helps to balance the emissions from near-band-edge recombination and deep-level transitions. For WLED applications, unintentional hydrogen doping should be avoided so that visible emission can be achieved with the highest possible intensity.

*Cu doping.* Comprehensive studies have shown that Cu doping is responsible for intense green luminescence in ZnO. An early study by Dingle showed that a broad structured green band near 510 nm at low temperatures was due to copper atoms on zinc sites. [129] The ionic radii of  $Cu^{2+}$  (87 pm) and  $Cu^+$  (91 pm) are both close to  $Zn^{2+}$  (88 pm) and their formation energies are rather low, so it is favorable for Cu ions to substitute Zn in the unit cell of ZnO. A further study by Garces *et al.* suggested that both  $Cu^{2+}$  and  $Cu^+$  existed in ZnO, assigning  $Cu^+$  to an unstructured green band near 500 nm while concurring the assignment by Dingle of  $Cu^{2+}$  to the structured band. [130]

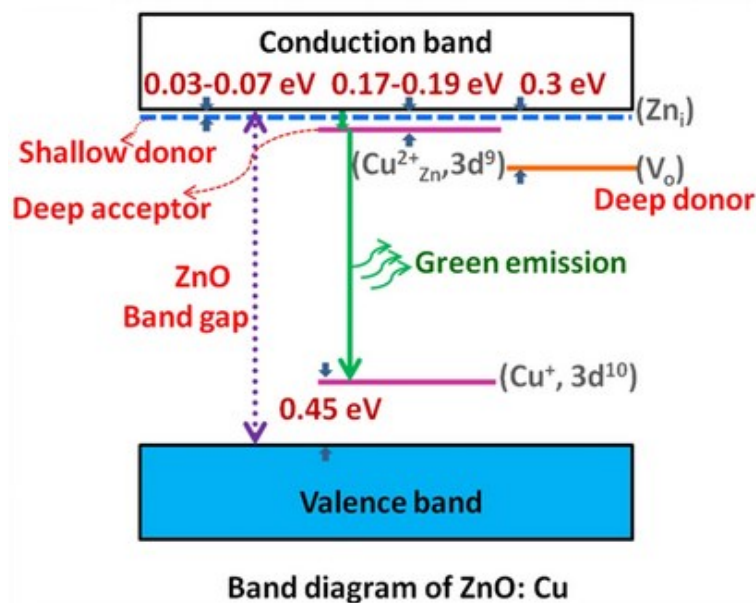


**Figure 1.14** Schematic of the energy level diagram of Cu-doped ZnO system. [131]

The mechanism behind the green emission can be visualized in **Figure 1.14**. At room temperature, Cu-doped ZnO exhibits rapid increase in green luminescence intensity at low doping concentrations. In addition to the green emission originating from intrinsic  $V_O$  defect, Cu doping enhances the green emission in two ways. On the one hand, concentration of  $V_O$  increases as more Cu atoms are incorporated into ZnO lattice. On the other hand,  $Cu^{2+}$  ( $3d^9 4s^2$ ) ion in place of Zn creates an acceptor level below the CB in ZnO bandgap, while  $Cu^+$  ( $3d^{10} 4s^2$ ) ion, *i.e.*, singly ionized acceptor, recombines with the donor.

Such mechanism is particular to copper, since other non-RE dopants, to our best knowledge, have not been reported to introduce new luminescent levels in ZnO. However, when the doping concentration increases above solubility limit, which is very low, the intensity of the green emission decreases, as excess Cu atoms agglomerate into metallic copper clusters or CuO. [131] The understanding of the luminescence of Cu-doped ZnO is well established, which is significant for studies of ZnO doping, since copper is also a common unintentional impurity in ZnO.

*Ni doping.* Nickel, along with cobalt, iron and manganese, is recognized as the one of most efficient TMs to tune the magnetic, electrical and optical properties of ZnO. Having a smaller ionic radius of 83 pm,  $\text{Ni}^{2+}$  ions are also easy to incorporate into ZnO lattice. However, unlike copper with two stable valence states, Ni impurity has not been reported to introduce intermediate radiative energy levels in ZnO bandgap. Nevertheless, similar enhancement of green emission by Ni doping has been reported. Iqbal *et al.* observed significantly intense green emission band centered at 2.18 eV (569 nm) for Ni-doped ZnO nanorods compared to undoped ZnO nanorods and they attributed such enhancement of green emission to  $V_{\text{O}}$  located at the surface of nanorods. [132] On the contrary, Tong *et al.* found that Ni doping below 5 at% in ZnO nanoparticles quenched green emission while enhancing UV emission. They concluded that Ni doping led to an increase in electron concentration and a concomitant decrease in intrinsic defects (such as  $V_{\text{O}}$  and  $\text{O}_{\text{Zn}}$ ) density. [133] Such discrepancy of the doping effect on ZnO is common in the literature considering various synthesis techniques and ZnO morphologies. [109], [118]

*Co doping.* As another efficient TM dopant in ZnO, cobalt is also able to tune the magnetic and optical properties of ZnO due to its abundant electron states. The solubility of  $\text{Co}^{2+}$  in ZnO can be as high as 7 at%. [134] One eminent effect of Co doping in ZnO is the alteration of energy band structure, which is manifested in the shift of UV emission in PL spectra. Both blue shift and red shift of UV emission have been reported. [135]–[138] The blue shift can be explained by the Moss-Burstein effect, in which case the electron from the top of VB can only be excited above Fermi level, which lies in the CB, due to populated states in CB. [139] The red shift can be explained by *sp-d* exchange interactions between the band electrons and the localized *d* electrons of  $\text{Co}^{2+}$  ions substituting Zn ions. [138], [140] In addition, the size of the ZnO nanostructure is also a factor to consider. In most cases, Co doping induces an increasing quenching effect in visible emission with increasing doping concentration. Chang *et al.* explained this phenomenon as a result of the competition between increased native defects density induced by doping and suppression of defect luminescence originated from interaction between Co and defects. [141] Such competition mechanism is relevant for other dopants as well.

*Fe doping.* Studies on Fe doping usually concern  $\text{Fe}^{3+}$ , since  $\text{Fe}^{2+}$  is less stable although possible to (co)exist in ZnO. Techniques such as XPS, electron paramagnetic resonance (EPR) and Mössbauer spectroscopy can be employed to confirm the (co)existence of  $\text{Fe}^{2+}$  in ZnO. [142]–[144] Fe exerts doping effect on the optical properties of ZnO similarly to Co doping. Fe doping does not introduce new

radiative energy levels. Green emission from Fe-doped ZnO is quenched upon increasing doping concentration due to stronger suppression of defect luminescence. [145], [146] On the higher energy end, UV emission is also quenched and shifted by Fe doping for the same reasons as Co doping. [143] A blue or violet emission, however, can be present at high doping concentrations due to radiative defects related to interface traps existing at the grain boundaries. [143], [146] Zhang *et al.* indicated that  $Zn_i$  was the dominating defect responsible for the appearance of blue emission at high doping concentrations. [147] Fe doping is more complicated than other dopants because of the two possible valence states and the formation of second phases at high doping concentrations. Very different effects of Fe doping have been reported in the literature; therefore, it is difficult to pin down a general rule for Fe doping.

*Mn doping.* Mn is best known for introducing ferromagnetism in ZnO and Mn doping has facilitated the successful synthesis of diluted magnetic semiconductors (DMS) with ZnO-based materials.  $Mn^{2+}$  has a solubility of  $\sim 14\%$  in ZnO, but incorporation of Mn in ZnO can still be difficult at low synthesis temperature due to high Mn-O bond energy. [148] The incorporation of Mn also alters the bandgap of ZnO, resulting in a shift of UV emission. At low doping concentrations, UV emission displays a red shift caused by *sp-d* exchange interactions and band tailing effect; at high doping concentrations, a blue shift is seen due to the Moss-Burstein effect. [149] In general, Mn doping imposes a quenching effect on the visible emission of ZnO because Mn does not introduce radiative energy levels but promotes non-radiative recombination processes. [149]–[153] However, Mahmood *et al.* proposed that Mn tail states lie approximately 1.15 eV below CB of ZnO, which gives rise to a radiative recombination of electron and hole releasing a photon in the green band. [154] Enhancement of PL intensity was also reported by several research groups who concurrently attributed it to the increasing native defect density produced by Mn incorporation. [148], [155], [156]

*Cr doping.* Being a non-magnetic TM, chromium can also exhibit room temperature ferromagnetism when doped in ZnO, but the incorporation of Cr does not necessarily improve PL of ZnO. The quenching effect pertains for UV emission since  $Cr^{3+}$  can easily trap an electron and reduce to  $Cr^{2+}$ , suppressing the excitonic recombination. For the visible emission, Cr doping seems to induce a broader band despite the quenching effect reported by many. [157]–[161] The broad band spans from violet ( $\sim 430$  nm) to orange ( $\sim 600$  nm), or even to red ( $\sim 690$  nm) when excited by visible light. [162], [163] More interestingly, a higher doping concentration (6 at%  $\sim$  7 at%) may improve PL intensity due to a steady increase of  $V_o$  density. [162], [164]

*Ag doping.*  $Ag^+$  is an effective dopant with a larger ionic radius than  $Zn^{2+}$  to enhance the optical properties of ZnO, especially its absorption and UV emission intensity. While most researchers attribute the UV emission to excitonic recombination, a particular study by Wang *et al.* suggests that it corresponds to a DAP transition, as Ag atoms incorporate into ZnO and disrupt the concentration of

acceptor impurities. [165] The UV emission intensity was found to increase up to 2.8 at% Ag doping concentration and decrease with heavier doping due to formation of metallic Ag clusters. Zhang *et al.* also discovered that low doping was favorable for the improvement of UV emission and that Ag doping did not lead to new emissions. [166] Other results confirm that the luminescence mechanism of ZnO cannot be altered through Ag doping, while the intensity of the visible emission varies. [167]–[169]

*Al doping.* Moving away from TMs, aluminum is the most popular dopant in ZnO to tune its electrical and optical properties for transparent conductive oxide (TCO) applications.  $\text{Al}^{3+}$  can substitute  $\text{Zn}^{2+}$  or occupy an interstitial site, hence modifying the PL of ZnO, in a similar manner as TM doping. The quenching effect is also observed for Al-doped ZnO, which is ascribed to the introduction of non-radiative defect centers. [170]–[173] However, when doped with an increasing concentration,  $\text{Al}^{3+}$  doping is beneficial for increasing  $\text{O}_i$  concentration, because excess oxygen is necessarily introduced to equilibrate positive charges. [174], [175] The increase in  $\text{O}_i$  concentration results in an enhancement of blue (450 nm) emission, as reported by Srinatha *et al.* [176]  $\text{Al}^{3+}$  doping can enhance or reduce the intensity of visible emission, while a peak shift of visible emission is often observed. Such peak shift is the result of competition between native defects  $V_{\text{O}}$  and  $\text{O}_i$  caused by  $\text{Al}^{3+}$  incorporation. The UV emission is found to shift with  $\text{Al}^{3+}$  doping as well, which is due to the Moss-Burstein effect.

*Bi doping.* Bismuth is a less studied dopant in ZnO. Because of the large ionic radius of  $\text{Bi}^{3+}$ , doping with Bi significantly affects the morphology of ZnO, which, in turn, affects the optical properties of doped ZnO. Xiu *et al.* found that Bi doping could introduce shallow acceptors in ZnO thin films by temperature-dependent and excitation power-dependent PL measurements. [177] A red shift in near-band-edge emission is therefore often observed in Bi-doped ZnO. [178], [179] Visible emission is significantly quenched by Bi doping, as demonstrated in references [178] and [180], which can be ascribed to the decrease of oxygen-related defects after Bi doping. Although blue or violet emission peaks have been reported to be enhanced at certain doping concentrations, the mechanism of the enhancement is still unclear. [179], [181], [182] One possibility is the energy transition from  $^3\text{P}_1$  to  $^1\text{S}_0$  of  $\text{Bi}^{3+}$ , as proposed by Ginting *et al.* [178]

### 1.3.3 Summary on doping

A variety of dopants in ZnO has been reported extensively in the literature. The main known dopants to bring about extrinsic deep-level defects in ZnO are Li, Cu, Fe, Mn, and OH, which have been reported to emit at different wavelengths as discussed in more detail by Klingshirn *et al.* and Özgür *et al.* [66], [183] Other dopants usually have a quenching effect on PL intensity, meaning that they introduce non-radiative levels or decrease the effect of the intrinsic defects. However, the enhancement of PL intensity has also been reported, notably at low doping concentration. Both UV emission and visible emission

manifest position shift after doping, indicating that dopants modify the bandgap or the energy levels of intrinsic defects in the bandgap. There still lacks a consensus on the general effect of doping in ZnO despite numerous studies, which report different ZnO structures synthesized via different methods.

## 1.4 ZnO nanostructures

ZnO has a rich variety of nanostructure morphologies, as exemplified in **Figure 1.15**. ZnO nanostructures can be fabricated by various methods, such as thermal evaporation, hydrothermal synthesis, chemical vapor deposition, template-based synthesis, laser ablation, *etc.* In recent years, more and more nanostructures of ZnO-based materials have been reported for a wide range of applications including laser diodes and LEDs. In particular, one-dimensional nanowires were fabricated for laser diodes and LEDs as the orientation of the nanowires is critical in these devices, but for most applications, the orientation does not affect the properties of the nanostructure.

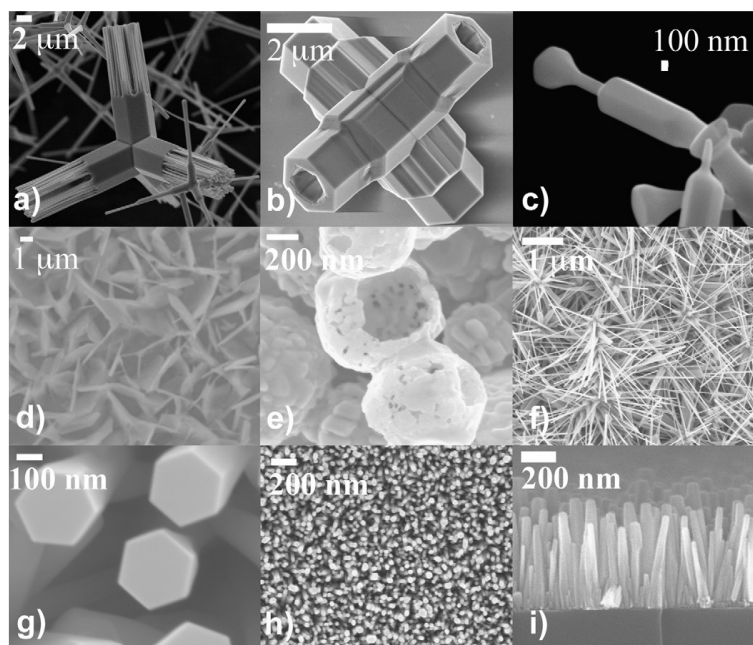


**Figure 1.15** Various morphologies of ZnO nanostructures: (a) and (b) tetrapod structures; (c) variable diameter structures; (d) nanosheets; (e) nanoshells; (f) multipods; (g), (h), and (i) nanorods. [120]

Nanostructured ZnO exhibits different optical properties from bulk ZnO, primarily because of the size effect and the increase in surface-to-volume ratio. The PL spectrum of bulk ZnO typically consists of a strong narrow emission in the UV range and a weak broad emission in the visible range, corresponding to excitonic emission and trap emission, respectively. Both intrinsic and extrinsic defects are found in the bulk and at the surface of ZnO. When the surface-to-volume ratio is large enough, surface defects are no longer negligible and may even become the determining factor for PL. Often surface defects, either deep or shallow, provide pathways for non-radiative relaxation processes of electrons and holes.

[93] The surface of ZnO nanostructure is also characteristic of defect states such as adsorbed hydroxyl (OH), which is known to quench the UV emission. [184] As illustrated in **Figure 1.16**, once the  $e^-h^+$  pair is generated by photoexcitation, the electron is captured by intrinsic or extrinsic defects while the hole is trapped by surface states or defects. Then the surface-trapped hole tunnels back into the nanocrystal where it recombines with an electron, giving visible emission. Such mechanism was proposed by van Dijken *et al.* for green emission and further confirmed by Zhang *et al.* through passivating the surface of ZnO nanocrystals with Mn. [93], [185] The passivated surface prevents surface states from trapping photogenerated electrons or holes, thus quenching the green emission. As we can see, controlling the surface states is of paramount importance for the optical properties of ZnO nanostructures.

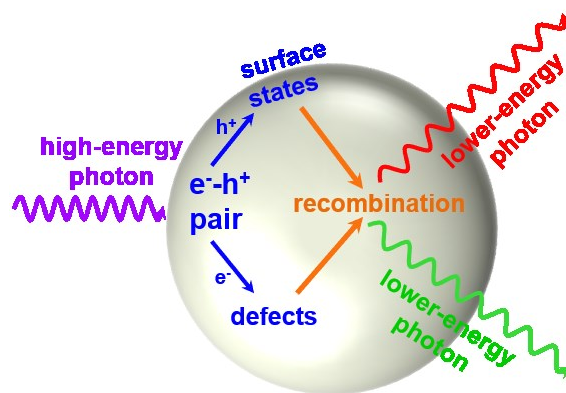


**Figure 1.16** Illustration of the mechanism on the origin of the visible emission in ZnO nanocrystal.

Doping in ZnO nanostructure can further modulate its optical properties. In general, doping imposes similar effects on ZnO nanostructures to the case in bulk ZnO as discussed in Section 1.3. Some dopants can introduce new radiative levels, such as H, Li, Cu, Fe, and Mn, while most dopants quench the intensity of PL. The impurities also affect the crystallization of ZnO nanoparticles and the morphology of the nanostructure. As the size of ZnO nanocrystals decreases, the impurities are more likely to segregate from the bulk, forming more defects at the surface. Hence, the major difference between doping in bulk and nanostructured ZnO lies in the influence of the dopants on the surface states.



## Chapter 2 Materials and Characterizations

### 2.1 Syntheses of ZnO-based nanomaterials

#### 2.1.1 Hydrolysis of ZnEt<sub>2</sub>

The materials concerned in the present thesis were all synthesized via a chemical hydrolysis protocol based on diethyl zinc ( $\text{Zn}(\text{CH}_2\text{CH}_3)_2$ , or  $\text{ZnEt}_2$ ) developed by S. Daniele's team at IRCE Lyon. This protocol was adopted because it has proven effective in modifying the surface states of ZnO nanoparticles in previous studies. [186], [187] In addition, it is an environmentally friendly reaction in aqueous environment, which does not produce harmful waste or require rigorous conditions, such as high temperature or high pressure. The hydrolysis reaction is given as follows:

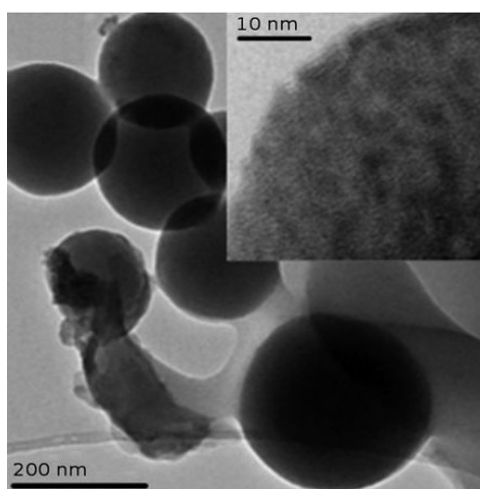


**Figure 2.1** Mesospheres of ZnO nanocrystals embedded in PAA matrix. The inset permits to notice small nanocrystals of ZnO, smaller than 10 nm. [187]

In a typical synthesis process, 1.8 mL of commercial  $\text{ZnEt}_2$  solution in toluene at 15 wt% (weight percent) is added dropwise into an aqueous solution of polyacrylic acid (PAA,  $(\text{CH}_2\text{CHCOOH})_n$ ) at 0.63 wt% under vigorous stirring. The molecular weight of the weak polymeric acid (PAA) is determined to be  $2000 \text{ g} \cdot \text{mol}^{-1}$  since low molecular weight is beneficial for the formation of ZnO nanocrystals embedded in polymeric mesospheres, as shown in **Figure 2.1**. [187] The synthesis is performed under inert atmosphere for  $\text{ZnEt}_2$  is pyrophoric. Stirring continues overnight for 24 hours at room temperature while ethane generated from the reaction is constantly extracted via a bubbler. The resulting ZnO is subsequently separated by centrifugation at 4000 rpm for 10 minutes, which permits to obtain a white

powder. The white powder is then washed in ethanol and rinsed twice with water, and finally dried at 70 °C for 4 hours.

The hydrolysis process described above was designed to fabricate ZnO/PAA mesospheres as shown in **Figure 2.1**. The hybrid inorganic-organic (ZnO-polymer) nanomaterial was found promising for WLEDs application. It exhibits intense visible emission peaking at around 540 nm and a stable PL QY up to 70 %. [187] **Figure 2.2** presents the photoluminescence (PL) spectrum of ZnO/PAA mesospheres excited at 266 nm. The high PL QY was attributed to the nanosize of the ZnO crystals and the modification of their surface states by the incorporation of PAA.

Based on this nanohybrid structure, the influence of metallic elements doping is studied in the present thesis in order to tune the visible emission spectrum of the material. Furthermore, the influence of silica coating on the nanohybrid is investigated with the motivation to improve the emission efficiency and the thermal stability of the material.

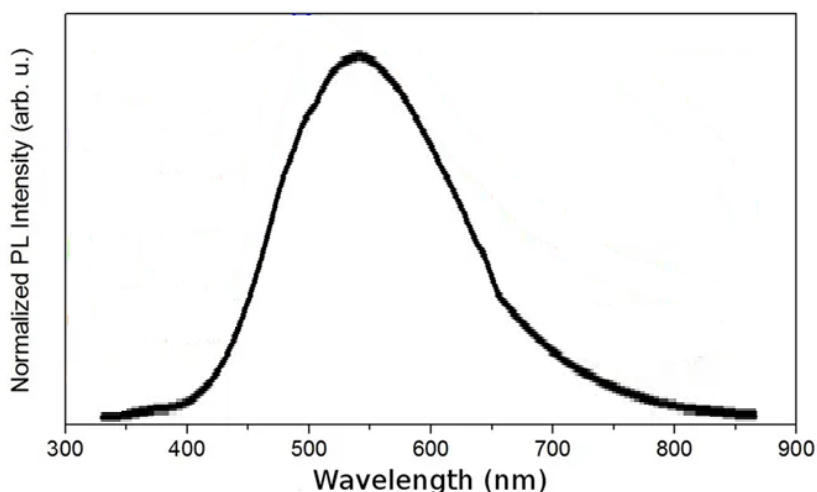


**Figure 2.2** PL spectrum of ZnO nanohybrid obtained in previous study. [187]

### 2.1.2 Metal-doped ZnO nanohybrids

As introduced in Section 1.3, doping is a common strategy to tune the visible emission of ZnO since the native defects in ZnO have relatively fixed positions in the bandgap. The ability to tune the color of the emitted light of ZnO nanohybrids would facilitate the application of the material in the lighting industry. Therefore, various metallic elements, as listed in **Table 2.1**, have been chosen as dopants to tune the emission of ZnO nanohybrid. All these elements are non-RE elements, except for cerium, which is included in the study for comparison. Some of these dopants have been studied extensively in the literature. For instance, copper is known to introduce radiative energy states in the bandgap of ZnO.

[130] Some are less studied or extensively studied for purposes other than photoluminescence. For instance doping with iron, cobalt, and manganese is known to introduce ferromagnetism or produce diluted magnetic semiconductors. [142], [188], [189] These elements are bound to have different impacts on the PL of ZnO nanohybrids as they have different ionic radii (smaller or bigger than that of  $Zn^{2+}$ ) and different valence states (from +1 to +4). On top of that, iron and copper were doped at two different valence states, respectively, in order to investigate the impact of valence state of the same dopant. Chromium was doped with two different precursors, namely  $CrCl_3$  and  $Cr(NO_3)_3 \cdot 9H_2O$ , for the investigation on the impact of anions in the hydrolysis solution. Furthermore, each dopant was introduced at three different concentrations, *i.e.*, 0.1 at%, 1 at%, and 5 at% with respect to Zn.

**Table 2.1** List of elements doped in ZnO nanohybrid sorted in the ascending order of their ionic radii.  $Zn^{2+}$  has an ionic radius of 88 pm.

| Element | Precursor compound               | Ionic radius (pm) | Ionic radius ratio (% of Zn) |
|---------|----------------------------------|-------------------|------------------------------|
| Al      | $Al(NO_3)_3$                     | 67.5              | 76.6                         |
| Fe      | $FeCl_3$                         | 69                | 78.4                         |
|         | $(NH_4)_2Fe(SO_4)_2 \cdot 6H_2O$ | 75                | 85.2                         |
| Cr      | $CrCl_3$                         | 75.5              | 85.8                         |
|         | $Cr(NO_3)_3 \cdot 9H_2O$         |                   |                              |
| Co      | $Co(NO_3)_2 \cdot 6H_2O$         | 79                | 89.8                         |
| Mn      | $MnCl_2 \cdot 4H_2O$             | 81                | 92.0                         |
| Ni      | $Ni(NO_3)_2 \cdot 6H_2O$         | 83                | 94.3                         |
| Cu      | $Cu(NO_3)_2 \cdot H_2O$          | 87                | 98.8                         |
|         | $CuCl$                           | 91                | 103.4                        |
| Ce      | $(NH_4)_2Ce(NO_3)_6$             | 101               | 114.8                        |
| Bi      | $Bi(NO_3)_3 \cdot 5H_2O$         | 117               | 133.0                        |
| Ag      | $AgNO_3$                         | 129               | 146.6                        |

The syntheses of the doped ZnO nanohybrids followed the same procedure as mentioned above in Section 2.1.1 with one additional step of the introduction of dopant. Dopant precursors were firstly dissolved in the aqueous solution of PAA before commercial  $ZnEt_2$  solution was added into the solution

under continuous and rigorous stirring. In this manner, we obtained 39 powder samples of metal-doped ZnO nanohybrids plus 1 powder sample of undoped ZnO nanohybrid for comparison. Each sample will be denoted by its doping concentration, dopant element, and dopant valence when necessary. For example, “0.1 % Cu<sup>2+</sup>” and “0.1 % Cu(II)” both denote Cu-doped ZnO with Cu(NO<sub>3</sub>)<sub>2</sub>·H<sub>2</sub>O at doping concentration of 0.1 at%. It should be noted that the final valence state of the dopants in the powder samples was not confirmed by any technique. Therefore, the valence state herein refers to the valence state of the metallic element in its precursor compound.

Synthesizing the doped ZnO nanohybrids in the same manner provides us with the means to study the effect of dopant systematically under the same conditions. It is advantageous over the studies of a single dopant, which sometimes provide contradictory results in the literature due to different synthesis processes. [109], [118] Therefore, one aim of the study is to obtain a general idea on the effects of the dopants on the optical properties of ZnO by minimizing the number of variables between different dopants.

### 2.1.3 Silica-coated ZnO nanohybrids

Doping may be able to modify the PL spectrum of ZnO; however, it may also quench the emission efficiency as discussed in Section 1.3. Continuous efforts are being made to improve the PL QY of ZnO nanohybrid, especially with the goal of application in LED industry. Despite the fact that mesospheric PAA can improve the PL QY of ZnO nanocrystals, the polymeric matrix for ZnO nanocrystals may also result in instability of the material under tough environment over long period of time. In particular, the operating condition of LED requires the material to be functional at temperature high up to 100 °C. It is therefore a crucial task to ameliorate the thermal stability of ZnO/PAA nanohybrid.

Silica has been considered an effective coating substance for nanomaterials due to the ease of incorporation, good environmental stability and material compatibility. A core-shell structure with silica offers not only the protection for the core material, but also the modification of charge states, functionality and reactivity of the core surface. [190] Therefore, coating silica on ZnO/PAA nanohybrid is a feasible and promising method to improve its optical properties.

Herein, once again, the hydrolysis synthesis is utilized to fabricate silica-coated ZnO/PAA nanohybrids. The uncoated ZnO/PAA nanohybrid undergoes the coating process in the presence of tetraethyl orthosilicate (TEOS). In a typical coating process, TEOS is added into the suspension of ZnO/PAA powder (300 mg) in ethanol (1000 mg) under constant stirring at 700 rpm at room temperature. After 30 min of stirring, 2 ml of a mixed solution (solution A) of ethanol (EtOH), water (H<sub>2</sub>O), and ammonium hydroxide (NH<sub>4</sub>OH) is added into the suspension. The nominal mass ratio of EtOH:H<sub>2</sub>O:NH<sub>4</sub>OH is 1:0.93:0.027. The stirring continues at 700 rpm at room temperature for another 4 h to obtain the final

suspension. The resulting solid is recovered by centrifugation and then washed twice with ethanol and dried for 4 h at 70 °C.

After preliminary analyses, it was found that the morphology of the coated nanostructure mainly depends on the amount of TEOS and  $\text{NH}_4\text{OH}$ . The amount of TEOS in the primary suspension determines the thickness of silica coating, while the amount of  $\text{NH}_4\text{OH}$  affects the integrity of ZnO/PAA mesospheres. Hence, samples with different amounts of TEOS and  $\text{NH}_4\text{OH}$  were synthesized, as listed in **Table 2.2**. The samples are denoted by the weight ratio between TEOS and ZnO in starting compounds, where ZnO is set as 1. For instance, a sample with TEOS:ZnO = 3.8:1 in weight ratio is denoted as 3.8Si. Samples with different amount of  $\text{NH}_4\text{OH}$  are denoted as 1A, 1.5A, 2A, *etc.*, where the numbers represent the multipliers of the nominal  $\text{NH}_4\text{OH}$  mass ratio (0.027) in solution A while the ratios of EtOH and  $\text{H}_2\text{O}$  are fixed. It should be noted that the 14 ZnO/PAA samples were synthesized independently under similar conditions with slight differences in synthesis temperature and washing solvent, which are not considered determining factors for the optical properties. Six of them that were synthesized under exactly the same conditions were subsequently used as the precursor for the silica coating process of 3.8Si-*y*A samples.

**Table 2.2** List of silica-coated samples with different amounts of TEOS and  $\text{NH}_4\text{OH}$ .

| Sample denotation | Weight ratio of TEOS to ZnO                  | Weight ratio of $\text{NH}_4\text{OH}$ in solution A | Number of samples |
|-------------------|--|--|-------------------|
| ZnO/PAA           | 0  | 0  | 14                |
| <i>x</i> Si-1A    | <i>x</i> = 1.1, 2, 3, 3.8, 5, 6, 7, 8, 9, 10 | 1  | 10                |
| 3.8Si- <i>y</i> A | 3.8  | <i>y</i> = 1, 1.5, 2, 2.5, 3, 4                      | 6                 |
| 0Si-2A            | 0  | 2  | 1                 |

## 2.2 Structural characterizations

The structure of the metal-doped ZnO nanohybrids and silica-coated ZnO/PAA nanohybrids was characterized by several techniques including X-Ray Diffraction (XRD), Transmission Electron Microscopy (TEM), Rutherford Backscattering Spectrometry (RBS), and Fourier Transform Infrared Spectroscopy (FTIR). XRD and TEM are powerful tools to determine the crystalline structure of the nanomaterials and to estimate the ZnO nanocrystal size. It was also possible to perform Energy Dispersive X-ray Spectroscopy (EDX) and High Angle Annular Dark-Field (HAADF) imaging on the

transmission electron microscope, which help distinguish the distribution of ZnO and silica coating. RBS is capable of determining the presence of the dopants in ZnO and FTIR is useful for detecting the chemical bonds of the nanomaterials. Each of these techniques will be introduced in this section.

### 2.2.1 X-Ray Diffraction

X-ray diffraction (XRD) is one of the most fundamental techniques in materials science for structural analysis of crystallized materials. The periodic lattice of crystals interacts with X-rays, producing a unique diffraction pattern that is indicative of the crystal structure of the material. The materials in question are expected to be ZnO nanocrystals in the form of powder; therefore, polycrystalline diffraction was performed and its principles are described here.

**Figure 2.3** illustrates the XRD setup of polycrystalline diffraction for powder samples. The X-ray source is generated by bombarding a metal target, usually Cu, with a high-energy electron beam emitted from a filament. A beam of X-ray irradiates the powder sample flattened on the sample holder at an angle of  $\theta$ . The X-ray beam is scattered by the sample and the scattered X-rays are collected by the detector that is also set at an angle of  $\theta$  to the plane of the sample. This configuration is called Bragg-Brentano  $\theta$ - $\theta$  configuration, which is a convenient configuration for loose powder samples.

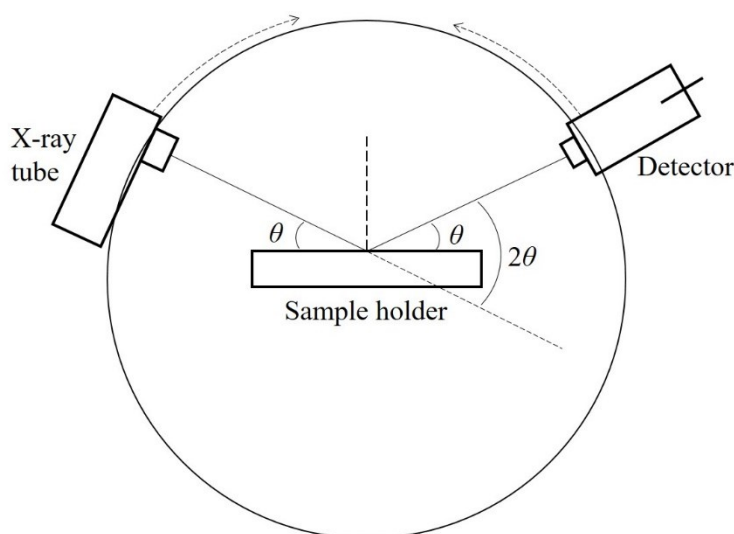


**Figure 2.3** XRD setup for the study of polycrystalline materials.

Since the interplanar distance  $d$ , or lattice spacing, is comparable to the wavelength of X-rays, constructive or destructive interference occurs with the scattered waves, as shown in **Figure 2.4**. Constructive interference occurs when  $\theta$  satisfies Bragg's law of diffraction as expressed in Equation (2.2):

$$2d \sin \theta = n\lambda, \quad (2.2)$$

where  $n$  is a positive integer and  $\lambda$  is the wavelength of the X-ray. The X-ray detector records the intensity of the scattered X-rays and attains a pattern with strong peaks at angles that satisfy Bragg diffraction. Such a pattern can also be accurately calculated once the complete crystalline parameters are known. **Figure 2.5** presents a theoretical diffraction pattern of wurtzite ZnO crystal.

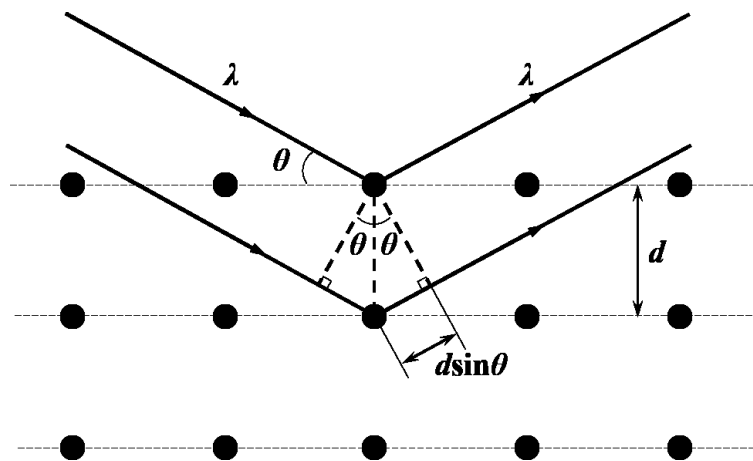


**Figure 2.4** X-ray scattering from crystalline planes.

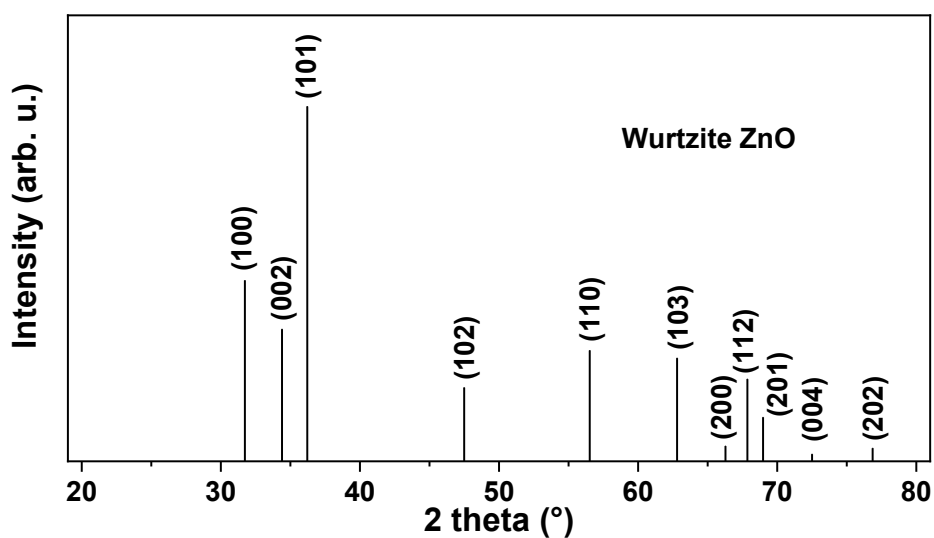


**Figure 2.5** Theoretical diffraction lines of polycrystalline wurtzite ZnO.

The XRD equipment employed in our studies was a Bruker AXS D8 diffractometer. The X-ray source was  $K_{\alpha}$  radiation of Cu. The diffraction patterns were obtained in Bragg-Brentano  $\theta$ - $\theta$  configuration and analyzed by software DIFFRAC.EVA by Bruker. The software can help identify the diffraction peaks and index the diffraction pattern to a crystal structure by comparing the diffractogram to standard ICDD PDF files in its reference databases. The mean size of the diffractive domains can also be estimated by the software according to Scherrer equation as follows:

$$\tau = \frac{K\lambda}{\beta \cos \theta}, \quad (2.3)$$

where  $\tau$  is the mean size of crystalline domains,  $K$  a constant with a typical value of 0.9,  $\lambda$  the wavelength of the X-rays,  $\beta$  the full width at half maximum (FWHM) of the diffraction peak intensity, and  $\theta$  the incident angle of the X-ray beam. For crystallites with a lot of defects, the position of the diffraction peaks may shift from the standard position, which suggests a change in lattice parameters. If we rearrange Bragg's law as  $d = \lambda / (2 \sin \theta)$ , where  $n = 1$ , the lattice spacing  $d_{hkl}$  can be calculated for each  $hkl$  plane. Since wurtzite ZnO has a hexagonal structure ( $a = b \neq c$ ,  $\alpha = \beta = 90^\circ$ ,  $\gamma = 120^\circ$ ), the lattice parameters can be calculated from the following equation:

$$\frac{1}{d^2} = \frac{4}{3} \left( \frac{h^2 + k^2 + l^2}{a^2} \right) + \frac{l^2}{c^2}. \quad (2.4)$$

### 2.2.2 Transmission Electron Microscopy

Transmission electron microscopy (TEM) is another powerful technique for structural analyses. In a transmission electron microscope (also TEM), a high-energy electron beam is produced by the filament from the field emission electron gun. The electron beam transmits through the sample of a thickness less than 100 nm to form an image after the interaction of electrons with the sample, which can be recorded by a charge-coupled device (CCD camera) for subsequent analysis. Two basic operation modes are available in TEM, as illustrated in **Figure 2.6**. In imaging mode, an image is formed by selecting transmitted electron beams with an objective aperture inserted in the back focal plane; in diffraction mode, a diffraction pattern is obtained by selecting a region with a selected area aperture inserted in the intermediate image plane. The former mode contributes bright field (BF) images, dark field (DF) images and high-resolution TEM (HRTEM) images while the latter contributes selected area electron diffraction (SAED) images.

The TEM equipment employed in our study was JEOL 2010F (from the CLYM platform (FED 4092)) and the experiments were performed by Karine Masenelli-Varlot. The powder sample was transferred onto a copper grid coated with an ultra-thin carbon film. Since the materials in question are powders of nanocrystals, it was not possible to select a region of a single ZnO crystal for analysis. Therefore, only imaging mode was used for analyses of the morphology of the materials. The crystallites can be observed, however, in HRTEM images, from which the crystal size can be estimated and crystal structure can be analyzed by fast Fourier transform (FFT) in software such as DigitalMicrograph by Gatan Inc. While the selected area aperture was futile for our nanocrystals, periodic structure in selected areas of HRTEM images can be converted into a diffraction pattern in reciprocal space by FFT for crystal structure indexing.

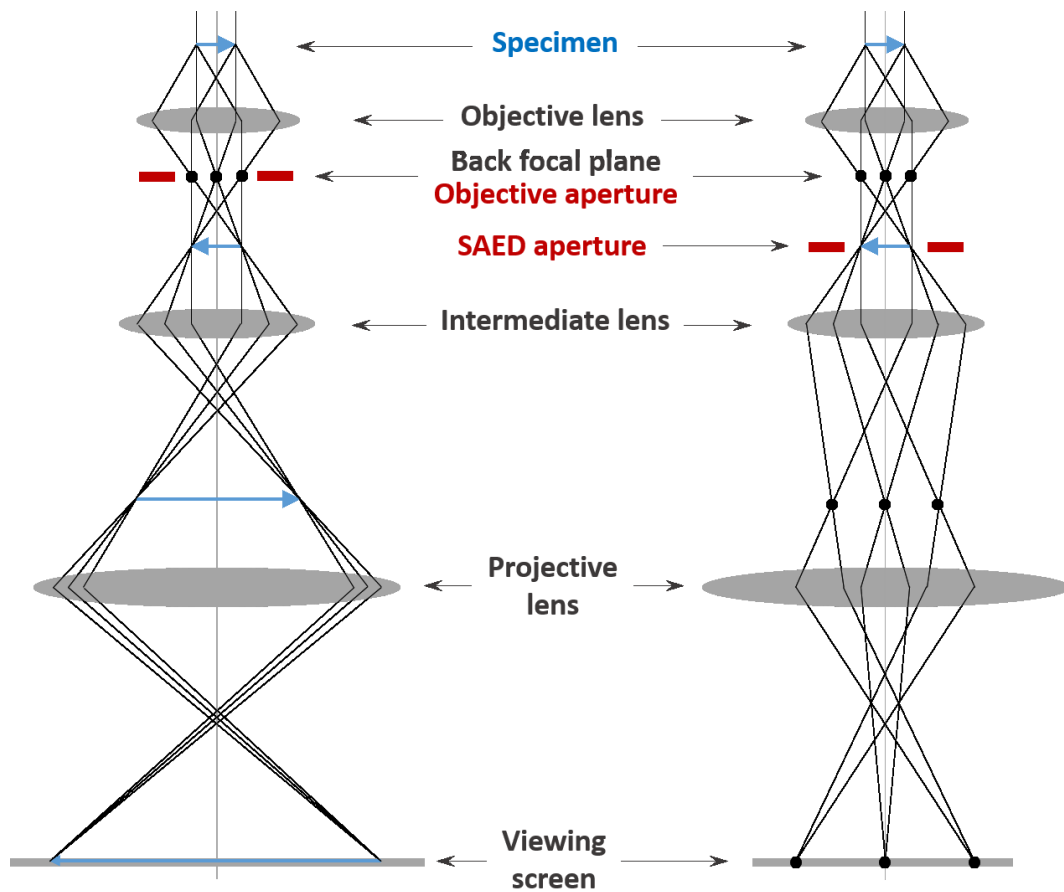


**Figure 2.6** Schemes of imaging mode (left) and diffraction mode (right) of TEM.

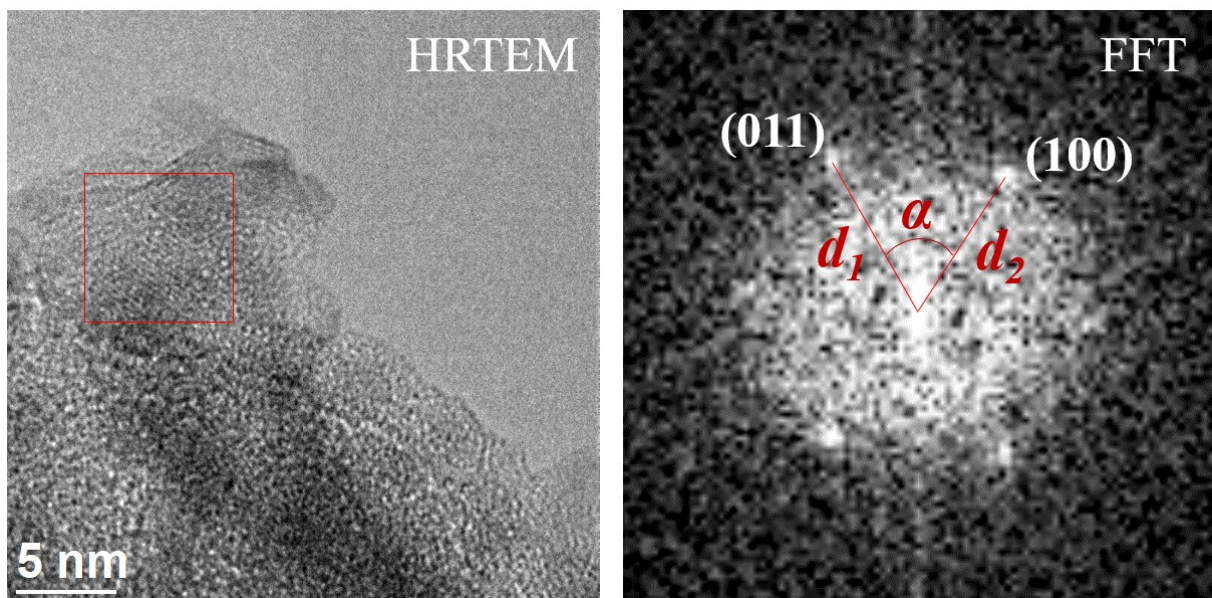


**Figure 2.7** Structure indexing via fast Fourier transform (FFT) in HRTEM image.

As demonstrated in **Figure 2.7**, for example, an area of a single crystal (in the red square) in HRTEM image (left) was converted into the diffraction pattern in FFT image (right). The diffraction spots in

reciprocal space represent atomic planes in real space. The parameters of the diffraction spots in the FFT image were measured, namely, the distance  $d_1$  and  $d_2$  from the diffraction spots to the center and the angle  $\alpha$  made by two diffraction spots via the center. The distance  $d$  is reciprocal to the plane spacing  $d_{hkl}$  in real space and the angle  $\alpha$  corresponds to the angle between two planes. By comparing the distance and the angle with the standard ZnO crystal diffraction parameters, the crystal in question was confirmed to be ZnO and the planes were determined as indicated in **Figure 2.7**.

In addition to the morphology and structure analyses in imaging mode, supplementary information on elemental distribution can be obtained under STEM (scanning transmission electron microscopy) mode. High angle annular dark-field (HAADF) imaging was performed on JEOL 2010F microscope in parallel with energy dispersive X-ray spectroscopy (EDX or EDS). For HAADF imaging, only signals from incoherently scattered electrons are collected from a small region of the sample by the annular dark field detector. HAADF imaging is sensitive to the atomic number and therefore provides direct visualization of structures with different elements. For EDX, the X-ray detector collects X-rays emitted from the sample under high-energy electron beam bombarding, producing an emission spectrum. Since each element has a unique atomic structure, each element exhibits characteristic peaks on the emission spectrum. The precision of this technique is often close to 1 at%, depending on the nature of the investigated element. EDX is helpful in analyzing the chemical composition of the scanned area qualitatively and quantitatively.

### 2.2.3 Rutherford Backscattering Spectrometry

TEM can provide substantial information on the crystal structure and chemical distribution of the material. Zn, Si, and O were distinguished without difficulty in our cases. However, the metal dopants were not easy to probe due to the low sensitivity for low doping concentrations. Moreover, the results from TEM are regional and cannot necessarily represent the whole sample. Therefore, Rutherford backscattering spectroscopy (RBS) was necessary as a complimentary tool for chemical characterization, as its sensitivity is higher ( $\pm 0.5$  at%).

In an RBS experiment, a beam of ions (usually  $H^+$  or  $He^+$  of typical energy of 0.5 to 2.5 MeV) is directed perpendicularly on the sample surface and the backscattered ions are detected by a detector. Rutherford backscattering is assumed as an elastic collision between the incident ion beam and the sample. During the collision, no energy is transferred between the incident ions and the sample particles and the collision does not lead to nuclear reaction. When the positively charged incident ion approaches the positively charged nucleus of an atom, the ion is repelled by the nucleus and a part of its energy is lost in the collision process. The ratio of the energy after the collision ( $E_1$ ) to the energy before the collision ( $E_0$ ) can be derived from binary collision theory, as written in Equation (2.5),

$$\frac{E_1}{E_0} = \left[ \frac{(M_2^2 - M_1^2 \sin^2 \theta)^{1/2} + M_1 \cos \theta}{M_2 + M_1} \right]^2, \quad (2.5)$$

where  $M_1$  is the mass of the incident ion,  $M_2$  is the mass of the target atom, and  $\theta$  is the scattering angle. [191] It can be seen that the energy loss depends on the mass of the nucleus (*i.e.*, atomic number) of the target atom and the scattering angle. By measuring the energy of the backscattered ions at a given scattering angle, a spectrum can be obtained for the analysis of element composition and depth.

In our RBS experiments for metal-doped ZnO and silica-coated ZnO nanohybrids, 2 MeV  $^4\text{He}^+$  ions were used as the incident ion beam. The backscattered ions were detected at an angle  $\theta$  of  $172^\circ$ . The technique was able to determine the composition of C, O, Zn, Si, and dopant atoms, as they are all heavier than  $^4\text{He}^+$  ions. The energy spectra were analyzed by SIMNRA software. Since the samples were nanoparticles in powder form, element depth analysis was not performed. All the RBS experiments were performed by Bruno Canut.

#### 2.2.4 Fourier Transform Infrared spectroscopy

In materials science, infrared spectroscopy (IR spectroscopy) is a common technique typically used for chemical bonds identification. It exploits the characteristic interaction of a chemical bond with the photons in the infrared range, the energy of which can be absorbed by the chemical bond according to its vibration modes. In Fourier transform infrared spectroscopy (FTIR), the IR light beam is separated into two beams by a beamsplitter and the two beams are subsequently guided to recombine and interfere by a stationary mirror and a moving mirror. The interference is realized in an interferometer called Michelson interferometer, as demonstrated in **Figure 2.8**. The modulated infrared beam is transmitted or deflected by the sample and the light output is then recorded by the detector to obtain an interferogram. The directly recorded interferogram is a function of change in path length between the two beams depending on the position of the moving mirror. The interferogram can be Fourier transformed into a spectrum in function of infrared wavelength, or more frequently, in function of wavenumber in reciprocal centimeter. The main interest of using FTIR is that it can be performed in a short time, while the same experiment with a scanning grating spectrometer would take much longer.

FTIR was performed for metal-doped and silica-coated ZnO nanohybrids in order to confirm the incorporation of PAA and silica, which are assumed to be amorphous and therefore cannot be identified by XRD or TEM analyses. The powder samples were pressed onto an indium foil before being positioned in the sample chamber of Bruker Vertex 80 FTIR spectrometer. The light source was heated SiC Globar source emitting in the mid-IR range between 2.5 and 25  $\mu\text{m}$  and the spectra were obtained in transmittance detection mode.

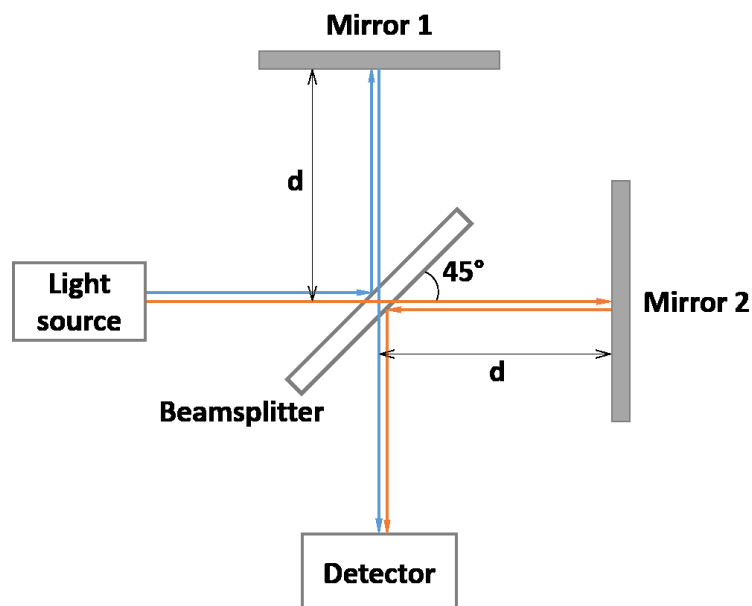


**Figure 2.8** Schematic of a Michelson interferometer.

It is expected that Zn-O bond would also yield absorption bands in the FTIR spectra. Inter-atomic vibrations in metal oxides generally give transmission bands in the fingerprint region below  $1000\text{ cm}^{-1}$ . [192] In the case of ZnO, as exemplified in **Figure 2.9**, the band is present in the region from  $400 - 700\text{ cm}^{-1}$ , which is attributed to Zn-O stretching mode of wurtzite ZnO. [193], [194]

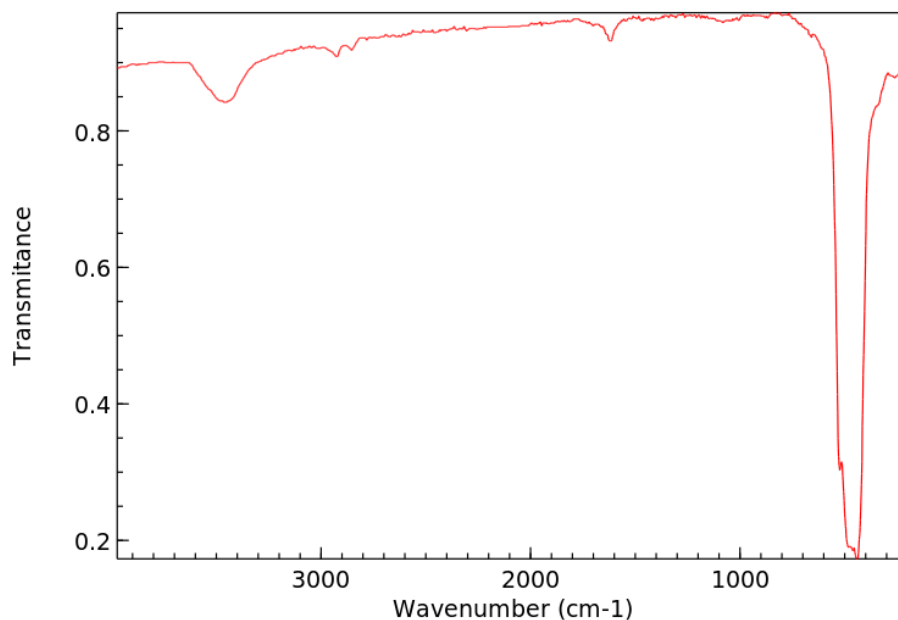


**Figure 2.9** Exemplary IR spectrum of bulk ZnO. The transmittance is normalized between 0 and 1. [193]

## 2.3 Optical characterizations

Optical properties are the most significant characteristics for luminescent materials. In particular, photoluminescence (PL) spectrum and PL quantum yield (PL QY) are the signatures of our ZnO nanohybrid, with a wide emission spectrum in the visible range and a high PL QY up to 70 %. [186], [187] The mechanism of PL in ZnO has been discussed in Section 1.2. In this section, the measurement techniques of PL and PL QY will be introduced and the calculation and calibration of PL QY will be elaborated. PL excitation (PLE) spectroscopy and PL at high temperature will be described briefly as well.

### 2.3.1 Photoluminescence spectroscopy

In order to obtain a photoluminescence (PL) spectrum of a luminescent material, we first need an excitation source. The most common excitation source is a continuous laser, the photon energy of which has to be larger than the bandgap of the material for successful excitation. Then we need a photo detector. Two types of detectors are commonly available, namely photomultiplier tube (PMT) and CCD. A PMT detects a photon by multiplying the photocurrent produced by the photon absorption to achieve high gain. It is usually coupled with a monochromator that separates photons from a broad band of wavelengths into “single” wavelengths, *i.e.*, narrow wavelengths. A CCD records a range of wavelengths via arrays of image sensors, or pixels, based on semiconducting capacitors that register electric charge proportional to the light intensity and integration time. In the CCD configuration, diffraction gratings are used to disperse the incident light and project the separated wavelengths onto the array of pixels. Finally, mirrors, lenses and optical fibers are necessary for the setup.

**Figure 2.10** shows the PL spectroscopy setup designed for our ZnO nanohybrid materials. The excitation source was a continuous laser (8 mW, Crylas FQCW 266-10) operating at 266 nm at room temperature. The emitted light was collected by an optic fiber and recorded by a CCD (iHR Triax 320 Jobin-Yvon) cooled down to 155 K by liquid nitrogen. The diffraction grating in the CCD configuration was blazed at 500 nm with 600 grooves per millimeter. All the powder samples were individually pressed onto an indium foil and mounted on the sample holder for laser excitation. The CCD recorded emission spectra for an integration time of 0.5 s from the samples covering the visible range completely. The setup inherently suffers from deviation of recorded emission spectrum from the true spectrum, due to the use of optic fiber, diffraction gratings in CCD and the nature of the CCD (sensitivity at different wavelengths, dark current, *etc.*). Therefore, the recorded spectra have to be calibrated by a standard reference spectrum, which, in our case, is produced by a standard tungsten lamp.

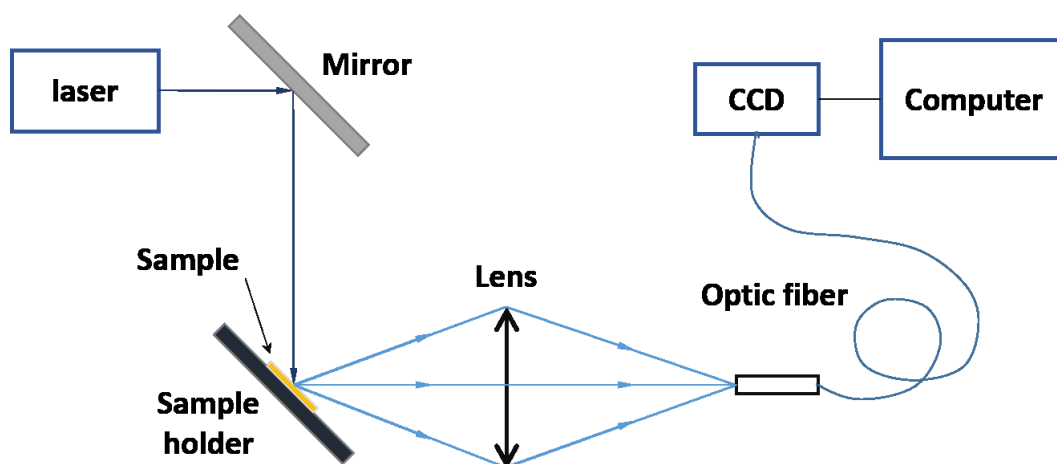


**Figure 2.10** PL spectroscopy experimental setup

A tungsten lamp is considered as a grey body whose theoretical spectral radiation can be calculated by Planck's law of radiation (Equation (1.1)). The theoretical emission spectrum can then be obtained by multiplying the radiation with the tungsten emissivity. The emitted spectrum of the tungsten lamp was recorded by CCD under the same conditions as the PL emission spectra of the powder samples. By comparing the theoretical spectrum and recorded spectrum from the tungsten lamp, a calibration function was obtained, which was applied to all the recorded emission spectra. The true spectra of the samples were thus obtained and they were all normalized to their maximum emission intensity for convenient comparison.

### 2.3.2 Photoluminescence Excitation spectroscopy

Photoluminescence excitation (PLE) is a particular PL spectroscopy aimed for the characterization of optical transitions in materials. Unlike conventional PL spectroscopy where a single excitation wavelength induces an emission spectrum in a range of wavelengths, PLE registers emission intensity at a single wavelength while the excitation wavelength varies in a range. **Figure 2.11** displays a typical PLE spectrum along with the PL spectrum of ZnO. [195] The PLE spectrum was monitored at 2.15 eV (577 nm). The peak near 3.5 eV (354 nm) in the PLE spectrum indicates that the strong emission is achieved when the excitation photon energy is near the bandgap. At higher excitation energies (above 3.5 eV), the emission intensity at 2.15 eV is always high, indicating that the emission at 2.15 eV has a persistent emission path. As demonstrated from the example, PLE spectrum can provide information on the excitation mechanism and emission paths of the material. Therefore, PLE was employed to help interpret the PL emission from ZnO nanohybrids.

PLE spectra were obtained from selected powder samples by a fluorescence spectrometer (FLS920 series, Edinburgh Instruments, Livingston, UK). The spectrometer is equipped with a 450-W Xe900

continuous xenon arc lamp as the excitation source and diffraction grating monochromators to separate the excitation wavelengths and emission wavelengths. The excitation was set in the spectral range between 220 nm and 450 nm with an interval of 1 nm; the emission wavelength was chosen at the wavelength with the highest emission intensity with a width of 1 nm. The dwell time was set to be 1 s. The instrument also causes deviations from true spectra for both excitation spectrum and emission spectrum; however, the system automatically corrects each spectrum with its own reference.

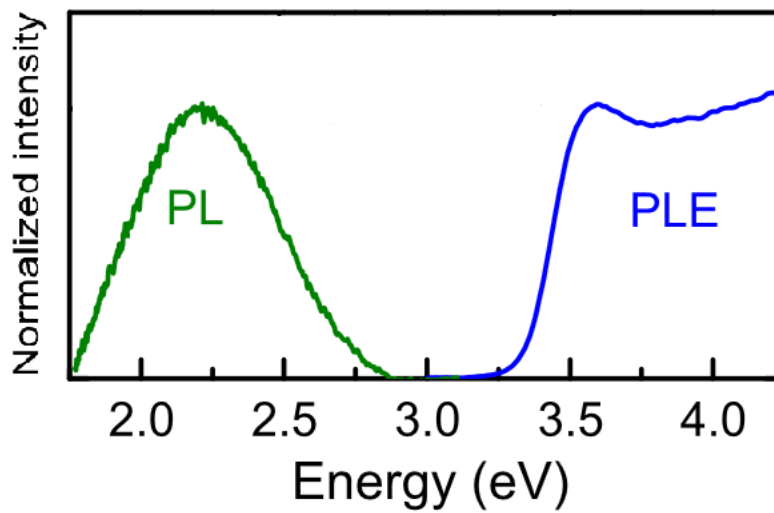


**Figure 2.11** Typical PLE spectrum (in blue) of ZnO along with its PL spectrum (in green).  $\lambda_{em} = 577$  nm,  $\lambda_{ex} = 266$  nm. [195]

### 2.3.3 Measurement and calculation of photoluminescence quantum yield

As mentioned in Section 1.1.1, the photoluminescence quantum yield (PL QY) in the present thesis represents the internal quantum efficiency (IQE), which is an inherent characteristic of a luminescent material. The PL QY is thus calculated by Equation (2.6):

$$\text{PL QY} = \frac{\text{number of photons emitted}}{\text{number of photons absorbed}}. \quad (2.6)$$

An integrating sphere is usually used in order to measure the number of photons. An integrating sphere is a hollow optical sphere with a highly diffuse reflective coating on its interior. Only small holes are opened on the sphere to allow light to enter and exit. It is assumed that every point on the interior of the sphere is equal and that all the light within the integrating sphere is guided to the exit for complete collection by an optic fiber.

Using an integrating sphere, de Mello *et al.* developed an advanced absolute method to measure the value of PL QY precisely. [196] They considered the reabsorption by the sample of the diffused incident laser light, which should not be included as a contribution to the PL QY, and proposed three separate measurements as illustrated in **Figure 2.12** to establish a calculation formula of PL QY as follows:

$$\text{PL QY} = \frac{P_c - (1-A)P_b}{L_a A}, \quad (2.7)$$

where  $A$  is the absorption coefficient, which can be calculated from measurements (b) and (c) by  $A = 1 - L_c/L_b$ .  $L$  is the integrated area under the laser profile, representing the unabsorbed laser light in a given configuration;  $P$  is the integrated area under the emission profile, representing the emitted light from the sample. This method has proven reliable for highly scattering samples.

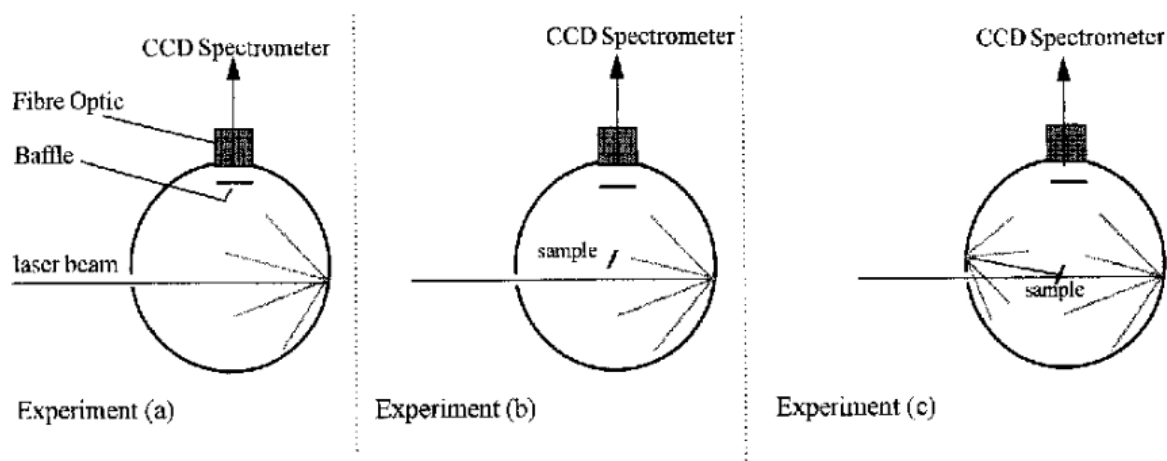


**Figure 2.12** Illustration of three configurations with an integrating sphere for PL QY measurement. (a) The sample is not present in the sphere. (b) The sample is present but the laser is not directed onto the sample. (c) The sample is present and the laser is directed onto the sample.

The method by de Mello *et al.* was adopted in our studies for all the samples. The experimental setup is illustrated in **Figure 2.13**. The integrating sphere was from Labsphere (model number RTC-060-SF). The interior coating material of the integrating sphere is Spectralon, the reflectance of which is shown in **Figure 2.14**. [197] The excitation source is the same laser at 266 nm as for PL spectroscopy. The powder sample is still pressed onto the indium foil. We took advantage of the uniformity of the integrating sphere and fixated the sample on a hole. The position of the sample on the sphere does not make a difference in the results. The three configurations in **Figure 2.12** were realized by changing the incident angle of the laser beam. The light from the integrating sphere was guided into an optic fiber to be recorded by the CCD (iHR Triax 320 Jobin-Yvon) cooled down to 155 K by liquid nitrogen. The acquisition time of the signal was 0.2 s for the excitation source and 0.5 s for the emission in the visible range.

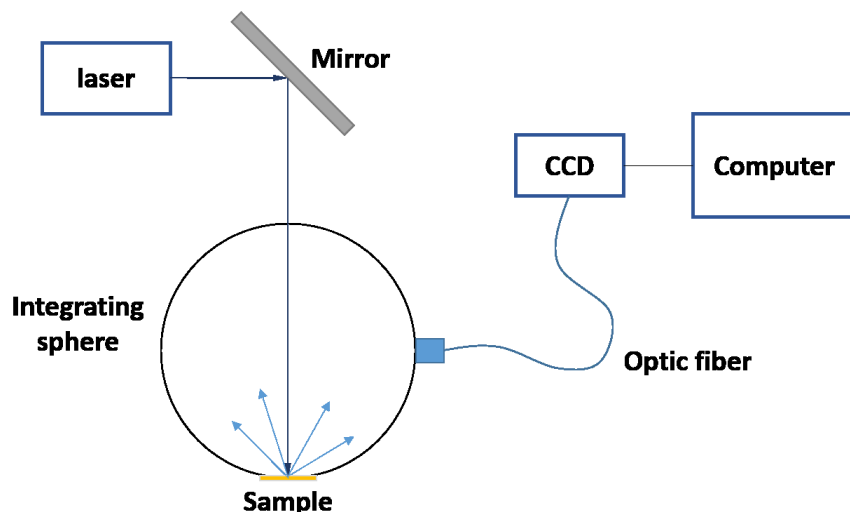


Figure 2.13 Schematic of the setup for PL QY measurements.

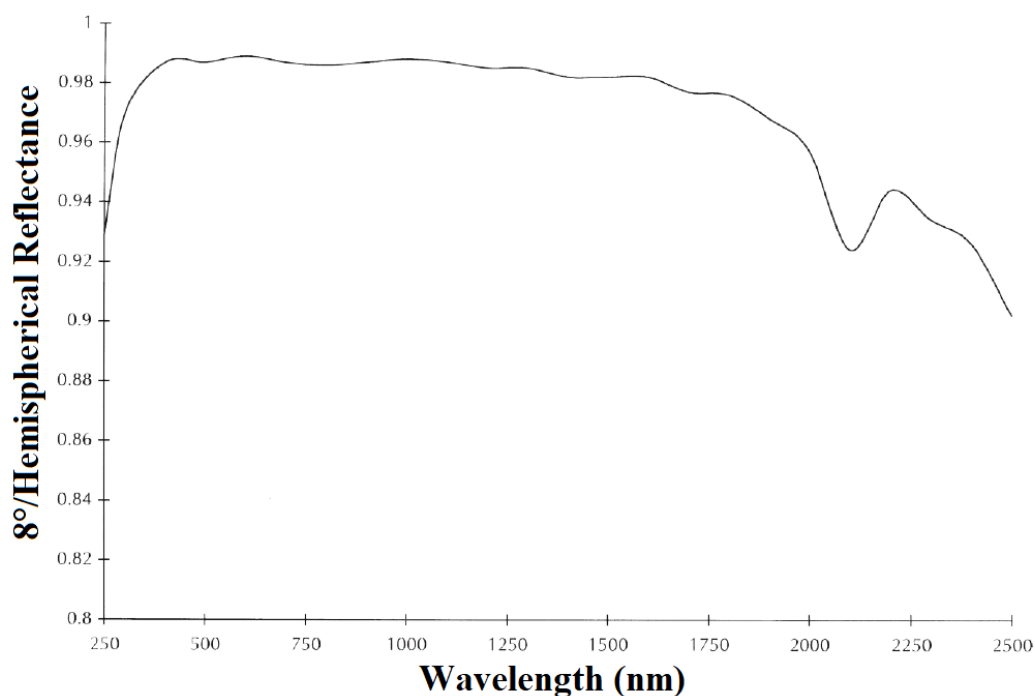
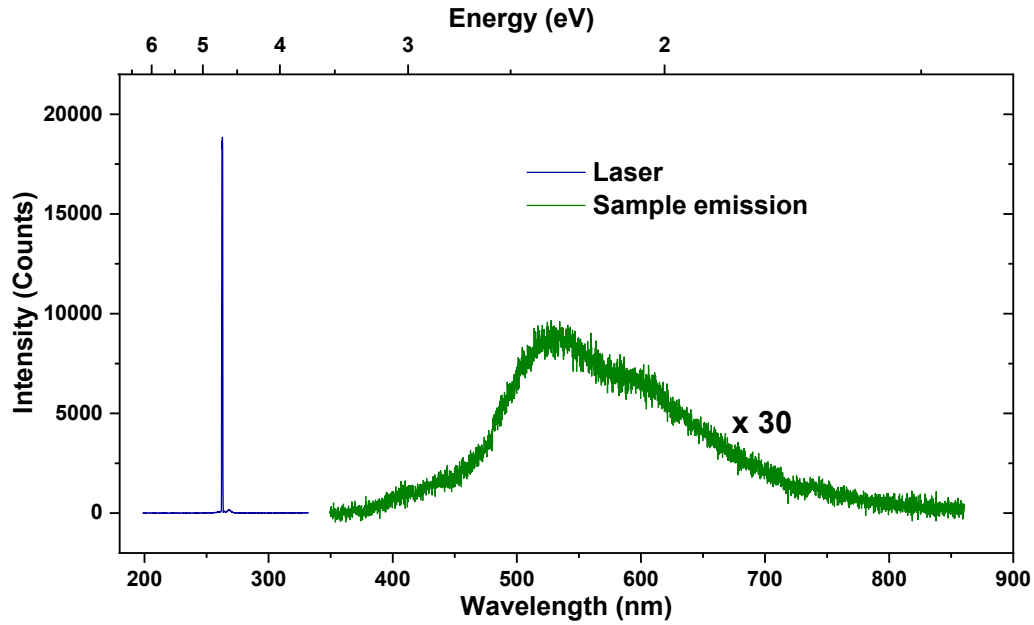


Figure 2.14 Reflectance spectrum of Spectralon coating material of the integrating sphere.

Figure 2.15 shows the laser profile and emission profile of measurement (c) for a typical ZnO nanohybrids sample. As we can see, the intensity of the recorded spectra is in number of counts, which should not be assumed equal to the number of photons, considering the difference in energy for each wavelength. CCD registers electric charge, not photons. Therefore, the recorded data need calibration to convert number of counts into number of photons.



**Figure 2.15** Typical laser profile and emission profile from measurement (c) for ZnO nano hybrids. The emission profile is enlarged 30 times.

A conversion factor was developed by calibrating the integrating sphere with a tungsten halogen lamp whose irradiance is known as  $I_\lambda$  at each wavelength. Since the energy ( $E_\lambda$ ) of a photon at each wavelength is also known, the number of photons is determined by the following equation:

$$N_{\text{photon},\lambda} = I_\lambda t / E_\lambda, \quad (2.8)$$

where  $t$  is the integration time for the collection of the spectrum. We illuminated the integrating sphere with the tungsten halogen lamp and obtained a spectrum by measuring the intensity of the lamp at each wavelength in number of counts ( $N_{\text{count},\lambda}$ ). Thus, a conversion factor  $C_\lambda$  was obtained for each wavelength as

$$C_\lambda = (I_\lambda t) / (E_\lambda N_{\text{count},\lambda}). \quad (2.9)$$

Since the calibration lamp does not emit at 266 nm, the conversion factor at 266 nm ( $C_{266}$ ) is calculated and calibrated by the laser itself. The calculation involves the power of the laser (8 mW) and the number of counts recorded at 266 nm. Therefore, we can convert the count at each wavelength into number of photons by multiplying  $C_\lambda$  to each spectrum. Finally, Equation (2.7) was applied in number of photons to obtain the PL QY of each sample.

In addition to the calibration by the tungsten halogen lamp, the method was further improved by another calibration with CdSe/CdS quantum rods colloidal solution with a known PL QY of 79 %. The quantum rods solution was disposed in a cuvette, which was installed inside the integrating sphere for the three measurements in **Figure 2.12**. The PL QY of the quantum rods was calculated after multiplying the

emission spectrum with the conversion factor. In this way, another coefficient ( $\eta$ ) was obtained as the ratio of the nominal PL QY to the measured PL QY. The final and true PL QY was therefore determined for each sample.

While PL spectroscopy provides qualitative evidence for the photoluminescence process in ZnO nanohybrids, PL QY complements the optical characterization by providing quantitative analysis. A higher PL QY is indicative of a more efficient microstructure of the material. Ultimately, materials with high PL QY are more promising for WLED applications.

### **2.3.4 Photoluminescence at high temperature**

Towards the characterization for WLED application, PL at high temperature is one aspect to mimic the working condition of WLEDs. In the present thesis, silica-coated ZnO nanohybrids are likely to have a stable structure to withstand heat. Therefore, a new setup developed by the team of Christophe Dujardin at iLM (institut Lumière Matière) was employed to heat the silica-coated samples up to 100 °C for PL measurements.

In this new setup, a Xenon lamp was used as the excitation source and the excitation wavelength was set at 340 nm. The powder samples were again pressed onto the indium foil and firmly mounted onto the sample holder. The heating system controlled the temperature of the sample holder, which was accepted as the temperature of the sample after stabilizing for 10 minutes. The PL measurements started from room temperature until 100 °C. Then the sample was cooled down to room temperature for another measurement. The emitted light was collected by an optic fiber and recorded by a CCD in the range between 450 nm and 750 nm.



## Chapter 3 Metal-Doped ZnO Nanohybrids

ZnO as a luminescent material takes advantage of the intrinsic deep-level defects in its wide bandgap. The control of defect type, concentration and their position in the bandgap is hence critical for the control of emission spectrum and intensity. Doping is one of the measures to effectively tune the emission of ZnO, proven by the vast literature as demonstrated in Chapter 1. Unfortunately, the most effective dopants are usually rare-earth elements, which can impose serious environmental issues with excessive exploitation. Non-rare-earth doping is therefore the better option. Then again, no definite consensus has been achieved on the effect of non-rare-earth doping because of different synthesis conditions and microstructures of ZnO obtained.

In this chapter, the study of a series of non-rare-earth metal-doped ZnO nanohybrids will be presented. This study benefits from our previous research in undoped ZnO/PAA nanohybrid structure synthesized by hydrolysis method, which was applied to all the metal-doped samples herein. The doped samples were characterized by various techniques to reveal their structural and optical properties. The effect of doping on the optical properties is the major concern. Doping is liable to quench the PL emission from ZnO by introducing non-radiative energy levels in the bandgap. [96] Such quenching effect of dopant will be investigated in a few aspects, *i.e.*, dopant element, dopant ionic size, doping concentration and dopant valence. PL QY values of all the samples will be analyzed systematically in order to gain a comprehensive understanding of doping effect in ZnO. The study is therefore purposed to tune the visible emission of ZnO without degrading the PL QY and potentially apply the materials to WLEDs.

### 3.1 Microstructure of metal-doped ZnO nanohybrids

#### 3.1.1 Morphology

The hydrolysis synthesis method in the previous study by our group (Yao Zhu's thesis) yielded a mesosphere structure (see **Figure 2.1**), which was partially held responsible for a high PL QY. [186], [187] The introduction of dopant precursor may have an impact on such morphology and eventually affect the PL QY. The morphology of several samples was investigated using TEM and some representative images are shown in **Figure 3.1** and **Figure 3.2**. Respectively, doping species and doping concentration are found to influence the morphology.

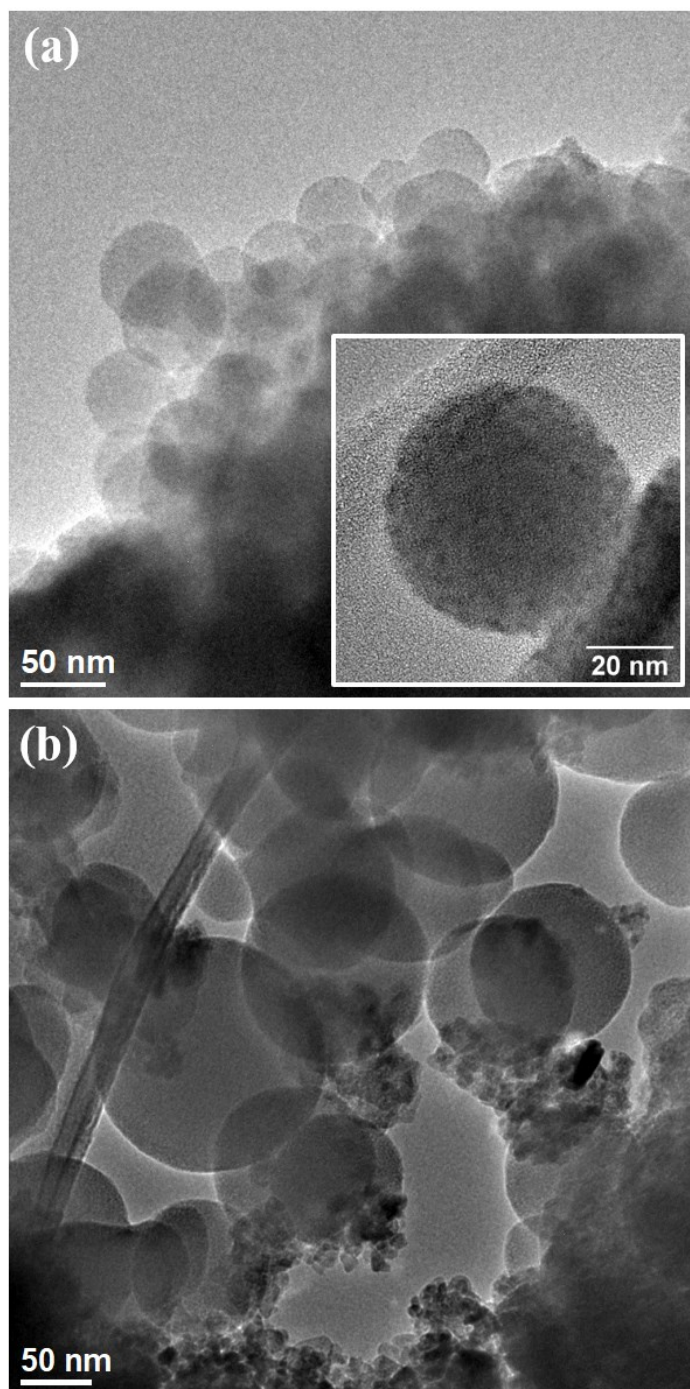


**Figure 3.1** Morphologies of (a) 0.1 % Mn-doped ZnO nanohybrid and (b) 5 % Mn-doped ZnO nanohybrid.

The influence of doping concentration is manifested by Mn doping at 0.1 % doping (**Figure 3.1** (a)) and 5 % doping (**Figure 3.1** (b)). At a low doping concentration of 0.1 %, the mesospheres in the undoped ZnO are preserved, with an average size of about 50 nm in diameter. The spheres are composed of nanoparticles embedded in an organic matrix of PAA, as demonstrated in the inset of **Figure 3.1** (a). At 5 % doping, the mesospheres are still present, but with bigger average size of about 100 nm in diameter.

Nanoparticles with heterogeneous size from 5 to 10 nm are also found distributed outside of the big mesospheres in 5 % Mn-doped ZnO. Based on the above observations on Mn-doped ZnO nanohybrids, it can be speculated that higher doping concentration of the doping precursor has an impact on the formation of homogeneous mesospheres. The dopant precursor probably interacts with the polymeric acid (PAA) or Zn precursor ( $\text{ZnEt}_2$ ) and the interaction may be intensified as the doping concentration increases.

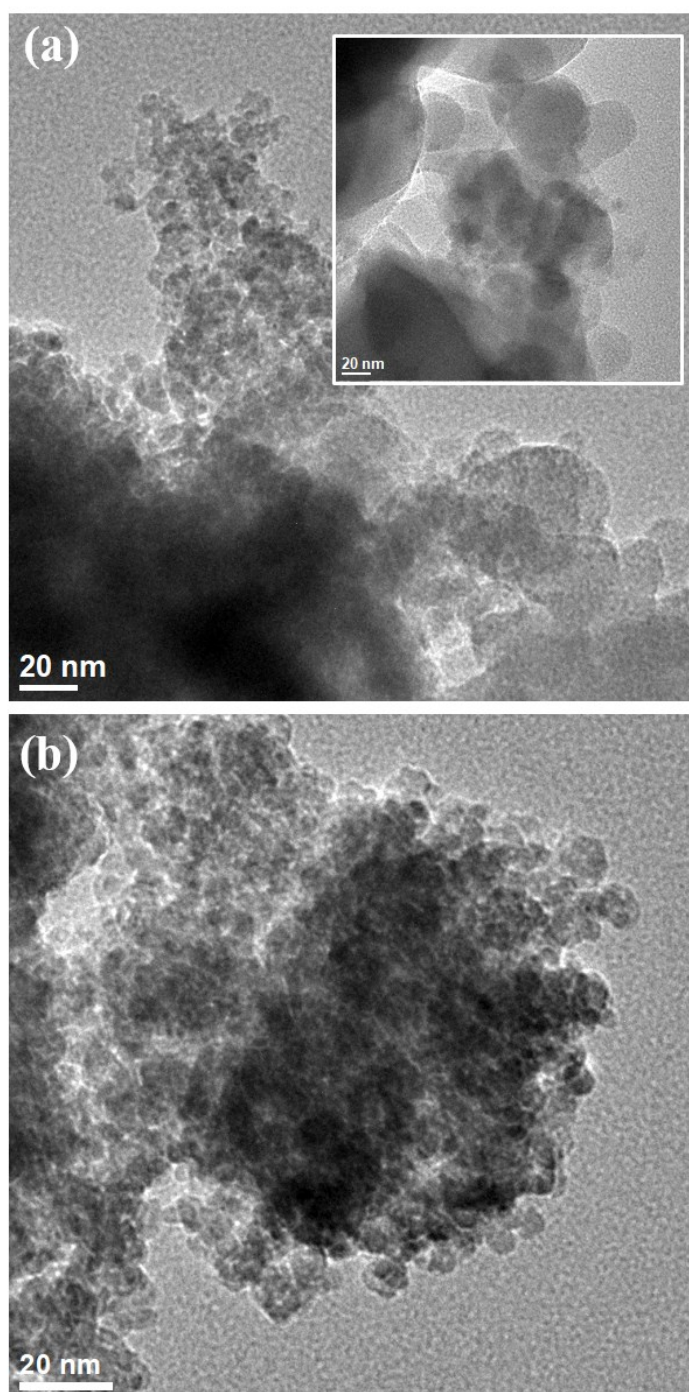


**Figure 3.2** Morphologies of ZnO nanohybrids doped with different elements at 0.1 %. (a) Cu(II) doping. (b) Bi doping.



The crystal structure of the materials was studied by XRD and TEM. XRD was performed on selected samples. **Figure 3.3** presents the XRD spectra of Co doped samples, which are representative of most of the doping cases as given in Appendix I (Al, CrCl<sub>3</sub>, Mn, Ni, and Cu<sup>+</sup> doping). Whatever the doping species is, the XRD spectra look mostly similar. At all three distinct doping concentrations, the spectra can be indexed to wurtzite ZnO phase and no additional crystalline phase is present. The position of the diffraction peaks from wurtzite ZnO remains the same for all the samples, indicating that the lattice parameters are not modified by any dopant.

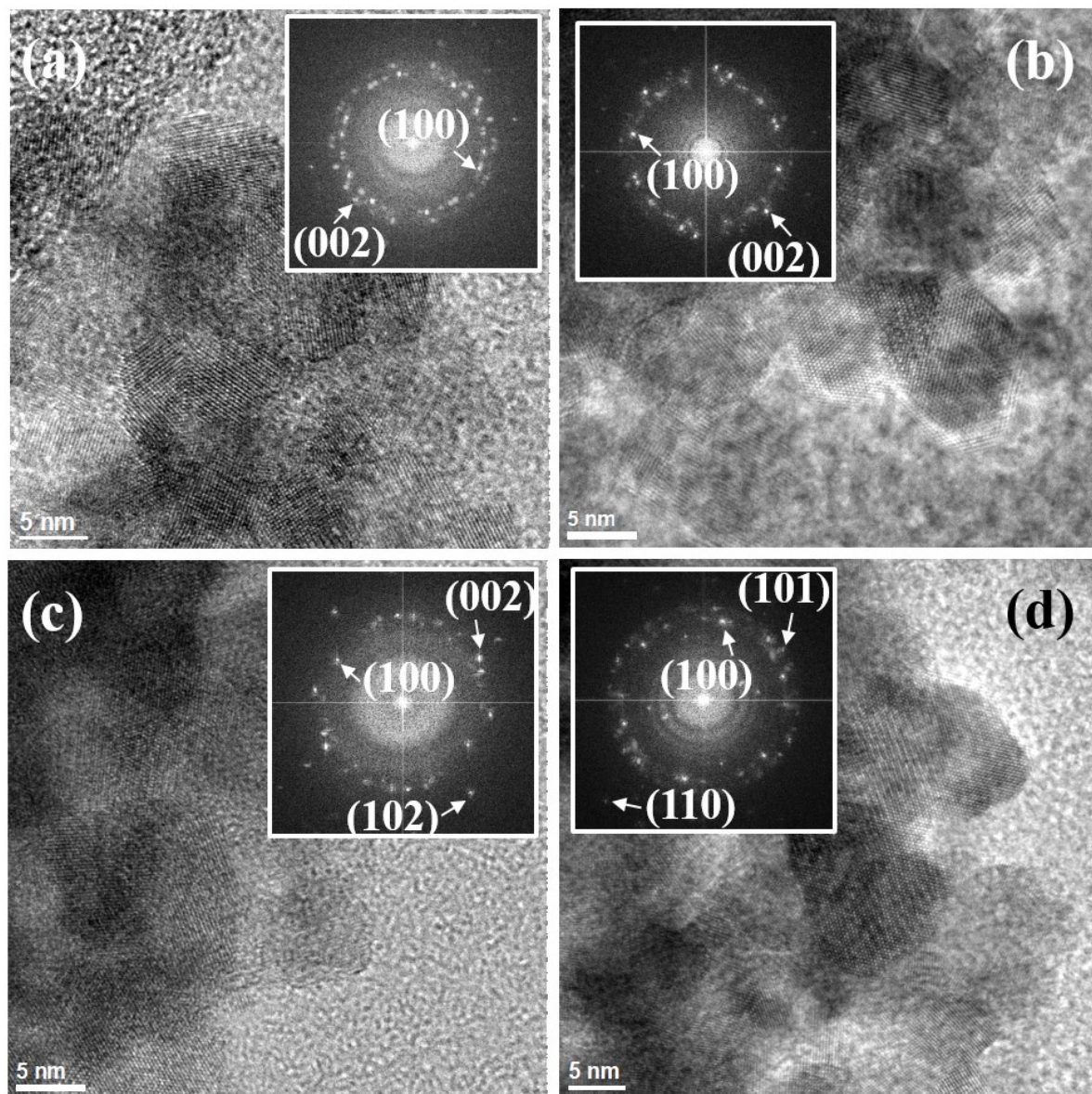


**Figure 3.4** HRTEM images of (a) 0.1 % Mn, (b) 5 % Mn, (c) 0.1 % Cu(II) and (d) 0.1 % Bi doping, showing nanocrystals of ZnO. The insets are FFT images of each HRTEM image, indexed to wurtzite ZnO polycrystalline structure, respectively. More HRTEM images of these samples can be found in Appendix II.

The wurtzite structure is further confirmed by HRTEM images as shown in **Figure 3.4**. Representative HRTEM images of several doping cases, namely 0.1 % Mn, 5 % Mn, 0.1 % Cu(II) and 0.1 % Bi, were Fourier transformed into the reciprocal space (see insets in each image), respectively. The diffraction patterns in reciprocal space manifest characteristic polycrystalline diffraction rings with a few diffraction spots, which can be indexed to wurtzite ZnO structure as indicated in the inset images.

Additionally, the size of the ZnO nanocrystals is indicated in the HRTEM images to be between 5 and 10 nm, although such regional observation under TEM is not representative of the whole sample. Complementarily, the mean crystalline domain size is estimated by Scherrer equation (Equation (2.3)) to be between 10 and 50 nm for different samples. The size evolution of different doping cases will be discussed in Section 3.1.5.3 based on the estimation from XRD spectra, since the result is more reliable for each sample as a whole.

### 3.1.3 Presence of PAA

Neither XRD nor TEM was able to prove the existence of PAA in the studied materials, although amorphous matrix was observed under TEM. Therefore, FTIR was performed on all the doped samples in order to state the presence and to characterize PAA. **Figure 3.5** presents the FTIR spectra of Co-doped ZnO nanohybrids at three distinct doping concentrations as an example. FTIR spectra for other doped samples are shown in Appendix III.

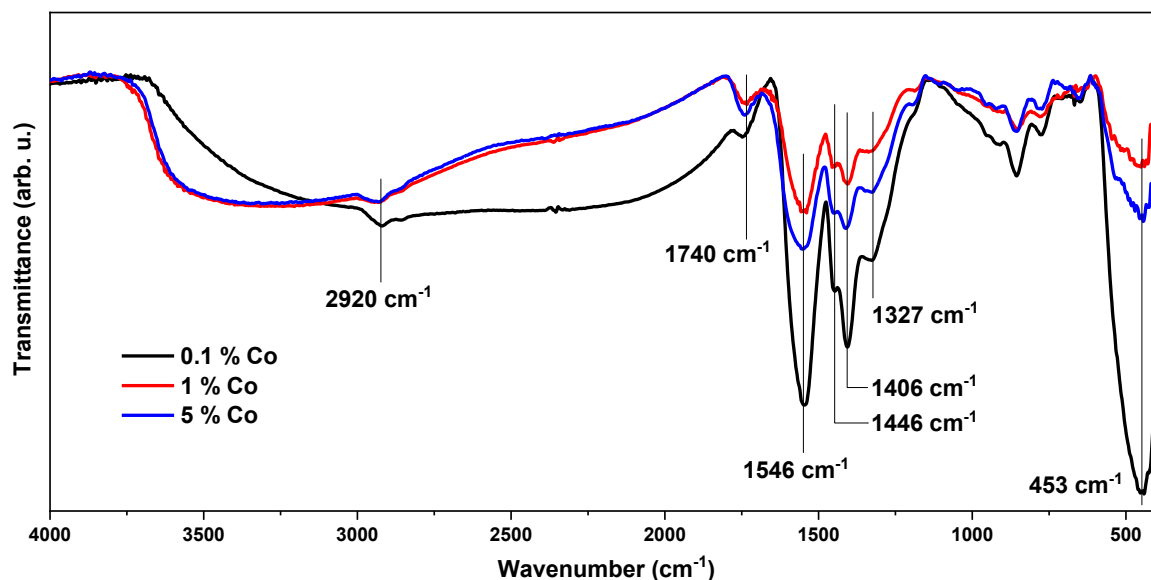


**Figure 3.5** FTIR spectra of Co-doped ZnO nanohybrids at 0.1 %, 1 % and 5 % doping.

Above all, the presence of ZnO is confirmed for all the samples. The broad peak at 453 cm<sup>-1</sup> is attributed to Zn–O stretching mode. [198] This peak is the most intense when the dopant precursor concentration

is the smallest (0.1 %), indicating good crystallization at 0.1 % doping. Higher doping concentrations hinder the crystallization of ZnO, most likely because the dopant ions incorporate into ZnO lattice, thus degrading the crystalline quality. The broad feature around  $3400\text{ cm}^{-1}$  is related to water or OH groups. The peaks between  $1327\text{ cm}^{-1}$  and  $2920\text{ cm}^{-1}$  present at all doping concentrations are attributed to the bonds in PAA, which is a direct proof of successful incorporation of PAA in the doped ZnO nanohybrids. The two strong peaks at  $1406\text{ cm}^{-1}$  and  $1546\text{ cm}^{-1}$  are the evidence of the symmetric and asymmetric modes of carboxylate anion ( $\text{COO}^-$ ), respectively. The peak near  $1740\text{ cm}^{-1}$  corresponds to C=O stretching mode of free non-hydrogen-bonded carboxylic acid (COOH) groups. [199] It can thus be deduced that some of the polymeric acid was deprotonated to form the amorphous matrix after the interaction with ZnO and dopant precursor.

### 3.1.4 Presence of dopants

At this stage, the structure of our metal-doped ZnO nanohybrids is completely confirmed to be wurtzite ZnO nanoparticles embedded in PAA matrix. However, none of the results above provides direct evidence of successful incorporation of metal dopants. Therefore, RBS and EDX were performed to probe the presence of dopants. These two techniques take advantage of the different atomic mass of different elements. The intensity of the resulting spectrum depends on the concentration of the given element. That is to say, the techniques are less accurate for low doping concentrations below their sensitivity. In order to successfully distinguish the dopant element from Zn, only 5 % doped samples were examined, which is representative of other doping concentrations since the synthesis process is generic for all the samples.

**Figure 3.6** displays the RBS spectrum (black curve) of 5 % Mn-doped ZnO nanohybrid with a simulated curve (red curve) and the contributions from each element (other colored curves). At low energy under 500 keV, it is a notorious issue in simulation that the calculated value of counts is smaller than the experimental data. [200] However, on the high-energy side, the simulation shown here is considered a good fit. The simulation results indicate that the atomic ratio of Mn to Zn is 0.17:1, *i.e.*, the Mn concentration is 17 %, which is larger than the intended doping concentration. Considering the weak sensitivity of the technique for such low concentration, the result probably overestimates the real Mn concentration. Nevertheless, it is certain that Mn is present in this sample. Since the synthesis process is generic for all the samples at all three doping concentrations, we can safely assume that the dopants are successfully incorporated in all the ZnO nanohybrids, regardless of the doping concentration. RBS spectrum also provides evidence that the precursor anion was not incorporated in the samples since no trace of Cl was observed when the dopant precursor compound was  $\text{MnCl}_2$ .

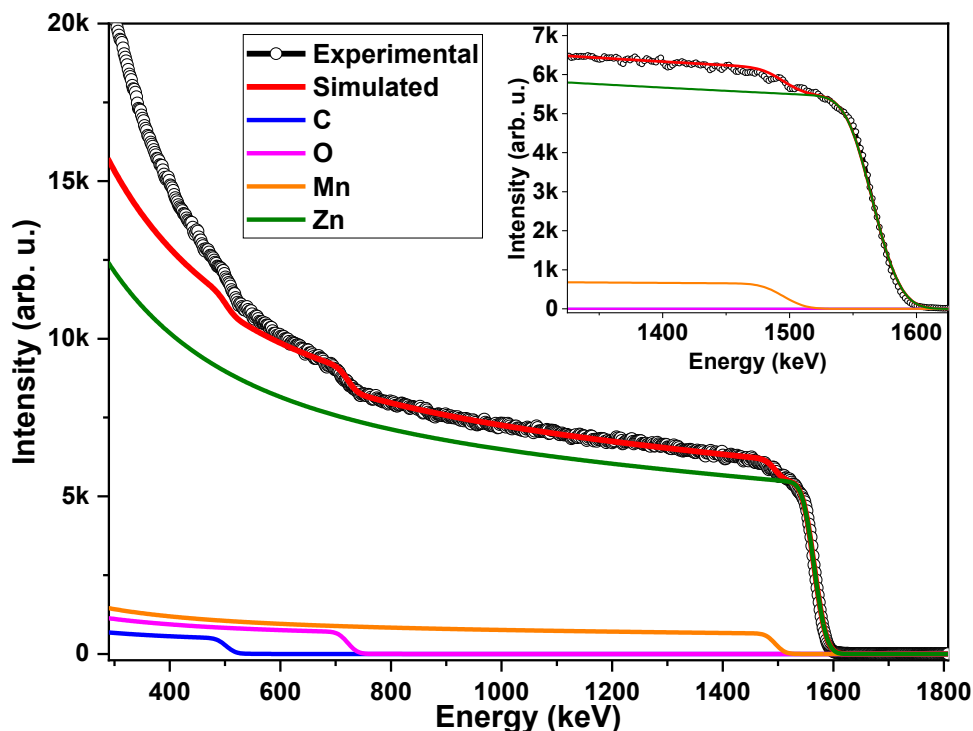


**Figure 3.6** RBS spectrum of 5 % Mn-doped ZnO nanohybrid with simulated curve (red curve) and contribution of each element (other colored curves). The inset shows contribution from Mn in detail.

More RBS spectra of 5 % doped ZnO nanohybrids are listed in Appendix IV (5 %  $\text{Fe}^{3+}$ ,  $\text{Fe}^{2+}$ , and  $\text{Cu}^{2+}$  doping). For different dopant species, the results show that the dopant concentrations are between 10 % and 20 %, all bigger than intended 5 %. On the other hand, as overestimating as it can be, the consistency of the technique for different samples validates our assumption of successful doping for all dopants.

While RBS produces inaccurate yet global concentration of the dopant in the sample, EDX provides results that are more accurate at a local region under TEM. EDX was performed on a few isolated mesospheres of 5 % Mn-doped ZnO nanohybrid and the result is shown in **Figure 3.7**. Signal of Cu arises from the copper grid. The corresponding Mn concentration was determined to be  $3.4 \pm 1$  %. We can confirm that Mn not only exists in the sample, but more importantly, exists in the mesospheres, probably incorporated in the ZnO lattice. Since the results were obtained from small regions, the Mn concentration obtained from EDX does not represent the global concentration of the sample. We cannot rule out the possibility that Mn can be segregated at a doping level higher than 5 %. The discrepancy of the dopant concentration in the mesosphere from the intended concentration indicates that a portion of Mn may be segregated in phases outside of the mesospheres.

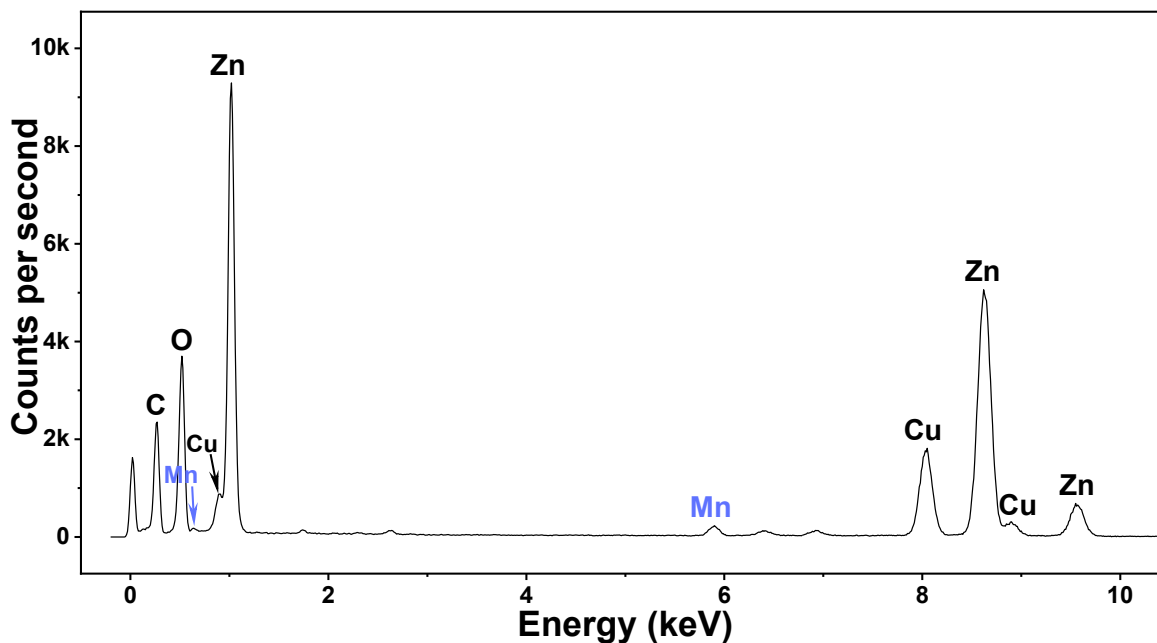


Figure 3.7 EDX spectrum of 5 % Mn-doped ZnO nanohybrid.

### 3.1.5 Effect of dopant on the microstructure

The characterizations so far have painted a clear picture of the microstructure of the materials: metal-doped wurtzite ZnO nanoparticles embedded in an amorphous PAA matrix. The microstructure is a determining factor for the optical properties and seems to be determined by the dopant precursor present in the hydrolysis synthesis. In this sub-section, the effect of dopant on the microstructure of ZnO nanohybrids will be discussed in terms of the mesosphere structure, crystal structure, and crystal size, each of which can significantly influence the optical properties.

#### 3.1.5.1 Mesosphere structure

As seen from **Figure 3.1** and **Figure 3.2**, different morphologies were obtained under different doping concentrations and species. The goal of the hydrolysis synthesis is to procure mesospheres with a homogeneous size, which is believed to be beneficial for high PL QY. Yet the introduction of dopant precursor, which is aimed at tuning the PL spectrum, seems to disrupt the formation of mesospheres. The presence of dopant elements has been confirmed by RBS and EDX and it clearly has an impact on the mesosphere structure. High doping concentration and big dopant ions tend to degrade the mesosphere structure, resulting in nanoparticles distributed outside of the mesospheres or even disappearance of mesospheres.

$\text{Mn}^{2+}$  has a smaller ionic radius (81 pm) and the same valence as  $\text{Zn}^{2+}$ . The incorporation of Mn ions is relatively easy and the disruption of mesospheres is minimum at a low doping concentration of 0.1 %. The case of Cu(II) doping at 0.1 % is similar to Mn, as these two dopant ions have similar ionic radius and the same valence; although, as the ionic radius of  $\text{Cu}^{2+}$  (87 pm) is bigger than  $\text{Mn}^{2+}$ , the presence of nanocrystals not embedded in mesospheres also increases in Cu(II)-doped sample, as illustrated in **Figure 3.2** (a).  $\text{Bi}^{3+}$  has an even bigger ionic radius (117 pm) and a different valence state from  $\text{Zn}^{2+}$ . Bi doping at 0.1 % completely inhibits the formation of mesospheres. Based on the above observations, it can be perceived that the difficulty of dopant incorporation is one of the determining factors for the integrity of the mesospheres embedded with ZnO nanoparticles.

For bigger dopant ions with a different valence from  $\text{Zn}^{2+}$ , more of the dopant ions are likely to be free from the participation in the crystallization of ZnO nanoparticles and the formation of mesospheres. These free dopant ions can then interact with PAA, possibly via chelation, and disrupt the formation of the organic mesospheric matrix. This argument is supported by the discrepancy of dopant concentration in the mesospheres from the intended dopant concentration in the case of 5 % Mn doping. A fraction of Mn ions exists outside of the mesospheres as free ions, since they were not involved with ZnO or mesospheres during hydrolysis. As a result, these free dopant ions may form a chelate with PAA, and less PAA is available to form mesospheres for ZnO nanocrystals. In the case of 5 % Mn doping, as shown in **Figure 3.1** (b), free Mn ions can render nanocrystals outside of mesospheres and possibly bigger mesospheres compared to 0.1 % doping (**Figure 3.1** (a)). However, it is still unclear how the free dopant ions interact with PAA, which is probably dependent on the nature of the dopant ions.

### 3.1.5.2 Crystal structure

In most doping cases, the crystal structure of wurtzite ZnO is not affected by the presence of dopant impurity, as demonstrated in **Figure 3.3** and Appendix I. However, Bi doping and Ag doping present different scenarios.

**Figure 3.8** displays the XRD spectra of Bi-doped ZnO nanohybrids at 0.1 %, 1 % and 5 % doping concentrations. 0.1 % Bi doping exhibits no impurity peaks despite the broadened wurtzite ZnO peaks compared to other doping cases; however, different impurity peaks appear at higher doping concentrations, *i.e.*, 1 % and 5 %. A broad diffraction peak around  $2\theta = 28^\circ$  can be attributed to an organic compound related to PAA. Sharp peaks at  $2\theta = 27.2^\circ$ ,  $37.9^\circ$  and  $39.6^\circ$  at 1 % doping are related to wulfingite  $\text{Zn}(\text{OH})_2$  phase.

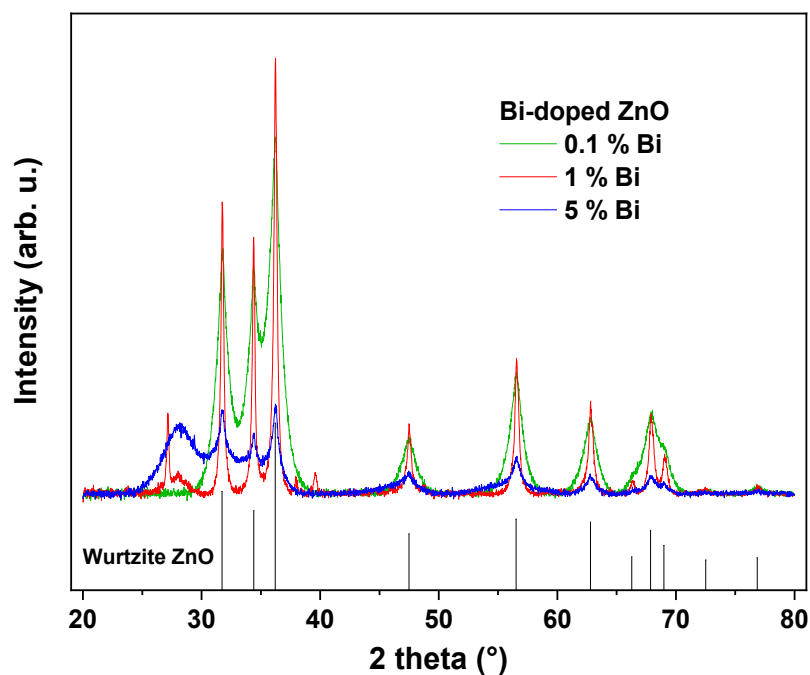


Figure 3.8 XRD spectra of Bi-doped ZnO nanohybrids.

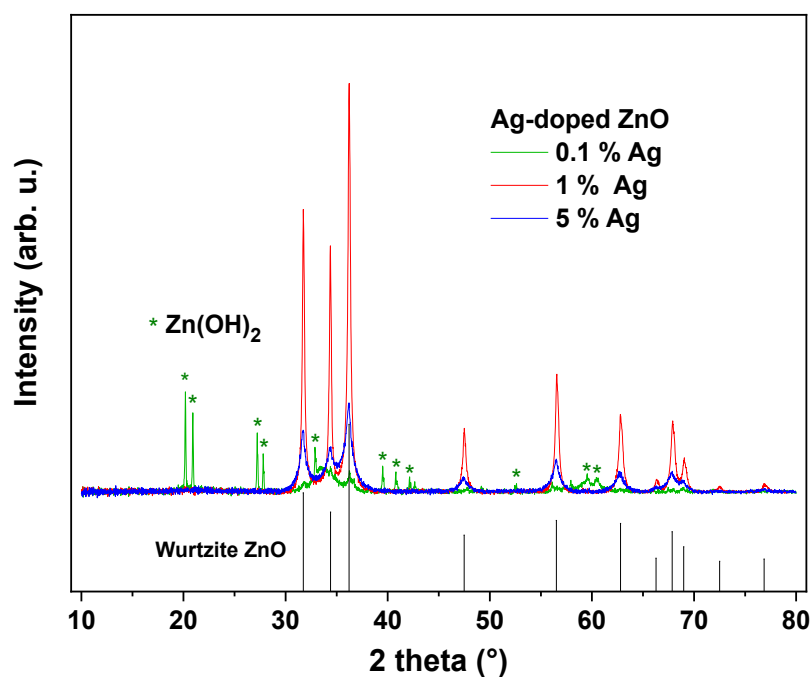


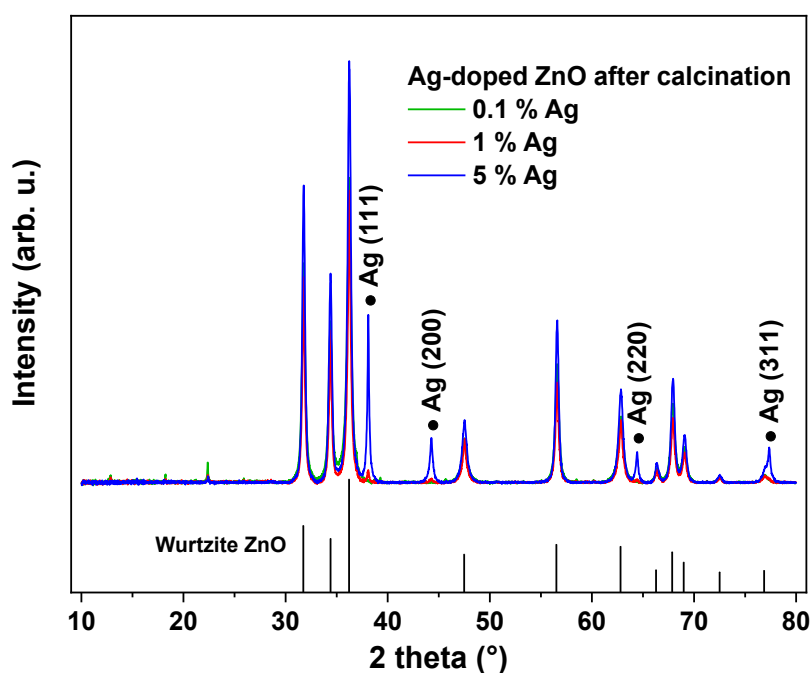
Figure 3.9 XRD spectra of Ag-doped ZnO nanohybrids.

Figure 3.9 displays the XRD spectra of Ag-doped ZnO nanohybrids at 0.1 %, 1 % and 5 % doping concentrations. At 0.1 % doping, wurtzite ZnO phase is present, but the dominant phase is wulfingite Zn(OH)<sub>2</sub>, which was observed in Yao Zhu's study as well. [186], [187] The presence of wulfingite Zn(OH)<sub>2</sub> indicates that the hydrolysis process was disrupted and not complete, since Zn(OH)<sub>2</sub> is an

intermediate product of hydrolysis synthesis of ZnO. Interestingly, the  $\text{Zn(OH)}_2$  phase is no longer present when the doping concentration increases to 1 % and 5 %.

Bi and Ag have the biggest ionic radii among all the dopant ions in the present study, making them the most difficult to substitute Zn atoms in the ZnO lattice. In fact, it is unlikely that Bi and Ag are incorporated in the ZnO lattice, since the positions of the diffraction peaks in Bi- and Ag-doped samples at all three concentrations correspond very well with the standard wurtzite ZnO phase. If the dopant atoms substitute Zn atoms, the lattice parameters of the doped ZnO would be changed, causing the diffraction peaks to shift from standard wurtzite ZnO.

Nevertheless, the incorporation of Bi and Ag cannot be completely ruled out. The Ag-doped samples were calcinated at 400 °C for 4 hours and XRD was performed again on the calcinated samples, resulting in the spectra shown in **Figure 3.10**. For 0.1 % doping,  $\text{Zn(OH)}_2$  phase disappeared and peaks of wurtzite ZnO became stronger after calcination. For 1 % doping, only weak peaks from Ag appeared after calcination due to small quantity of Ag. For 5 % doping, strong and sharp peaks from Ag appeared after calcination, indicating that Ag was previously incorporated in the material in the form of a compound or an amorphous phase. Ag ions could exist in ZnO lattice or in the polymeric matrix. XRD on calcinated Ag-doped samples also provides additional proof that the dopants are successfully introduced into the nanohybrids. While we cannot completely rule out Bi and Ag incorporation in ZnO lattice based on XRD diffractogram, the role of Bi and Ag ions in the solution is mostly to disrupt the crystallization of ZnO nanocrystals and the formation of mesospheres, and to induce phases other than wurtzite ZnO probably through interaction with PAA.



**Figure 3.10** XRD spectra of Ag-doped ZnO nanohybrids after calcination at 400 °C for 4 hours.

## 3.1.5.3 Crystal size

**Figure 3.11** plots the mean size of crystalline domain of doped ZnO nanohybrids estimated by Scherrer equation from XRD diffractograms. The presence of dopants affects the crystal size of ZnO as the mean crystalline size varies, depending on the types of dopants and doping concentrations. However, no clear trend can be observed in terms of dopant nature, except that the crystal size is between 10 nm and 50 nm for all the dopants. For Cu(I) and Ag doping, the crystal size seems to decrease when the doping concentration increases, whereas the opposite occurs for Al and Bi doping. Co doping and Cr doping yield biggest crystal size when the doping concentration is 1 %. Ni doping concentration seems to exert no effect on the crystal size of ZnO.

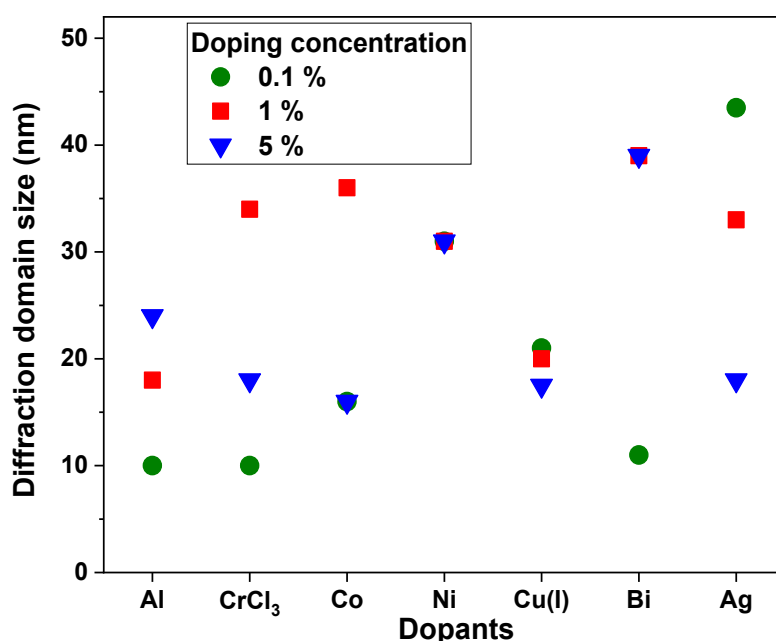


**Figure 3.11** Diffraction domain size of doped ZnO nanohybrids estimated by Scherrer equation in function of dopants and doping concentration. The dopants are arranged in the ascending order of the ionic radius.

With all sorts of variations, it is rather difficult to establish an exact mechanism responsible for the growth of crystals during the hydrolysis synthesis process. Several factors can play a role in the resulting crystal size, including dopant ions, protonated PAA (PAAH), and other ions from dopant precursors. Dopant ions are incorporated into ZnO lattice in most of the doping cases, as discussed above. Thus, their incorporation process affects the growth rate of doped ZnO nanocrystals. It has been established in the previous study that PAAH inhibits the nucleation of ZnO nanocrystals. [187] With the introduction of the dopant precursor that can interact with PAAH, the extent of the inhibition of the nucleation of ZnO nanocrystals is now dependent upon the extent of the interaction between PAAH and the dopant precursor. Part of the PAAH that is involved with precursor ions is no longer active in inhibiting ZnO

nucleation, resulting in efficient crystallization hence larger crystal size. It is also possible that some dopant precursors can enhance the inhibition of ZnO nucleation through interaction with PAAH, resulting in smaller crystal size. The complexation power of the dopant precursor with PAAH is therefore critical for the growth of ZnO nanocrystals. Considering the complexity of the present doping cases, the role of dopant precursor on the crystal size requires further investigation for confirmation.

#### 3.1.5.4 Summary

To summarize, the dopants impose various effects on the microstructure of the doped-ZnO nanohybrids. The mesospheres can be preserved by dopants with small ionic radius at low doping concentrations while excessive free dopant ions and bigger dopant ions inhibit the formation of mesospheres. Dopants with ionic radius bigger than  $Zn^{2+}$  can induce phases other than wurtzite ZnO. The mean crystal size is affected by the nature and concentration of dopants. In all three aspects discussed above, the interaction between the dopant precursor and PAA(H) is often one of the determining factors for the microstructure of the nanohybrids. Such interaction is not fully understood in the present thesis and thus requires further investigation.

## 3.2 Optical properties of metal-doped ZnO nanohybrids

The optical properties concerned in the present study are primarily PL and PL QY, which will be discussed in detail in this section. The investigation in PL spectra and PL QY values in terms of dopant type, concentration, size and valence allows us to understand the role of dopant in tuning the optical properties of doped ZnO nanohybrids. Keep in mind that the introduction of dopant usually means introduction of non-radiative energy levels in the bandgap of ZnO. [96] In addition to PL and PL QY, PLE and PL at high temperature will be presented briefly as well.

### 3.2.1 Photoluminescence

PL spectra of all samples were recorded and compared according to the dopant type, doping concentration and dopant valence. Appendix V gives all the spectra sorted according to the dopant type. All the spectra exhibit a broad emission spectrum spanning from UV to visible range with no sharp near-band-edge emission. For clarity, herein, only selected spectra will be presented to highlight the effect of doping accordingly.

### 3.2.1.1 Effect of dopant type

It is reasonable to predict that different dopants have different impacts on the PL spectra of ZnO nanohybrids. **Figure 3.12** plots some PL spectra of doped ZnO nanohybrids at the same doping concentration of 0.1 %. Compared to undoped ZnO, doping results in a redshift (shift to longer wavelength, or lower energy, in the spectrum) of the peak (maximum of the emission intensity) in the PL spectra for all types of dopant. The redshift is prominent even at a low doping concentration of 0.1 %. For most dopants, such as Co, Mn, and Cu(II), the PL peak shifts to different new positions; however, the redshift can be very similar for some dopants, such as Co and Fe(III).

Considering the cases of 0.1 % doping and undoped ZnO nanohybrids, the PL emission peak can be tuned by doping between 2.46 eV (undoped ZnO) and 2.16 eV, or between 504 nm and 574 nm. Considering all the doping cases at all doping concentrations (see Appendix V), the tuning range spans from 2.46 eV (undoped ZnO) to 2.08 eV, or from 504 nm to 596 nm. Hence, it can be concluded that metal doping can tune the emission color of ZnO nanohybrids in a wide range. It should be noted that the PL spectra of Ce-doped samples are similar to other doping cases. Therefore, Ce is as ordinary as other dopants in terms of emission peak tuning ability.

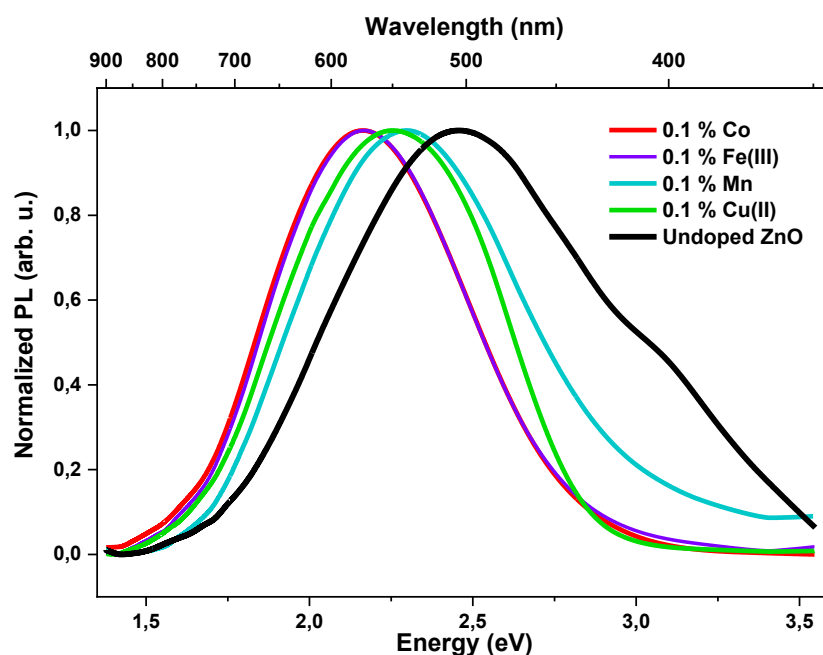


**Figure 3.12** Normalized PL spectra of Co-, Fe(III)-, Mn- and Cu(II)-doped ZnO nanohybrids at 0.1 % doping concentration in comparison with the PL spectrum of undoped ZnO nanohybrid.

### 3.2.1.2 Effect of doping concentration

As is already mentioned above, 0.1 % doping with different elements allows us to tune the PL emission peak in a wide range (between 504 nm and 574 nm); and increasing the doping concentration to 1 % and 5 % renders the tuning range a bit wider (between 504 nm and 596 nm). Therefore, doping concentration has an effect on the color tuning of ZnO nanohybrid.

**Figure 3.13** presents PL spectra of several dopants at all three doping concentrations. For 0.1 % doping as shown in **Figure 3.12** and **Figure 3.13** (a), the UV emission is significantly quenched for all the dopants except for the case of Cu(I) doping, where a weak near-band-edge emission is present in the UV range. This weak UV contribution in Cu(I) doping disappears when the doping concentration increases to 1 % and 5 %. The UV emission can persist under high doping concentrations, although only for Fe(III) doping at 1 % (see **Figure 3.13** (b)) and Fe(II) at 5 % (see **Figure 3.13** (c)). Generally speaking, the majority of the dopants quench the UV emission.

Despite a few peculiar cases where a weak UV emission persists, the effect of doping concentration is better manifested in the redshift of visible emission compared to undoped ZnO. For example, Mn doping at 0.1 % and 5 % leads to similar shift of the emission peak, whereas 1 % Mn doping leads to a larger redshift compared to the other two concentrations. On the other hand, the largest redshift is found at 5 % doping for Cu(I) and Fe(III) doping. There are also cases where doping concentration barely changes the redshift in the visible range (see Cr doping for example in Appendix V). For Cr doping, the change in the anion of Cr precursor compound does not lead to significant changes in PL spectra of Cr-doped ZnO at all three doping concentrations. Therefore, it is believed that the anion in the precursor has no significant effect on the PL spectra.

### 3.2.1.3 Effect of valence

The effect of valence on PL is demonstrated by Fe doping and Cu doping as shown in **Figure 3.13** and **Figure 3.14**, respectively. For Fe doping at all three doping concentrations, the shape of the PL spectra are different with different valences, indicating that Fe(II) and Fe(III) affect the radiative energy levels in the ZnO bandgap in different manners. They both exhibit a weaker quenching effect on UV emission (although at different doping concentrations) compared to other doping cases.

In the case of Cu doping, the shape of the PL spectra are similar except for 0.1 % Cu(I) doping, which exhibits an extra weak UV contribution compared with other spectra. The similarity in the visible part of the emission spectra suggests that the two valence states of Cu affect the deep-level defects in similar manners. In particular, at 1 % doping, the spectra are highly similar. A notable difference for the two valence states of Cu doping is that Cu(I) causes more drastic redshift than Cu(II). The emission peak

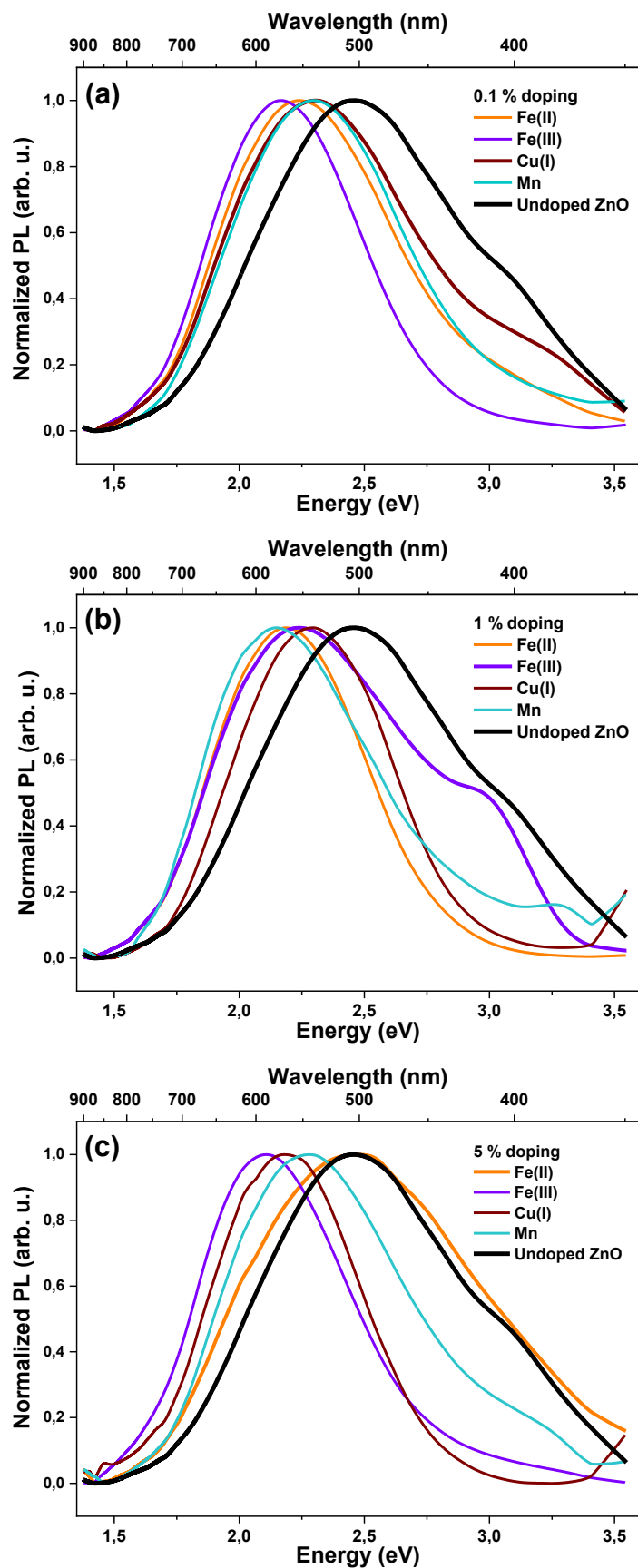


**Figure 3.13** PL spectra of undoped ZnO nanohybrid and Fe(II)-, Fe(III)-, Cu(I)-, and Mn-doped ZnO nanohybrids at (a) 0.1 %, (b) 1 %, and (c) 5 % doping concentrations.

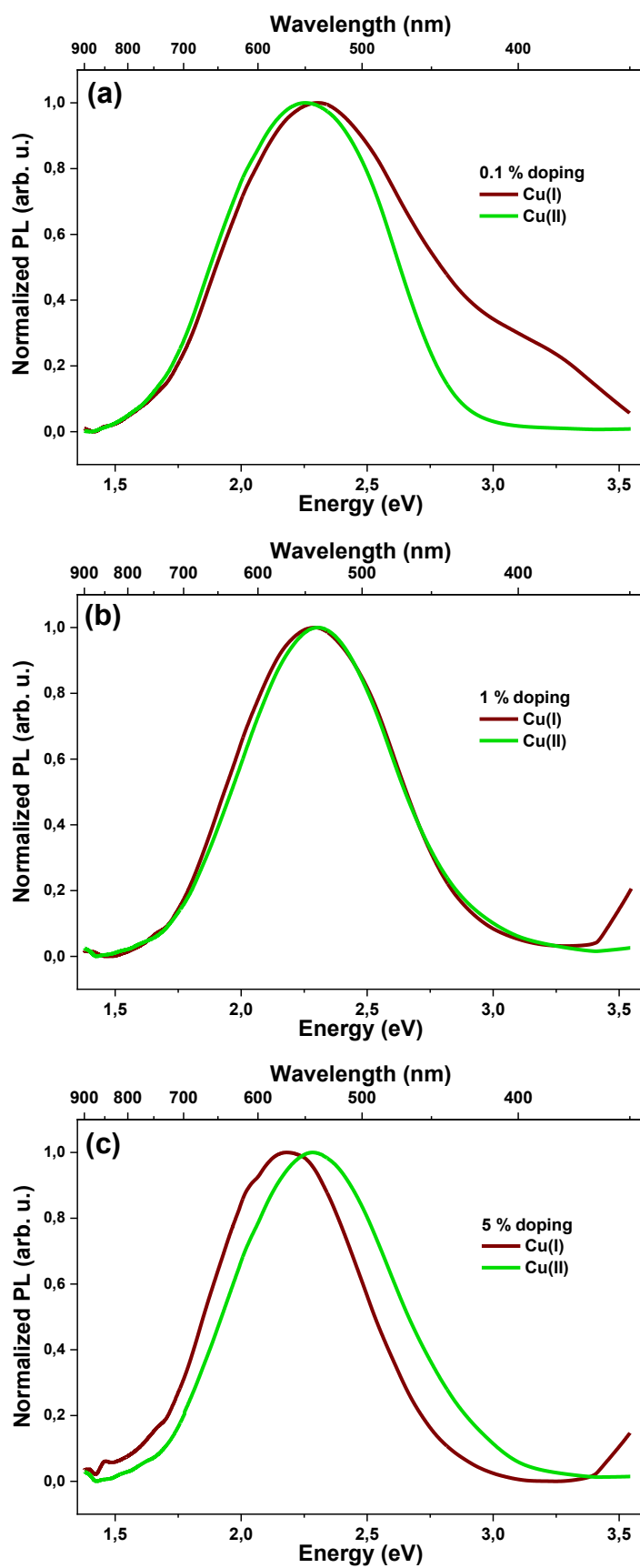


**Figure 3.14** PL spectra of Cu-doped ZnO nanohybrids with two different Cu valences (+1 and +2) at (a) 0.1 %, (b) 1 %, and (c) 5 % doping concentrations.

positions are in a small range between 2.30 eV and 2.25 eV for Cu(II) doping at three doping concentrations whereas 5 % Cu(I) sets the spectrum further towards the red end, giving a tuning range between 2.30 eV and 2.18 eV.

Although the final valence of the dopant in the materials was not determined by any technique, it can be clearly seen that the dopant valence in the precursor plays an important role in tuning the PL spectra of ZnO nanohybrid.

### 3.2.1.4 Summary

As discussed above, dopant type, concentration and valence all play a role in tuning the PL spectra of ZnO nanohybrid. However, no clear tendency is noticed in the peak shift for any of the three factors. **Figure 3.15** summarizes the PL spectra peak position of all the doped samples in function of dopant type. The PL peak position shifts towards lower energies and longer wavelength (redshift) for all the doping cases at all doping concentrations except for Fe(II) doping at 5 %, which does not cause significant peak shift from undoped ZnO. Furthest redshifts are achieved by 1 % Ag doping and 5 % Ag, Co, or Fe(III) doping. The initial valence of the dopant has an evident impact on the tuning ability of the dopant, as demonstrated by Cu and Fe doping with different valence states.

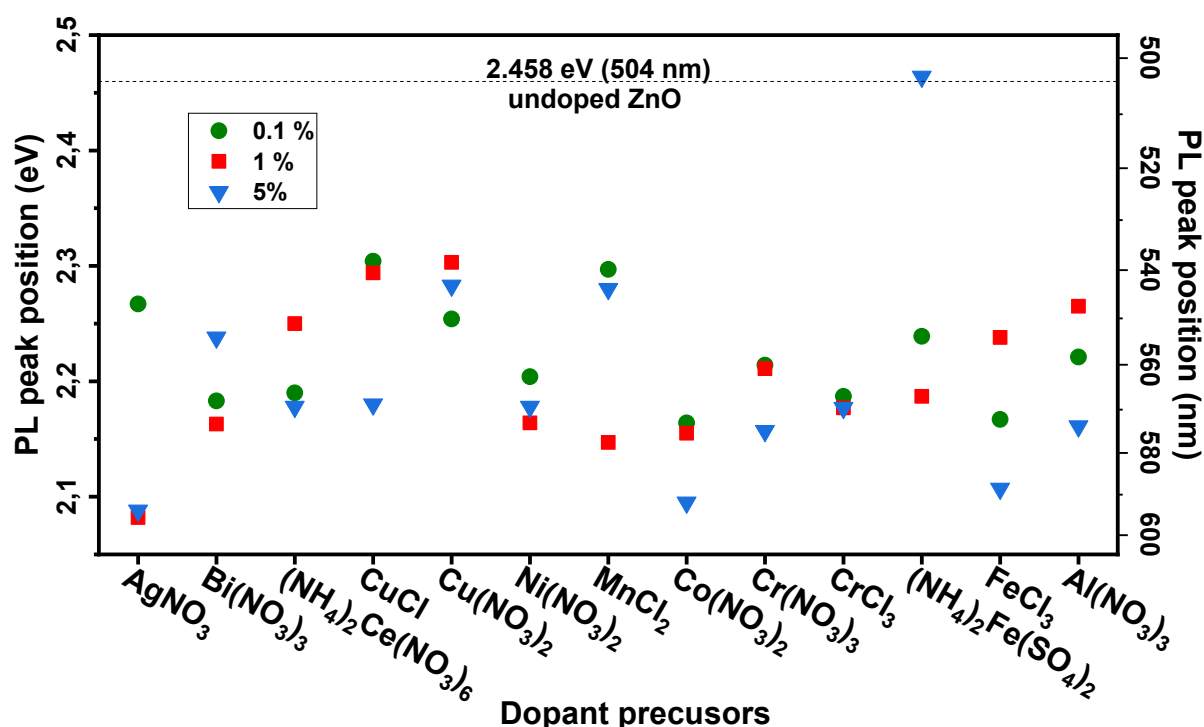


**Figure 3.15** PL spectra peak position of the doped-ZnO nanohybrids in energy (eV) and wavelength (nm). The horizontal dashed line indicates the peak position of undoped ZnO nanohybrid.

### 3.2.2 Photoluminescence quantum yield

The PL spectra show that the emission from ZnO nanohybrid can be tuned by doping, with different types of dopants, different valence states and at different doping concentrations. However, such tuning ability would be useless if the emission efficiency, *i.e.*, PL QY, cannot be preserved. Many studies in the literature have suggested that a large doping concentration can lead to marked quenching effect of the PL QY. [96], [131], [169], [201]–[203] Therefore, it is necessary to accurately measure the PL QY of doped samples and compare it to the PL QY of undoped ZnO.

Figure 3.16 plots the PL QY values of all the doped samples normalized to the PL QY of undoped ZnO nanohybrid sorted in descending order of ionic radius of the dopant ions. The PL QY is represented by relative PL intensity as displayed on the vertical axis. The horizontal dashed line indicates the relative PL intensity of undoped ZnO, which is set at 100 %. The absolute value of the PL QY of undoped ZnO is 3.54 %. The vertical dashed line indicates the ionic radius of  $\text{Zn}^{2+}$ .

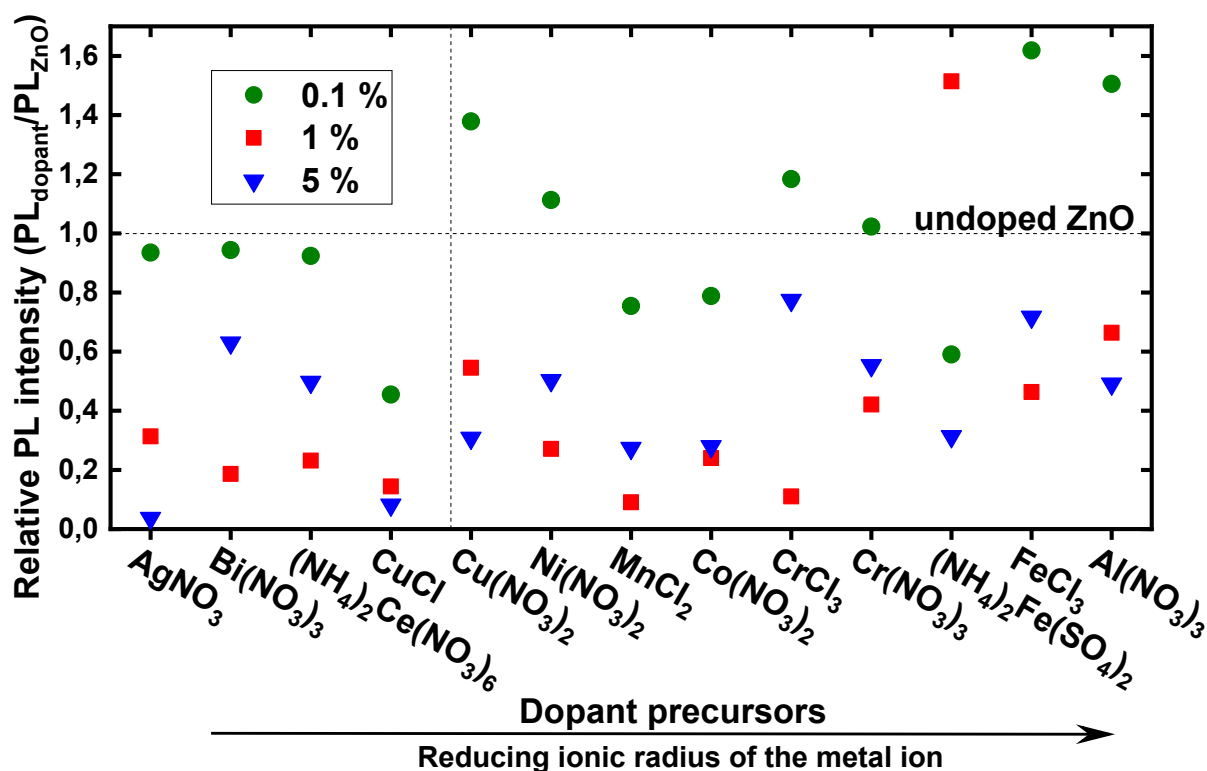


Figure 3.16 PL QY of doped ZnO nanohybrids normalized to the PL QY of undoped ZnO nanohybrid.

The majority of the doping cases have a PL QY lower than undoped ZnO nanohybrid. Distinctively, 0.1 % doping is the optimal doping concentration for all the dopants, except for Fe(II) doping where the highest PL QY is achieved at 1 % doping. The general trend is that, within the doping range in the present study, the lower the doping concentration, the higher the PL QY. The peculiarity of Fe(II) doping

remains to be explained. However, the results confirm the observation from the literature that large doping concentrations quench the PL QY.

Contrary to some reports in the literature, the PL QY can be preserved or even improved by doping at a low doping concentration of 0.1 %. The PL QY of several doping cases, such as Ag, Bi, Ce, and  $\text{Cr}(\text{NO}_3)_3$ , is nearly equal to that of undoped ZnO nanohybrids; and the PL QY of another few cases, such as Cu(II), Ni,  $\text{CrCl}_3$ , Fe(III), and Al, is improved by up to 62 % (Fe(III)). Interestingly, the cases with improved PL QY all fall into the upper-right rectangular of **Figure 3.16**. Moreover, the cases with the biggest improvement in PL QY are found in the upper-right corner, for dopants with a small ionic radius and a large valence state. For Cu and Fe doping, a larger valence state is beneficial for a higher PL QY at 0.1 % doping. Although, even with their smaller ionic radii than  $\text{Zn}^{2+}$ , 0.1 % Mn doping and 0.1 % Co doping do not improve the PL QY.

Considering all the doping cases, some of which remain peculiar, a conclusion can be drawn that one prerequisite for obtaining high PL QY by metal doping is to choose an element with small ionic radius and a small doping concentration around 0.1 %. The samples with improved PL QY in the present study still offer a tuning range of emission peak from 2.46 eV (undoped ZnO) to 2.17 eV (0.1 % Fe(III) doping), or from 504 nm to 571 nm.

### 3.2.3 Photoluminescence excitation

PLE can help interpret the optical transitions in the materials. For the metal-doped ZnO nanohybrids, PLE was employed to probe the differences in PL mechanism between samples with different doping concentrations. **Figure 3.17** displays the PLE spectra of Cu(II)-doped ZnO nanohybrids at 0.1 %, 1 %, and 5 % doping concentrations. The emission wavelength was set at 565 nm, where the highest emission intensity was recorded. The spectra are normalized to the intensity at the excitation wavelength ( $\lambda_{\text{ex}}$ ) of 266 nm according to the PL QY value of the samples. The noisy signal at  $\lambda_{\text{ex}} > 360$  nm comes from the setup aberration.

The excitation threshold is found to be near 360 nm (3.4 eV in energy), which indicates the bandgap of the doped ZnO nanohybrids. Compared to previous results, the bandgap of doped ZnO nanohybrids was not modified by the incorporation of dopants at any doping concentration. [187] ZnO nanoparticles in the doped samples are not small enough to induce quantum confinement effect. Furthermore, the shape of the PLE spectra at each doping concentration is similar, implying that the optical transitions in all the samples are essentially the same. The broad peak feature near 340 nm is attributed to the presence of PAA. [187] Doping concentration does not affect the position of the radiative energy levels. Finally, the highest emission intensity is achieved at around 255 nm.

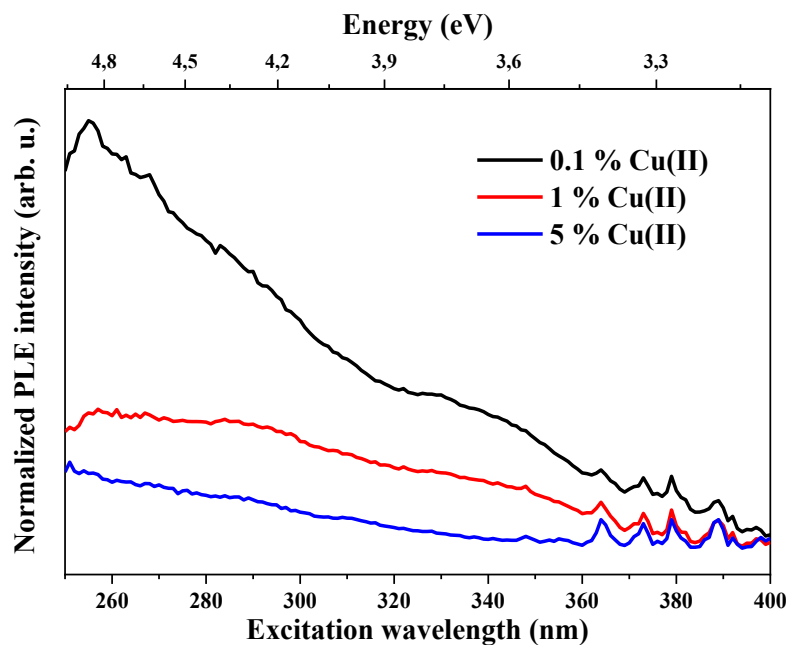


**Figure 3.17** PLE spectra of Cu(II)-doped ZnO nanohybrids at three doping concentrations.

### 3.2.4 Role of dopant

The structural and optical properties of metal-doped ZnO nanohybrids have demonstrated that the dopant plays an important role in tuning the PL and PL QY of ZnO. Metal doping influences the properties of ZnO nanohybrids in two major aspects: 1) the role of dopant during hydrolysis process and 2) the role of dopant in the final nanohybrid structure. The role of dopant is schematically exposed in **Figure 3.18** as it is discussed as follows.

#### 3.2.4.1 Dopants during hydrolysis synthesis

On the first aspect, the presence of dopant during hydrolysis essentially determines the architecture of the nanohybrid. In other words, the dopant can control the formation of mesospheres that contain ZnO nanocrystals in PAA matrix and the size of these nanocrystals, which ultimately control the PL QY. The interaction between the dopant precursor and PAA is scarcely reported in the literature. It appears that the function of PAA in the solution can be modified by complexing with the dopant to some extent, depending on the chemical nature of the dopant precursor. [204], [205] Such complexation modifies the pH of the solution and the conformation of PAA chains, thus interrupting the interaction between PAA and ZnO to form homogeneous mesospheres.

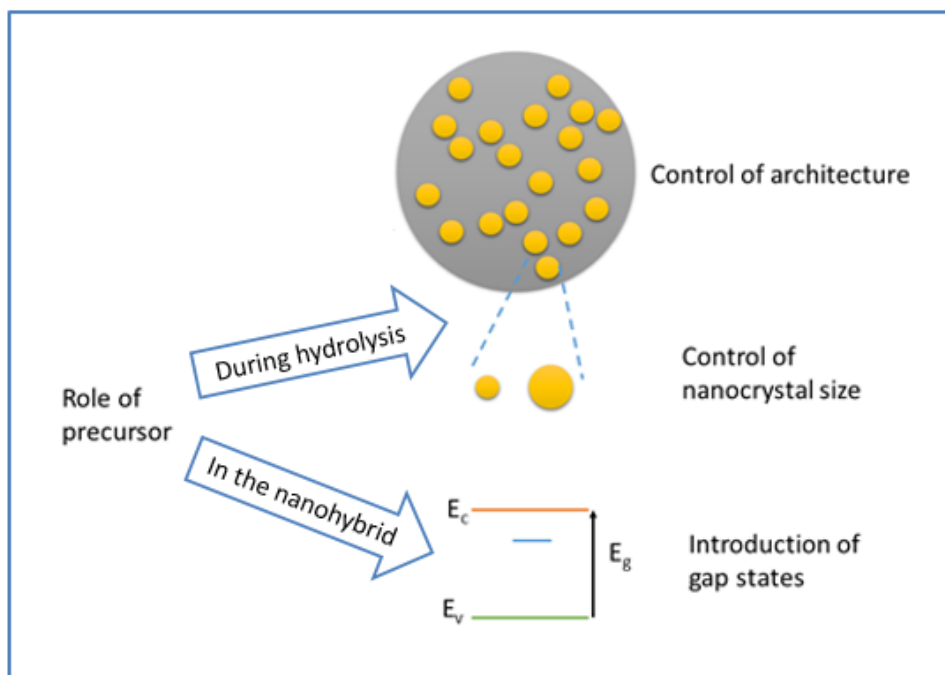


**Figure 3.18** Role of dopant during hydrolysis synthesis and in the nanohybrid composite

Unfortunately, the characterizations so far fail to fully explain the multifaceted action of the precursor on the resulting microstructure. XRD results show no clear tendency on the evolution of the crystal size, except that it is always under 50 nm. FTIR cannot provide quantitative information on the fraction of polymer chains that are deprotonated on the surface of ZnO nanocrystals, despite that the evidence on the presence of  $\text{PAA}^-$  is manifested. Only TEM images establish a decent connection between the morphology and the dopant. The probable modification of pH and chain conformation can explain the degradation of mesospheres for high doping concentrations and dopants with a large ionic radius (Bi for instance). The free dopant ions that are not incorporated into ZnO crystal lattice contribute to the modification of pH in the solution. They may also hinder the formation of PAA mesospheres by complexing PAA. Eventually and correspondingly, they will induce the change in the size of ZnO nanocrystals as well as their presence inside or outside the mesospheres. The fact that these effects are all entangled makes it difficult to clearly assess the role of dopant or dopant precursors during the synthesis.

The mesospheric architecture of ZnO nanohybrids mainly has two positive consequences on the optical properties. First, the light-matter interaction may be enhanced by light scattering among mesospheres and among nanocrystals inside the mesospheres. Second, the concentration of non-radiative surface states can be reduced by PAA matrix, since it can passivate the surface of ZnO nanocrystals in favor of visible emission. However, these two positive effects are not the only predominant factors that determine the PL QY, since the mesospheric 0.1 % Mn-doped sample has an even smaller PL QY value than 0.1 % Bi-doped sample with low content of mesospheres. The size of the nanocrystals is another important

factor. Smaller nanocrystals generally tend to yield higher PL QY. [206] It is true for most doping cases in the present study as most samples with large crystals have low PL QY (see **Figure 3.11** and **Figure 3.16**). Yet, it is worth noting that the PL QY decreases as the crystal size increases in the case of Ag doping, and that the same crystal size produces largely different PL QY values in the case of Ni doping.

#### 3.2.4.2 Dopants in the nanohybrid

All the effects mentioned above originate from the role of dopant during synthesis, ultimately influencing the PL QY of the doped ZnO nanohybrids. The PL spectrum, on the other hand, is essentially influenced by the way dopants are incorporated in the sample and in particular into ZnO nanocrystal lattice.

Therefore, on the second aspect, the presence of dopant in the sample determines how light is emitted from ZnO nanohybrids. Undoped ZnO nanohybrid exhibits a broad spectrum over UV and visible range as demonstrated in **Figure 3.12** and **Figure 3.13**. Visible emission prevails over band-to-band emission thanks to the nanostructure of the hybrid material, which passivates the surface states and creates numerous deep-level defects. The weak UV emission near 3.1 eV is near-band-edge emission attributed to optical transitions related to shallow defects. The visible emissions are deep-level emissions attributed to defects deep in the ZnO bandgap (*cf.* Chapter 1). Successful incorporation of dopants in the mesospheres has been confirmed by XRD, RBS, and EDX. Since the dopant atoms may be incorporated inside the ZnO nanocrystal lattice, at least partially, new electronic levels are introduced by the dopant within the nanocrystal energy diagram. These new energy levels can be radiative or non-radiative, either way, resulting in changes of shape and position of the PL spectrum.

The dopant atoms incorporated in ZnO lattice are bound to introduce defect levels in the bandgap. These defect levels can be new levels. For example, Cu(II) doping can introduce radiative energy levels in the ZnO bandgap when Cu ions substitute Zn ions (*cf.* Chapter 1). [130] On the other hand, most dopants are likely to introduce degenerate levels, since doping leads to a reduction of PL QY in most doping cases. For example, Mn and Co can occupy vacancy sites in ZnO nanocrystals, eliminating optical transitions through those vacancy sites, in other words, introducing quenching energy levels. [207], [208] Therefore, most dopants essentially favor the presence of non-radiative levels, whether intrinsic or extrinsic.

The dopants can also modify the concentration of crystalline defects. For example, presence of Ni was reported to induce oxygen vacancies, which are deep radiative levels. [132] The shape of the visible emission is similar among most doping cases, suggesting that doping does not create new radiative energy levels in these cases. It is highly unlikely that specific radiative defect levels are introduced by various dopants considering their vastly different chemical nature, even though we cannot rigorously

discard this hypothesis. Instead, the dopants can modify defect concentration and enhance or reduce the presence of intrinsic radiative levels, leading to the redshift of visible emission observed in PL spectra. The redshift may also result from the modification of the position of existing radiative energy levels, as the bandgap is not changed after doping, which was proved by PLE.

Furthermore, the strong quenching effect on the UV end of the PL spectrum evidences that deep-level recombination prevails over near-band-edge emission even more after doping. Two possible mechanisms can explain further UV quenching by doping. First, since no new emission peaks appear, the concentration of deep-level defects must be enhanced by doping, further forbidding UV emission. In this case, the PL QY is likely to be improved, for example, Al doping and Fe(III) doping at 0.1 %. Second, in cases where the PL QY is not improved, the dopant probably introduces non-radiative deep levels that trap charges, also leading to the forbiddance of UV emission.

Finally, it is worth mentioning that the initial valence of the dopant in the precursor can also affect the PL spectrum (see **Figure 3.14**). The valence of the precursor ion can affect the incorporation of the ion both during the hydrolysis process and in the ZnO nanocrystals. However, it is yet difficult to draw a conclusion, since the final valence of the dopant within the ZnO nanocrystals is not determined.

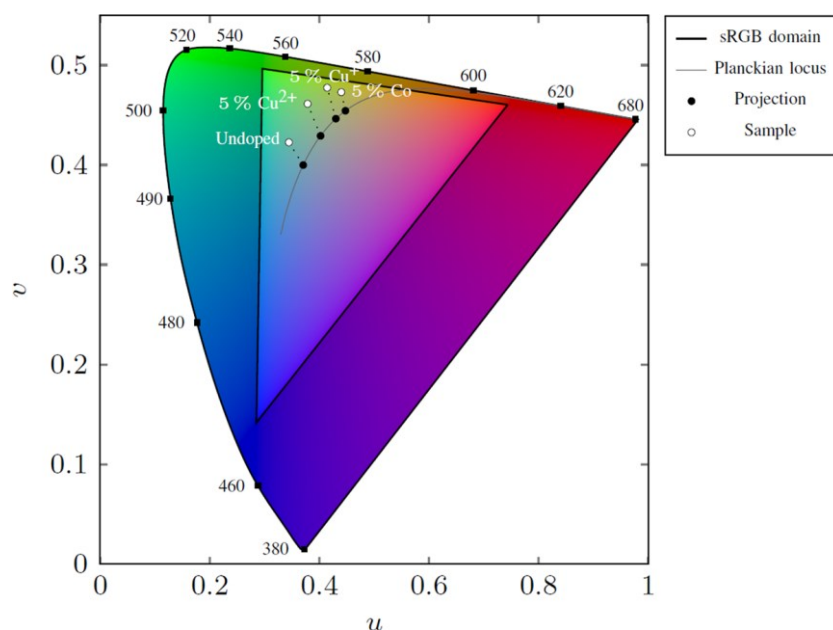


**Figure 3.19** Position of the spectra of selected doped samples in the gamut chart in Judd's UCS diagram (figure produced by Fabien Mandorlo).

From a practical point of view, the present study supports the fact that doping can be utilized to control the visible emission spectrum and to improve the PL QY of ZnO nanohybrid. Thanks to the modification of radiative defect levels by certain dopants (Al, Fe<sup>3+</sup>, Cr, Ni and Cu<sup>2+</sup>) at 0.1 % doping, the emission spectrum from ZnO nanohybrids can be tuned between 2.47 eV and 2.17 eV with an improved PL QY. **Figure 3.19** plots the emission color of several doped samples on a gamut chart in Judd's Uniform

Chromaticity Scale (UCS) diagram. The projection from the samples on the Planckian locus shows a large amplitude of allowed color tuning range by doping, although the emission colors of the samples are not equivalent to black body irradiation. It has been demonstrated that metal doping at low concentration is an effective approach to producing rare-earth-free phosphors based on ZnO nanohybrid for white LEDs, the color of which can be readily tuned to yield warm or cold white light.

### 3.2.5 Photoluminescence at high temperature

To test the robustness of the promising WLEDs materials, the PL of doped ZnO nanohybrids were studied at temperatures up to 100 °C, as the emissive materials in LEDs heat up to such temperatures. The results obtained for ZnO doped with 0.1 % Fe(III) are shown in **Figure 3.20**. As the temperature rises from room temperature (RT) to 100 °C, the PL intensity maximum decreases drastically by 69 % from initial intensity. After the temperature is lowered to RT again, the PL intensity (spectrum in dots) recovers to 49 % of the initial intensity, indicating that the structure of the nanohybrid was irreversibly damaged by heating.

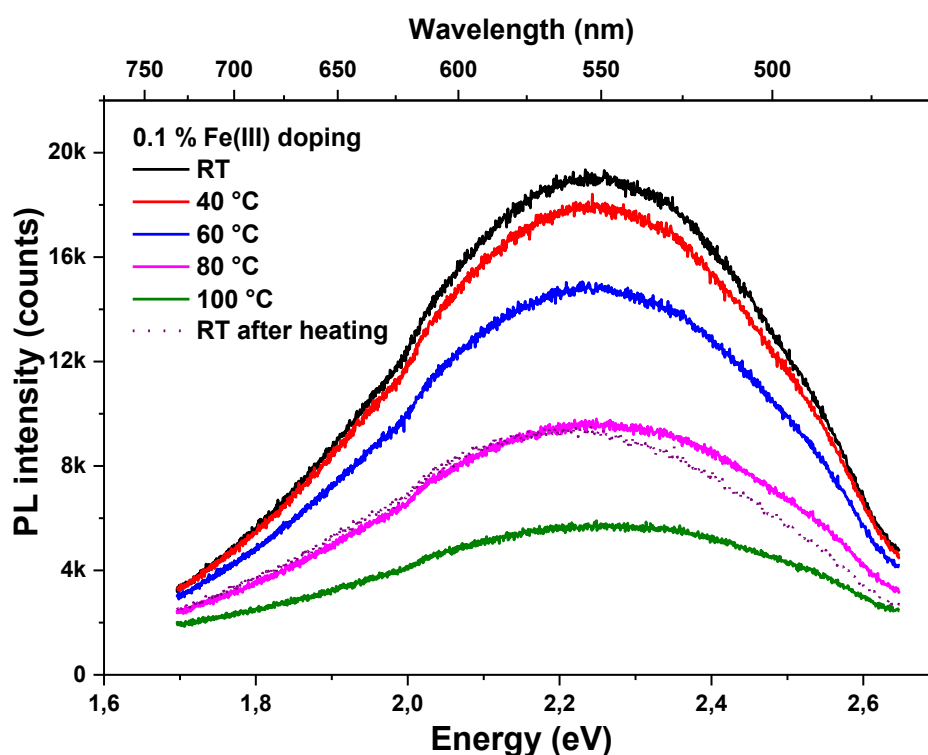


**Figure 3.20** PL spectra of 0.1 % Fe(III) doped ZnO nanohybrid obtained at various temperatures from room temperature (RT) to 100 °C.

Heat can degrade the material in two possible ways. First, the polymer PAA is susceptible to heat. At 100 °C, some residual solvent molecules (e.g., water and ethanol) trapped in the materials are

evaporated. The mesosphere structure can therefore be damaged, leading to the decrease of PL intensity. Second, the defect concentration in ZnO nanocrystals was modified by heating. Either the radiative defect concentration was reduced, or the non-radiative defect concentration was increased. Since the spectrum shape remains the same at different temperatures with lower intensity, the loss of emission is likely to result from the modification of defect concentration. The electrons and holes are more active under high temperature, thus more likely to recombine non-radiatively.

Our experiments show that the samples are sensitive to heat and, presently, they cannot be used as they are in WLEDs. Therefore, further research is required to improve the stability of the materials if they were to be applied in WLEDs.

### 3.3 Conclusion

In this chapter, a comprehensive and quantitative study of the effect of dopant on metal-doped ZnO nanohybrids is presented by structural and optical characterizations.

Firstly, the structural characterizations confirmed the successful synthesis of metal-doped ZnO nanohybrids via hydrolysis at doping concentrations of 0.1 %, 1 %, and 5 %. The materials are composed of mesospheres of ZnO nanocrystals embedded in PAA organic matrix. The crystal structure was indexed to be wurtzite ZnO by TEM and XRD. Presence of PAA was confirmed by FTIR. Presence of dopants was proved by RBS and EDX on 5 % doped samples, in addition to XRD on calcinated samples. The presence of dopants affects the resulting microstructure of the materials. Different types of dopants influence the microstructure in different ways. Dopants with a large ionic radius tend to degrade the integrity of the mesospheres. High doping concentration induces larger mesospheres and nanocrystals outside of mesospheres. The nanocrystals showed no clear trend in size evolution according to the dopant type or doping concentration, although it is under 50 nm for all the samples.

Secondly, the optical characterizations demonstrated that the PL spectrum could be tuned without degrading PL QY by doping at a low concentration. All the dopants are able to shift the PL spectrum towards the red end in the visible range. Differences in dopant type, doping concentration, and dopant valence all induce different redshifts in PL spectrum, producing a wide tuning range of the emission peak between 2.46 eV and 2.08 eV. The PL QY is also influenced by the above doping factors, as well as the morphology and crystal size of the nanohybrids. The dopants modify the PL and PL QY in two aspects: 1) by interacting with PAA during hydrolysis and 2) by incorporating into ZnO crystal lattice. The first aspect involves free dopant ions that are not incorporated in ZnO lattice. These free dopant ions may complex with PAA to interrupt the formation of mesospheres that are responsible for high PL QY. The second aspect involves the introduction of non-radiative energy levels in the bandgap of ZnO by the dopant ions incorporated in ZnO lattice. Most dopants introduce non-radiative energy levels,

quenching the near-band-edge and deep-level emissions. They may also modify the position or the concentration of the deep defects, resulting in the redshift of the PL spectrum and the enhancement of PL QY, respectively. By doping small ions at a low doping concentration of 0.1 %, the color of the emission can be tuned from cold to warm between 2.46 eV and 2.17 eV without degrading PL QY.

Finally, the nanohybrids were found to be sensitive to heat up to 100 °C, probably due to the instability of the organic matrix or the increase of the concentration of non-radiative deep-level defects. The thermal stability of the material thus requires improvement before application in WLEDs.

## Chapter 4 Silica-Coated ZnO Nanohybrids

In Chapter 3, it has been demonstrated in PL at high temperature that ZnO nanohybrids are sensitive to heat and suffer from instability. The absolute PL QY value of the undoped and doped ZnO nanohybrids is still rather low. For the materials to be applied in WLEDs, it is necessary to overcome these shortcomings by developing a more stable nanohybrid with a higher PL QY. A core-shell structure with silica coating can be a favorable design to improve the stability of the core material. Silica is commonly used as the coating substance thanks to its high stability, especially in aqueous environment, as well as its easy coating process, compatibility with other materials and optical transparency. [209] Silica shell can also induce surface passivation to modify the functionality of the core material. [190], [210], [211] Therefore, silica-coated ZnO nanohybrids were synthesized and characterized as introduced in Chapter 2.

In this chapter, the study of a series of silica-coated ZnO nanohybrids will be presented. This study employs the hydrolysis process as described in Section 2.1.1 to synthesize the ZnO nanohybrid (ZnO/PAA) precursors. The as-prepared ZnO/PAA from different synthesis batches exhibit different absolute PL QY values and instability under laser excitation. This issue will be addressed first in this chapter. Silica coating is then carried out for samples from each batch under the presence of tetraethyl orthosilicate ( $\text{Si}(\text{OC}_2\text{H}_5)_4$ , TEOS) in ZnO/PAA suspension. Characterization techniques as described in Sections 2.2 and 2.3 are applied to probe the structural and optical properties of silica-coated ZnO/PAA nanohybrids, respectively. The role of silica shell on the mesospheres will be studied with specific focuses on the enhancement of visible luminescence and on the stability with respect to high temperature. Two correlated factors in the coating process will be investigated, namely, the ratio of TEOS ( $x$ ) to ZnO and the amount of  $\text{NH}_4\text{OH}$  in the alkaline solution (solution A, *i.e.*, EtOH,  $\text{H}_2\text{O}$  and  $\text{NH}_4\text{OH}$  at mass ratios of 1:0.93:0.027y), as they may determine the integrity of the core-shell structure and ultimately the PL QY.

### 4.1 Instability of ZnO/PAA precursors

In order to investigate the effect of silica coating on ZnO/PAA, the optical properties of ZnO/PAA precursor were examined at the beginning of the study as a reference. **Figure 4.1** shows the normalized PL spectra of ZnO/PAA nanohybrids from two different batches. It was found that the PL spectrum of the newly synthesized ZnO/PAA peaked at a different position compared to the undoped ZnO nanohybrid reported in Chapter 3. It is perceivable that these two samples have different PL QY values. This finding poses a question on the consistency of the synthesis process. The same synthesis procedure

does not necessarily yield samples with the same optical properties. PL QY is considered a major optical property for silica-coated ZnO/PAA in the present study. If the ZnO/PAA precursors possess different PL QY values, it is meaningless to compare the absolute PL QY values among coated samples synthesized with ZnO/PAA precursors from different batches. One solution is to evaluate the improvement of PL QY of a silica-coated sample, in comparison with its uncoated ZnO/PAA precursor.

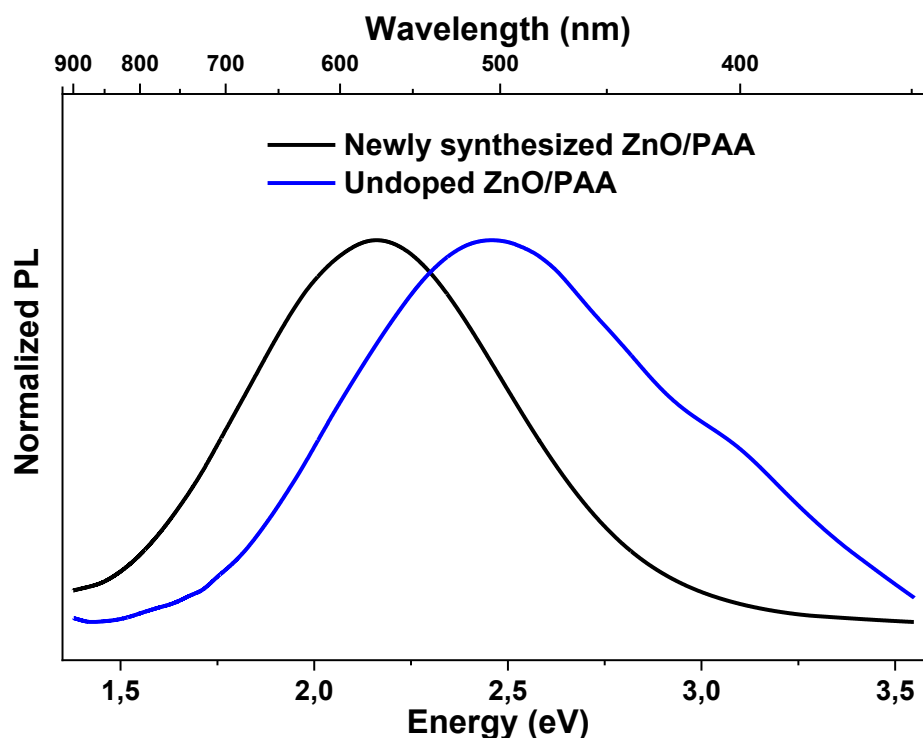


**Figure 4.1** Normalized PL spectra of ZnO/PAA synthesized in two different batches.

A series of ZnO/PAA precursor samples were therefore synthesized in 14 different batches under the same synthesis conditions and their absolute PL QY values are plotted in **Figure 4.2** as samples 1 to 14. These samples were subsequently coated by silica with different TEOS ratio and different amount of  $\text{NH}_4\text{OH}$ . The PL QY improvement of the coated samples can therefore be evaluated based on the PL QY of these precursor samples. The 15<sup>th</sup> sample (0Si-2A) in **Figure 4.2** was obtained from the 10<sup>th</sup> sample. This sample underwent the same synthesis protocol but without any TEOS injection. It was meant to check the effect of the alkaline solution (solution A) alone on properties of the ZnO/PAA nanohybrid. Therefore, it is uncoated ZnO/PAA and it is presented here as a referential sample to examine the effect of ammonia on the PL QY of ZnO/PAA. As indicated by “0Si-2A”, no TEOS was present during the synthesis with solution A, while other synthesis conditions remained the same as for silica-coated samples ( $x\text{Si-}y\text{A}$ ).

The error bars in **Figure 4.2** indicate PL QY values from different measurements as the excitation laser was found to cause possible damage to the samples, which is another sign of instability of the ZnO/PAA precursor. Under continuous laser excitation, the absorption of the laser light increases and the intensity

of the visible emission decreases over time. The absorption and emission signals tend to stabilize after a long period (more than 5 minutes depending on the sample). The materials are irreversibly modified by the laser excitation light, since the signals cannot be recovered after laser irradiation. Therefore, for the measurements of PL QY, each sample was illuminated by the UV laser for 5 minutes, before the collection of signals was performed several times within the subsequent 20 minutes. In this manner, the average PL QY of the uncoated ZnO/PAA samples was determined and illustrated as black squares in **Figure 4.2**, with error bars indicating the range of absolute PL QY obtained from different measurements.

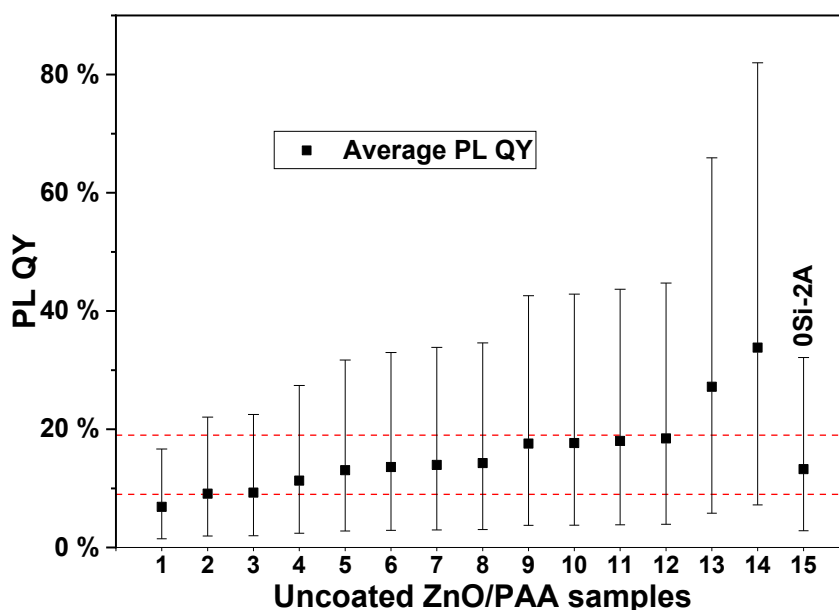


**Figure 4.2** Absolute PL QY values of 14 samples of ZnO/PAA precursor. The 15<sup>th</sup> uncoated sample was obtained in the same manner as the silica-coated samples but without any TEOS coating and is used as a reference. The red dashed lines indicate a PL QY window between 9 % and 19 %.

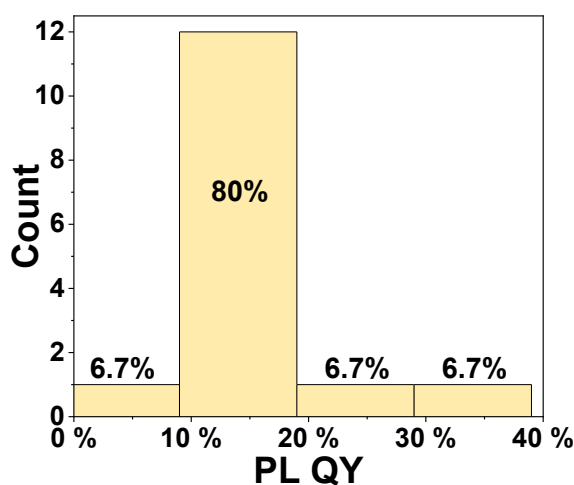


**Figure 4.3** Distribution of PL QY of 15 uncoated ZnO/PAA samples.

It can be seen from **Figure 4.2** that the average PL QY is likely to fall into a small window between 9 % and 19 %, as indicated by red horizontal dashed lines. For clarity, **Figure 4.3** displays a histogram of the distribution of PL QY of the 15 uncoated samples. The average PL QY of the referential sample (15<sup>th</sup> sample) is in the second column, with an equivalent value to that of most ZnO/PAA precursor samples. Since only NH<sub>4</sub>OH (or solution A) was added to the ZnO/PAA suspension in the synthesis of the referential sample, it suggests that the presence of NH<sub>4</sub>OH alone does not modify the PL QY of the initial sample. Thus, ammonia is most likely not responsible for any PL QY improvement. On the contrary, ammonia may lead to a decrease in PL QY, since the average PL QY of the 15<sup>th</sup> sample is lower than that of the 10<sup>th</sup> sample.

The instability of ZnO/PAA precursor is manifested in two facets, both likely related to the polymer matrix of PAA. The first facet is in the synthesis. The nanohybrid of PAA and ZnO nanocrystals may be assembled differently, even under the same synthesis conditions. As a result, the size of ZnO nanocrystals may vary in a small range. The visible emission from ZnO nanocrystals is achieved by passivating the surface states of ZnO nanocrystals with PAA, which is bound to cover the surface area of all ZnO nanocrystals. The extent of passivation might be different for samples from different batches (depending on the PAA coverage on ZnO nanocrystals), resulting in different PL spectra and different PL QY. The difference in average PL QY is in a comparable range that the samples are still relevant. The second facet concerns the residual molecules (*e.g.*, ethanol and water) trapped in PAA matrix. As discussed in Section 3.2.5, the nanohybrid material is gradually degraded as the temperature rises from room temperature to 100 °C. The strong UV laser beam can locally heat the material and evaporate the residual solvent molecules, irreversibly damaging the material, leading to the discrepancy between different measurements.

Silica coating can be a solution to the instability issue. A silica shell on top of the PAA matrix embedded with ZnO nanocrystals can further passivate the surface states of uncoated ZnO nanocrystals. Silica coating also provides protection for the hybrid mesospheres in the ambient environment. Besides, the role of ammonia is crucial for the silica coating. Ammonia is a neutralizer of protonated PAAH and catalyst for the sol-gel reaction of TEOS to form the silica shell. [212] As seen from the 15<sup>th</sup> sample in **Figure 4.2**, ammonia can lead to a decrease in PL QY without the presence of TEOS. One possible mechanism is the amination of protonated PAAH, where ammonia neutralizes COOH groups in the PAA chains to form PAA-NH<sub>4</sub>. The amination compromises the integrity of the PAA matrix, resulting in some bare ZnO nanocrystals outside of PAA matrix. The surface states of these ZnO nanocrystals then act as PL quenching centers. However, the formation of PAA-NH<sub>4</sub> may be beneficial for the release of adsorbed and trapped molecules in PAAH matrix. The amount of both TEOS and ammonia should be studied, in order to obtain an optimal silica shell that enhances the surface states passivation and protects the nanohybrid.

## 4.2 Effect of TEOS ratio

The attempt to coat ZnO/PAA mesospheres started with adding different amount of TEOS after hydrolysis synthesis. The weight ratio of TEOS to ZnO ranged from 0.94:1 to 600:1. High PL QY was achieved only for small TEOS to ZnO ratios smaller than 10:1. Consequently, we only focus on these samples. The first part of the study concerns samples with different TEOS contents but the same amount of  $\text{NH}_4\text{OH}$ . These samples are denoted as  $x\text{Si-1A}$ , where  $x$  is the TEOS mass ratio to ZnO and 1A denotes 1 time of the nominal  $\text{NH}_4\text{OH}$  ratio of 0.027 in solution A. The structural and optical properties of  $x\text{Si-1A}$  ( $x = 1.1, 2, 3, 3.8, 5, 6, 7, 8, 9,$  and 10) samples will be discussed herein.

### 4.2.1 Microstructure

#### 4.2.1.1 X-ray diffraction

The hydrolysis process in our study produces wurtzite ZnO nanocrystals, as demonstrated previously. **Figure 4.4** (a) presents XRD spectra of silica-coated ZnO nanohybrids synthesized at different TEOS to ZnO ratios, namely, 2:1, 3:1, and 10:1. The vertical lines indicate the theoretical diffraction peaks from wurtzite ZnO. The diffraction peaks of the as-prepared materials correspond well to wurtzite ZnO with two extra peaks at  $2\theta = 33.4^\circ$  and  $59.4^\circ$  (marked by black dots). The mean crystal size of ZnO is estimated to be around 30 nm by Scherrer equation for all the samples. The XRD spectra are essentially identical despite the difference in TEOS content, suggesting that the presence of TEOS does not change the crystallographic structure or the crystal size of the nanocrystals. The two extra peaks cannot be indexed to any known phase related to zinc or silicon. It is possible that they are attributed to a polymer phase. The samples were therefore calcinated at  $400^\circ\text{C}$  for 4 h in order to investigate the unassigned phase.

The XRD spectra of the calcinated samples are presented in **Figure 4.4** (b). After calcination, the unassigned peaks disappear and only wurtzite ZnO phase remains, confirming that the peaks are related to the PAA. The spectra are still identical for different samples after calcination, indicating that the unassigned phase is independent of the introduction of TEOS. It is also indicative that a silicon-based amorphous phase exists in the materials. The mean crystal size remains the same for all the samples after calcination although the position of the diffraction peaks shifts slightly towards higher angle, due to the curing of crystal defects. [213] The calcinated samples are not luminescent since the polymeric structure and the defect-related emission centers are both compromised by the calcination.

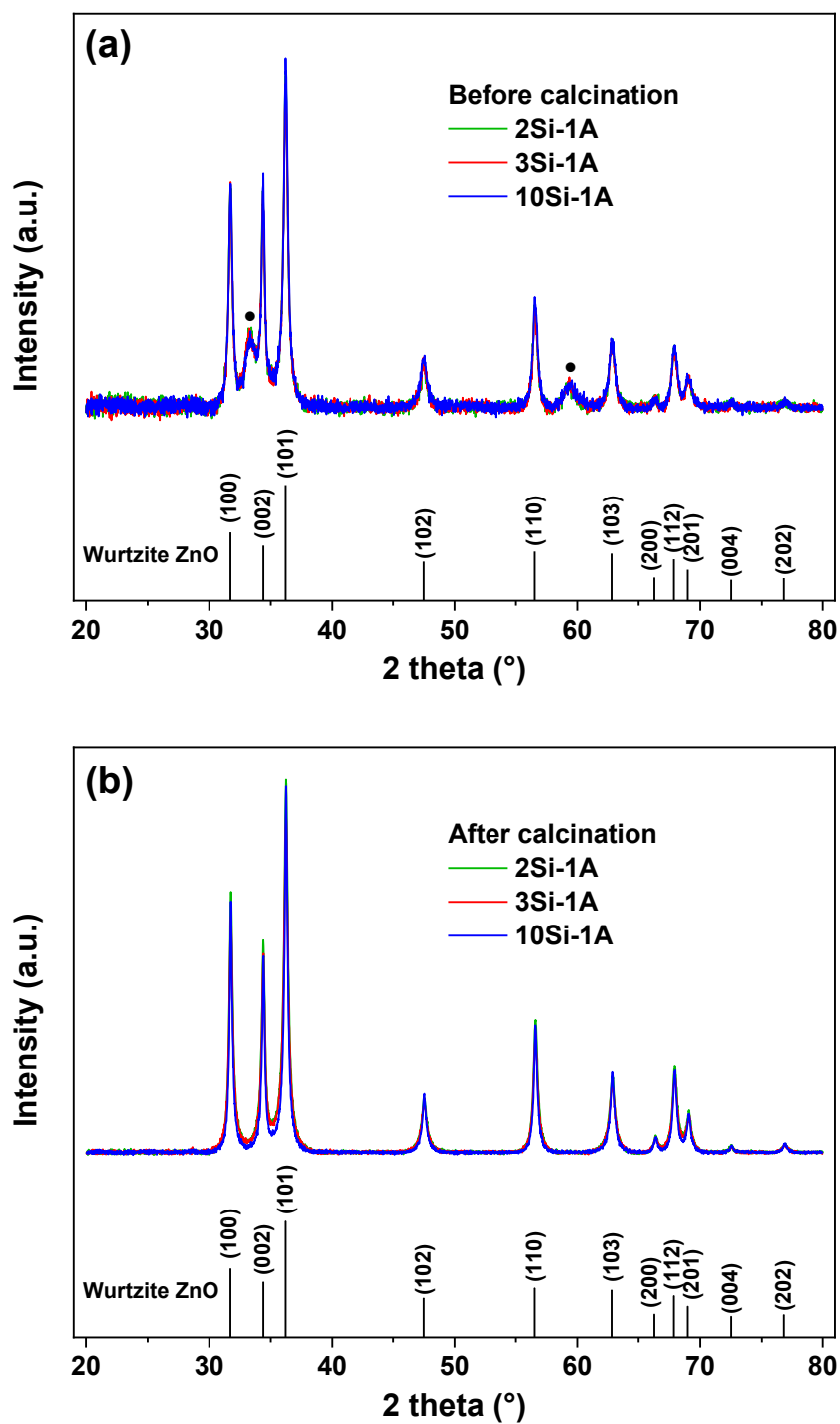


**Figure 4.4** XRD spectra of  $x$ Si-1A ( $x = 2, 3$  and  $10$ ) ZnO nanohybrids (a) before calcination and (b) after calcination at  $400\text{ }^\circ\text{C}$  for 4 h.

## 4.2.1.2 Transmission electron microscopy

Since crystalline silica was not observed from XRD spectra, TEM was employed to search for evidence of its presence. ZnO nanocrystals were observed both inside and outside of the mesospheres for all the studied samples ( $x$ Si-1A ( $x = 1.1, 3.8$  and  $10$ )). However, the images were taken mostly from regions with nanocrystals outside of the mesospheres, since the mesospheres are rather thick ( $\sim 100$  nm) for TEM measurement. **Figure 4.5** shows some representative HRTEM images of silica-coated ZnO nanostructures from  $x$ Si-1A samples.

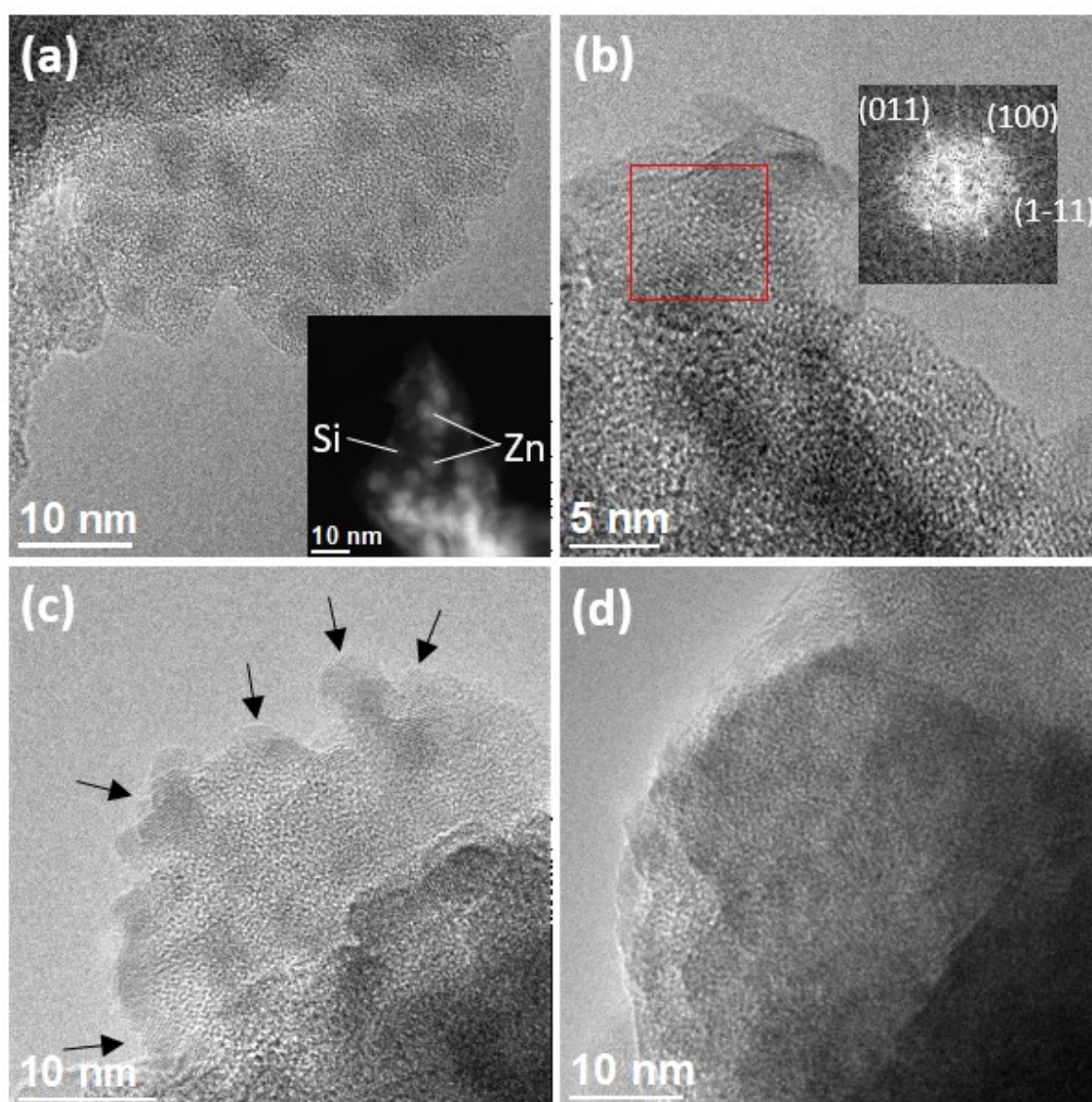


**Figure 4.5** TEM images of  $x$ Si-1A ZnO nanohybrids. (a) TEM and HAADF image (inset) of 3.8Si-1A. (b) HRTEM image of 3.8Si-1A with the inset showing fast Fourier transformed (FFT) image of the red square area. (c) HRTEM of 1.1Si-1A. (d) HRTEM of 10Si-1A.

It can be seen from **Figure 4.5** (a) and (b) that ZnO nanoparticles of  $\sim 5$  nm in size are uniformly dispersed in an amorphous matrix for sample 3.8Si-1A. The size of the ZnO nanocrystals pictured here is somewhat smaller than the average size determined from XRD. One possible reason is that the observed region is small, therefore not statistically relevant. Another explanation is that the edges of the nanocrystals are not clear due to the presence of the surrounding amorphous matrix. Consequently, the size of the nanocrystals is underestimated. The crystal structure is indexed to be wurtzite ZnO from the diffraction patterns in FFT image in **Figure 4.5** (b), in agreement with the results from XRD.

The inset in **Figure 4.5** (a) shows a HAADF image from sample 3.8Si-1A where the brighter areas are signals from Zn and the dim areas are from Si. The HAADF image not only confirms the presence of Si, but also demonstrates that Zn and Si are clearly segregated. However, it is difficult to get an absolute composition of the corresponding silicon-based phase, *i.e.*, to confirm that Si is present in a stoichiometric silica phase. EDX was also performed to analyze the chemical composition of the samples. The results (see Appendix VI for sample 3.8Si-1A) further proved the existence of silicon in the samples, although the Si to Zn ratio can be different at different scanning locations.

**Figure 4.5** (c) and (d) display silica-coated ZnO with the lowest and highest loadings of TEOS, from samples 1.1Si-1A and 10Si-1A respectively. In sample 1.1Si-1A, some ZnO nanocrystals (as indicated by the black arrows) are not fully coated by the amorphous matrix, whereas a much thicker layer of silica is found in 10Si-1A, since ZnO crystals are barely visible, buried deep in the amorphous matrix. Since the amount of PAA is the same for all the samples, the difference in the thickness of the amorphous phase probably results from the silicon-based coating, despite the fact that its composition cannot be accurately determined.

#### 4.2.1.3 Fourier transform infrared spectroscopy

TEM results presented evidence of the presence of silica, or at least of an amorphous silicon-based phase, but PAA has not yet been characterized. On the other hand, XRD spectra detected two unassigned peaks that are related to PAA. FTIR can provide information on the presence of PAA, as shown in Section 3.1.3. **Figure 4.6** presents the FTIR spectrum of sample 3.8Si-1A in comparison with that of uncoated ZnO/PAA.

For both samples, the broad feature between  $3000\text{ cm}^{-1}$  and  $3500\text{ cm}^{-1}$  is associated with water or OH groups. Characteristic peaks of PAA are observed between  $1219\text{ cm}^{-1}$  and  $1800\text{ cm}^{-1}$ . The peak at  $1736\text{ cm}^{-1}$  is attributed to C=O stretching mode of free non-hydrogen-bonded carboxylic acid (COOH) groups. The two strong peaks at  $1551\text{ cm}^{-1}$  and  $1408\text{ cm}^{-1}$  are ascribed to asymmetric and symmetric modes of carboxylate anion ( $\text{COO}^-$ ), respectively. [199] The features above correspond well with the FTIR results obtained for metal-doped ZnO nanohybrids, as shown in **Figure 3.5**.

Between  $816\text{ cm}^{-1}$  and  $1219\text{ cm}^{-1}$ , a broad peak is observed for sample 3.8Si-1A while it is absent for uncoated ZnO/PAA. The peaks at  $1018\text{ cm}^{-1}$  and  $945\text{ cm}^{-1}$  are assigned to asymmetric stretching modes of Si-O-Si vibrations and stretching modes of surface silanol groups ( $\equiv\text{Si-OH}$ ) or vibrational mode of Si-O-Zn, respectively. [211], [214] It is therefore confirmed that silica exists in the studied materials. Although the absolute composition of  $\text{SiO}_x$  is not determined, the coating is referred to as silica in the present study for convenience. In view of possible Si-O-Zn bonds, the surface states of ZnO nanoparticles may be modified after the incorporation of silica.

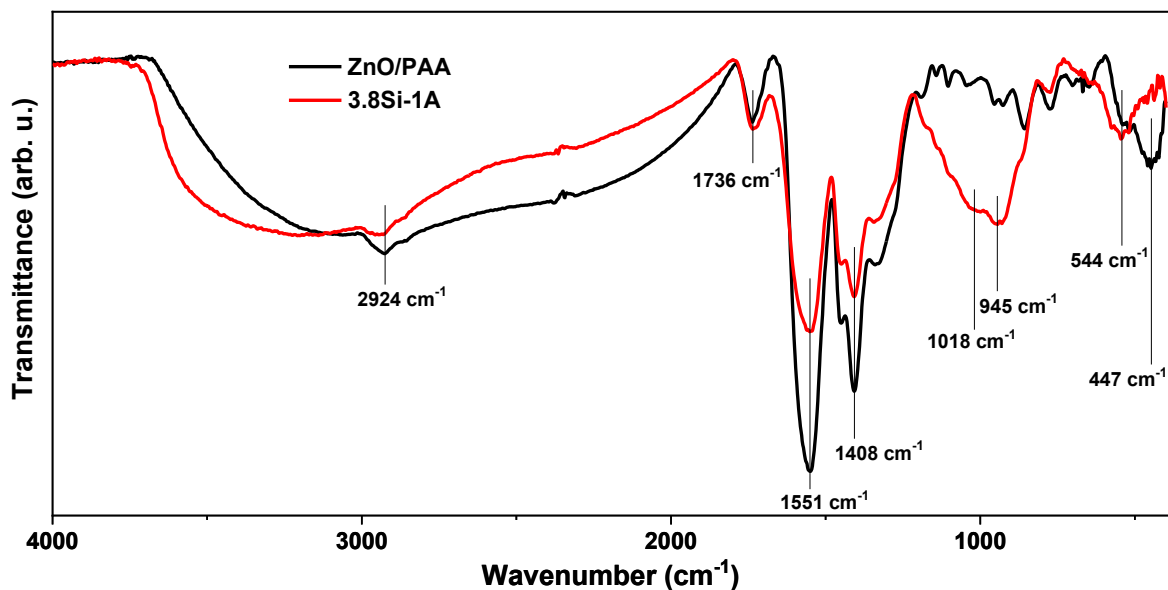


**Figure 4.6** FTIR spectra of ZnO/PAA and 3.8Si-1A nanohybrids.

The peak at  $447\text{ cm}^{-1}$  from ZnO/PAA sample is assigned to Zn-O stretching mode, which is further evidence of the presence of ZnO. Interestingly, a peak at  $544\text{ cm}^{-1}$  is present instead of at  $447\text{ cm}^{-1}$  for sample 3.8Si-1A. This peak has a weak contribution in ZnO/PAA sample as well. The position of the peak from Zn-O bond is dependent on the size, morphology and the axial ratio ( $c/a$ ) of ZnO nanocrystals. [215] Oxygen-related defect complexes are also associated with FTIR peaks near this range. [216] Therefore, the peak at  $544\text{ cm}^{-1}$  can be assigned to highly defected ZnO, which constitutes the majority of ZnO nanocrystals in sample 3.8Si-1A but only a small fraction of ZnO nanocrystals in uncoated ZnO/PAA.

#### 4.2.1.4 Summary

The characterizations above can well depict the microstructure of the as-prepared  $x\text{Si-1A}$  samples: silica-coated PAA mesospheres embedding ZnO nanocrystals. The silica coating does not change the crystallographic structure of ZnO, nor does it destroy the PAA matrix around ZnO nanocrystals, leading

to a direct coating on the whole mesosphere of the nanohybrid. The amount of TEOS has little impact on the microstructure and only affects the thickness of the silica coating. The coating may modify the surface states of the materials, which can in turn modify their optical properties.

## 4.2.2 Optical properties

### 4.2.2.1 Photoluminescence

Regarding the optical properties, the effect of the silica coating on the PL was investigated first. Normalized PL spectra of selected  $x$ Si-1A samples are presented in **Figure 4.7**, along with the PL spectrum of the uncoated ZnO/PAA. All the samples emit in the visible range peaking around 2.2 eV, regardless of the amount of TEOS. It is evident that silica coating does not change the shape of the spectrum of ZnO/PAA, implying that the nature of the specific crystalline defects of ZnO nanocrystals is not affected by silica coating or the amount of TEOS.

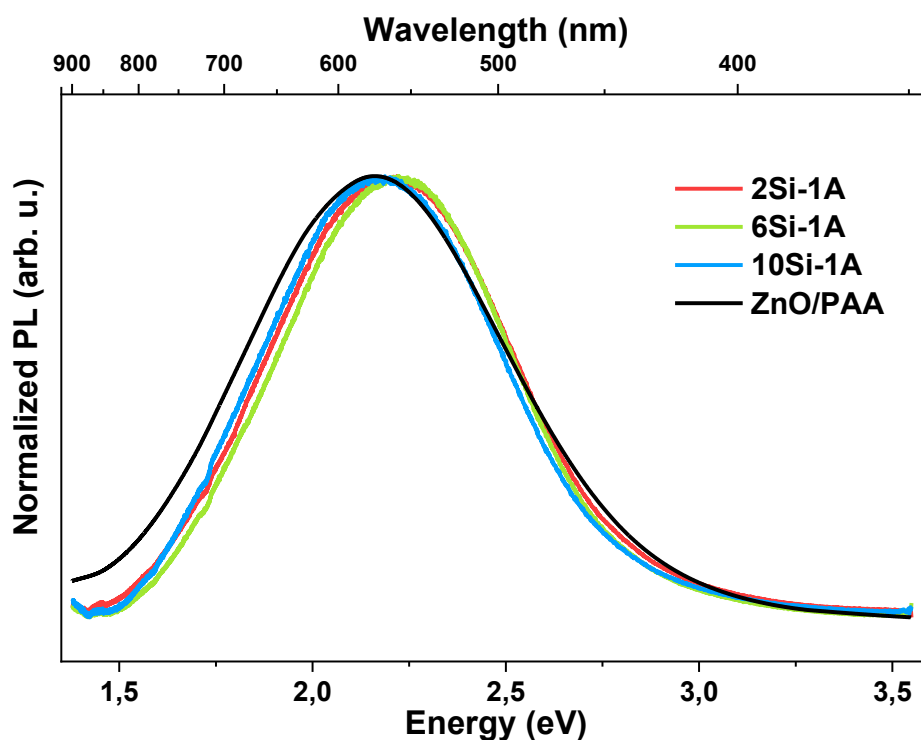


**Figure 4.7** Normalized PL spectra of silica-coated ZnO/PAA with different amount of TEOS loading.

### 4.2.2.2 Photoluminescence quantum yield

As the spectrum of ZnO/PAA was not modified by silica coating, PL QY becomes a key parameter for the optical properties of silica-coated ZnO nanohybrids. The PL QY of the  $x$ Si-1A samples are plotted

in **Figure 4.8** as PL QY improvement compared to the PL QY of the uncoated ZnO/PAA. The ZnO/PAA precursor for these samples is from the same batch and it has an absolute PL QY of 3.5 %. When  $x$  (TEOS:ZnO ratio) is smaller than 5, the PL QY is significantly improved by silica coating. A drastic improvement by a factor of nearly five (484 %) is found at  $x = 3.8$ . When  $x$  is larger than 5, the PL QY is only improved by a small margin (for  $x = 8, 9$  and  $10$ ) or even degraded (for  $x = 6$  and  $7$ ) by silica coating. The optimal ratio of TEOS to ZnO seems to locate between  $x = 3$  and  $5$ .

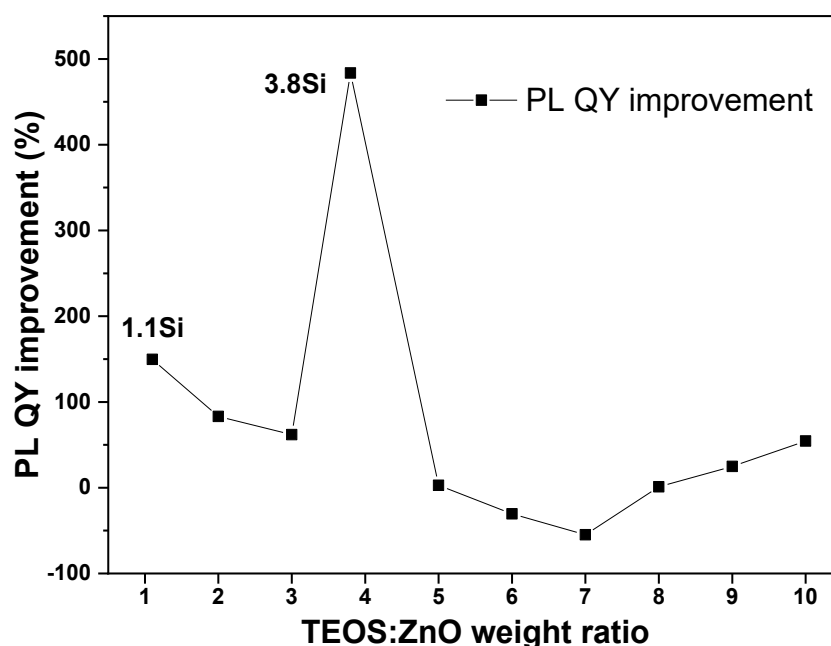


**Figure 4.8** PL QY improvement of  $x$ Si-1A samples in function of TEOS:ZnO ratio.

An appropriate amount of silica coating is important for the enhancement of PL QY. If the silica is scarce to cover the ZnO/PAA nanohybrid (as for sample 1.1Si-1A in **Figure 4.5** (c)), the surface states of the exposed nanoparticles would decrease the PL QY by lowering the charge trapping efficiency of the deep-level defects, as the charges would be captured by non-luminescent surface states. On the other hand, if the silica is superabundant (as for sample 10Si-1A in **Figure 4.5** (d)), UV excitation source would be partially absorbed by silica before reaching the effective material of ZnO. Therefore, TEOS ratio of 3.8 has been considered an appropriate amount of silica coating, as it presents full coverage of nanoparticles and, seemingly, an optimal thickness of a few nanometers.

### 4.3 Effect of ammonia content

The integrity of the mesospheres is not affected by TEOS to ZnO ratio, but it is subject to the alkaline solution (solution A) containing  $\text{NH}_4\text{OH}$ , which can neutralize protonated PAAH. Therefore, the amount of  $\text{NH}_4\text{OH}$  in solution A is crucial for successful silica coating and for the improvement of the stability

of the coated ZnO/PAA. The second part of the study is presented in this section, concerning sample series 3.8Si- $\gamma$ A. TEOS to ZnO ratio of 3.8 was chosen because it retained an optimum of PL QY improvement.

### 4.3.1 Microstructure

#### 4.3.1.1 X-ray diffraction

**Figure 4.9** presents the XRD spectra of silica-coated ZnO/PAA nanohybrids prepared with different amount of ammonia in solution A. All the spectra can be indexed to wurtzite ZnO with no peak shift from standard wurtzite ZnO. Two extra peaks at  $2\theta = 33.4^\circ$  and  $59.4^\circ$  (marked by black diamonds) are present again for all the samples, as observed in **Figure 4.4** (a) for  $x$ Si-1A samples. Since the phase corresponding to these two peaks is related to PAA, its formation is probably dependent on the amount of ammonia due to the amination of protonated PAAH. For sample 3.8Si-4A, a broad peak appears around  $2\theta = 27^\circ$ , which is a signature peak of amorphous silica.

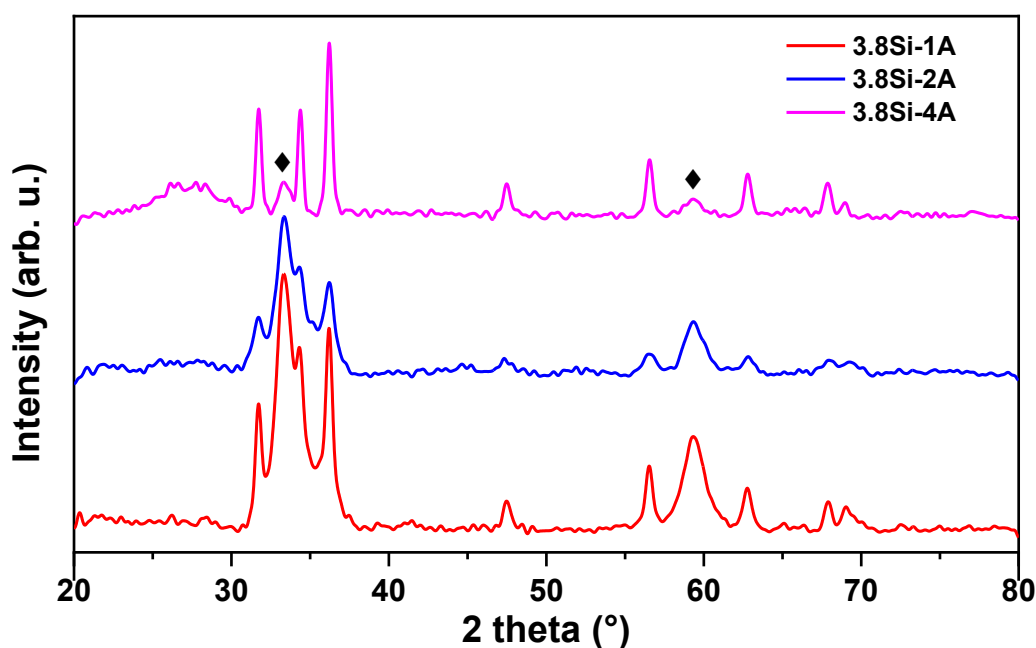


**Figure 4.9** XRD spectra of 3.8Si- $\gamma$ A ( $\gamma = 1, 2$  and 4) ZnO/PAA nanohybrids.

The mean crystal size was estimated for the three 3.8Si- $\gamma$ A samples by Scherrer equation and the results are plotted in **Figure 4.10** in function of the amount of  $\text{NH}_4\text{OH}$  ( $\gamma$ ). The size of both wurtzite ZnO phase and the unassigned phase was calculated. ZnO nanocrystals in all the samples have a mean crystal size smaller than 30 nm. The variation of the size of ZnO nanocrystals is in a reasonable range and probably results from the instability from batch to batch as mentioned in Section 4.1. The ZnO nanocrystals are

mostly embedded in PAA matrix. Their size is not affected by silica coating, which has been proved by XRD spectra in **Figure 4.4** (a). Ammonia is unlikely to modify the size of ZnO nanocrystals, as it mainly interacts with PAA and has an impact on the presence of the unassigned phase related to PAA. It can be seen from **Figure 4.10** that the crystalline domain size of the unassigned phase is sensitive to the amount of ammonia. It increases from 6.9 nm to 13.5 nm with the increase of ammonia from the nominal amount to 4 times the nominal amount. The change in the size of the unassigned phase is probably related to the excessive amount of OH<sup>-</sup> from NH<sub>4</sub>OH, which modifies the pH of the solution, hence perturbing the integrity of the PAA matrix. Overall, however, this crystalline polymeric phase represents a limited fraction of the PAA matrix.

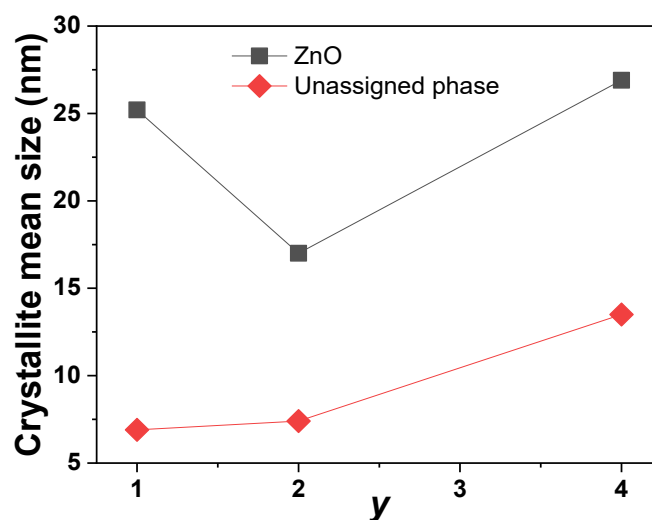


**Figure 4.10** Diffraction domain size of ZnO (squares) and the unassigned phase (diamonds) of three silica-coated samples (3.8Si- $y$ A ( $y = 1, 2,$  and  $4$ )) in function of the amount of NH<sub>4</sub>OH in solution A. The size of the unassigned phase is estimated by Scherrer equation from the peak at  $2\theta = 33.4^\circ$ .

#### 4.3.1.2 Transmission electron microscopy

In order to examine the effect of ammonia on the structure of silica-coated ZnO nanohybrids, in particular the effect on the PAA matrix, TEM was carried out for the three 3.8Si- $y$ A samples. Representative TEM images are shown in **Figure 4.11**. The nanohybrid structure of ZnO nanocrystals embedded in amorphous matrix is found in all the samples. When  $y = 1$ , *i.e.*, when the ratio of NH<sub>4</sub>OH in solution A is 0.027, the atomic planes of ZnO can be observed under HRTEM (**Figure 4.11** (a)). Low magnification TEM image (**Figure 4.11** (b)) shows typical thick structure of this sample. The formation of such structure is probably due to agglomeration of the nanohybrids as shown in **Figure 4.11** (a). When  $y$  increases to 2, *i.e.*, when the ratio of NH<sub>4</sub>OH in solution A is 2 times of 0.027, the atomic planes of some nanocrystals are not clearly observed (**Figure 4.11** (c)) due to the thickening of the amorphous

silica coating. Under low magnification TEM (**Figure 4.11** (d)), the mesospheres with a rough surface are present along with ZnO nanocrystals outside of the mesospheres. Some of the nanocrystals outside of the mesospheres may still be embedded in an amorphous matrix, as indicated by the arrows. Finally, when  $y$  increases to 4, the contrast of ZnO nanocrystals in the amorphous matrix declines as the amorphous coating continues to thicken (**Figure 4.11** (e)). The mesospheres are no longer present and mostly unembedded nanocrystals are observed (**Figure 4.11** (f)).

The nanocrystals become less distinguishable as the amount of ammonia increases, as observed in **Figure 4.11** (a), (c) and (e), indicating that the amorphous matrix thickens with the increase of  $\text{NH}_4\text{OH}$  concentration. On the other hand, considering its neutralization effect, ammonia seems to degrade the mesospheres, as demonstrated in **Figure 4.11** (b), (d) and (f), while leading to larger crystal size of the unassigned phase observed from XRD. PAA aggregates to form the mesospheres during the hydrolysis due to the repulsion among positively charged carboxyl ( $\text{COOH}$ ) groups in the polymer chains. [217], [218] When ammonia is added into the system, the  $\text{COOH}$  groups are aminated to form  $\text{COO-NH}_4$ , reducing the repulsion among the chains and disturbing the mesospheric aggregates. As the amount of ammonia increases, the mesospheres can even be completely broken apart.

Ammonia also acts as a catalyst for the hydrolysis of TEOS to form silica. [217] When the amount of  $\text{NH}_4\text{OH}$  is low at the nominal amount, only a thin layer of silica shell is formed. One reason is that the hydrolysis happens slowly; another possible reason is that insufficient amount of  $\text{COOH}$  groups in PAA chains are aminated to absorb TEOS hydrolysis and condensation, regardless of the TEOS loading. On the other hand, the repulsion among the mesospheres may be reduced and they tend to agglomerate into thick structure, as shown in **Figure 4.11** (b). When  $\text{NH}_4\text{OH}$  increases to twice the nominal amount, more  $\text{COOH}$  groups are aminated to form  $\text{COO-NH}_4$ , leading to the rough surface of the mesospheres as observed in **Figure 4.11** (d). More silica is also formed due to the increase of the amount of catalytic ammonia, most likely on the surface of the mesospheres. Finally, when  $\text{NH}_4\text{OH}$  increases to four times the nominal amount, most  $\text{COOH}$  groups are aminated, resulting in the absence of mesospheres as observed in **Figure 4.11** (f). Even more silica can be produced around PAA chains, coating the nanohybrid of ZnO and PAA. As the mesospheres are broken apart, some ZnO nanocrystals are no longer embedded in PAA matrix but subject to the silica coating.

Since both PAA and silica are present in an amorphous form, it is rather difficult to distinguish them or determine their respective thickness from the TEM images, especially when the silica shell (a few nanometers in thickness) is much thinner than the PAA matrix (around 100 nm in thickness). It can be deduced though that silica shell is present on the surface of nanohybrid mesospheres at relatively low  $\text{NH}_4\text{OH}$  concentrations, when the PAA matrix is not significantly perturbed by excessive  $\text{NH}_4\text{OH}$ . At higher  $\text{NH}_4\text{OH}$  concentrations, the silica shell is sufficient to cover the mesospheres, and may even coat the nanocrystals outside of the mesospheres when enough silica is produced. The coverage of the silica

coating determines how well the nanocrystals are protected and how light propagates within the material, thus influencing its optical properties and possibly its stability under laser excitation.

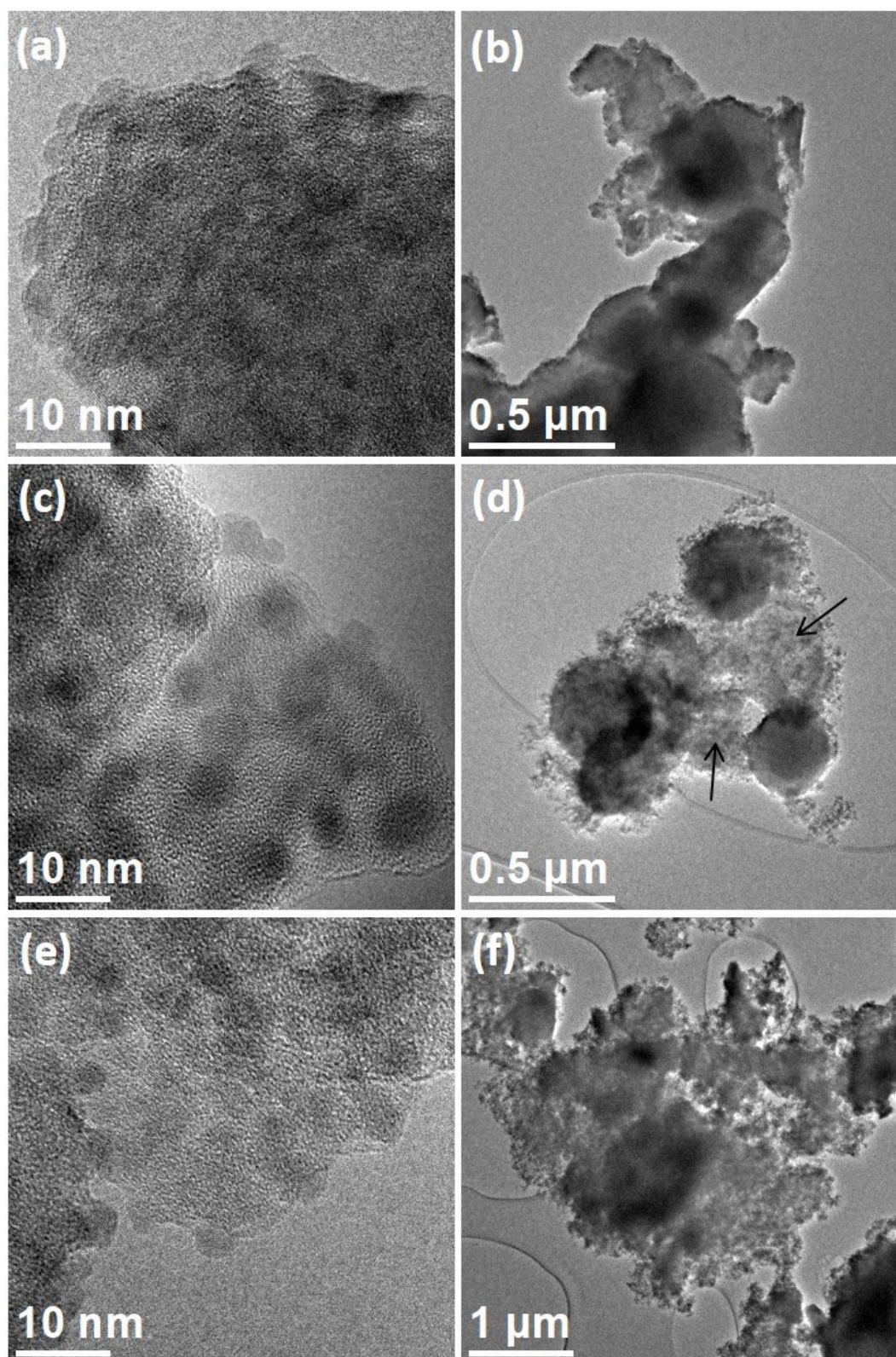


**Figure 4.11** TEM images of 3.8Si- $y$ A silica-coated ZnO nanohybrids. (a) and (b) 3.8Si-1A; (c) and (d) 3.8Si-2A; (e) and (f) 3.8Si-4A.

## 4.3.1.3 Rutherford backscattering spectrometry

XRD and TEM are only able to perform qualitative analyses on the microstructure of 3.8Si- $\gamma$ A samples. Although the initial TEOS content is the same for 3.8Si- $\gamma$ A series, TEM suggests different amount of amorphous coating in different samples. Therefore, RBS was adopted to perform a global quantitative analysis on the amount of Si and Zn and the results are shown in **Figure 4.12**.

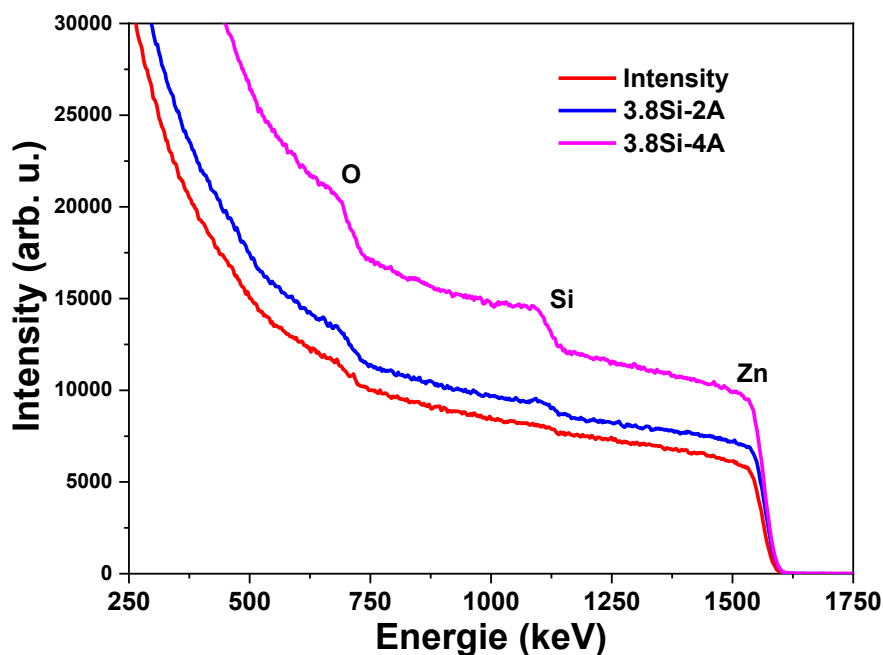


**Figure 4.12** RBS spectra of 3.8Si- $\gamma$ A ( $\gamma = 1, 2,$  and  $4$ ) samples.

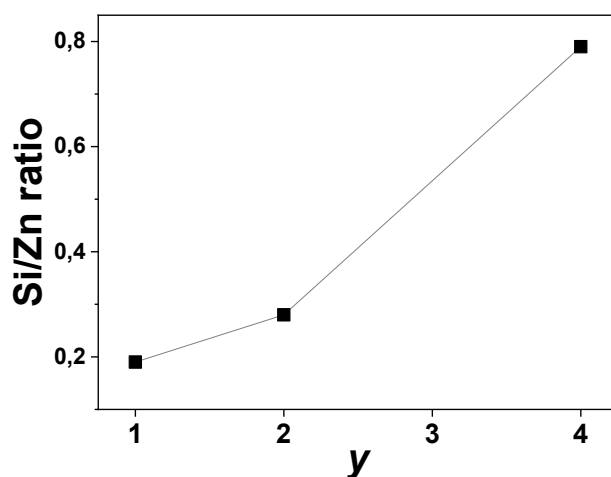


**Figure 4.13** Atomic ratio of Si to Zn in 3.8Si- $\gamma$ A samples calculated by RBS.

All the spectra exhibit distinct signals from Zn, Si and O. It is evident that the signal from Si increases as the  $\text{NH}_4\text{OH}$  concentration increases. The contribution of each element was calculated via simulation and the atomic ratios of Si to Zn are plotted in **Figure 4.13** in function of the amount of  $\text{NH}_4\text{OH}$  ( $y$ ). With the same initial amount of TEOS in the coating process, different amount of silica was successfully coated on the ZnO/PAA precursor. Doubling the ammonia concentration does not double the amount of Si in the final sample, whereas multiplying the ammonia concentration by a factor of 4 induces an increase of the Si content by an identical factor of 4. A clear trend is present: more silica is produced as  $y$  increases, in agreement with the appearance of the amorphous silica peak observed in XRD (see **Figure 4.9**). The presence of  $\text{NH}_4\text{OH}$  is beneficial for the silica formation. It is therefore confirmed that the thickened amorphous phase observed under TEM is attributed to thicker silica coating.

Retrospectively, considering  $x\text{Si-1A}$  sample series again, since the amount of  $\text{NH}_4\text{OH}$  is limited during the coating process (*i.e.*,  $y = 1$ ), it is possible that a maximal amount of silica coating is achieved under high TEOS loading ( $x > 5$ ). This can explain why further increase in TEOS content does not change the structure or significantly improve the PL QY.

#### 4.3.1.4 Structure model

Based on the observations above, a structure model is proposed for the silica-coated ZnO/PAA nanohybrids, as illustrated in **Figure 4.14**. The key to the changes in the structure of the mesospheres is the amination of COOH groups in PAA chains, which modifies the repulsion among PAA chains. Where silica coating is formed is closely related to the location of PAA.

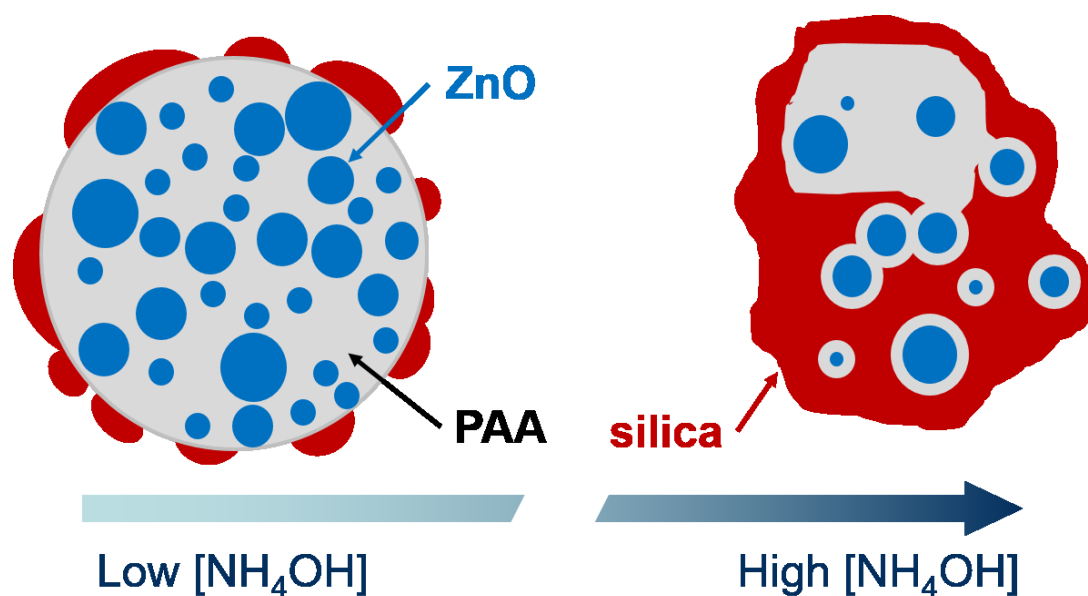


**Figure 4.14** Structure model of silica-coated ZnO/PAA nanohybrids under different concentrations of  $\text{NH}_4\text{OH}$  in solution A.

Under the same loading of TEOS, a low  $\text{NH}_4\text{OH}$  ratio in solution A leads to a thin coating on the mesospheric nanohybrid (left of **Figure 4.14**). A relatively small amount of silica is produced due to the low concentration of catalyst. The PAA matrix of the mesospheres are not degraded by the amination of COOH groups, therefore the ZnO nanocrystals remain embedded in the mesospheres.

On the other hand, a high  $\text{NH}_4\text{OH}$  ratio leads to a thick coating on the unembedded nanocrystal (right of **Figure 4.14**). The mesospheres are greatly degraded after profound amination of COOH groups. The ZnO nanocrystals are no longer embedded in the mesospheres although some of them may still be surrounded by PAA. Meanwhile, large amount of silica is produced on top of PAA-coated ZnO nanocrystals and it can even form a new amorphous matrix.

A medium and optimal concentration may exist, where mesosphere structure is not degraded by the presence of  $\text{NH}_4\text{OH}$  but enhanced by the silica coating. In this case, the mesospheres are slightly degraded, but overall can maintain the spherical shape. Some embedded ZnO nanocrystals may be exposed to silica coating over the mesospheres. The mesosphere tends to break apart but the silica coating formed around it may hold it together. This optimal structure can be obtained when the amination process and the formation of silica coating are well balanced, which depends on the ratio of both  $\text{NH}_4\text{OH}$  and TEOS.

The model above can explain the increase in the thickness of amorphous phase, the increase of Si composition and the degradation of the mesospheres observed under TEM with the increase of  $\text{NH}_4\text{OH}$  ratio. It should be noted that a small amount of ZnO nanocrystals might already exist outside of the mesospheres, uncoated by PAA, in the ZnO/PAA precursors. These nanocrystals are not efficient emitting material due to abundant PL-quenching surface states, therefore not considered in this model.

## 4.3.2 Optical properties

### 4.3.2.1 Photoluminescence

Normalized PL spectra of  $3.8\text{Si-}y\text{A}$  ( $y = 1, 2, 3$ ) samples are presented in **Figure 4.15** in comparison with the spectrum of their respective uncoated ZnO/PAA precursor. More spectra of  $3.8\text{Si-}y\text{A}$  samples are given in Appendix VII. For all the silica-coated samples, the PL spectrum is similar to that of their respective precursor with no significant emission peak shift, indicating that the silica coating does not change the nature of the radiative defect centers in ZnO crystallites. Therefore, the ZnO nanocrystals, or the majority of them, are still covered with PAA and not impacted by the silica coating on top of PAA. It is also noticed that the ZnO/PAA precursors demonstrate different PL spectra, resulting from the instability of the samples synthesized in different batches. Such difference in the PL spectra indicates that the radiative defect species are different among the ZnO/PAA precursors, probably due to different

extent of the passivation of the surface states. In turn, it results in the discrepancy in the PL QY of the ZnO/PAA precursors.

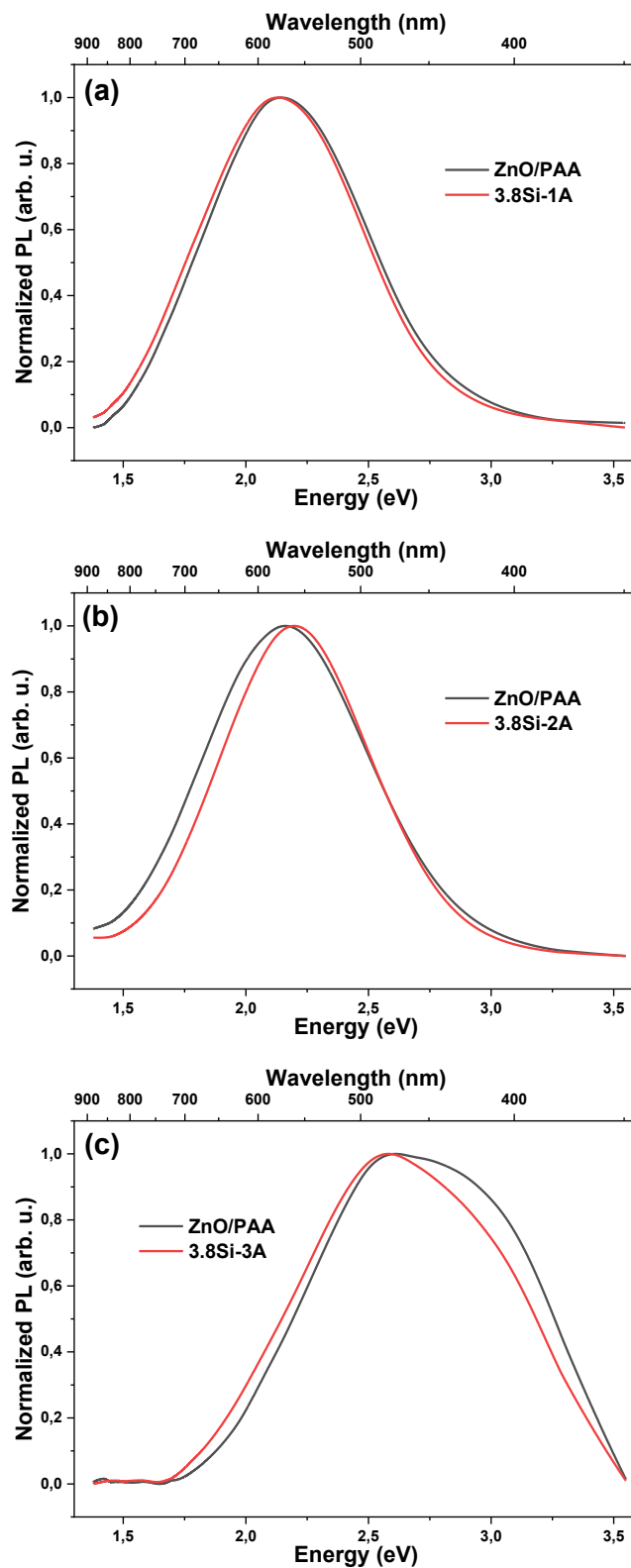


**Figure 4.15** Normalized PL spectra of (a) 3.8Si-1A, (b) 3.8Si-2A, and (c) 3.8 Si-3A, with the spectrum of their respective uncoated ZnO/PAA precursor as the reference.

## 4.3.2.2 Photoluminescence quantum yield

Considering the instability of the uncoated ZnO/PAA nanohybrids synthesized in different batches, it was deemed necessary to analyze the PL QY of the coated samples in comparison with their respective precursor. **Figure 4.16** plots the PL QY improvement of 3.8Si- $y$ A silica-coated ZnO nanohybrids in function of  $\text{NH}_4\text{OH}$  content (represented by  $y$ ). The improvement factor shown in the graph was obtained by comparing the PL QY of each sample with its ZnO/PAA precursor. The PL QY is improved for all the samples after silica coating and the optimal PL QY improvement is obtained for sample 3.8Si-2A, its absolute PL QY reaching up to 64 %.

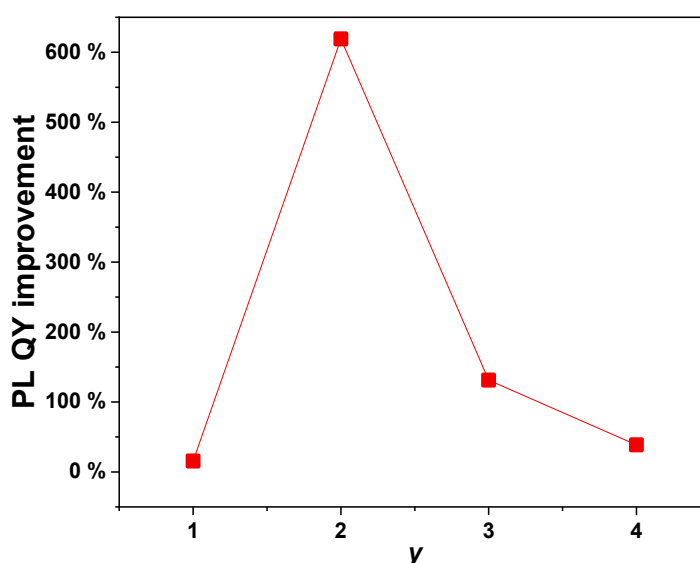


**Figure 4.16** PL QY improvement of 3.8Si- $y$ A silica-coated ZnO nanohybrids compared to their respective uncoated ZnO/PAA precursor in function of the ratio of  $\text{NH}_4\text{OH}$   $y$  in solution A.

When  $y = 1$ , *i.e.*, when the ratio of ammonia in solution A is the nominal ratio, the PL QY is improved from 21.4 % to 24.7 % (by 15.4 %). According to the model in **Figure 4.14** (a), a thin layer of silica shell is present on the surface of the mesospheres at such ammonia ratios. The thin silica coating is beneficial for the PL QY probably due to further passivation of some ZnO nanocrystals by silica coating. When  $y = 2$ , the PL QY is improved from 8.9 % to 64.0 % (by 619 %). In this case, the silica coating is thicker around the mesospheres, according to the model in **Figure 4.14** (b). The PL QY is significantly improved by the silica-coated structure for several possible reasons. First, the mesospheres are still present, which ensures the efficient absorption of the excitation light. Second, the silica coating may protect and strengthen the mesospheres. Last, the silica coating can further passivate the surface states of some ZnO nanocrystals, reducing non-radiative processes. When  $y$  is larger than 2, the PL QY is also improved to some degree, from 5.4 % to 12.4 % (by 130 %) at  $y = 3$  and from 10.7 % to 14.8 % (by 38.3

%) at  $y = 4$ . In these scenarios, some of the mesospheres are degraded, as shown in the model in **Figure 4.14** (c), which can lower the absorption efficiency. Silica coating can also absorb the excitation light before it reaches the ZnO nanocrystals, resulting in a decrease of PL QY improvement.

It is worth noting that sample 3.8Si-1A has a much higher PL QY improvement (by 484 %) in the previous batch, as presented in **Figure 4.8**. One explanation is that the ZnO/PAA precursor of the previous batch has a low initial PL QY of 3.5 %, whereas the precursor here has a much higher PL QY of 21.4 %, which is also higher than that of most other ZnO precursors (see **Figure 4.2**). It can be perceived that the magnitude of PL QY improvement may also depend on the initial PL QY of the precursor.

It can be summarized that silica coating plays an important role in the passivation of the surface states of ZnO nanocrystals, which is the main reason for the improvement of PL QY. However, the PL QY can also be reduced at the same time, due to the absorption of excitation light by the silica coating when it is too thick. The tradeoff between these two effects, as it is determined by the amount of ammonia, is closely related to the integrity of the mesospheres. Therefore, it is tricky business to control the silica coating on the mesospheres in order to obtain an optimal improvement of PL QY.

#### 4.3.2.3 Photoluminescence excitation

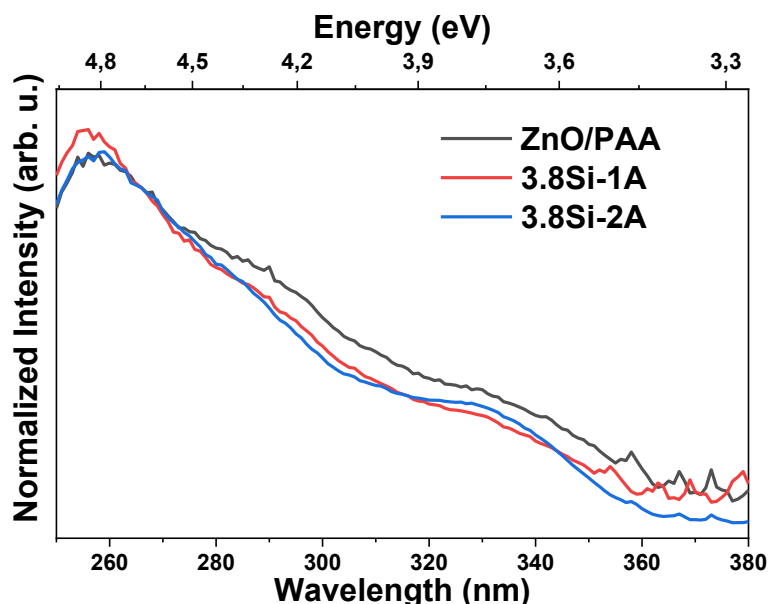


**Figure 4.17** PLE spectra at  $\lambda_{em} = 550$  nm of ZnO/PAA precursor and 3.8Si- $y$ A ( $y = 1$  and 2) samples. The spectra are normalized to the intensity at  $\lambda_{ex} = 266$  nm.

The amount of ammonia clearly has an effect on the emission properties. Therefore, PLE experiments were performed in order to check its effect on the excited states responsible for PL. The results are

presented in **Figure 4.17** for 3.8Si- $y$ A ( $y = 1$  and 2) samples in comparison with the spectrum of the uncoated ZnO/PAA. No modification of the PLE spectra is observed, meaning that no modification of the PL path is induced for such  $\text{NH}_4\text{OH}$  concentrations, in agreement with the PL results in **Figure 4.15**. It is thus confirmed that silica coating does not affect the type of luminescent species in the ZnO nanocrystals.

### 4.3.3 Thermal stability

In the perspective of applying the silica-coated ZnO/PAA nanomaterials in WLED applications, we examined the thermal stability of both coated and uncoated samples. PL spectra were obtained at various temperatures high up to 100 °C, a typical operating temperature in WLEDs. The results are presented in **Figure 4.18**.

It is evident that increasing the temperature of the materials leads to a continuous reduction of the PL intensity. **Figure 4.19** (a) plots the evolution of the maximum PL intensity of the three samples at different temperatures. It can be seen that the maximum intensity decreases linearly as the temperature rises. **Figure 4.19** (b) displays the retention of maximum PL intensity at different temperatures. When the temperature is raised to 100 °C, the maximum PL intensity is reduced to 18 % of the initial value for uncoated ZnO/PAA, while such reduction is only to 34 % for 3.8Si-1A and 32 % for 3.8Si-2A. It can be concluded that the silica-coated samples have to a slightly better tolerance for heat. When the sample is cooled down to 25 °C again, the PL intensity cannot be fully recovered, but to approximately 75 % of the initial value for uncoated ZnO/PAA and 3.8Si-2A, and to 70 % for 3.8Si-1A. What differentiates the three samples is, of course, the absolute value of the PL intensity as seen from **Figure 4.19** (a). Since the PL QY is improved by the silica coating, the intensity of silica-coated samples can retain a relatively high value compared to the uncoated ZnO/PAA. In other words, the detrimental thermal quenching has a reduced impact on the silica-coated ZnO/PAA. Thus, the instability issue of ZnO/PAA nanohybrid is not completely resolved but alleviated by the silica coating.

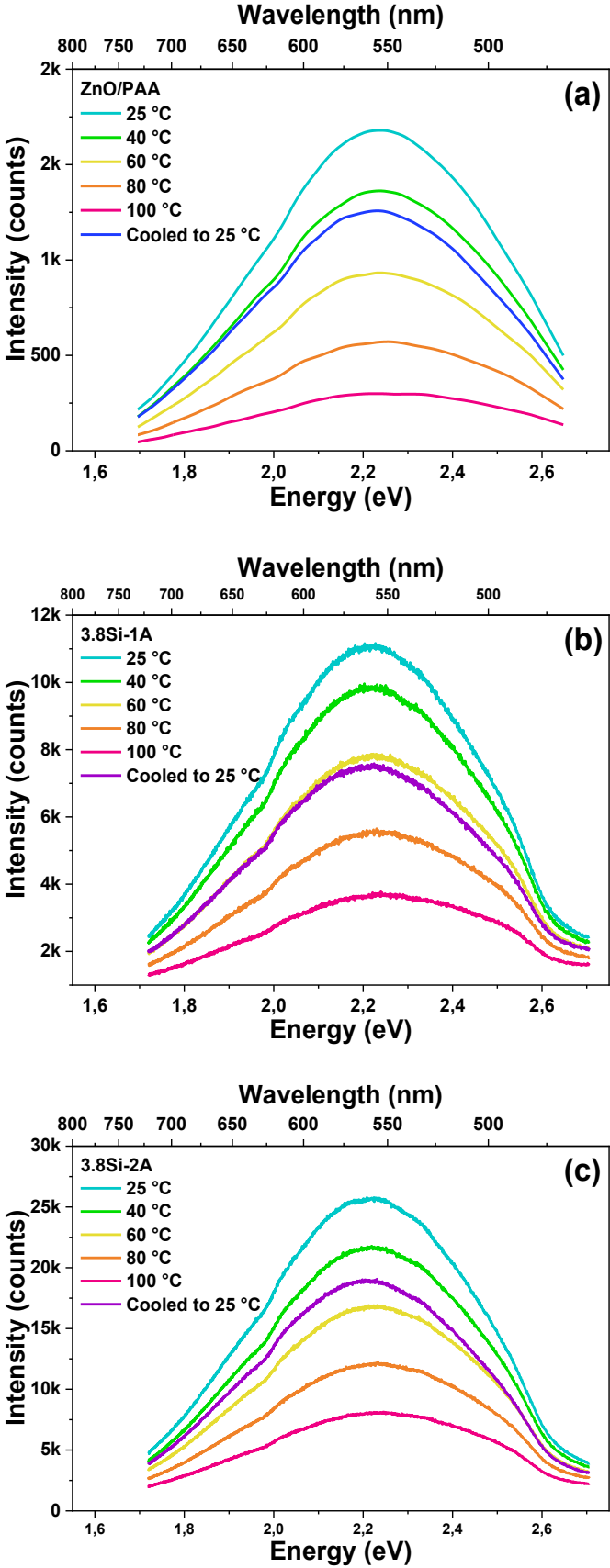
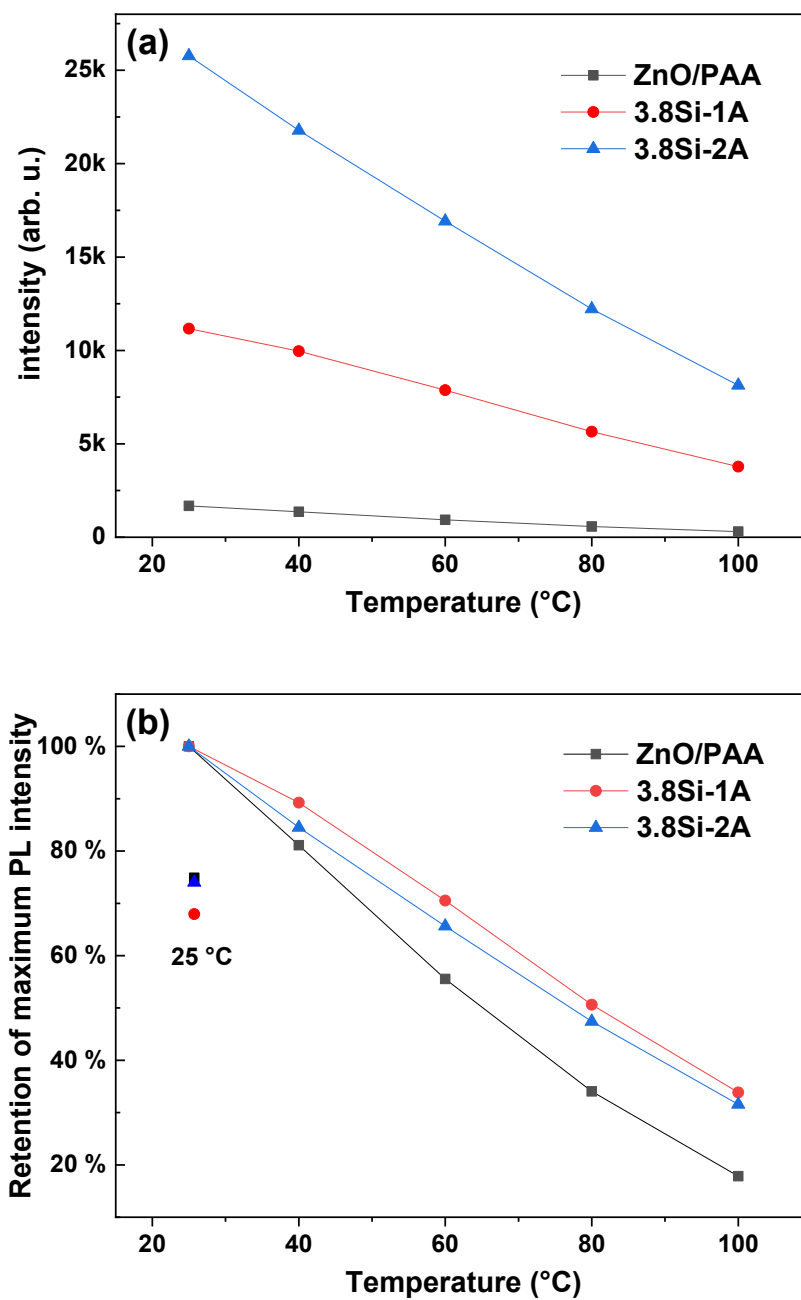


Figure 4.18 PL spectra of (a) ZnO/PAA, (b) 3.8Si-1A and (c) 3.8Si-2A at different temperatures from 25 °C to 100 °C.



**Figure 4.19** Evolution of (a) maximum PL intensity and (b) retention of maximum PL intensity relative to the initial maximum at different temperatures up to 100 °C of uncoated ZnO/PAA, 3.8Si-1A, and 3.8Si-2A. The three points standing alone at 25 °C in (b) represent the retentions of maximum PL intensity after cooling down.

## 4.4 Role of silica coating

In this section, the role of silica coating is discussed, based on the results from the two previous sections. The role of silica coating depends on two correlated parameters that can affect the successful coating of silica, namely the ratio of TEOS to ZnO and the ratio of ammonia in solution A.

Starting with the effect of ammonia in solution A,  $\text{NH}_4\text{OH}$  has a profound effect on the microstructure of ZnO/PAA as it can change the pH of the solution and neutralize protonated PAAH. The model in **Figure 4.14** (c) was proposed to explain the effect of ammonia on the structure of the silica-coated ZnO/PAA nanohybrids. In this model, a high concentration of ammonia can degrade the mesospheres via amination of COOH groups in the PAA chains. The mesospheres then break down into ZnO nanocrystals coated with PAA. The PAA matrix may even be partially removed from ZnO nanocrystals, leading to exposed ZnO nanocrystals that are prone to be directly coated by silica. The extra PAA that no longer forms the mesosphere matrix may subsequently enlarge the crystalline domain of an unassigned phase, as observed from XRD. Eventually, the materials are composed of ZnO nanocrystals coated by both PAA and silica with no mesospheres. The surface states of ZnO nanocrystals are modified and some are passivated by direct silica coating, inducing substantial changes of PL QY (by up to 130 % for our samples).

As established in our previous studies, the mesospheres are beneficial for high PL QY because the excitation light can be sufficiently scattered within the mesospheres. [186], [187] In order to achieve high PL QY, ammonia in solution A has to be kept at an appropriate ratio to prevent the degradation of the mesospheric structure. At this ratio, there is not enough ammonia to destroy the mesospheres. The mesospheric structure can be preserved on the brink of breaking down, as modelled in **Figure 4.14** (b). In other words, the mesospheres are infiltrated by ammonia and barely holding together. However, the silica coating is likely to be formed at the infiltrated locations, where ammonia is present as the catalyst for the hydrolysis of TEOS. As a result, the mesospheres are bound together by silica coating. In the case of our 3.8Si-2A sample, TEM image in **Figure 4.11** (d) shows the mesospheres with rough edges, which is the evidence of infiltration by ammonia. Silica coating therefore not only exists on the surface of the mesospheres, but may also be formed close to the embedded ZnO nanocrystals. ZnO nanocrystals with thin PAA coating may be exposed to direct silica coating, whether inside or outside of the mesospheres. Unembedded ZnO nanocrystals are likely to exist even in samples with a majority of mesospheres. These nanocrystals are inefficient in PL, since their surface states act as quenching centers. Silica coating can help passivate the surface states of these nanocrystals and make them efficient emitters. In short, the silica coating in this model strengthens the mesospheric structure and passivates unembedded nanocrystals, leading to marked improvement in PL QY (by 619 % for our sample).

The model in **Figure 4.14** (a) describes the situation where the amount of ammonia is low. A low ammonia concentration does not significantly affect the integrity of the PAA matrix. Therefore, the mesospheres preserve their structure, while only a thin layer of silica is coated on their surface. In this case, the silica coating has little effect on the structure of the materials, hence little effect on the optical properties as well. It is conceivable that the thickness of silica coating reaches the maximal value under such low ammonia concentration, as suggested by RBS results. This assumption can in turn explain the effect of TEOS ratio to ZnO.

Now coming to the effect of the ratio of TEOS to ZnO. For our  $x\text{Si-1A}$  sample series, the most interesting finding is that the optimal ratio of TEOS to ZnO is at 3.8 among ratios between 1.1 and 10. At smaller TEOS ratios, the formation of silica coating around the mesosphere is expected to be incomplete due to lack of Si source. Therefore, the silica coating does not play a significant role in improving the PL QY of ZnO/PAA nanohybrid. At larger ratios, the resulting silica coating is too thick and it can reach the maximal coating thickness (the thickness “saturates”). In these cases, the thick silica coating absorbs the UV excitation light, preventing it from exciting the ZnO nanocrystals embedded in the PAA mesospheres. Consequently, a bigger fraction of excitation light is inefficiently absorbed, leading to a decrease of PL QY improvement. At the optimal TEOS ratio with a fixed amount of ammonia, a balance is reached between a beneficial protecting and passivating effect of the silica shell and a detrimental effect of its excess absorption of the UV light.

Finally, despite the best samples being 3.8Si-2A in the present study, this combination of TEOS ratio and ammonia ratio is not necessarily the general optimum for silica coating, since these two parameters are highly dependent. The ideal case is presented in **Figure 4.14** (b) without unembedded ZnO nanocrystals from degraded mesospheres. As seen in **Figure 4.11** (d), such ideal is probably not achieved for 3.8Si-2A, since unembedded ZnO nanocrystals are present, which could result from the degradation of mesospheres. Therefore, more research is required to further improve the PL QY and thermal stability of ZnO/PAA nanohybrids and the interaction between PAA and ammonia still needs to be better understood.

## 4.5 Conclusion

In this chapter, we presented a structural and optical study of silica-coated ZnO/PAA nanohybrids. The coating process was carried out after hydrolysis synthesis of ZnO, with TEOS as the coating agent and a solution (solution A) containing ammonia to modify the pH. The study was focused on the role of silica coating in two aspects, namely the effect of TEOS to ZnO weight ratio and the effect of ammonia ratio in solution A.

The effect of TEOS ratio was studied first under the same ratio of ammonia in sample series  $x\text{Si-1A}$ . The coating process did not change the crystallographic structure of ZnO, although an unassigned phase related to PAA was observed from XRD for all the samples. The unassigned phase may be related to the thermal instability of the materials. At the nominal ratio of ammonia in solution A, the difference in TEOS ratio has no effect on the PL spectra but only on the PL QY. An optimal ratio of TEOS to ZnO was found at 3.8. Smaller ratios lead to incomplete thin coating, which does not significantly improve the PL QY. Larger ratios lead to thick coating that absorbs the UV excitation and inhibits the UV light from reaching ZnO nanocrystals, which can even reduce the PL QY.

The results above led to the study of the effect of ammonia ratio in solution A through a new sample series  $3.8\text{Si-}y\text{A}$  under the same TEOS ratio of 3.8. Different concentrations of ammonia do not change the crystallographic structure of ZnO either, but the diffracting size of the unassigned phase increases with the increasing amount of ammonia, indicating a certain interaction between  $\text{NH}_4\text{OH}$  and the PAA matrix. TEM images revealed that the PAA mesospheric structure was compromised by high concentration of  $\text{NH}_4\text{OH}$ . A model was proposed to explain the effect of ammonia ratio based on the amination of COOH groups in the PAA chains. At low ammonia ratios, the silica coating is a thin shell on the surface of the PAA matrix and it does not significantly improve PL QY, in accordance with the results from  $x\text{Si-1A}$  samples. At high ammonia ratios, the mesospheres are destroyed and some of the resulted ZnO nanocrystals with thin PAA coating are partially coated by silica. An optimal ratio of ammonia is found at  $y = 2$ , where mesospheres are preserved and strengthened by the silica coating on the surface and possibly at locations infiltrated by ammonia, while unembedded ZnO nanocrystals are passivated by silica coating. The PL spectra are not modified by silica coating, regardless of the ammonia ratio, but the PL QY can be substantially improved at the optimal ammonia ratio.

Finally, the  $3.8\text{Si-2A}$  does not necessarily represent the general optimal combination of TEOS to ZnO ratio and ammonia ratio. The thermal stability is improved but the instability issue of ZnO/PAA nanohybrid is not completely eliminated by silica coating. More research is required to better understand the interaction between  $\text{NH}_4\text{OH}$  and PAA, in order to produce the optimal silica coating and further improve the optical properties and thermal stability of the material.



## General Conclusions

The thesis presented the studies on ZnO nanocrystals embedded in polyacrylic acid (PAA) mesospheres as a potential substitute for rare-earth-based phosphors in white light-emitting diodes (WLEDs). Two notable optical properties, namely photoluminescence (PL) and photoluminescence quantum yield (PL QY), were considered the key parameters to evaluate the applicability of the materials in WLEDs. PL spectrum of the ZnO/PAA nanohybrid was tuned by doping metal elements, and the PL QY was enhanced by silica coating. The effect of doping and the effect of silica coating were investigated independently in two studies.

In the first study, metal-doped ZnO nanohybrids were synthesized via hydrolysis at three distinct doping concentrations, namely atomic ratios of 0.1 %, 1 %, and 5 %. The majority of doped nanohybrids were confirmed to comprise ZnO nanocrystals embedded in PAA mesospheres by structural analyses (XRD, TEM, and FTIR). Dopants of different nature were successfully incorporated into the nanohybrid, as confirmed by elemental studies (RBS and EDX) on 5 % doping samples and XRD on calcinated samples. The effect of doping is twofold: during the hydrolysis and in the nanohybrid.

The presence of dopant precursor during the hydrolysis does not change the wurtzite structure of the ZnO nanocrystals; however, it can affect the presence of the mesospheres by interacting with PAA chains. The presence of mesospheres can determine the PL QY. The mesospheres are degraded by doping ions with a larger ionic radius than  $\text{Zn}^{2+}$ . Large doping concentrations can induce larger mesospheres and ZnO nanocrystals outside of the mesospheres. Doping concentration also affects the size of the ZnO nanocrystals, although no clear trend can be drawn for all the dopants.

The dopant ions incorporated into the ZnO crystal lattice can modify the PL spectrum of the nanohybrid by introducing energy levels in the bandgap of ZnO, which are usually non-radiative. The undoped ZnO nanohybrid exhibits a broad visible emission with a weak UV emission in the PL spectrum. The incorporation of the dopants induces redshifts of the emission peak and quenches the UV emission in most cases. Considering all the studied dopants and concentrations, the emission peak can be tuned between 2.46 eV and 2.08 eV. The PL QY is reduced for most doped samples, because the dopants introduce non-radiative energy levels, quenching both visible and UV emissions. However, the PL QY can be improved for dopants with a small ionic radius and at a low doping concentration of 0.1 %. The emission peak can be tuned between 2.46 eV and 2.17 eV without degrading PL QY.

In the second study, silica-coated ZnO nanohybrids were synthesized with ZnO/PAA nanohybrid as the precursor, tetraethyl orthosilicate (TEOS) as the coating agent, and ammonia as the pH modifier and catalyst for TEOS hydrolysis. ZnO nanocrystals retained the wurtzite structure after the coating process. The incorporation of amorphous silica coating was confirmed by various techniques (TEM, EDX, RBS, and FTIR), although the stoichiometry of silica could not be determined. An unassigned phase related

to PAA was discovered by XRD and its presence proved to be related to the amount of ammonia. The integrity of the mesospheres could be compromised by the coating process, as the COOH groups in the PAA chains were aminated by ammonia.

Silica coating did not significantly modify the PL spectrum of the ZnO/PAA nanohybrid precursor regardless of the coating conditions, but it improved the PL QY by different extents under different coating conditions. A referential sample synthesized without TEOS proved that ammonia was not responsible for PL QY improvement. An optimal PL QY improvement of 619 % was achieved for a mass ratio of TEOS to Zn/PAA at 3.8 and ammonia at twice the nominal ratio. The effect of silica coating is closely related to the ratio of TEOS and the amount of ammonia, which collectively determine the integrity of the mesospheres and the thickness of silica coating, which in turn determines the PL QY improvement.

The effect of silica coating on ZnO/PAA nanohybrid can be explained by a structure model describing the evolution of mesospheres as a result of the coating process. At a fixed TEOS ratio, a low ratio of ammonia leads to a thin silica coating on the surface of PAA mesospheres, due to the low extent of amination of COOH groups and the low rate of TEOS hydrolysis. A high ratio of ammonia results in the degradation of mesospheres and thick silica matrix. The optimal ratio of ammonia (twice the nominal ratio in this study) leads to a silica coating with an appropriate thickness on the surface of the mesospheres that are protected and strengthened. The PL QY is significantly improved in this case because of further passivation of the surface states of ZnO nanocrystals, preservation of mesospheres, and low absorption of excitation light by silica. At a fixed ratio of ammonia (nominal ratio in this study), the ratio of TEOS determines the thickness of the silica coating while the integrity of the mesospheres is not affected. The PL QY can be improved the most when the optimal silica coating protects the mesospheres and does not absorb too much of excitation light.

Finally, the thermal stability of the nanohybrids was examined at temperatures up to 100 °C to simulate the operating condition of WLEDs. Both metal-doped and silica-coated ZnO/PAA nanohybrids showed gradual decrease of emission intensity as the temperature increased from room temperature to 100 °C. The thermal instability of the materials may be related to the trapped solvent molecules (such as water and ethanol). The thermal quenching effect is reduced for silica-coated samples due to the protection of silica and the drastic improvement of PL QY. The issue is alleviated but not eliminated by silica coating and more research is required to further improve the thermal stability of the nanohybrids.

---

## References

- [1] J. Y. Tsao and P. Waide, “The World’s Appetite for Light: Empirical Data and Trends Spanning Three Centuries and Six Continents,” *LEUKOS*, vol. 6, no. 4, pp. 259–281, Apr. 2010, doi: 10.1582/LEUKOS.2010.06.04001.
- [2] S. Nakamura, T. Mukai, and M. Senoh, “Candela-class high-brightness InGaN/AlGaN double-heterostructure blue-light-emitting diodes,” *Appl. Phys. Lett.*, vol. 64, no. 13, pp. 1687–1689, Mar. 1994, doi: 10.1063/1.111832.
- [3] H. Amano, M. Kito, K. Hiramatsu, and I. Akasaki, “P-Type Conduction in Mg-Doped GaN Treated with Low-Energy Electron Beam Irradiation (LEEBI),” *Jpn. J. Appl. Phys.*, vol. 28, no. Part 2, No. 12, pp. L2112–L2114, Dec. 1989, doi: 10.1143/JJAP.28.L2112.
- [4] “TheLEDFuture.” <https://regions20.org/wp-content/uploads/2016/08/TheLEDFuture.pdf>.
- [5] Y. Nanishi, “The birth of the blue LED,” *Nat. Photonics*, vol. 8, no. 12, pp. 884–886, Dec. 2014, doi: 10.1038/nphoton.2014.291.
- [6] S. Nakamura, M. Senoh, N. Iwasa, S. Nagahama, T. Yamada, and T. Mukai, “Superbright Green InGaN Single-Quantum-Well-Structure Light-Emitting Diodes,” *Jpn. J. Appl. Phys.*, vol. 34, no. Part 2, No. 10B, pp. L1332–L1335, Oct. 1995, doi: 10.1143/JJAP.34.L1332.
- [7] P. Pust, P. J. Schmidt, and W. Schnick, “A revolution in lighting,” *Nat. Mater.*, vol. 14, no. 5, pp. 454–458, May 2015, doi: 10.1038/nmat4270.
- [8] A. A. Setlur *et al.*, “Ce<sup>3+</sup>-based phosphors for blue LED excitation,” presented at the Optical Science and Technology, SPIE’s 48th Annual Meeting, San Diego, California, USA, Jan. 2004, p. 142, doi: 10.1117/12.529127.
- [9] L. Wang, R.-J. Xie, T. Suehiro, T. Takeda, and N. Hirosaki, “Down-Conversion Nitride Materials for Solid State Lighting: Recent Advances and Perspectives,” *Chem. Rev.*, vol. 118, no. 4, pp. 1951–2009, Feb. 2018, doi: 10.1021/acs.chemrev.7b00284.
- [10] T. Matsuzawa, “A New Long Phosphorescent Phosphor with High Brightness, SrAl<sub>2</sub>O<sub>4</sub>:Eu<sup>2+</sup>,Dy<sup>3+</sup>,” *J. Electrochem. Soc.*, vol. 143, no. 8, p. 2670, 1996, doi: 10.1149/1.1837067.
- [11] K. Van den Eeckhout, P. F. Smet, & D. Poelman, “Persistent Luminescence in Eu<sup>2+</sup>-Doped Compounds: A Review,” *Materials*, vol. 3, no. 4, pp. 2536–2566, 2010, doi: 10.3390/ma3042536.
- [12] P. Pust *et al.*, “Narrow-band red-emitting Sr[LiAl<sub>3</sub>N<sub>4</sub>]:Eu<sup>2+</sup> as a next-generation LED-phosphor material,” *Nat. Mater.*, vol. 13, no. 9, pp. 891–896, Sep. 2014, doi: 10.1038/nmat4012.
- [13] P.-P. Dai *et al.*, “A single Eu<sup>2+</sup>-activated high-color-rendering oxychloride white-light phosphor for white-light-emitting diodes,” *Light Sci. Appl.*, vol. 5, no. 2, pp. e16024–e16024, Feb. 2016, doi: 10.1038/lsa.2016.24.
- [14] X. Li *et al.*, “New yellow Ba<sub>0.93</sub>Eu<sub>0.07</sub>Al<sub>2</sub>O<sub>4</sub> phosphor for warm-white light-emitting diodes through single-emitting-center conversion,” *Light Sci. Appl.*, vol. 2, no. 1, pp. e50–e50, Jan. 2013, doi: 10.1038/lsa.2013.6.
- [15] M. Janulevicius *et al.*, “Luminescence and luminescence quenching of highly efficient Y<sub>2</sub>Mo<sub>4</sub>O<sub>15</sub>:Eu<sup>3+</sup> phosphors and ceramics,” *Sci. Rep.*, vol. 6, no. 1, p. 26098, Sep. 2016, doi: 10.1038/srep26098.
- [16] G. Blasse and A. Bril, “Investigation of Some Ce<sup>3+</sup>-Activated Phosphors,” *J. Chem. Phys.*, vol. 47, no. 12, pp. 5139–5145, Dec. 1967, doi: 10.1063/1.1701771.

- [17] B. Yan, "Rare Earth, Rare Earth Luminescence, Luminescent Rare Earth Compounds, and Photofunctional Rare Earth Hybrid Materials," in *Photofunctional Rare Earth Hybrid Materials*, vol. 251, Singapore: Springer Singapore, 2017, pp. 3–21, doi: 10.1007/978-981-10-2957-8\_1.
- [18] F. Xiao, Y. N. Xue, Y. Y. Ma, and Q. Y. Zhang, "Ba<sub>2</sub>Ca(B<sub>3</sub>O<sub>6</sub>)<sub>2</sub>:Eu<sup>2+</sup>,Mn<sup>2+</sup>: A potential tunable blue–white–red phosphors for white light-emitting diodes," *Phys. B Condens. Matter*, vol. 405, no. 3, pp. 891–895, Feb. 2010, doi: 10.1016/j.physb.2009.10.009.
- [19] C.-H. Huang and T.-M. Chen, "Ca<sub>9</sub>La(PO<sub>4</sub>)<sub>7</sub>:Eu<sup>2+</sup>,Mn<sup>2+</sup>: an emission-tunable phosphor through efficient energy transfer for white light-emitting diodes," *Opt. Express*, vol. 18, no. 5, p. 5089, Mar. 2010, doi: 10.1364/OE.18.005089.
- [20] W.-J. Yang and T.-M. Chen, "White-light generation and energy transfer in SrZn<sub>2</sub>(PO<sub>4</sub>)<sub>2</sub>:Eu,Mn phosphor for ultraviolet light-emitting diodes," *Appl Phys Lett*, vol 88, no. 10, p.101903, Mar. 2006, doi: 10.1063/1.2182026.
- [21] J. Hou *et al.*, "White-light-emitting from single-phased (Ca,Eu,Mn)<sub>9</sub>Al(PO<sub>4</sub>)<sub>7</sub> phosphor with blue-white-yellow tunable luminescence properties for UV-based LEDs," *Mater. Technol.*, vol. 34, no. 3, pp. 135–142, Feb. 2019, doi: 10.1080/10667857.2018.1540331.
- [22] C. Guo, L. Luan, Y. Xu, F. Gao, and L. Liang, "White Light-Generation Phosphor Ba<sub>2</sub>Ca(BO<sub>3</sub>)<sub>2</sub>:Ce<sup>3+</sup>, Mn<sup>2+</sup> for Light-Emitting Diodes," *J. Electrochem. Soc.*, vol. 155, no. 11, pp. J310–314, 2008, doi: 10.1149/1.2976215.
- [23] V. Sivakumar and U. V. Varadaraju, "Eu<sup>2+</sup>, Ce<sup>3+</sup> Luminescence and Ce<sup>3+</sup>→Eu<sup>2+</sup> Energy-Transfer Studies on Sr<sub>2</sub>LiSiO<sub>4</sub>F: A White Light-Emitting Phosphor," *J. Electrochem. Soc.*, vol. 156, no. 7, pp. J179–J184, 2009, doi: 10.1149/1.3122663.
- [24] C. Guo, L. Luan, F. G. Shi, and X. Ding, "White-Emitting Phosphor Ca<sub>2</sub>BO<sub>3</sub>Cl:Ce<sup>3+</sup>, Eu<sup>2+</sup> for UV Light-Emitting Diodes," *J. Electrochem. Soc.*, vol. 156, no. 6, pp. J125–J128, doi: 10.1149/1.3106039.
- [25] C.-K. Chang and T.-M. Chen, "Sr<sub>3</sub>B<sub>2</sub>O<sub>6</sub>:Ce<sup>3+</sup>,Eu<sup>2+</sup>: A potential single-phased white-emitting borate phosphor for ultraviolet light-emitting diodes," *Appl. Phys. Lett.*, vol. 91, no. 8, p. 081902, Aug. 2007, doi: 10.1063/1.2772195.
- [26] Y. Song, G. Jia, M. Yang, Y. Huang, H. You, and H. Zhang, "Sr<sub>3</sub>Al<sub>2</sub>O<sub>5</sub>Cl<sub>2</sub>:Ce<sup>3+</sup>,Eu<sup>2+</sup>: A potential tunable yellow-to-white-emitting phosphor for ultraviolet light emitting diodes," *Appl. Phys. Lett.*, vol. 94, no. 9, p. 091902, Mar. 2009, doi: 10.1063/1.3094753.
- [27] F. Xiao, Y. N. Xue, and Q. Y. Zhang, "Warm white light from Y<sub>4</sub>MgSi<sub>3</sub>O<sub>13</sub>:Bi<sup>3+</sup>,Eu<sup>3+</sup> nanophosphor for white light-emitting diodes," *Spectrochim. Acta. A. Mol. Biomol. Spectrosc.*, vol. 74, no. 2, pp. 498–501, Oct. 2009, doi: 10.1016/j.saa.2009.06.050.
- [28] H. Jiao and Y. Wang, "Ca<sub>2</sub>Al<sub>2</sub>SiO<sub>7</sub>:Ce<sup>3+</sup>, Tb<sup>3+</sup>: A White-Light Phosphor Suitable for White-Light-Emitting Diodes," *J. Electrochem. Soc.*, vol. 156, no. 5, pp. J117–J120, 2009, doi: 10.1149/1.3097191.
- [29] Y. Pan, M. Wu, and Q. Su, "Tailored photoluminescence of YAG:Ce phosphor through various methods," *J. Phys. Chem. Solids*, vol. 65, no. 5, pp. 845–850, May 2004, doi: 10.1016/j.jpcs.2003.08.018.
- [30] J. L. Wu, G. Gundiah, and A. K. Cheetham, "Structure–property correlations in Ce-doped garnet phosphors for use in solid state lighting," *Chem. Phys. Lett.*, vol. 441, no. 4–6, pp. 250–254, Jun. 2007, doi: 10.1016/j.cplett.2007.05.023.
- [31] P. Dorenbos, "The 5d level positions of the trivalent lanthanides in inorganic compounds," *J. Lumin.*, vol. 91, no. 3–4, pp. 155–176, Nov. 2000, doi: 10.1016/S0022-2313(00)00229-5.
- [32] P. Dorenbos, "Crystal field splitting of lanthanide 4f<sup>n</sup>-5d-levels in inorganic compounds," *J. Alloys Compd.*, vol. 341, no. 1-2, pp. 156–159, Feb. 2002, doi: 10.1016/S0925-8388(02)00056-7.

- [33] V. Bachmann, C. Ronda, and A. Meijerink, "Temperature Quenching of Yellow Ce<sup>3+</sup> Luminescence in YAG:Ce," *Chem. Mater.*, vol. 21, no. 10, pp. 2077–2084, May 2009, doi: 10.1021/cm8030768.
- [34] S. Ye, F. Xiao, Y. X. Pan, Y. Y. Ma, and Q. Y. Zhang, "Phosphors in phosphor-converted white light-emitting diodes: Recent advances in materials, techniques and properties," *Mater. Sci. Eng. R Rep.*, vol. 71, no. 1, pp. 1–34, Dec. 2010, doi: 10.1016/j.mser.2010.07.001.
- [35] L. Kong, S.C. Gan, G.Y. Hong, and J.L. ZHANG, "Luminescence Properties of YAG:Ce Co-doped with Pr<sup>3+</sup> or Sm<sup>3+</sup>," *Chinese Journal of Luminescence*, vol. 28, no. 3, p. 393, 2007.
- [36] L. KONG, S.C. GAN, G.Y. HONG, H.P YOU, and J.L. ZHANG, "Effects of Doping Lanthanide Ions in YAG:Ce System on the Spectral Properties of Ce<sup>3+</sup>," *Chemical Journal of Chinese Universities*, vol. 4, pp. 27–30, 2008.
- [37] W. Wang, J. Tang, S. T. (Victor) Hsu, J. Wang, and B. P. Sullivan, "Energy transfer and enriched emission spectrum in Cr and Ce co-doped Y<sub>3</sub>Al<sub>5</sub>O<sub>12</sub> yellow phosphors," *Chem. Phys. Lett.*, vol. 457, no. 1–3, pp. 103–105, May 2008, doi: 10.1016/j.cplett.2008.04.001.
- [38] H. S. Jang, W. B. Im, D. C. Lee, D. Y. Jeon, and S. S. Kim, "Enhancement of red spectral emission intensity of Y<sub>3</sub>Al<sub>5</sub>O<sub>12</sub>:Ce<sup>3+</sup> phosphor via Pr co-doping and Tb substitution for the application to white LEDs," *J. Lumin.*, vol. 126, no. 2, pp. 371–377, Oct. 2007, doi: 10.1016/j.jlumin.2006.08.093.
- [39] A. A. Setlur, W. J. Heward, M. E. Hannah, and U. Happek, "Incorporation of Si<sup>4+</sup>-N<sup>3-</sup> into Ce<sup>3+</sup>-Doped Garnets for Warm White LED Phosphors," *Chem. Mater.*, vol. 20, no. 19, pp. 6277–6283, Oct. 2008, doi: 10.1021/cm801732d.
- [40] Z. Xia, Z. Xu, M. Chen, and Q. Liu, "Recent developments in the new inorganic solid-state LED phosphors," *Dalton Trans.*, vol. 45, no. 28, pp. 11214–11232, 2016, doi: 10.1039/C6DT01230B.
- [41] Y.-C. Lin, M. Karlsson, and M. Bettinelli, "Inorganic Phosphor Materials for Lighting," *Top. Curr. Chem.*, vol. 374, no. 2, p. 21, Apr. 2016, doi: 10.1007/s41061-016-0023-5.
- [42] C. C. Lin and R.-S. Liu, "Advances in Phosphors for Light-emitting Diodes," *J. Phys. Chem. Lett.*, vol. 2, no. 11, pp. 1268–1277, Jun. 2011, doi: 10.1021/jz2002452.
- [43] R.-J. Xie and N. Hirosaki, "Silicon-based oxynitride and nitride phosphors for white LEDs—A review," *Sci. Technol. Adv. Mater.*, vol. 8, no. 7–8, pp. 588–600, Jan. 2007, doi: 10.1016/j.stam.2007.08.005.
- [44] Y. H. Kim, N. S. M. Viswanath, S. Unithrattil, H. J. Kim, and W. B. Im, "Review—Phosphor Plates for High-Power LED Applications: Challenges and Opportunities toward Perfect Lighting," *ECS J. Solid State Sci. Technol.*, vol. 7, no. 1, pp. R3134–R3147, 2018, doi: 10.1149/2.0181801jss.
- [45] L. K. Bharat, S.-K. Jeon, K. G. Krishna, and J. S. Yu, "Rare-earth free self-luminescent Ca<sub>2</sub>KZn<sub>2</sub>(VO<sub>4</sub>)<sub>3</sub> phosphors for intense white light-emitting diodes," *Sci. Rep.*, vol. 7, no. 1, p. 42348, Mar. 2017, doi: 10.1038/srep42348.
- [46] Y. K. Mishra *et al.*, "Direct Growth of Freestanding ZnO Tetrapod Networks for Multifunctional Applications in Photocatalysis, UV Photodetection, and Gas Sensing," *ACS Appl. Mater. Interfaces*, vol. 7, no. 26, pp. 14303–14316, Jul. 2015, doi: 10.1021/acsami.5b02816.
- [47] D.-Y. Guo, C.-X. Shan, S.-N. Qu, and D.-Z. Shen, "Highly Sensitive Ultraviolet Photodetectors Fabricated from ZnO Quantum Dots/Carbon Nanodots Hybrid Films," *Sci. Rep.*, vol. 4, no. 1, p. 7469, May 2015, doi: 10.1038/srep07469.
- [48] D. Gedamu *et al.*, "Rapid Fabrication Technique for Interpenetrated ZnO Nanotetrapod Networks for Fast UV Sensors," *Adv. Mater.*, vol. 26, no. 10, pp. 1541–1550, Mar. 2014, doi: 10.1002/adma.201304363.

- [49] V. Kumar, R. G. Singh, F. Singh, and L. P. Purohit, "Highly transparent and conducting boron doped zinc oxide films for window of Dye Sensitized Solar Cell applications," *J. Alloys Compd.*, vol. 544, pp. 120–124, Dec. 2012, doi: 10.1016/j.jallcom.2012.07.124.
- [50] J. Huang, Z. Yin, and Q. Zheng, "Applications of ZnO in organic and hybrid solar cells," *Energy Environ. Sci.*, vol. 4, no. 10, p. 3861, 2011, doi: 10.1039/c1ee01873f.
- [51] V. Kumar *et al.*, "Doped zinc oxide window layers for dye sensitized solar cells," *J. Appl. Phys.*, vol. 114, no. 13, p. 134506, Oct. 2013, doi: 10.1063/1.4824363.
- [52] K. K. Naik *et al.*, "Field emission properties of ZnO nanosheet arrays," *Appl. Phys. Lett.*, vol. 105, no. 23, p. 233101, Dec. 2014, doi: 10.1063/1.4903271.
- [53] Z. Q. Zheng, J. D. Yao, B. Wang, and G. W. Yang, "Light-controlling, flexible and transparent ethanol gas sensor based on ZnO nanoparticles for wearable devices," *Sci. Rep.*, vol. 5, no. 1, p. 11070, Sep. 2015, doi: 10.1038/srep11070.
- [54] S. Tian, F. Yang, D. Zeng, and C. Xie, "Solution-Processed Gas Sensors Based on ZnO Nanorods Array with an Exposed (0001) Facet for Enhanced Gas-Sensing Properties," *J. Phys. Chem. C*, vol. 116, no. 19, pp. 10586–10591, May 2012, doi: 10.1021/jp2123778.
- [55] A. Janotti and C. G. Van de Walle, "Fundamentals of zinc oxide as a semiconductor," *Rep. Prog. Phys.*, vol. 72, no. 12, p. 126501, Dec. 2009, doi: 10.1088/0034-4885/72/12/126501.
- [56] F. H. Nicoll, "ULTRAVIOLET ZnO LASER PUMPED BY AN ELECTRON BEAM," *Appl. Phys. Lett.*, vol. 9, no. 1, pp. 13–15, Jul. 1966, doi: 10.1063/1.1754578.
- [57] C. Klingshirn, "The Luminescence of ZnO under High One- and Two-Quantum Excitation," *Phys. Status Solidi B*, vol. 71, no. 2, pp. 547–556, Oct. 1975, doi: 10.1002/pssb.2220710216.
- [58] J. M. Hvam, "Exciton-exciton interaction and laser emission in high-purity ZnO," *Solid State Commun.*, vol. 12, no. 2, pp. 95–97, Jan. 1973, doi: 10.1016/0038-1098(73)90513-9.
- [59] J.M. Hvam, "Temperature-induced wavelength shift of electron-beam-pumped lasers from CdSe, CdS, and ZnO," *Physical review B*, vol. 4, no.12, p.4459. Dec. 1971, doi: <https://doi.org/10.1103/PhysRevB.4.4459>.
- [60] D. M. Bagnall, Y. F. Chen, Z. Zhu, T. Yao, M. Y. Shen, and T. Goto, "High temperature excitonic stimulated emission from ZnO epitaxial layers," *Appl. Phys. Lett.*, vol. 73, no. 8, pp. 1038–1040, Aug. 1998, doi: 10.1063/1.122077.
- [61] A. Ohtomo *et al.*, "Room temperature ultraviolet laser emission from ZnO nanocrystal thin films grown by laser MBE," *Mater. Sci. Eng. B*, vol. 54, no. 1–2, pp. 24–28, Jun. 1998, doi: 10.1016/S0921-5107(98)00120-2.
- [62] Z. K. Tang *et al.*, "Room-temperature ultraviolet laser emission from self-assembled ZnO microcrystallite thin films," *Appl. Phys. Lett.*, vol. 72, no. 25, pp. 3270–3272, Jun. 1998, doi: 10.1063/1.121620.
- [63] D.C. Reynolds, D.C. Look and B. Jogai, "Optically pumped ultraviolet lasing from ZnO," *Solid State Communications*, vol. 99, no.12, pp.873-875, Feb. 1996, doi: 10.1016/0038-1098(96)00340-7.
- [64] B. J. Jin, S. Im, and S. Y. Lee, "Violet and UV luminescence emitted from ZnO thins grown on sapphire by pulsed laser deposition," *Thin Solid Films*, vol. 363, no. 1–2, pp. 107–110, May. 2000, doi: 10.1016/S0040-6090(00)00746-X.
- [65] Y. Chen, D. Bagnall, and T. Yao, "ZnO as a novel photonic material for the UV region," *Mater. Sci. Eng. B*, vol. 75, no. 2–3, pp. 190–198, Jun. 2000, doi: 10.1016/S0921-5107(00)00372-X.
- [66] Ü. Özgür *et al.*, "A comprehensive review of ZnO materials and devices," *J. Appl. Phys.*, vol. 98, no. 4, p. 041301, Aug. 2005, doi: 10.1063/1.1992666.

- [67] A. Teke *et al.*, “Excitonic fine structure and recombination dynamics in single-crystalline ZnO,” *Phys. Rev. B*, vol. 70, no. 19, p. 195207, Nov. 2004, doi: 10.1103/PhysRevB.70.195207.
- [68] D. C. Reynolds, D. C. Look, B. Jogai, C. W. Litton, G. Cantwell, and W. C. Harsch, “Valence-band ordering in ZnO,” *Phys. Rev. B*, vol. 60, no. 4, pp. 2340–2344, Jul. 1999, doi: 10.1103/PhysRevB.60.2340.
- [69] D. C. Reynolds, D. C. Look, B. Jogai, and T. C. Collins, “Polariton and free-exciton-like photoluminescence in ZnO,” *Appl. Phys. Lett.*, vol. 79, no. 23, pp. 3794–3796, Dec. 2001, doi: 10.1063/1.1412435.
- [70] D. W. Hamby, D. A. Lucca, M. J. Klopstein, and G. Cantwell, “Temperature dependent exciton photoluminescence of bulk ZnO,” *J. Appl. Phys.*, vol. 93, no. 6, pp. 3214–3217, Mar. 2003, doi: 10.1063/1.1545157.
- [71] J. F. Muth, R. M. Kolbas, A. K. Sharma, S. Oktyabrsky, and J. Narayan, “Excitonic structure and absorption coefficient measurements of ZnO single crystal epitaxial films deposited by pulsed laser deposition,” *J. Appl. Phys.*, vol. 85, no. 11, pp. 7884–7887, Jun. 1999, doi: 10.1063/1.370601.
- [72] S. F. Chichibu, T. Sota, G. Cantwell, D. B. Eason, and C. W. Litton, “Polarized photoreflectance spectra of excitonic polaritons in a ZnO single crystal,” *J. Appl. Phys.*, vol. 93, no. 1, pp. 756–758, Jan. 2003, doi: 10.1063/1.1527707.
- [73] Y. S. Park, C. W. Litton, T. C. Collins, and D. C. Reynolds, “Exciton Spectrum of ZnO,” *Phys. Rev.*, vol. 143, no. 2, pp. 512–519, Mar. 1966, doi: 10.1103/PhysRev.143.512.
- [74] D. G. Thomas, “The exciton spectrum of zinc oxide,” *J. Phys. Chem. Solids*, vol. 15, no. 1–2, pp. 86–96, Aug. 1960, doi: 10.1016/0022-3697(60)90104-9.
- [75] W. Y. Liang and A. D. Yoffe, “Transmission Spectra of ZnO Single Crystals,” *Phys. Rev. Lett.*, vol. 20, no. 2, pp. 59–62, Jan. 1968, doi: 10.1103/PhysRevLett.20.59.
- [76] H. Cao, Y. G. Zhao, S. T. Ho, E. W. Seelig, Q. H. Wang, and R. P. H. Chang, “Random Laser Action in Semiconductor Powder,” *Phys. Rev. Lett.*, vol. 82, no. 11, pp. 2278–2281, Mar. 1999, doi: 10.1103/PhysRevLett.82.2278.
- [77] T. Makino, Y. Segawa, M. Kawasaki, and H. Koinuma, “Optical properties of excitons in ZnO-based quantum well heterostructures,” *Semicond. Sci. Technol.*, vol. 20, no. 4, pp. S78–S91, Apr. 2005, doi: 10.1088/0268-1242/20/4/010.
- [78] A. Janotti and C. G. Van de Walle, “Native point defects in ZnO,” *Phys. Rev. B*, vol. 76, no. 16, Oct. 2007, doi: 10.1103/PhysRevB.76.165202.
- [79] M. Willander *et al.*, “Luminescence from Zinc Oxide Nanostructures and Polymers and their Hybrid Devices,” *Materials*, vol. 3, no. 4, pp. 2643–2667, Apr. 2010, doi: 10.3390/ma3042643.
- [80] E. G. Bylander, “Surface effects on the low-energy cathodoluminescence of zinc oxide,” *J. Appl. Phys.*, vol. 49, no. 3, pp. 1188–1195, Mar. 1978, doi: 10.1063/1.325059.
- [81] Z. Fang, Y. Wang, D. Xu, Y. Tan, and X. Liu, “Blue luminescent center in ZnO films deposited on silicon substrates,” *Opt. Mater.*, vol. 26, no. 3, pp. 239–242, Aug. 2004, doi: 10.1016/j.optmat.2003.11.027.
- [82] P. S. Xu, Y. M. Sun, C. S. Shi, F. Q. Xu, and H. B. Pan, “The electronic structure and spectral properties of ZnO and its defects,” *Nucl. Instrum. Methods Phys. Res. Sect. B Beam Interact. Mater. At.*, vol. 199, pp. 286–290, Jan. 2003, doi: 10.1016/S0168-583X(02)01425-8.
- [83] A. B. Djurišić *et al.*, “Green, yellow, and orange defect emission from ZnO nanostructures: Influence of excitation wavelength,” *Appl. Phys. Lett.*, vol. 88, no. 10, p. 103107, Mar. 2006, doi: 10.1063/1.2182096.

- [84] S. A. M. Lima, F. A. Sigoli, M. J. Jr, and M. R. Davolos, "Luminescent properties and lattice defects correlation on zinc oxide," *Int. J. Inorg. Mater.*, vol. 3, no. 7, pp. 749–754, 2001, doi: 10.1016/S1466-6049(01)00055-1.
- [85] B. Lin, Z. Fu, and Y. Jia, "Green luminescent center in undoped zinc oxide films deposited on silicon substrates," *Appl. Phys. Lett.*, vol. 79, no. 7, pp. 943–945, Aug. 2001, doi: 10.1063/1.1394173.
- [86] N. H. Nickel and E. Terukov, Eds., *Zinc Oxide - A Material for Micro- and Optoelectronic Applications*, Dordrecht: Springer Netherlands, vol. 194, 2005.
- [87] C. G. Van de Walle, "Hydrogen as a Cause of Doping in Zinc Oxide," *Phys. Rev. Lett.*, vol. 85, no. 5, pp. 1012–1015, Jul. 2000, doi: 10.1103/PhysRevLett.85.1012.
- [88] D. Zwingel, "Trapping and recombination processes in the thermoluminescence of Li-doped ZnO single crystals," *J. Lumin.*, vol. 5, no. 6, pp. 385–405, Dec. 1972, doi: 10.1016/0022-2313(72)90001-4.
- [89] O. F. Schirmer and D. Zwingel, "The yellow luminescence of zinc oxide," *Solid State Commun.*, vol. 8, no. 19, pp. 1559–1563, Oct. 1970, doi: 10.1016/0038-1098(70)90608-3.
- [90] C. H. Ahn, Y. Y. Kim, D. C. Kim, S. K. Mohanta, and H. K. Cho, "A comparative analysis of deep level emission in ZnO layers deposited by various methods," *J. Appl. Phys.*, vol. 105, no. 1, p. 013502, Jan. 2009, doi: 10.1063/1.3054175.
- [91] D. Li *et al.*, "Different origins of visible luminescence in ZnO nanostructures fabricated by the chemical and evaporation methods," *Appl. Phys. Lett.*, vol. 85, no. 9, pp. 1601–1603, Aug. 2004, doi: 10.1063/1.1786375.
- [92] K. Vanheusden, W. L. Warren, C. H. Seager, D. R. Tallant, J. A. Voigt, and B. E. Gnade, "Mechanisms behind green photoluminescence in ZnO phosphor powders," *J. Appl. Phys.*, vol. 79, no. 10, pp. 7983–7990, May 1996, doi: 10.1063/1.362349.
- [93] A. van Dijken, E. A. Meulenkaamp, D. Vanmaekelbergh, and A. Meijerink, "Identification of the transition responsible for the visible emission in ZnO using quantum size effects," *J. Lumin.*, vol. 90, no. 3–4, pp. 123–128, Aug. 2000, doi: 10.1016/S0022-2313(99)00599-2.
- [94] Y. Y. Tay *et al.*, "Correlation between the characteristic green emissions and specific defects of ZnO," *Phys. Chem. Chem. Phys.*, vol. 12, no. 10, p. 2373, 2010, doi: 10.1039/b922372j.
- [95] S. A. Studenikin, N. Golego, and M. Cocivera, "Fabrication of green and orange photoluminescent, undoped ZnO films using spray pyrolysis," *J. Appl. Phys.*, vol. 84, no. 4, pp. 2287–2294, Aug. 1998, doi: 10.1063/1.368295.
- [96] S. Vempati, J. Mitra, and P. Dawson, "One-step synthesis of ZnO nanosheets: a blue-white fluorophore," *Nanoscale Res. Lett.*, vol. 7, no. 1, p. 470, 2012, doi: 10.1186/1556-276X-7-470.
- [97] K. H. Tam *et al.*, "Defects in ZnO Nanorods Prepared by a Hydrothermal Method," *J. Phys. Chem. B*, vol. 110, no. 42, pp. 20865–20871, Oct. 2006, doi: 10.1021/jp063239w.
- [98] A. B. Djurišić *et al.*, "Defect emissions in ZnO nanostructures," *Nanotechnology*, vol. 18, no. 9, p. 095702, Mar. 2007, doi: 10.1088/0957-4484/18/9/095702.
- [99] N. S. Norberg and D. R. Gamelin, "Influence of Surface Modification on the Luminescence of Colloidal ZnO Nanocrystals," *J. Phys. Chem. B*, vol. 109, no. 44, pp. 20810–20816, Nov. 2005, doi: 10.1021/jp0535285.
- [100] C. R. Cornejo, "Luminescence in Rare Earth Ion-Doped Oxide Compounds," *Luminescence - An Outlook on the Phenomena and their Applications*, J. Thirumalai, Ed. InTech, 2016.
- [101] A. Edgar, "Luminescent Materials," *Springer Handbook of Electronic and Photonic Materials*, S. Kasap and P. Capper, Eds. Cham: Springer International Publishing, 2017.

- [102] L.-W. Sun *et al.*, “Lanthanum-doped ZnO quantum dots with greatly enhanced fluorescent quantum yield,” *J. Mater. Chem.*, vol. 22, no. 17, p. 8221, 2012, doi: 10.1039/c2jm00040g.
- [103] O. M. Ntwaeaborwa, S. J. Mofokeng, V. Kumar, and R. E. Kroon, “Structural, optical and photoluminescence properties of Eu<sup>3+</sup> doped ZnO nanoparticles,” *Spectrochim. Acta. A. Mol. Biomol. Spectrosc.*, vol. 182, pp. 42–49, Jul. 2017, doi: 10.1016/j.saa.2017.03.067.
- [104] J. Sowik *et al.*, “Optical and photocatalytic properties of rare earth metal-modified ZnO quantum dots,” *Appl. Surf. Sci.*, vol. 464, pp. 651–663, Jan. 2019, doi: 10.1016/j.apsusc.2018.09.104.
- [105] Q. Shi *et al.*, “Enhancing blue luminescence from Ce-doped ZnO nanophosphor by Li doping,” *Nanoscale Res. Lett.*, vol. 9, no. 1, p. 480, Dec. 2014, doi: 10.1186/1556-276X-9-480.
- [106] Q. Luo *et al.*, “Blue luminescence from Ce-doped ZnO thin films prepared by magnetron sputtering,” *Appl. Phys. A*, vol. 108, no. 1, pp. 239–245, Jul. 2012, doi: 10.1007/s00339-012-6883-9.
- [107] V. Kumar, O. M. Ntwaeaborwa, T. Soga, V. Dutta, and H. C. Swart, “Rare Earth Doped Zinc Oxide Nanophosphor Powder: A Future Material for Solid State Lighting and Solar Cells,” *ACS Photonics*, vol. 4, no. 11, pp. 2613–2637, Nov. 2017, doi: 10.1021/acsp Photonics.7b00777.
- [108] A. George, S. K. Sharma, S. Chawla, M. M. Malik, and M. S. Qureshi, “Detailed of X-ray diffraction and photoluminescence studies of Ce doped ZnO nanocrystals,” *J. Alloys Compd.*, vol. 509, no. 20, pp. 5942–5946, May 2011, doi: 10.1016/j.jallcom.2011.03.017.
- [109] W. K. Tan, K. Abdul Razak, Z. Lockman, G. Kawamura, H. Muto, and A. Matsuda, “Photoluminescence properties of rod-like Ce-doped ZnO nanostructured films formed by hot-water treatment of sol–gel derived coating,” *Opt. Mater.*, vol. 35, no. 11, pp. 1902–1907, Sep. 2013, doi: 10.1016/j.optmat.2013.01.011.
- [110] N. F. Djaja and R. Saleh, “Characteristics and Photocatalytic Activities of Ce-Doped ZnO Nanoparticles,” *Mater. Sci. Appl.*, vol. 04, no. 02, pp. 145–152, 2013, doi: 10.4236/msa.2013.42017.
- [111] A. Chelouche, T. Touam, M. Tazerout, F. Boudjouan, D. Djouadi, and A. Doghmane, “Low cerium doping investigation on structural and photoluminescence properties of sol-gel ZnO thin films,” *J. Lumin.*, vol. 181, pp. 448–454, Jan. 2017, doi: 10.1016/j.jlumin.2016.09.061.
- [112] N. Kannadasan, N. Shanmugam, S. Cholan, K. Sathishkumar, G. Viruthagiri, and R. Poonguzhali, “The effect of Ce<sup>4+</sup> incorporation on structural, morphological and photocatalytic characters of ZnO nanoparticles,” *Mater. Charact.*, vol. 97, pp. 37–46, Nov. 2014, doi: 10.1016/j.matchar.2014.08.021.
- [113] M. Yousefi, M. Amiri, R. Azimirad, and A. Z. Moshfegh, “Enhanced photoelectrochemical activity of Ce doped ZnO nanocomposite thin films under visible light,” *J. Electroanal. Chem.*, vol. 661, no. 1, pp. 106–112, Oct. 2011, doi: 10.1016/j.jelechem.2011.07.022.
- [114] Q. Luo, L. S. Wang, Z. W. Wang, Y. Z. Chen, G. H. Yue, and D. L. Peng, “Effects of Ce Doping on the Properties of ZnO Thin Films Prepared by DC Reactive Magnetron Sputtering,” *Adv. Mater. Res.*, vol. 476–478, pp. 2403–2406, Feb. 2012, doi: 10.4028/www.scientific.net/AMR.476-478.2403.
- [115] J. Lang *et al.*, “Fabrication and optical properties of Ce-doped ZnO nanorods,” *J. Appl. Phys.*, vol. 107, no. 7, p. 074302, Apr. 2010, doi: 10.1063/1.3318613.
- [116] N. R. Panda, B. S. Acharya, Th. B. Singh, and R. K. Gartia, “Luminescence properties and decay kinetics of nano ZnO powder doped with cerium ions,” *J. Lumin.*, vol. 136, pp. 369–377, Apr. 2013, doi: 10.1016/j.jlumin.2012.12.002.
- [117] C. Liu, X. Tang, C. Mo, and Z. Qiang, “Characterization and activity of visible-light-driven TiO<sub>2</sub> photocatalyst codoped with nitrogen and cerium,” *J. Solid State Chem.*, vol. 181, no. 4, pp. 913–919, Apr. 2008, doi: 10.1016/j.jssc.2008.01.031.

- [118] W. E. Mahmoud, "Synthesis and optical properties of Ce-doped ZnO hexagonal nanoplatelets," *J. Cryst. Growth*, vol. 312, no. 21, pp. 3075–3079, Oct. 2010, doi: 10.1016/j.jcrysgro.2010.07.040.
- [119] L. F. Koao, F. B. Dejene, H. C. Swart, and J. R. Botha, "The effect of Ce<sup>3+</sup> on structure, morphology and optical properties of flower-like ZnO synthesized using the chemical bath method," *J. Lumin.*, vol. 143, pp. 463–468, Nov. 2013, doi: 10.1016/j.jlumin.2013.05.045.
- [120] A. B. Djurišić, A. M. C. Ng, and X. Y. Chen, "ZnO nanostructures for optoelectronics: Material properties and device applications," *Prog. Quantum Electron.*, vol. 34, no. 4, pp. 191–259, Jul. 2010, doi: 10.1016/j.pquantelec.2010.04.001.
- [121] M. Samadi, M. Zirak, A. Naseri, E. Khorashadizade, and A. Z. Moshfegh, "Recent progress on doped ZnO nanostructures for visible-light photocatalysis," *Thin Solid Films*, vol. 605, pp. 2–19, Apr. 2016, doi: 10.1016/j.tsf.2015.12.064.
- [122] L. Zhu and W. Zeng, "Room-temperature gas sensing of ZnO-based gas sensor: A review," *Sens. Actuators Phys.*, vol. 267, pp. 242–261, Nov. 2017, doi: 10.1016/j.sna.2017.10.021.
- [123] A. Dev, R. Niepelt, J. P. Richters, C. Ronning, and T. Voss, "Stable enhancement of near-band-edge emission of ZnO nanowires by hydrogen incorporation," *Nanotechnology*, vol. 21, no. 6, p. 065709, Feb. 2010, doi: 10.1088/0957-4484/21/6/065709.
- [124] A. Dev, J. P. Richters, J. Sartor, H. Kalt, J. Gutowski, and T. Voss, "Enhancement of the near-band-edge photoluminescence of ZnO nanowires: Important role of hydrogen incorporation versus plasmon resonances," *Appl. Phys. Lett.*, vol. 98, no. 13, p. 131111, Mar. 2011, doi: 10.1063/1.3569951.
- [125] N. Ohashi, T. Ishigaki, N. Okada, T. Sekiguchi, I. Sakaguchi, and H. Haneda, "Effect of hydrogen doping on ultraviolet emission spectra of various types of ZnO," *Appl. Phys. Lett.*, vol. 80, no. 16, pp. 2869–2871, Apr. 2002, doi: 10.1063/1.1470703.
- [126] X. H. Huang *et al.*, "Universal photoluminescence evolution of solution-grown ZnO nanorods with annealing: important role of hydrogen donor," *CrystEngComm*, vol. 13, no. 23, p. 7032, 2011, doi: 10.1039/c1ce05882g.
- [127] X. Xue, T. Wang, X. Jiang, J. Jiang, C. Pan, and Y. Wu, "Interaction of hydrogen with defects in ZnO nanoparticles – studied by positron annihilation, Raman and photoluminescence spectroscopy," *CrystEngComm*, vol. 16, no. 6, p. 1207, 2014, doi: 10.1039/c3ce42202j.
- [128] F. Herklotz, E. V. Lavrov, and J. Weber, "Photoluminescence study of hydrogen donors in ZnO," *Phys. B Condens. Matter*, vol. 404, no. 22, pp. 4349–4353, Dec. 2009, doi: 10.1016/j.physb.2009.09.031.
- [129] R. Dingle, "Luminescent Transitions Associated With Divalent Copper Impurities and the Green Emission from Semiconducting Zinc Oxide," *Phys. Rev. Lett.*, vol. 23, no. 11, pp. 579–581, Sep. 1969, doi: 10.1103/PhysRevLett.23.579.
- [130] N. Y. Garces, L. Wang, L. Bai, N. C. Giles, L. E. Halliburton, and G. Cantwell, "Role of copper in the green luminescence from ZnO crystals," *Appl. Phys. Lett.*, vol. 81, no. 4, pp. 622–624, Jul. 2002, doi: 10.1063/1.1494125.
- [131] D. C. Agarwal *et al.*, "Enhanced room temperature ferromagnetism and green photoluminescence in Cu doped ZnO thin film synthesised by neutral beam sputtering," *Sci. Rep.*, vol. 9, no. 1, p. 6675, Dec. 2019, doi: 10.1038/s41598-019-43184-9.
- [132] J. Iqbal, B. Wang, X. Liu, D. Yu, B. He, and R. Yu, "Oxygen-vacancy-induced green emission and room-temperature ferromagnetism in Ni-doped ZnO nanorods," *New J. Phys.*, vol. 11, no. 6, p. 063009, Jun. 2009, doi: 10.1088/1367-2630/11/6/063009.

- [133] L.-N. Tong *et al.*, “Photoluminescence studies on structural defects and room temperature ferromagnetism in Ni and Ni–H doped ZnO nanoparticles,” *J. Appl. Phys.*, vol. 108, no. 2, p. 023906, Jul. 2010, doi: 10.1063/1.3460644.
- [134] P. Singh, R. Kumar, and R. K. Singh, “Progress on Transition Metal-Doped ZnO Nanoparticles and Its Application,” *Ind. Eng. Chem. Res.*, vol. 58, no. 37, pp. 17130–17163, Sep. 2019, doi: 10.1021/acs.iecr.9b01561.
- [135] W. Baiqi *et al.*, “Photoluminescence properties of Co-doped ZnO nanorods array fabricated by the solution method,” *Phys. E Low-Dimens. Syst. Nanostructures*, vol. 41, no. 3, pp. 413–417, Jan. 2009, doi: 10.1016/j.physe.2008.09.001.
- [136] V. Gandhi, R. Ganesan, H. H. Abdulrahman Syedahamed, and M. Thaiyan, “Effect of Cobalt Doping on Structural, Optical, and Magnetic Properties of ZnO Nanoparticles Synthesized by Coprecipitation Method,” *J. Phys. Chem. C*, vol. 118, no. 18, pp. 9715–9725, May 2014, doi: 10.1021/jp411848t.
- [137] S. Yamamoto, “Photoluminescence quenching in cobalt doped ZnO nanocrystals,” *J. Appl. Phys.*, vol. 111, no. 9, p. 094310, May 2012, doi: 10.1063/1.4710533.
- [138] M. Ivill *et al.*, “Structure and magnetism of cobalt-doped ZnO thin films,” *New J. Phys.*, vol. 10, no. 6, p. 065002, Jun. 2008, doi: 10.1088/1367-2630/10/6/065002.
- [139] S. Vempati, A. Shetty, P. Dawson, K. Nanda, and S. B. Krupanidhi, “Cobalt-doped ZnO nanowires on quartz: Synthesis by simple chemical method and characterization,” *J. Cryst. Growth*, vol. 343, no. 1, pp. 7–12, Mar. 2012, doi: 10.1016/j.jcrysgro.2012.01.015.
- [140] L. Yanmei *et al.*, “Structure and photoluminescence of arrayed Zn<sub>1-x</sub>Co<sub>x</sub>O nanorods grown via hydrothermal method,” *J. Phys. Appl. Phys.*, vol. 40, no. 15, pp. 4592–4596, Aug. 2007, doi: 10.1088/0022-3727/40/15/034.
- [141] Y. Q. Chang, P. W. Wang, S. L. Ni, Y. Long, and X. D. Li, “Influence of Co Content on Raman and Photoluminescence Spectra of Co Doped ZnO Nanowires,” *J. Mater. Sci. Technol.*, vol. 28, no. 4, pp. 313–316, Apr. 2012, doi: 10.1016/S1005-0302(12)60060-7.
- [142] D. Karmakar *et al.*, “Ferromagnetism in Fe-doped ZnO nanocrystals: Experiment and theory,” *Phys. Rev. B*, vol. 75, no. 14, p. 144404, Apr. 2007, doi: 10.1103/PhysRevB.75.144404.
- [143] C. Wang, Z. Chen, Y. He, L. Li, and D. Zhang, “Structure, morphology and properties of Fe-doped ZnO films prepared by facing-target magnetron sputtering system,” *Appl. Surf. Sci.*, vol. 255, no. 15, pp. 6881–6887, May 2009, doi: 10.1016/j.apsusc.2009.03.008.
- [144] K. J. Kim and Y. R. Park, “Optical investigation of Zn<sub>1-x</sub>Fe<sub>x</sub>O films grown on Al<sub>2</sub>O<sub>3</sub>(0001) by radio-frequency sputtering,” *J. Appl. Phys.*, vol. 96, no. 8, pp. 4150–4153, Oct. 2004, doi: 10.1063/1.1790570.
- [145] B. Panigrahy, M. Aslam, and D. Bahadur, “Effect of Fe doping concentration on optical and magnetic properties of ZnO nanorods,” *Nanotechnology*, vol. 23, no. 11, p. 115601, Mar. 2012, doi: 10.1088/0957-4484/23/11/115601.
- [146] A. K. Srivastava, M. Deepa, N. Bahadur, and M. S. Goyat, “Influence of Fe doping on nanostructures and photoluminescence of sol–gel derived ZnO,” *Mater. Chem. Phys.*, vol. 114, no. 1, pp. 194–198, Mar. 2009, doi: 10.1016/j.matchemphys.2008.09.005.
- [147] Y. Zhang *et al.*, “Influence of Fe doping on the optical property of ZnO films,” *J. Alloys Compd.*, vol. 473, no. 1–2, pp. 319–322, Apr. 2009, doi: 10.1016/j.jallcom.2008.05.090.
- [148] A. K. Singh, G. S. Thool, P. R. Bangal, S. S. Madhavendra, and S. P. Singh, “Low Temperature Mn Doped ZnO Nanorod Array: Synthesis and Its Photoluminescence Behavior,” *Ind. Eng. Chem. Res.*, vol. 53, no. 22, pp. 9383–9390, Jun. 2014, doi: 10.1021/ie500077v.

- [149] N. S. Sabri, A. K. Yahya, and M. K. Talari, "Emission properties of Mn doped ZnO nanoparticles prepared by mechanochemical processing," *J. Lumin.*, vol. 132, no. 7, pp. 1735–1739, Jul. 2012, doi: 10.1016/j.jlumin.2012.02.020.
- [150] M. Liu, A. H. Kitai, and P. Mascher, "Point defects and luminescence centres in zinc oxide and zinc oxide doped with manganese," *J. Lumin.*, vol. 54, no. 1, pp. 35–42, Aug. 1992, doi: 10.1016/0022-2313(92)90047-D.
- [151] X. Yan, D. Hu, H. Li, L. Li, X. Chong, and Y. Wang, "Nanostructure and optical properties of M doped ZnO (M=Ni, Mn) thin films prepared by sol–gel process," *Phys. B Condens. Matter*, vol. 406, no. 20, pp. 3956–3962, Oct. 2011, doi: 10.1016/j.physb.2011.07.037.
- [152] G. Voicu, O. Oprea, B. S. Vasile, and E. Andronescu, "PHOTOLUMINESCENCE AND PHOTOCATALYTIC ACTIVITY OF Mn- DOPED ZnO NANOPARTICLES," *Digest Journal of Nanomaterials & Biostructures (DJNB)*, vol. 8, no. 2, pp. 667–675, Apr–Jun. 2013.
- [153] U. N. Maiti, P. K. Ghosh, S. Nandy, and K. K. Chattopadhyay, "Effect of Mn doping on the optical and structural properties of ZnO nano/micro-fibrous thin film synthesized by sol–gel technique," *Phys. B Condens. Matter*, vol. 387, no. 1–2, pp. 103–108, Jan. 2007, doi: 10.1016/j.physb.2006.03.090.
- [154] M. A. Mahmood, S. Baruah, and J. Dutta, "Enhanced visible light photocatalysis by manganese doping or rapid crystallization with ZnO nanoparticles," *Mater. Chem. Phys.*, vol. 130, no. 1–2, pp. 531–535, Oct. 2011, doi: 10.1016/j.matchemphys.2011.07.018.
- [155] M. Xin, L. Z. Hu, D.-P. Liu, and N.-S. Yu, "Effect of Mn doping on the optical, structural and photoluminescence properties of nanostructured ZnO thin film synthesized by sol–gel technique," *Superlattices Microstruct.*, vol. 74, pp. 234–241, Oct. 2014, doi: 10.1016/j.spmi.2014.06.009.
- [156] C. Ronning, P. X. Gao, Y. Ding, Z. L. Wang, and D. Schwen, "Manganese-doped ZnO nanobelts for spintronics," *Appl. Phys. Lett.*, vol. 84, no. 5, pp. 783–785, Feb. 2004, doi: 10.1063/1.1645319.
- [157] Y. Liu *et al.*, "Effects of Cr-doping on the optical and magnetic properties in ZnO nanoparticles prepared by sol–gel method," *J. Alloys Compd.*, vol. 486, no. 1–2, pp. 835–838, Nov. 2009, doi: 10.1016/j.jallcom.2009.07.076.
- [158] N. Xuan Sang, N. Minh Quan, N. Huu Tho, N. Tri Tuan, and T. Thanh Tung, "Mechanism of enhanced photocatalytic activity of Cr-doped ZnO nanoparticles revealed by photoluminescence emission and electron spin resonance," *Semicond. Sci. Technol.*, vol. 34, no. 2, p. 025013, Feb. 2019, doi: 10.1088/1361-6641/aaf820.
- [159] J. S. Tawale, A. Kumar, G. Swati, D. Haranath, S. J. Dhoble, and A. K. Srivastava, "Microstructural evolution and photoluminescence performance of nickel and chromium doped ZnO nanostructures," *Mater. Chem. Phys.*, vol. 205, pp. 9–15, Feb. 2018, doi: 10.1016/j.matchemphys.2017.10.067.
- [160] Y. M. Hu *et al.*, "The morphology and optical properties of Cr-doped ZnO films grown using the magnetron co-sputtering method," *Appl. Surf. Sci.*, vol. 254, no. 13, pp. 3873–3878, Apr. 2008, doi: 10.1016/j.apsusc.2007.12.014.
- [161] S. Singh, E. Senthil Kumar, and M. S. Ramachandra Rao, "Microstructural, optical and electrical properties of Cr-doped ZnO," *Scr. Mater.*, vol. 58, no. 10, pp. 866–869, May 2008, doi: 10.1016/j.scriptamat.2008.01.008.
- [162] B. Wang *et al.*, "Effects of Cr-doping on the photoluminescence and ferromagnetism at room temperature in ZnO nanomaterials prepared by soft chemistry route," *Mater. Chem. Phys.*, vol. 113, no. 1, pp. 103–106, Jan. 2009, doi: 10.1016/j.matchemphys.2008.07.031.

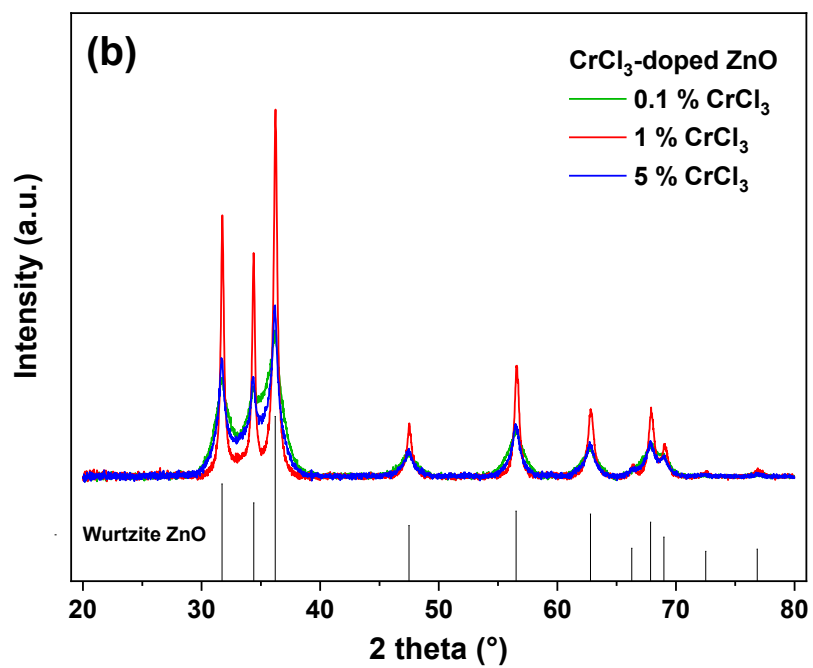
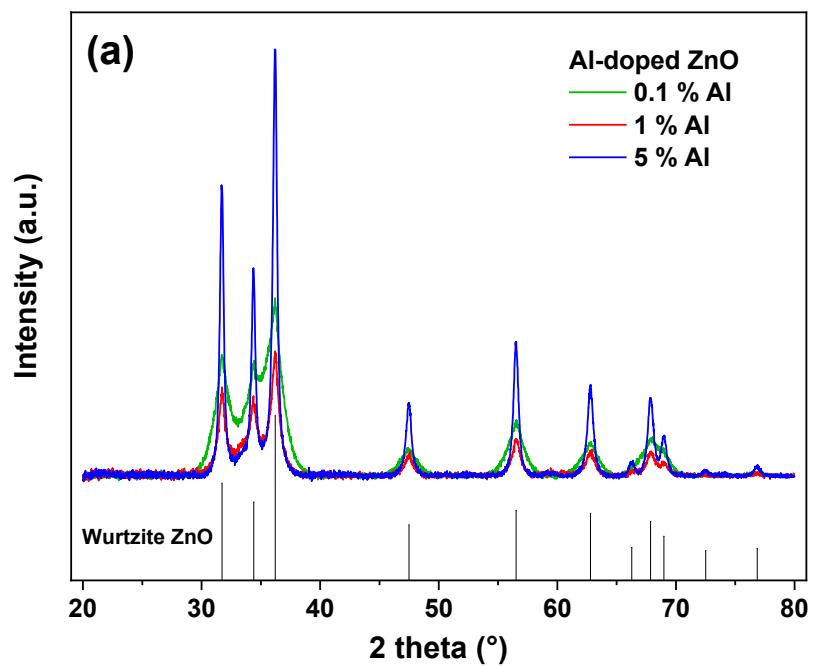
- [163] N. Pushpa, M. K. Kokila, B. M. Nagabhushana, H. Nagabhushana, and A. J. Reddy, “Red luminescence from ZnO : Cr<sup>3+</sup> nanophosphors under visible excitation,” *Bull. Mater. Sci.*, vol. 38, no. 5, pp. 1359–1365, Sep. 2015, doi: 10.1007/s12034-015-1021-x.
- [164] C. F. Fu, L. F. Han, C. Liu, and Y. F. Gao, “Effects of Cr-doping concentration on the structural, optical, and magnetic properties of ZnO thin films: Structural, optical, and magnetic properties of ZnO thin films,” *Phys. Status Solidi A*, vol. 210, no. 7, pp. 1358–1362, Jul. 2013, doi: 10.1002/pssa.201329014.
- [165] X. B. Wang, C. Song, K. W. Geng, F. Zeng, and F. Pan, “Luminescence and Raman scattering properties of Ag-doped ZnO films,” *J. Phys. Appl. Phys.*, vol. 39, no. 23, pp. 4992–4996, Dec. 2006, doi: 10.1088/0022-3727/39/23/014.
- [166] Y. Zhang, Z. Zhang, B. Lin, Z. Fu, and J. Xu, “Effects of Ag Doping on the Photoluminescence of ZnO Films Grown on Si Substrates,” *J. Phys. Chem. B*, vol. 109, no. 41, pp. 19200–19203, Oct. 2005, doi: 10.1021/jp0538058.
- [167] L. Kumari and A. K. Kar, “Morphology evolution and luminescence enhancement in hydrothermally synthesized Ag doped ZnO nanorods,” *Mater. Res. Express*, vol. 6, no. 9, p. 0950b1, Jul. 2019, doi: 10.1088/2053-1591/ab346f.
- [168] R. S. Zeferino, M. B. Flores, and U. Pal, “Photoluminescence and Raman Scattering in Ag-doped ZnO Nanoparticles,” *J. Appl. Phys.*, vol. 109, no. 1, p. 014308, Jan. 2011, doi: 10.1063/1.3530631.
- [169] H. Xue, X. L. Xu, Y. Chen, G. H. Zhang, and S. Y. Ma, “Influence of Ag-doping on the optical properties of ZnO films,” *Appl. Surf. Sci.*, vol. 255, no. 5, pp. 1806–1810, Dec. 2008, doi: 10.1016/j.apsusc.2008.06.021.
- [170] R. S. Kumar, R. Sathyamoorthy, P. Sudhagar, P. Matheswaran, C. P. Hrudhya, and Y. S. Kang, “Effect of aluminum doping on the structural and luminescent properties of ZnO nanoparticles synthesized by wet chemical method,” *Phys. E Low-Dimens. Syst. Nanostructures*, vol. 43, no. 6, pp. 1166–1170, Apr. 2011, doi: 10.1016/j.physe.2011.01.022.
- [171] K. J. Chen *et al.*, “The crystallization and physical properties of Al-doped ZnO nanoparticles,” *Appl. Surf. Sci.*, vol. 254, no. 18, pp. 5791–5795, Jul. 2008, doi: 10.1016/j.apsusc.2008.03.080.
- [172] M. Wang *et al.*, “Optical and photoluminescent properties of sol-gel Al-doped ZnO thin films,” *Mater. Lett.*, vol. 61, no. 4–5, pp. 1118–1121, Feb. 2007, doi: 10.1016/j.matlet.2006.06.065.
- [173] Y. Liu *et al.*, “Effect of Al doping on the visible photoluminescence of ZnO nanofibers,” *J. Alloys Compd.*, vol. 506, no. 2, pp. 772–776, Sep. 2010, doi: 10.1016/j.jallcom.2010.07.067.
- [174] J. J. Ding, S. Y. Ma, H. X. Chen, X. F. Shi, T. T. Zhou, and L. M. Mao, “Influence of Al-doping on the structure and optical properties of ZnO films,” *Phys. B Condens. Matter*, vol. 404, no. 16, pp. 2439–2443, Aug. 2009, doi: 10.1016/j.physb.2009.05.006.
- [175] B. Sundarakannan and M. Kottaisamy, “ZnO:Al – A yellowish orange emitting phosphor for Blue Light-Converted White Light Emitting Diode (WLEDs),” *Ceram. Int.*, vol. 44, no. 12, pp. 14518–14522, Aug. 2018, doi: 10.1016/j.ceramint.2018.05.067.
- [176] N. Srinatha, P. Raghu, H. M. Mahesh, and B. Angadi, “Spin-coated Al-doped ZnO thin films for optical applications: Structural, micro-structural, optical and luminescence studies,” *J. Alloys Compd.*, vol. 722, pp. 888–895, Oct. 2017, doi: 10.1016/j.jallcom.2017.06.182.
- [177] F. X. Xiu, L. J. Mandalapu, Z. Yang, J. L. Liu, G. F. Liu, and J. A. Yarmoff, “Bi-induced acceptor states in ZnO by molecular-beam epitaxy,” *Appl. Phys. Lett.*, vol. 89, no. 5, p. 052103, Jul. 2006, doi: 10.1063/1.2243732.
- [178] R. T. Ginting *et al.*, “A Simple Approach Low-Temperature Solution Process for Preparation of Bismuth-Doped ZnO Nanorods and Its Application in Hybrid Solar Cells,” *J. Phys. Chem. C*, vol. 120, no. 1, pp. 771–780, Jan. 2016, doi: 10.1021/acs.jpcc.5b11094.

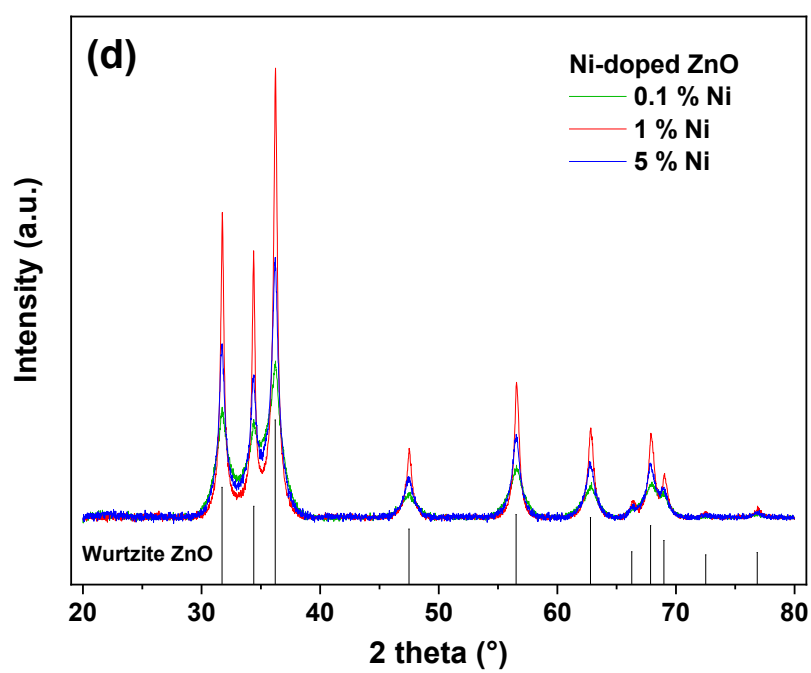
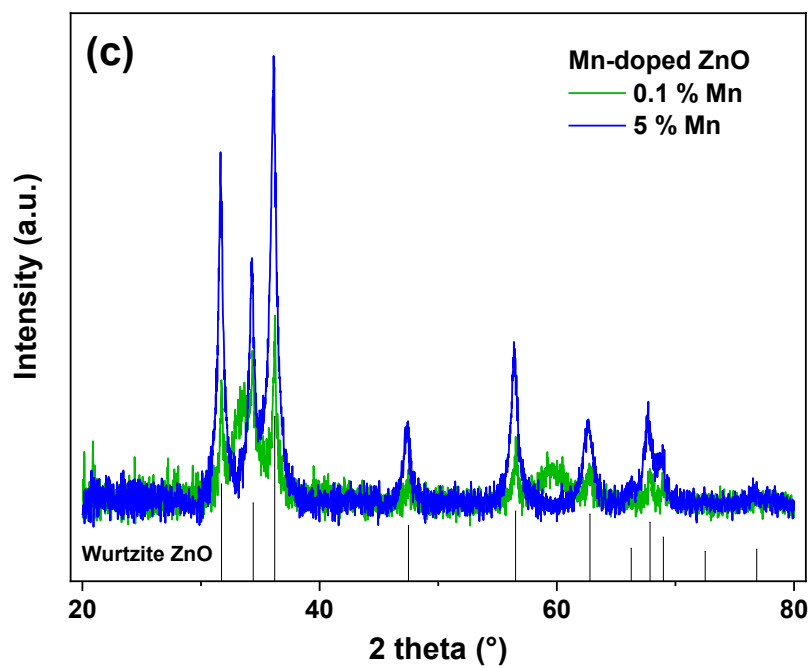
- [179] T. Prakash, G. Neri, A. Bonavita, E. Ranjith Kumar, and K. Gnanamoorthi, "Structural, morphological and optical properties of Bi-doped ZnO nanoparticles synthesized by a microwave irradiation method," *J. Mater. Sci. Mater. Electron.*, vol. 26, no. 7, pp. 4913–4921, Jul. 2015, doi: 10.1007/s10854-015-3002-7.
- [180] T. K. Pathak, H. C. Swart, and R. E. Kroon, "Influence of Bi doping on the structure and photoluminescence of ZnO phosphor synthesized by the combustion method," *Spectrochim. Acta. A. Mol. Biomol. Spectrosc.*, vol. 190, pp. 164–171, Feb. 2018, doi: 10.1016/j.saa.2017.09.026.
- [181] A. T. Ravichandran, R. Karthick, K. Ravichandran, D. Ravinder, and R. Chandramohan, "Revealing the influence of the Bi dopant on the structural, photoluminescence and antibacterial properties of ZnO nanoparticles," *J. Mater. Sci. Mater. Electron.*, vol. 29, no. 4, pp. 2784–2790, Feb. 2018, doi: 10.1007/s10854-017-8206-6.
- [182] S. Abed *et al.*, "Influence of Bi doping on the electrical and optical properties of ZnO thin films," *Superlattices Microstruct.*, vol. 85, pp. 370–378, Sep. 2015, doi: 10.1016/j.spmi.2015.06.008.
- [183] C. Klingshirn, "ZnO: From basics towards applications," *Phys. Status Solidi B*, vol. 244, no. 9, pp. 3027–3073, Sep. 2007, doi: 10.1002/pssb.200743072.
- [184] H. Zhou *et al.*, "Behind the weak excitonic emission of ZnO quantum dots: ZnO/Zn(OH)<sub>2</sub> core-shell structure," *Appl. Phys. Lett.*, vol. 80, no. 2, pp. 210–212, Jan. 2002, doi: 10.1063/1.1432763.
- [185] X. T. Zhang *et al.*, "Structure and photoluminescence of Mn-passivated nanocrystalline ZnO thin films," *J. Cryst. Growth*, vol. 254, no. 1–2, pp. 80–85, Jun. 2003, doi: 10.1016/S0022-0248(03)01143-6.
- [186] Y. Zhu, "ZnO nanoparticles as a luminescent down-shifting layer for solar cells," (Doctoral dissertation), 2015.
- [187] Y. Zhu *et al.*, "Intense visible emission from ZnO/PAAX (X = H or Na) nanocomposite synthesized via a simple and scalable sol-gel method," *Sci. Rep.*, vol. 6, no. 1, Sep. 2016, doi: 10.1038/srep23557.
- [188] H.-J. Lee, S.-Y. Jeong, C. R. Cho, and C. H. Park, "Study of diluted magnetic semiconductor: Co-doped ZnO," *Appl. Phys. Lett.*, vol. 81, no. 21, pp. 4020–4022, Nov. 2002, doi: 10.1063/1.1517405.
- [189] T. Fukumura, Z. Jin, A. Ohtomo, H. Koinuma, and M. Kawasaki, "An oxide-diluted magnetic semiconductor: Mn-doped ZnO," *Appl. Phys. Lett.*, vol. 75, no. 21, pp. 3366–3368, Nov. 1999, doi: 10.1063/1.125353.
- [190] J. Zhai, X. Tao, Y. Pu, X.-F. Zeng, and J.-F. Chen, "Core/shell structured ZnO/SiO<sub>2</sub> nanoparticles: Preparation, characterization and photocatalytic property," *Appl. Surf. Sci.*, vol. 257, no. 2, pp. 393–397, Nov. 2010, doi: 10.1016/j.apsusc.2010.06.091.
- [191] L. Palmetshofer, "Rutherford Backscattering Spectroscopy (RBS)," in *Surface and Thin Film Analysis*, G. Friedbacher and H. Bubert, Eds. Weinheim, Germany: Wiley-VCH Verlag GmbH & Co. KGaA, 2011, pp. 191–202.
- [192] H. Kumar and R. Rani, "Structural and Optical Characterization of ZnO Nanoparticles Synthesized by Microemulsion Route," *Int. Lett. Chem. Phys. Astron.*, Vol. 14, pp. 26–36, 2013.
- [193] "Zinc oxide (french process)."  
<https://webbook.nist.gov/cgi/cbook.cgi?ID=B6004648&Mask=80#Top>.
- [194] D. Yuvaraj and K. N. Rao, "Optical and electrical properties of ZnO films deposited by activated reactive evaporation," *Vacuum*, vol. 82, no. 11, pp. 1274–1279, Jun. 2008, doi: 10.1016/j.vacuum.2008.03.043.
- [195] P. Camarda *et al.*, "Luminescence mechanisms of defective ZnO nanoparticles," *Phys. Chem. Chem. Phys.*, vol. 18, no. 24, pp. 16237–16244, Jun. 2016, doi: 10.1039/C6CP01513A.

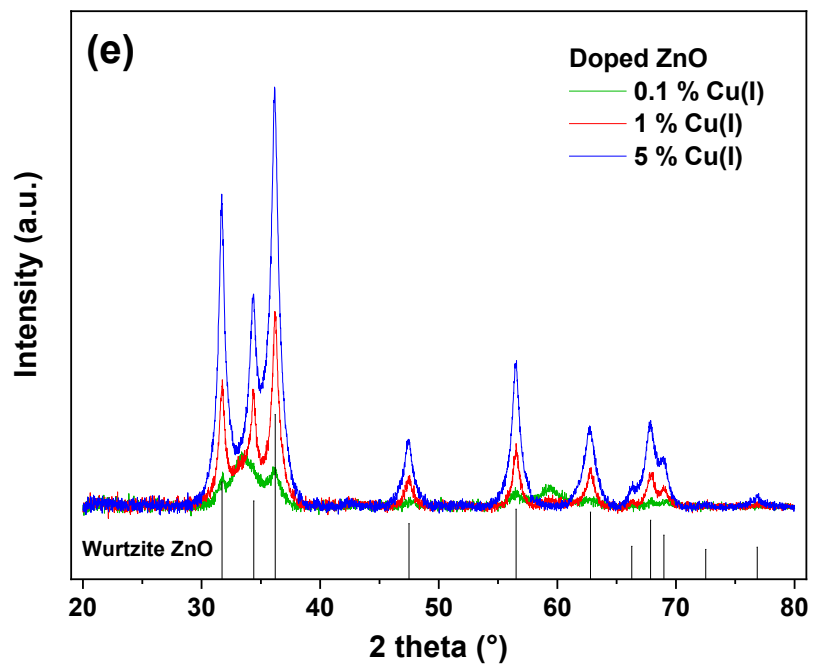
- [196] J. C. de Mello, H. F. Wittmann, and R. H. Friend, "An improved experimental determination of external photoluminescence quantum efficiency," *Adv. Mater.*, vol. 9, no. 3, pp. 230–232, Mar. 1997, doi: 10.1002/adma.19970090308.
- [197] "a-guide-to-reflectance-materials-and-coatings.pdf." <https://www.labsphere.com/site/assets/files/2553/a-guide-to-reflectance-materials-and-coatings.pdf>.
- [198] M. A. Vergés, A. Mifsud, and C. J. Serna, "Formation of rod-like zinc oxide microcrystals in homogeneous solutions," *J Chem Soc Faraday Trans*, vol. 86, no. 6, pp. 959–963, 1990, doi: 10.1039/FT9908600959.
- [199] B. Zhang, T. Kong, W. Xu, R. Su, Y. Gao, and G. Cheng, "Surface Functionalization of Zinc Oxide by Carboxyalkylphosphonic Acid Self-Assembled Monolayers," *Langmuir*, vol. 26, no. 6, pp. 4514–4522, Mar. 2010, doi: 10.1021/la9042827.
- [200] N. P. Barradas, "Calculation of the low energy yield in RBS," *Nucl. Instrum. Methods Phys. Res. Sect. B Beam Interact. Mater. At.*, vol. 261, no. 1–2, pp. 418–421, Aug. 2007, doi: 10.1016/j.nimb.2007.04.182.
- [201] X. Luo *et al.*, "Probing the magnetic profile of diluted magnetic semiconductors using polarized neutron reflectivity," *Sci. Rep.*, vol. 7, no. 1, pp. 1–8, Jul. 2017, doi: 10.1038/s41598-017-06793-w.
- [202] N. Ali, B. Singh, Z. A. Khan, V. A. R. K. Tarafder, and S. Ghosh, "Origin of ferromagnetism in Cu-doped ZnO," *Sci. Rep.*, vol. 9, no. 1, pp. 1–7, Feb. 2019, doi: 10.1038/s41598-019-39660-x.
- [203] Y.-H. Lu *et al.*, "A facile green antisolvent approach to Cu<sup>2+</sup>-doped ZnO nanocrystals with visible-light-responsive photoactivities," *Nanoscale*, vol. 6, no. 15, p. 8796, Jun. 2014, doi: 10.1039/C4NR01607F.
- [204] H. Nishikiori, D. Natori, H. Ebara, K. Teshima, and T. Fujii, "Zinc complex formation of organic ligands on zinc oxide and titanium dioxide," *J. Photochem. Photobiol. Chem.*, vol. 327, pp. 51–57, Aug. 2016, doi: 10.1016/j.jphotochem.2016.05.003.
- [205] D. Prochowicz, K. Sokołowski, and J. Lewiński, "Zinc hydroxides and oxides supported by organic ligands: Synthesis and structural diversity," *Coord. Chem. Rev.*, vol. 270–271, pp. 112–126, Jul. 2014, doi: 10.1016/j.ccr.2013.12.003.
- [206] P. Felbier *et al.*, "Highly Luminescent ZnO Quantum Dots Made in a Nonthermal Plasma," *Adv. Funct. Mater.*, vol. 24, no. 14, pp. 1988–1993, 2014, doi: 10.1002/adfm.201303449.
- [207] R. Baraki, P. Zierep, E. Erdem, S. Weber, and T. Granzow, "Electron paramagnetic resonance study of ZnO varistor material," *J. Phys. Condens. Matter*, vol. 26, no. 11, p. 115801, Mar. 2014, doi: 10.1088/0953-8984/26/11/115801.
- [208] T. Ruf, S. Repp, J. Urban, R. Thomann, and E. Erdem, "Competing effects between intrinsic and extrinsic defects in pure and Mn-doped ZnO nanocrystals," *J. Nanoparticle Res.*, vol. 18, no. 5, May 2016, doi: 10.1007/s11051-016-3408-z.
- [209] A. Guerrero-Martínez, J. Pérez-Juste, and L. M. Liz-Marzán, "Recent Progress on Silica Coating of Nanoparticles and Related Nanomaterials," *Adv. Mater.*, vol. 22, no. 11, pp. 1182–1195, Mar. 2010, doi: 10.1002/adma.200901263.
- [210] M. A. Correa-Duarte, M. Giersig, and L. M. Liz-Marzán, "Stabilization of CdS semiconductor nanoparticles against photodegradation by a silica coating procedure," *Chem. Phys. Lett.*, vol. 286, no. 5–6, pp. 497–501, Apr. 1998, doi: 10.1016/S0009-2614(98)00012-8.
- [211] F. El-Kabbany, S. Taha, M. Hafez, and I. S. Yahia, "Thermal and spectroscopic properties of the nano-system (ZnO<sub>(1-x)</sub>SiO<sub>2(x)</sub>)," *J. Mol. Struct.*, vol. 1111, pp. 33–45, May 2016, doi: 10.1016/j.molstruc.2016.01.061.

- [212] Y. Nakashima, C. Takai, H. Razavi-Khosroshahi, and M. Fuji, "Effects of cations on the size and silica shell microstructure of hollow silica nanoparticles prepared using PAA/cation/ $\text{NH}_4\text{OH}$  template," *Colloids Surf. Physicochem. Eng. Asp.*, vol. 593, p. 124582, May 2020, doi: 10.1016/j.colsurfa.2020.124582.
- [213] Z. Q. Chen, S. Yamamoto, M. Maekawa, A. Kawasuso, X. L. Yuan, and T. Sekiguchi, "Postgrowth annealing of defects in ZnO studied by positron annihilation, x-ray diffraction, Rutherford backscattering, cathodoluminescence, and Hall measurements," *J. Appl. Phys.*, vol. 94, no. 8, p. 4807, 2003, doi: 10.1063/1.1609050.
- [214] K. S. Babu, A. R. Reddy, and K. V. Reddy, "Controlling the size and optical properties of ZnO nanoparticles by capping with  $\text{SiO}_2$ ," *Mater. Res. Bull.*, vol. 49, pp. 537–543, Jan. 2014, doi: 10.1016/j.materresbull.2013.09.024.
- [215] B. H. Soni, M. P. Deshpande, S. V. Bhatt, N. Garg, and S. H. Chaki, "Studies on ZnO Nanorods Synthesized by Hydrothermal Method and their Characterization," *Журнал Нано- Та Електронної Фізики*, no. 5, № 4(2), pp. 04077(6)-04078, 2013.
- [216] G. Xiong, U. Pal, J. G. Serrano, K. B. Ucer, and R. T. Williams, "Photoluminescence and FTIR study of ZnO nanoparticles: the impurity and defect perspective," *Phys. Status Solidi C*, vol. 3, no. 10, pp. 3577–3581, 2006, doi: 10.1002/pssc.200672164.
- [217] Y. Wan and S.-H. Yu, "Polyelectrolyte Controlled Large-Scale Synthesis of Hollow Silica Spheres with Tunable Sizes and Wall Thicknesses," *J. Phys. Chem. C*, vol. 112, no. 10, pp. 3641–3647, Mar. 2008, doi: 10.1021/jp710990b.
- [218] M. Fuji, C. Takai, H. Imabeppu, and X. Xu, "Synthesis and shell structure design of hollow silica nanoparticles using polyelectrolyte as template," *J. Phys. Conf. Ser.*, vol. 596, p. 012007, Apr. 2015, doi: 10.1088/1742-6596/596/1/012007.

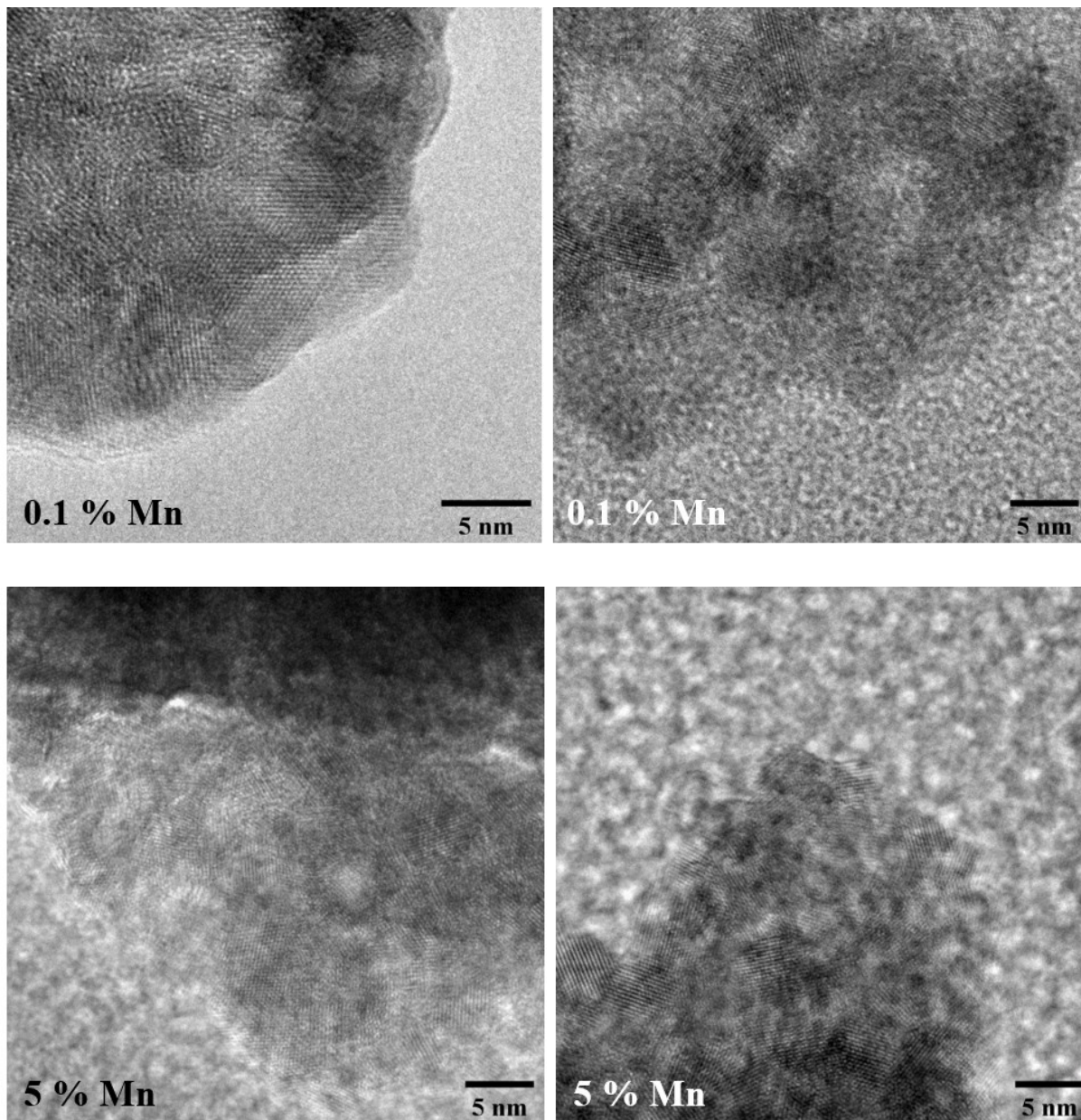
## Appendix I XRD spectra of metal-doped ZnO nanohybrids

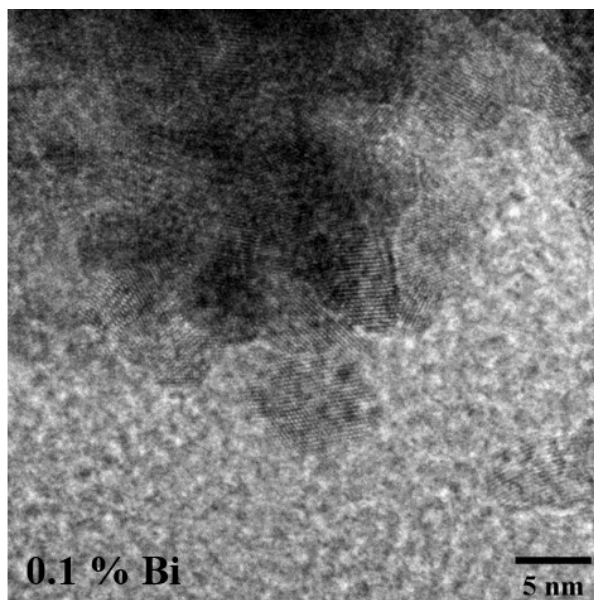
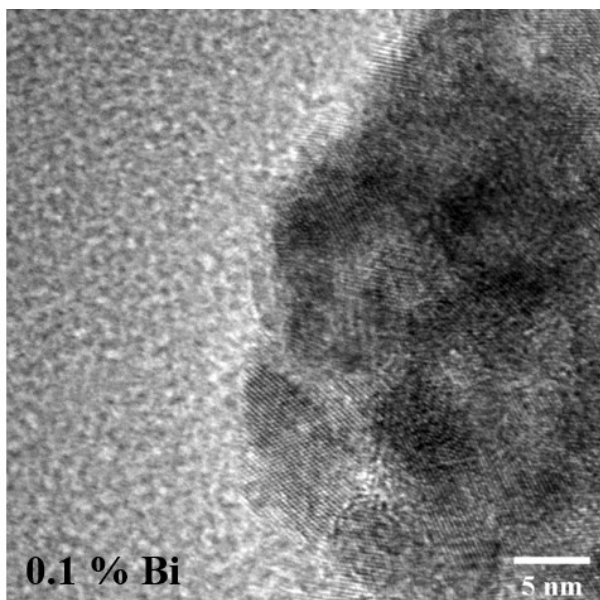
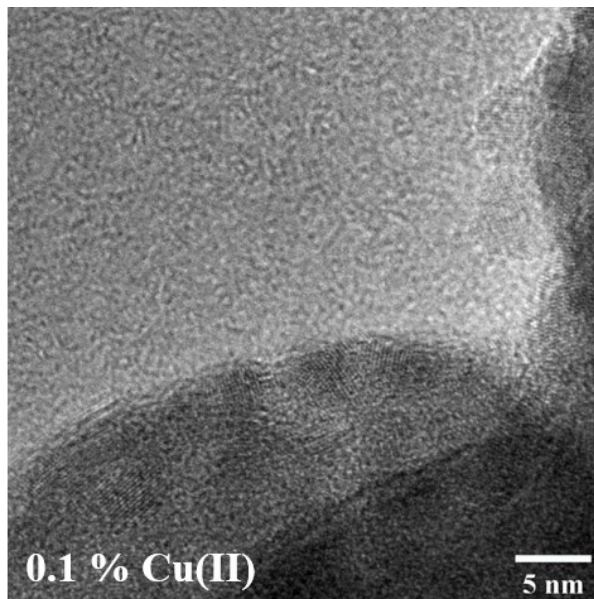
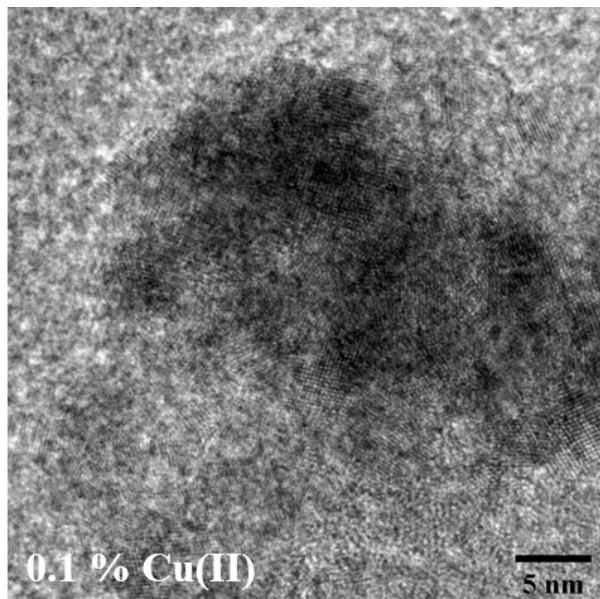




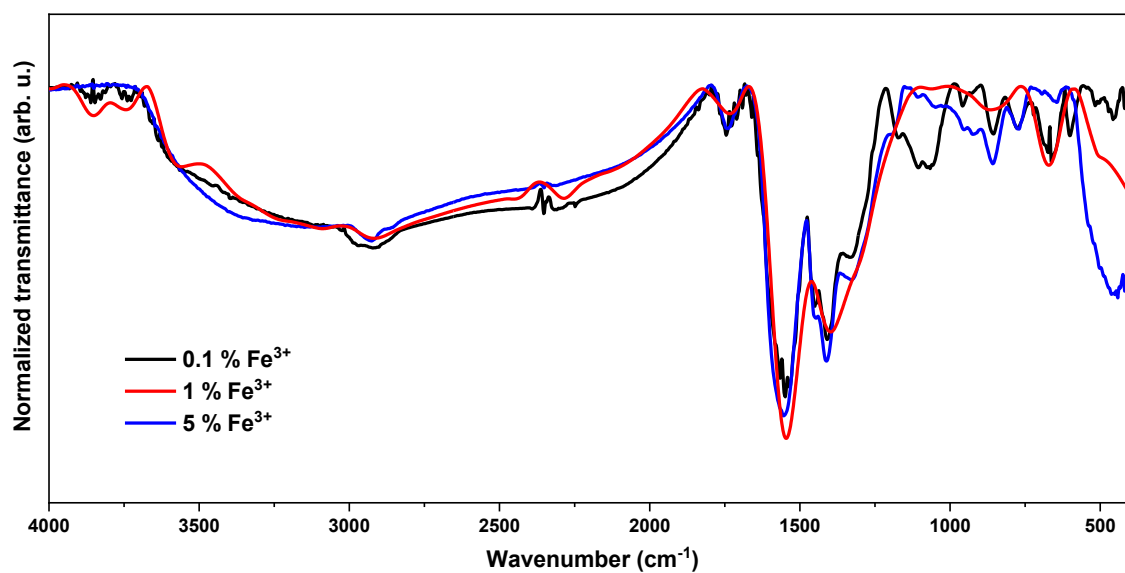
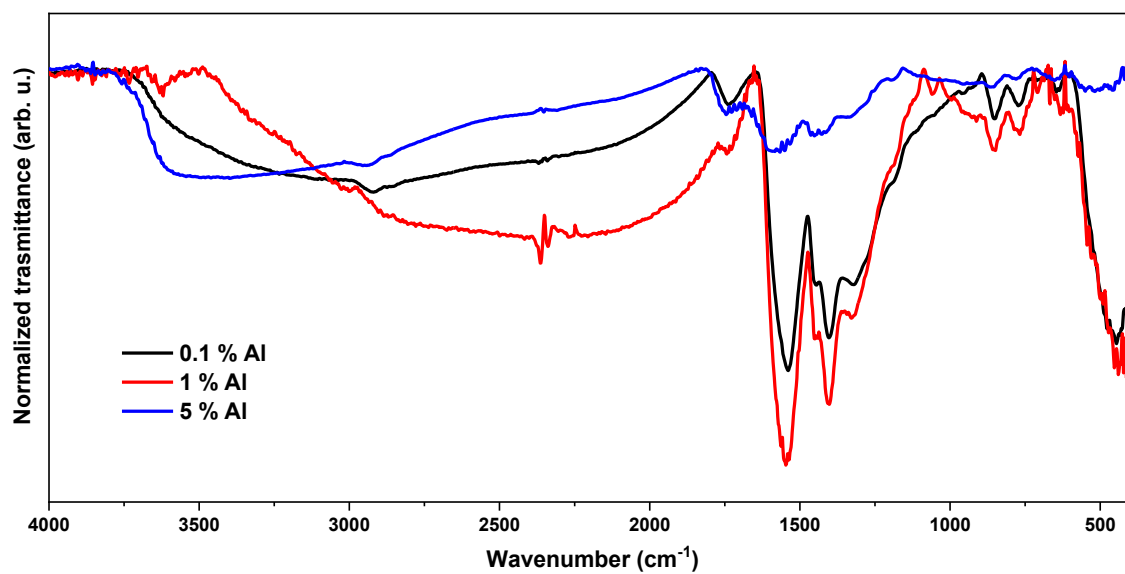


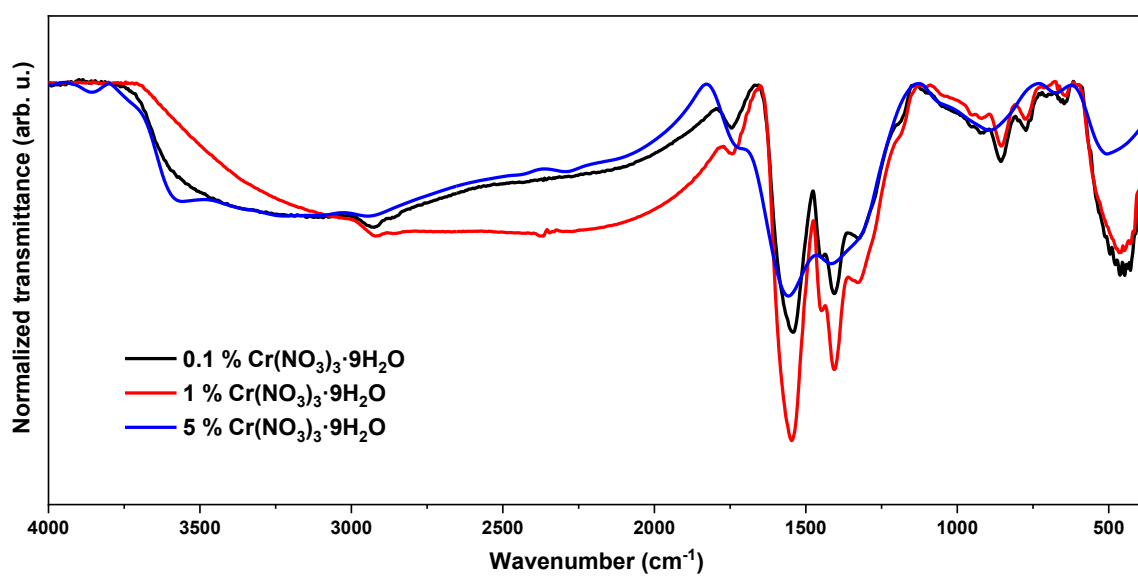
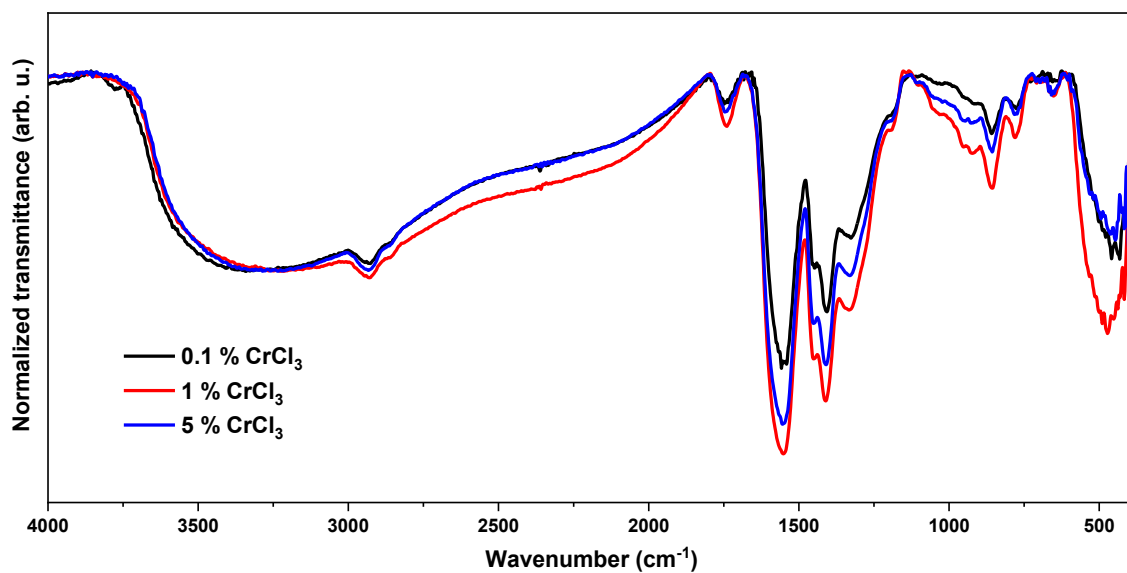
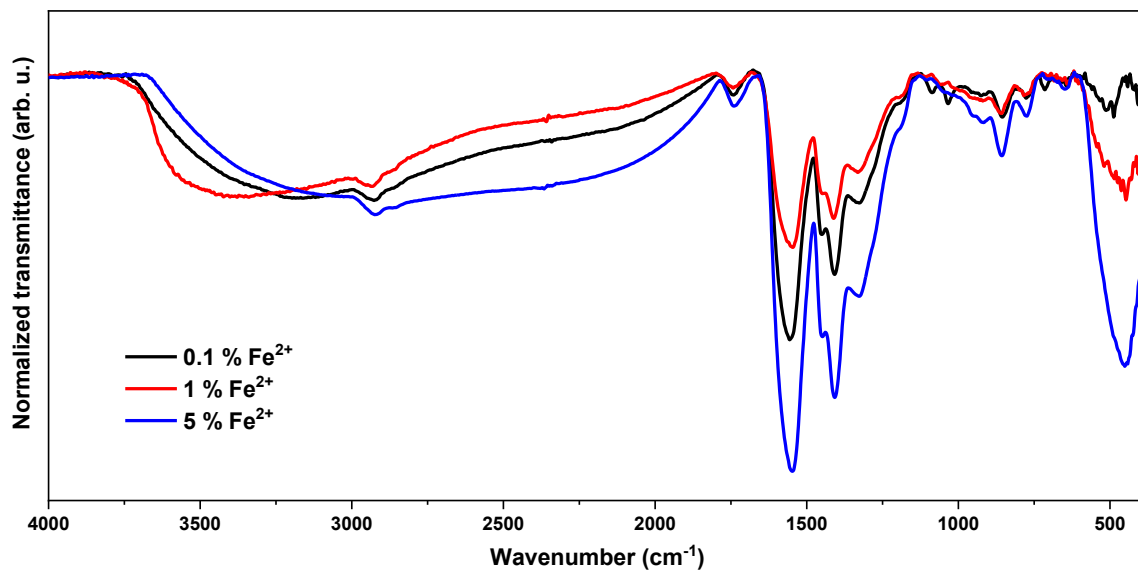
## Appendix II HRTEM images of metal-doped ZnO nanohybrids

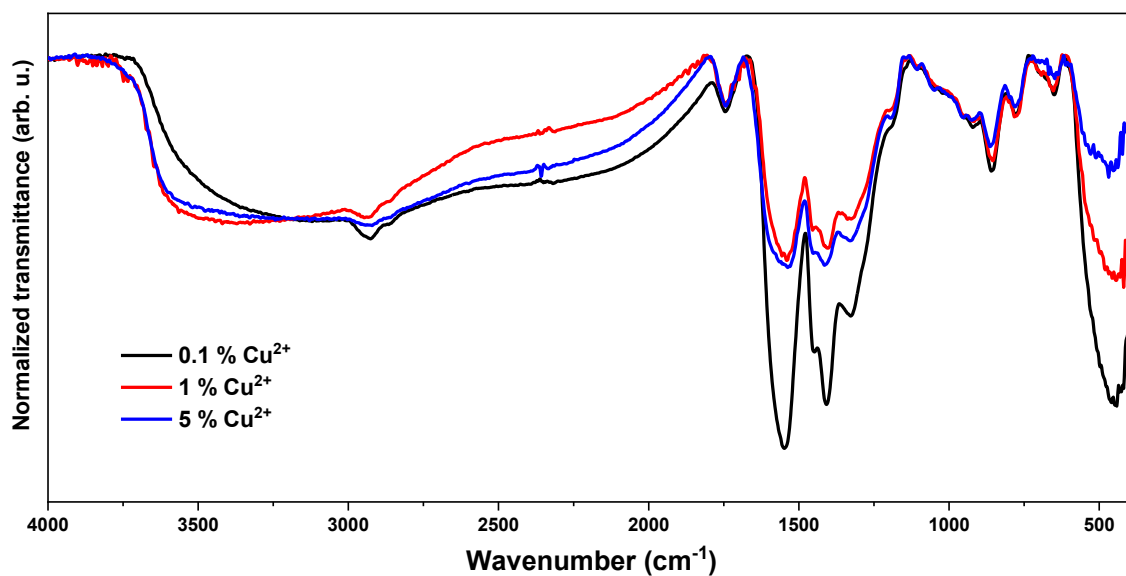
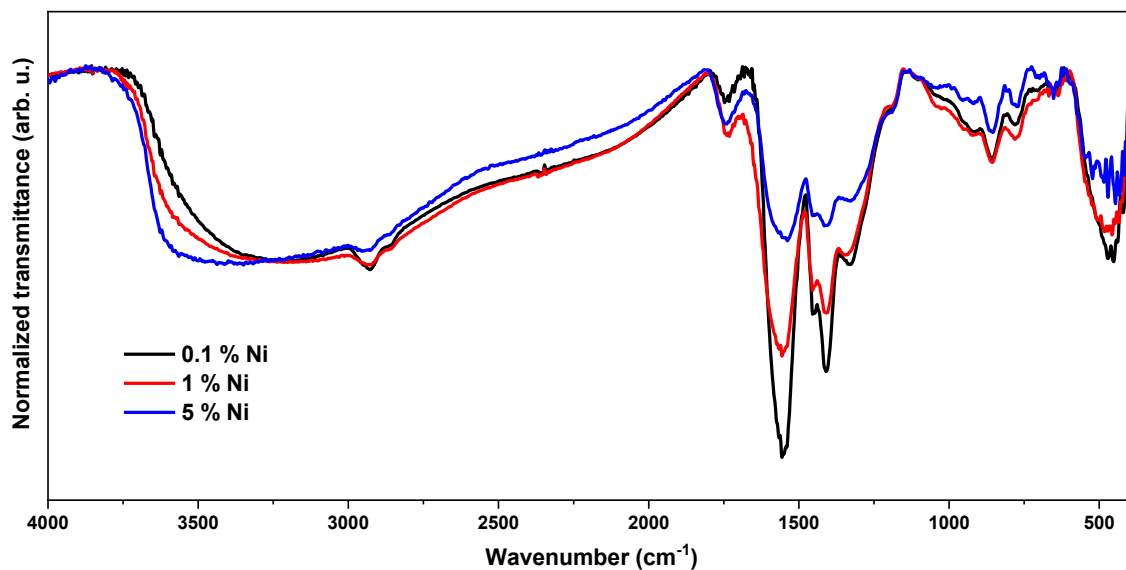
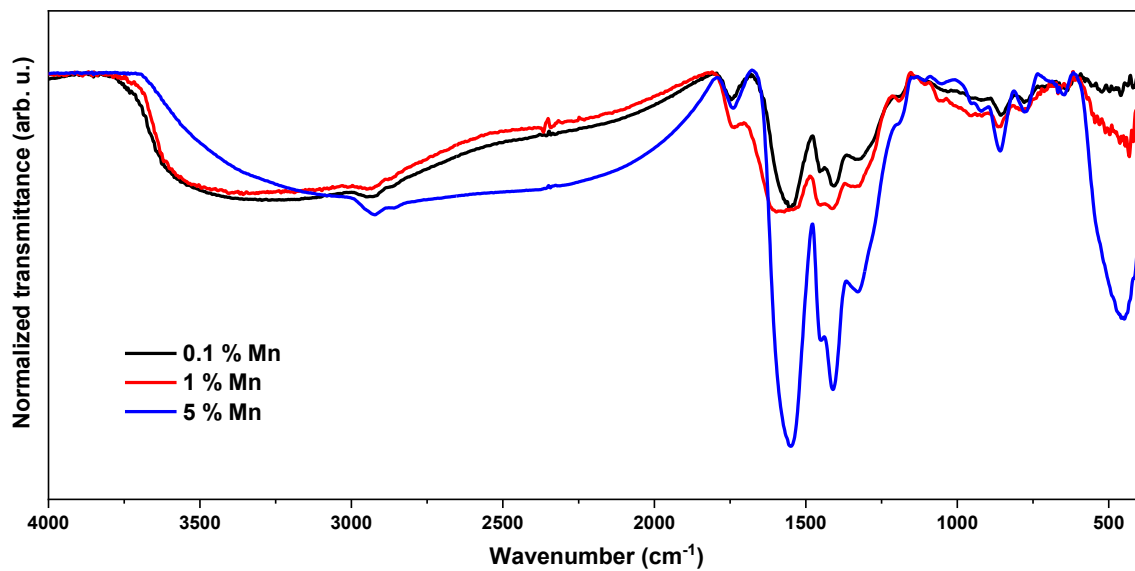


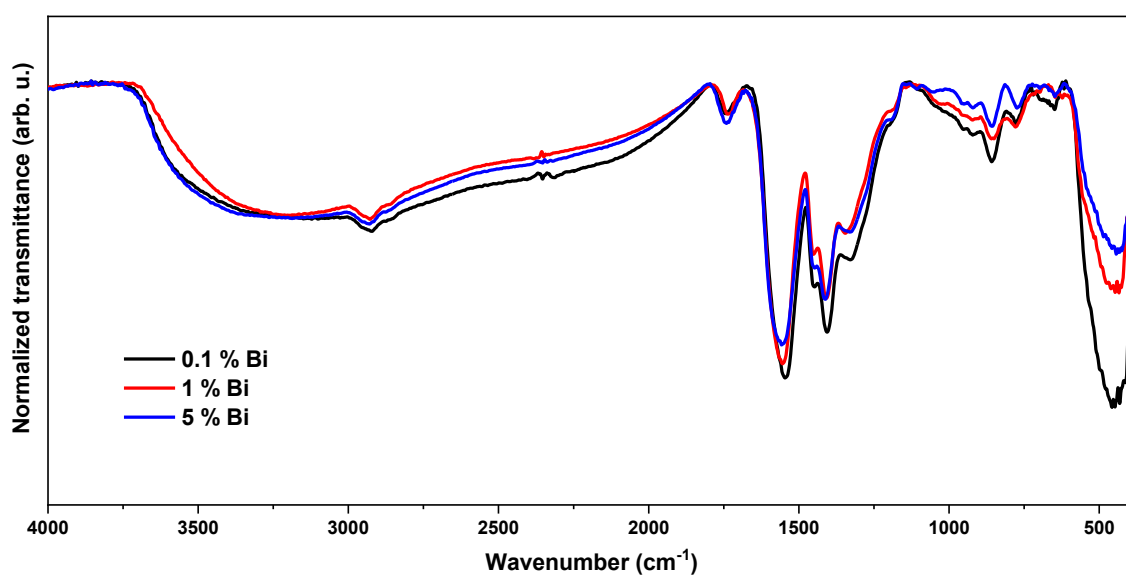
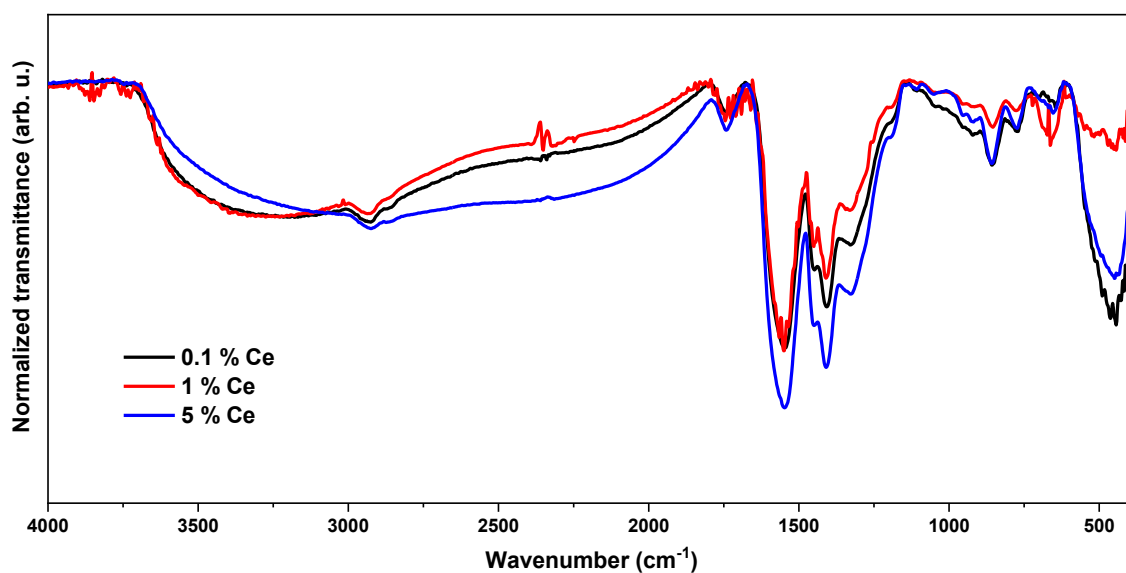
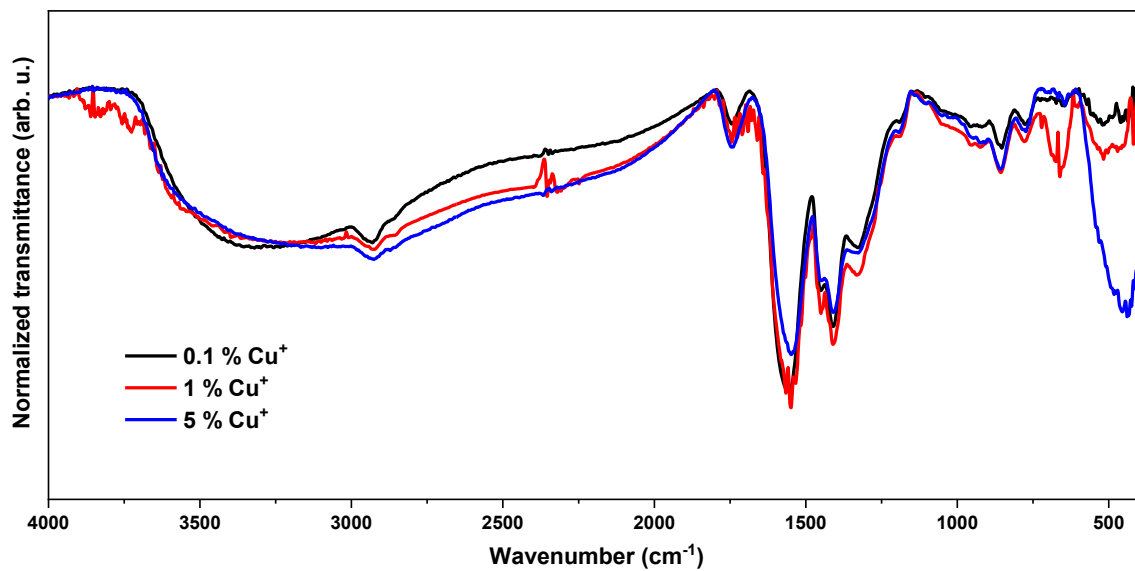


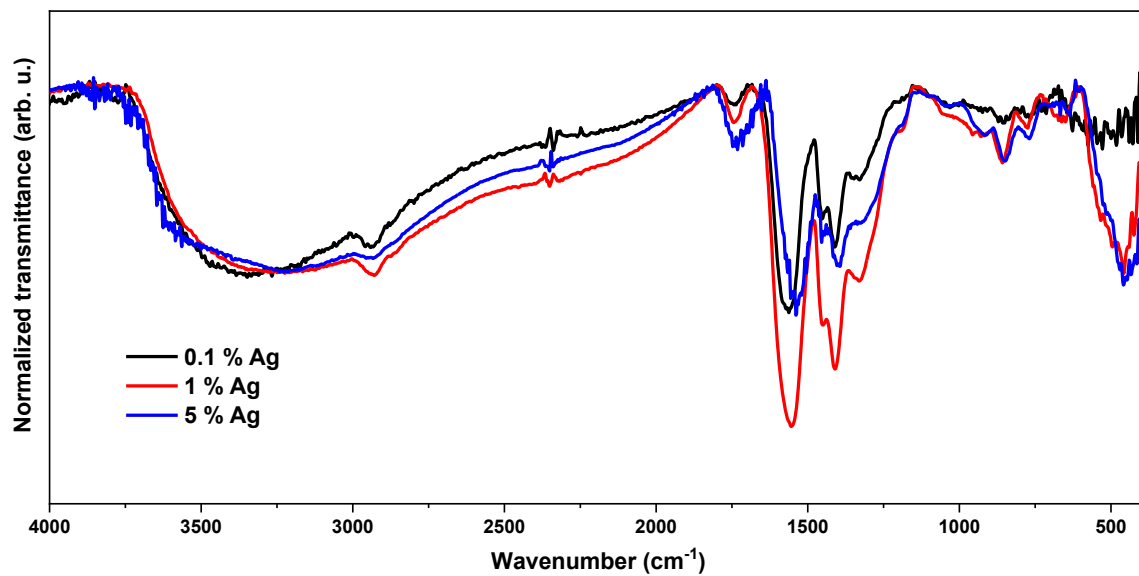
## Appendix III FTIR spectra of metal-doped ZnO nano hybrids



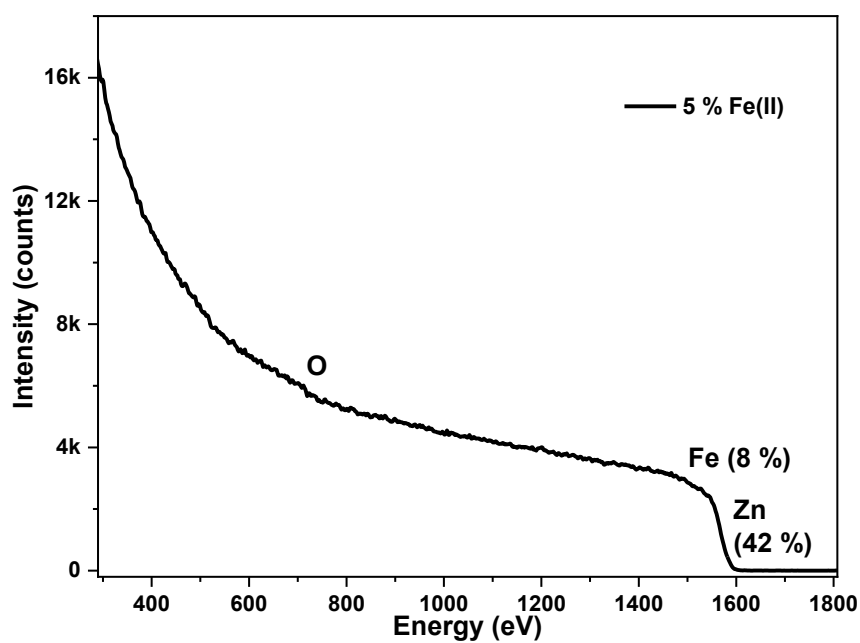
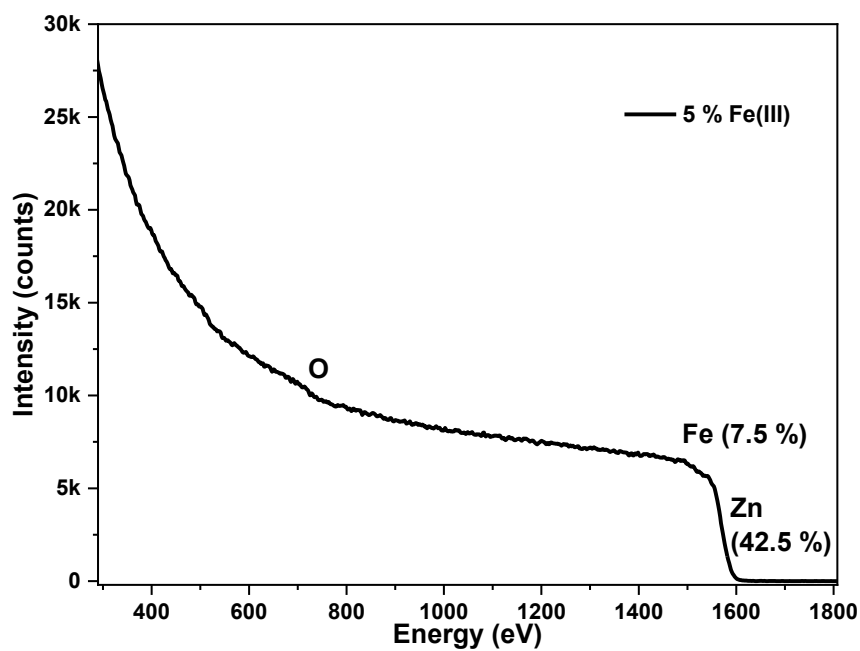


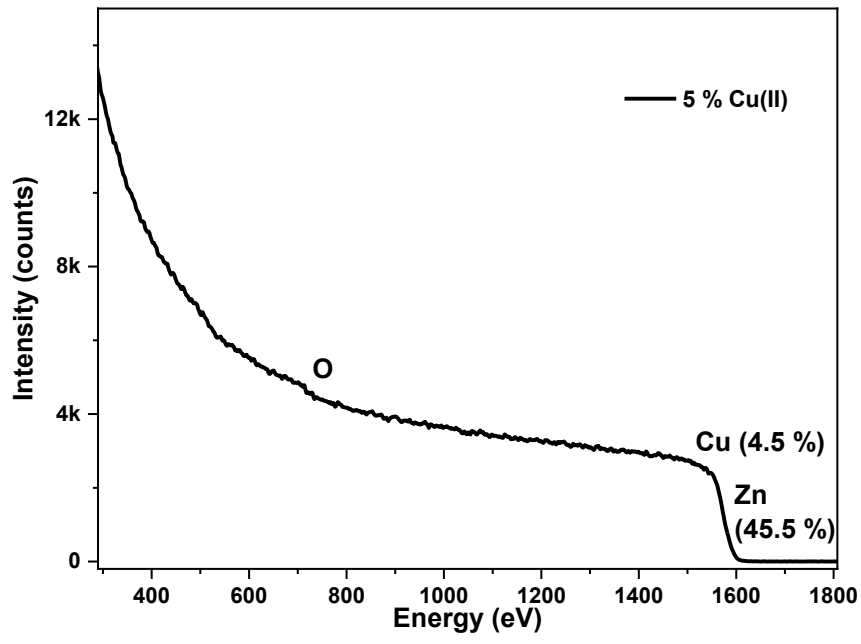




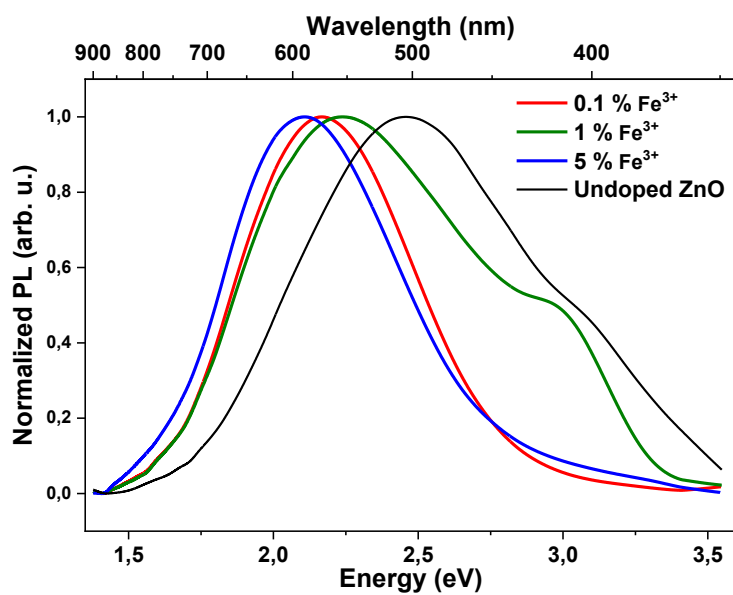
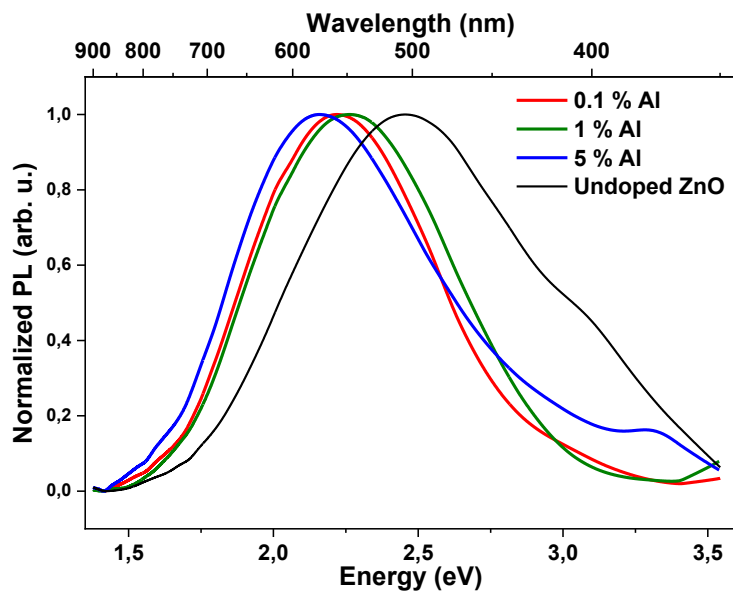


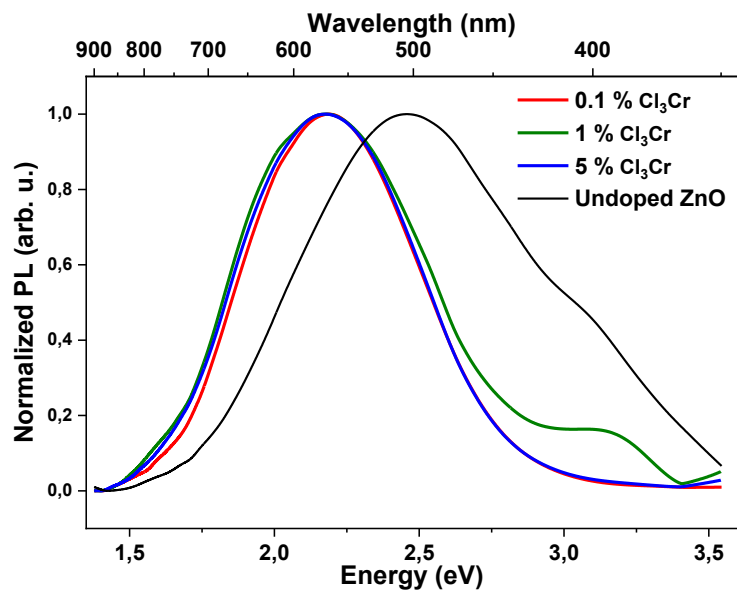
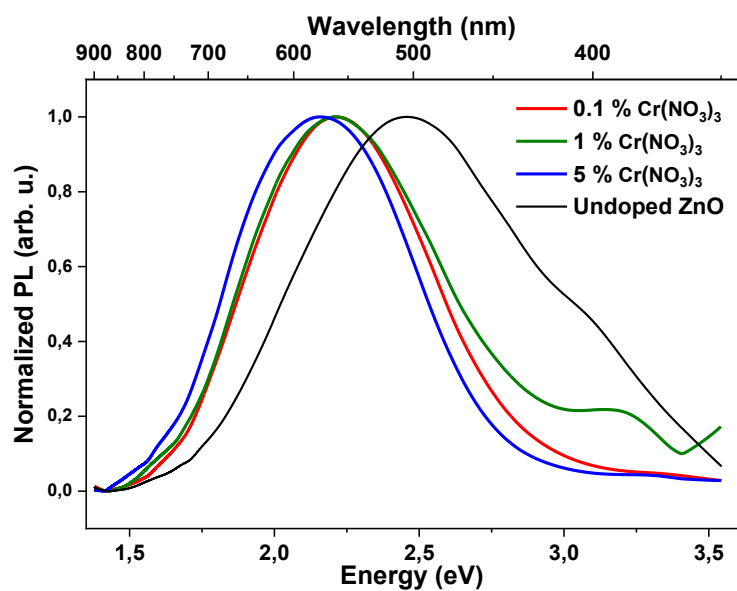
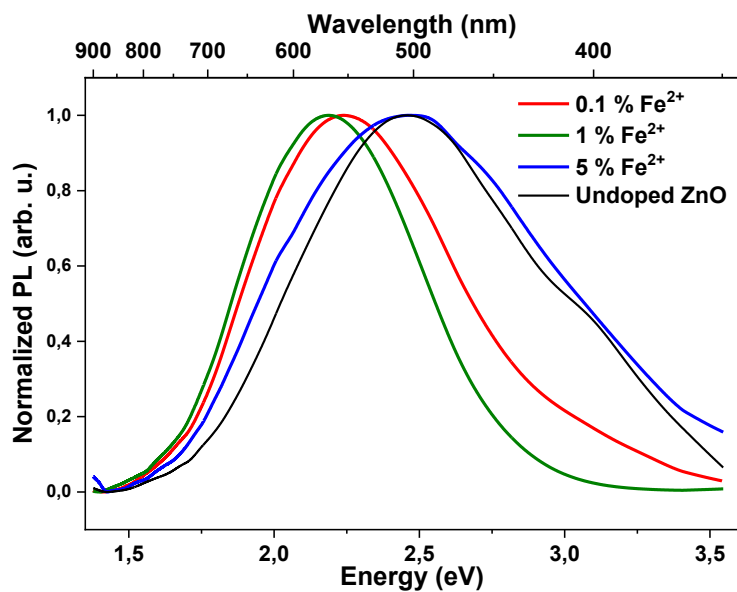
## Appendix IV RBS spectra of metal-doped ZnO nanohybrids

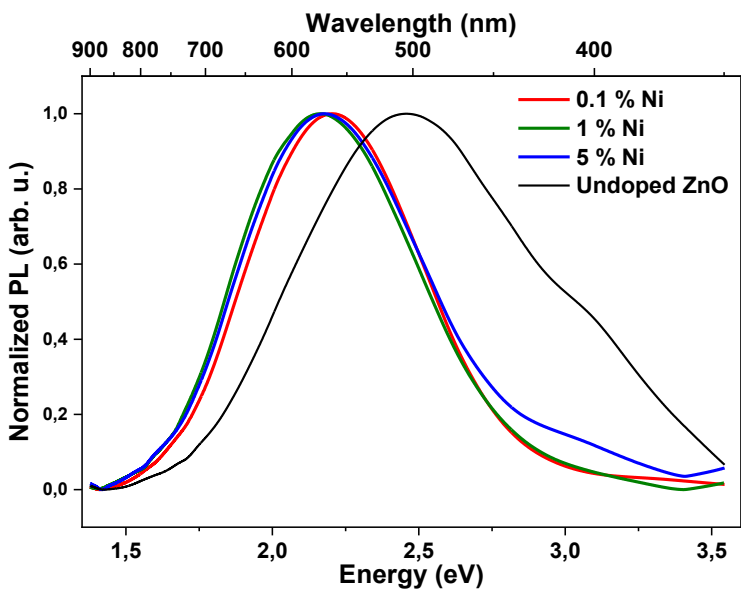
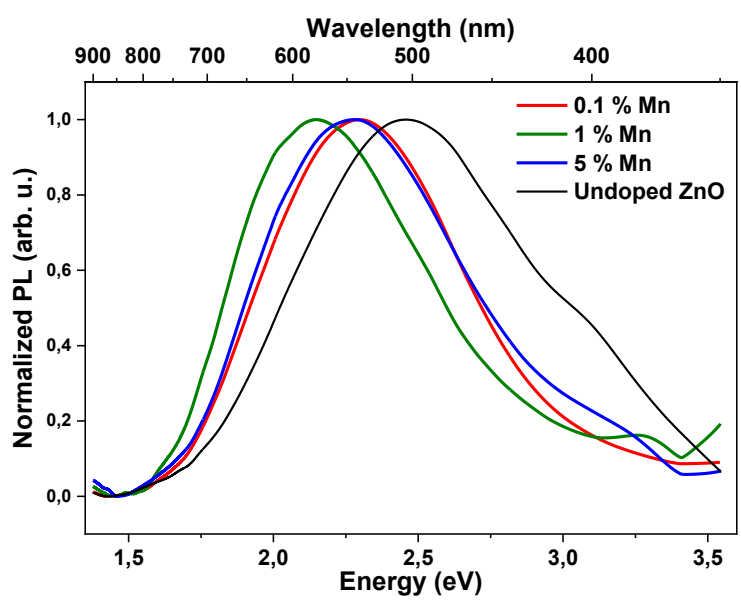
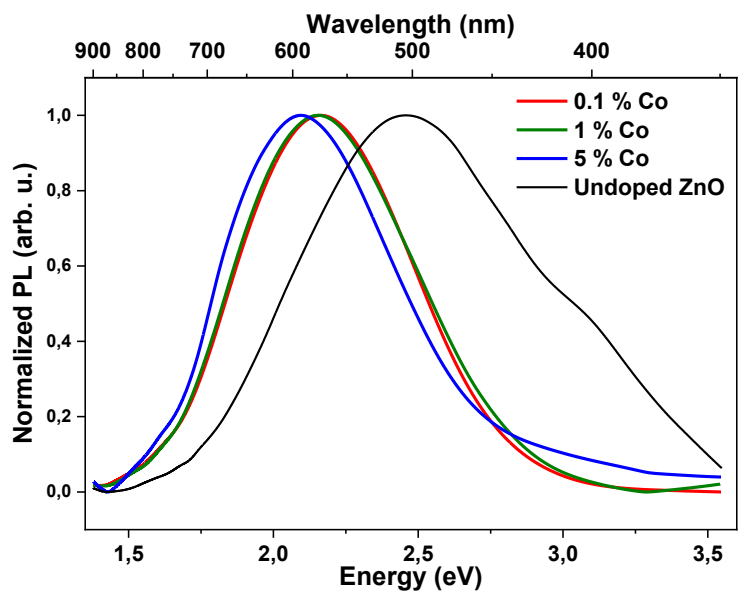


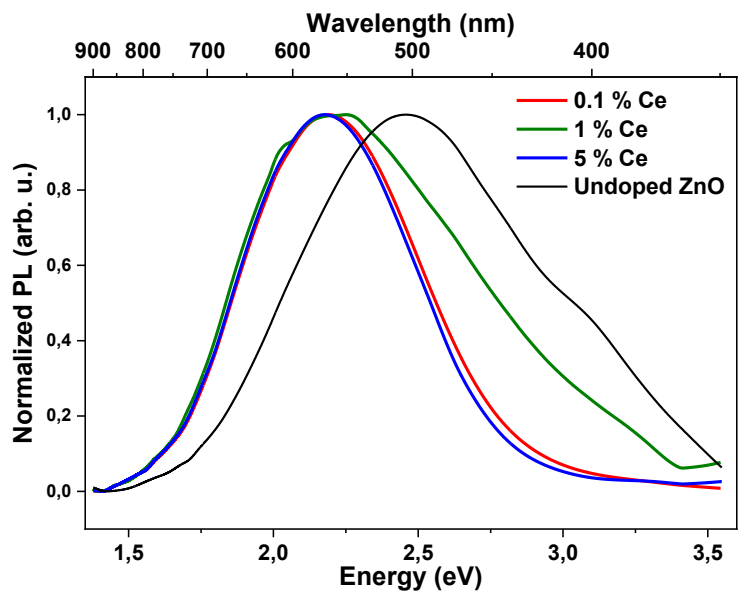
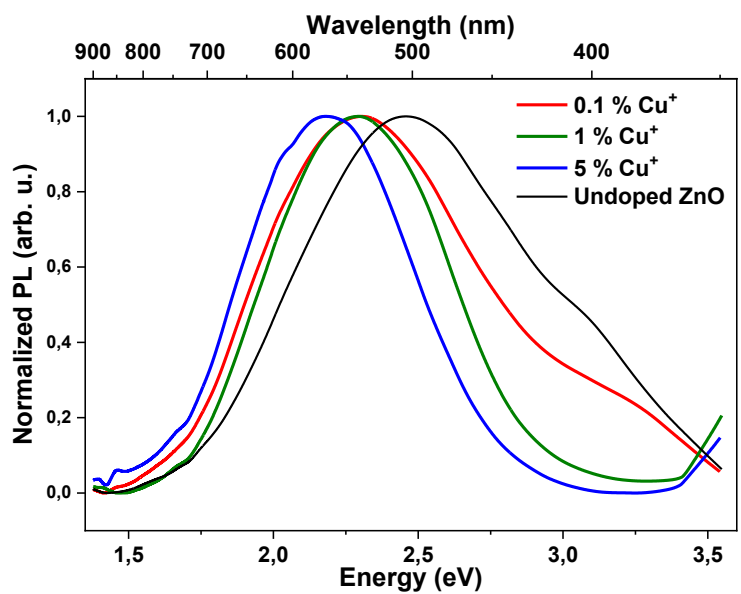
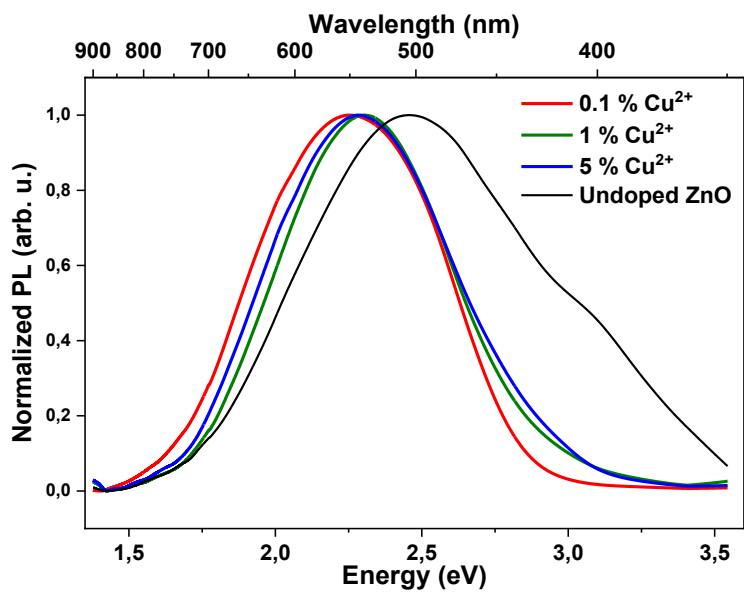


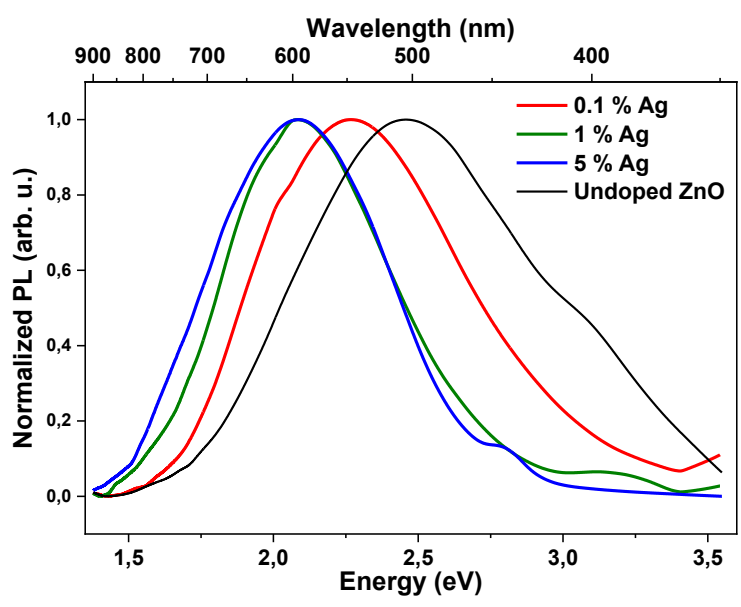
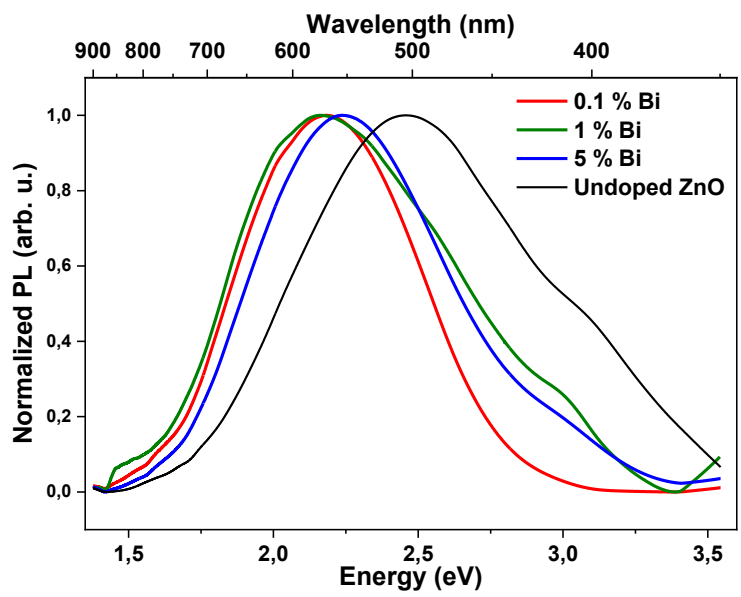
## Appendix V PL spectra of metal-doped ZnO nanohybrids



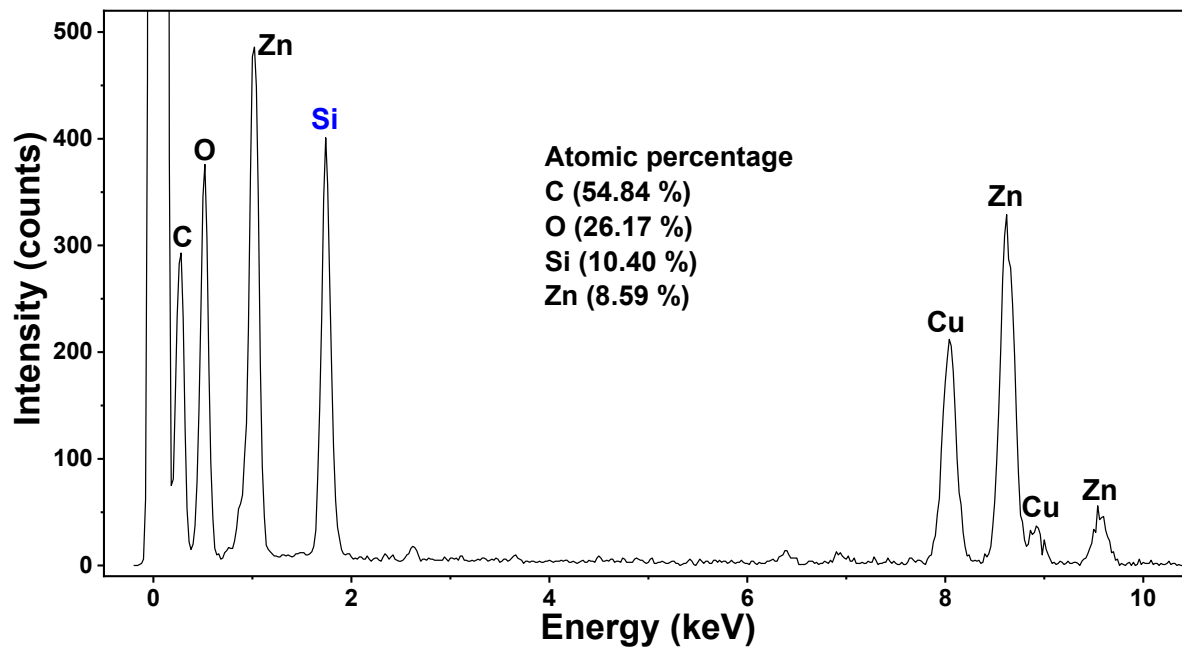




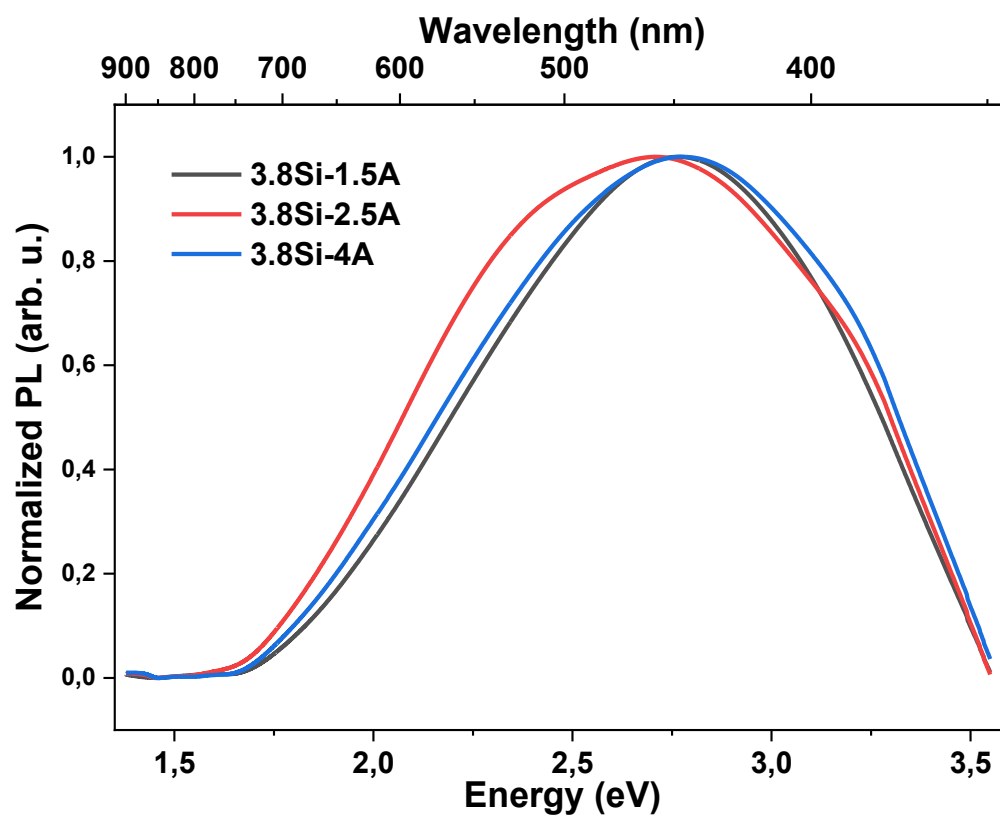




## Appendix VI EDX spectrum of silica-coated ZnO/PAA nanohybrid (3.8Si-1A)



## Appendix VII PL spectra of silica-coated ZnO/PAA nanohybrids







## FOLIO ADMINISTRATIF

### THESE DE L'UNIVERSITE DE LYON OPEREE AU SEIN DE L'INSA LYON

NOM : Zhang

DATE de SOUTENANCE : 30/06/2020

Prénoms : Yu

TITRE : Fabrication, structural and spectroscopic studies of wide bandgap semiconducting nanoparticles of ZnO for application as white light emitting diodes

NATURE : Doctorat

Numéro d'ordre : 2020LYSEI046

Ecole doctorale : MATÉRIAUX DE LYON

Spécialité : Matériaux

RESUME : The present thesis studies ZnO nanoparticles embedded in a mesospheric polyacrylic acid (PAA) matrix synthesized via a hydrolysis protocol. The mesospheric ZnO/PAA hybrid structure was previously proved efficient in emitting visible light in a broad range, which results from the deep-level intrinsic defects in ZnO nanocrystals. To further tune the photoluminescence (PL) spectrum and improve the PL quantum yield (PL QY) of the material, metal-doped ZnO and silica-coated ZnO/PAA are fabricated independently. For ZnO doped with metallic elements, the nature, concentration, size and valence of the dopant are found to affect the formation of the mesospheres and consequently the PL and PL QY. Ions larger than  $Zn^{2+}$  with a higher valence tend to induce larger mesospheres and unembedded ZnO nanoparticles. Doping generally leads to the quenching of PL, but the PL spectrum can still be tuned in a wide range (between 2.46 eV and 2.17 eV) without degrading the PL QY by doping small ions at a low doping concentration (0.1 %). For silica-coated ZnO/PAA, an optimal coating correlatively depends on the amount of TEOS and ammonia in the coating process. The amount of TEOS does not affect the crystal structure of ZnO or the PL spectrum of the material, but high concentration of ammonia can degrade the PAA mesospheres and thicken the silica shell. A thin layer of silica that does not absorb too much excitation light but completely covers the mesospheres proves to be the most efficient, with a drastic PL QY improvement of six times. Regarding the application, the materials suffer from thermal quenching at temperatures high up to 100°C, at which white light emitting diodes (WLEDs) generally operates. However, silica-coated ZnO/PAA induces higher emission intensity at room temperature to make up for the thermal quenching.

MOTS-CLÉS : ZnO nanoparticles, nanohybrids, photoluminescence, photoluminescence quantum yield, doping, silica coating

Laboratoire (s) de recherche : Institut des Nanotechnologies de Lyon

Directeur de thèse: Bruno Masenelli

Président de jury :

Composition du jury :

Prof. G. Chadeyron (ICCF-Sigma Clermont), Dr. F. Charra (IRAMIS-CEA Saclay), Dr. C. Andraud, (LC ENS Lyon), Prof. H. Rinnert (IJL-Univ. Lorraine), Prof. B.Masenelli (INL-INSA Lyon), Dr. A Apostoluk (INL-INSA Lyon)